Investigations of Carbon Nanohorns and Covalently-Linked Nanocomposites of Nanocarbons and other 2D-Materials

A Thesis Submitted for the Degree of
Doctor of Philosophy

By

K. Pramoda

New Chemistry Unit
Jawaharlal Nehru Centre for Advanced Scientific Research
(A Deemed University)
Bangalore-560064, INDIA

April 2017

DECLARATION

I hereby declare that the matter embodied in this thesis entitled **"Investigations of Carbon Nanohorns and Covalently-Linked Nanocomposites of Nanocarbons and other 2D-Materials"** is the result of investigations carried out by me under the supervision of Prof. C. N. R. Rao, FRS at the New Chemistry Unit, Jawaharlal Nehru Centre for Advanced Scientific Research, Bangalore, India and that it has not been submitted elsewhere for the award of any degree or diploma.

In keeping with the general practice in reporting scientific observations, due acknowledgement has been made whenever the work described is based on the findings of other investigators.

_____

(K. Pramoda)

CERTIFICATE

I hereby certify that the matter embodied in this thesis entitled **"Investigations of Carbon Nanohorns and Covalently-Linked Nanocomposites of Nanocarbons and other 2D-Materials"** has been carried out by Mr. K. Pramoda at the New Chemistry Unit, Jawaharlal Nehru Centre for Advanced Scientific Research, Bangalore, India under my supervision and it has not been submitted elsewhere for the award of any degree or diploma.

Prof. C. N. R. Rao

(Research Supervisor)

ACKNOWLEDGEMENTS

At the very onset, I take my opportunity to express deep sense of gratitude to **Prof. C. N. R. Rao, FRS, my research supervisor,** for introducing me to the fascinating field of Nanoscience. It was his enthusiasm that instigated in me the desire to pursue science and has continued to inspire me ever since. I acquired most, if not all, my scientific knowledge from him. His innovative ideas and ability to handle any problem in the simplest of the ways has been the strength behind the completion of this work. It has been a fulfilling experience to work under his encouraging and full spirited guidance. I shall remain ever indebted to him for bearing with me throughout the course of the work. He has not only been instrumental in shaping up my research, my career but my entire personality, my outlook towards life as a whole. I consider myself extremely lucky to receive all the love and care that he has bestowed me with. I do not have words to thank him; I express my deepest gratitude to him.

My sincere thanks to my collaborators; Prof. U. Ramamurty, Prof. S. K. Pati, U. Gupta, M. Chhetri, S. Kadambi, Dr. Ram Kumar, Dr. K. Gopalakrishnan, Dr. K. Moses, Dr. H. S. S. R. Matte, A. Bandyopadhyay for valuable discussions and help during the course of the experiments.

I use this opportunity to thank Dr. A. Govindaraj for helping me in experimental and official work.

I would like to thank Dr. Sebastian Peter, Prof. A. Sundaresan, Prof. G.U. Kulkarni, Prof. S. M. Shivaprasad for the courses they offered and the wonderful classes.

My sincere thanks to all Technical staffs of NCU and CPMU, especially Mr. Kannan (TEM), Mr. Karthik (TEM), Dr. Jay (TEM), Mrs. Usha (TEM), Mr. Vasu (TGA and IR), Mr. Mahesh (NMR), Mr. Shiva Kumar (Absorption spectroscopy), Mr. Anil (PXRD), Mr. Peer, Mr. Mune Gowda and Mr. Dileep.

My deepest thanks to Mrs. Indumati Rao and Mr. Sanjay Rao for their love, affection and hospitality extended to all of us during the course of my association with them.

I am extremely thankful to all my past and present labmates, Dr. H. S. S. R. Matte, Dr. Subrahmanyam, Dr. Leela, Dr. Neenu, Dr. Shashi, Dr. Urmimala, Dr. Nitesh, Dr. Moses, Dr. Barun das, Dr. K. Goplakrishnan Dr. Sunita Dey, Dr. Ram Kumar, Dr. Rana Saha, Lingampalli, Sreedhara, Manoj, Manjeet, Uttam, Anand Roy, Dr. Deepa, Dr. Manjunath, Dr. Pratap,

Manjunath, Manaswee, Monis, Amit, Dr. Manish, Dr. Salman for their fruitful discussions, help and co-operation.

I thank Administrative Staff, Academic staff, Complab staff, Library staff, Hostel Staff, Mess staff, House Keeping Staff and Security staff, Mr. Victor, Mr. Gowda, Mrs. Shashi, Shweta and Mr. Naveen for their help.

I would like to thank JNC friends Murthy, Rajasekhar, Jiaul, Satya and many others for providing a wonderful atmosphere in JNC which made my stay more comfortable.

I would like to thank all University of Mysore, Department of studies in Chemistry classmates and friends.

Above all, I would like to thank my family, specially my parents, brother and sister, for all the love, affection and support they give.

The short, yet long endeavor of Ph.D. has been made possible because of the help, advice, suggestions, and support provided by multiple hands. I have taken this opportunity to mention a few of them. However, my sincere thanks extend to everyone who has played a role in making this dream a reality.

PREFACE

The thesis consists of five parts of which the **first Part** gives a brief overview of the nanocarbons and related materials. **Part 2** deals with the results of investigations of a new form of nanocarbons, single-walled nanohorns (SWNHs). In this part, **Section 2.1** describes the synthesis of SWNHs by submerged arc discharge of graphite rods in liquid nitrogen medium. Along with this, covalent and non-covalent surface functionalization of SWNHs to make them soluble in organic and aqueous medium is also presented. **Section 2.2** presents a method to dope SWNHs with nitrogen. The submerged arc discharge technique to prepare SWNHs has been extended by carrying out arc discharge in liquid argon. Various other nanocarbons such as graphene and MWNTs are obtained by the submerged arc discharge of graphite rods in DMF and water media respectively. Mechanical properties of SWNHs incorporated in poly(vinyl alcohol)-matrix (PVA) are presented in **Section 2.3**. Even a small addition of SWNHs leads to a significant enhancement in the hardness and elastic modulus of the polymer. When binary combination of SWNHs with few-layer graphene reinforced in PVA, the mechanical properties of the resulting composites show synergy, improving the stiffness and hardness.

Covalently-linked nanocomposites based on graphene form the subject matter of **Part 3**. **Section 3.1** describes the synthesis of nanocomposites of graphene with single-walled carbon nanotubes using Sonogashira and EDC coupling reactions. Assemblies generated by Sonogashira coupling exhibit high surface area and good CO_2 uptake efficiency. Graphene composites containing covalently bonded metal oxides are discussed in **Section 3.2**. On calcining this graphene-metal oxide composites in air thin metal-oxide films of TiO_2 and/or SiO_2 are obtained.

Part 4 presents covalently cross-linked MoS_2 nanocomposites with **Section 4.1** providing a brief overview of the Molybdenum disulfide. **Section 4.2** describes the synthesis of hybrid nanocomposites of MoS_2 with ZIF-8 starting with layers of 1T-MoS_2 generated by Li intercalation of bulk MoS_2. MoS_2-ZiF-8 composites show enhanced CO_2 storage capacity compared to the parent ZIF-8. Use of MoS_2-RGO composite as an electrocatalyst for oxygen reduction reaction is presented in **Section 4.3. Section 4.4** presents covalently cross-linked porous assemblies of MoS_2 and of MoS_2–RGO synthesized by the Sonogashira coupling

strategy. These 3D frameworks show high CO_2 and H_2 uptake due to the presence of pores generated by cross-linking the individual layers.

C_3N_4, MoS_2 and nitrogenated RGO (NRGO) are some of the important catalytic materials investigated for the HER after Pt. But the observed catalytic activities in these materials are somewhat marginal due to the rapid recombination of the photogenerated electron-hole pair. Coupling of C_3N_4 with MoS_2 improves the catalytic activity owing to effective charge separation. **Section 4.5** reports the HER activity of covalently cross-linked C_3N_4-MoS_2 and C_3N_4-NRGO composites obtained by the carbodimide method, the hydrogen yield being impressive in the case of the former.

In **Part 5,** borocarbonitride-based nanocomposites are examined, with **Section 5.1** describing the use of the borocarbonitride-iron pthalocyanine composite as a non-precious catalyst for the oxygen reduction reaction. Selective and simultaneous detection of dopamine and uric acid by using BCN and MoS_2-RGO composite modified electrodes is presented in **Section 5.2**.

CONTENTS

Part 1

A Brief Overview of

Nanocarbons and Related Materials.

A Brief Overview of Nanocarbons and Related Materials

1.1: Introduction

Carbon is one of the most important essential elements for life. It has the ability to form extended chains of interconnecting C-C bonds which is known as catenation. Catenation makes carbon special with the highest number of carbon compounds reported in the literature compared to any other element. Carbon has the capability of forming complex networks. Furthermore, carbon forms allotropes such as diamond, graphite nanotube and fullerene which exhibit different physical and chemical properties. Nanocarbon term is used in recent years to specify the large array of carbon materials possessing a nanoscale feature and functional properties that greatly depend on the nanoscale dimensions.[1-9] The term 'nanoscale' usually refers to those structures with the length scale applicable to nanotechnology. Generally, materials with one of the dimensions in the range of 1-100 nm fit into this category. One-dimensional (1D) carbon nanotubes (CNTs) and two dimensional (2D) graphene belong to this category. Other types of carbon materials, such as fullerenes,[10] -diamonds,[11] -onions,[12] -horns,[13] and –fibers[14] also occur as nanostructures. Schematic diagrams of some of nanocarbons are shown in Figure 1.

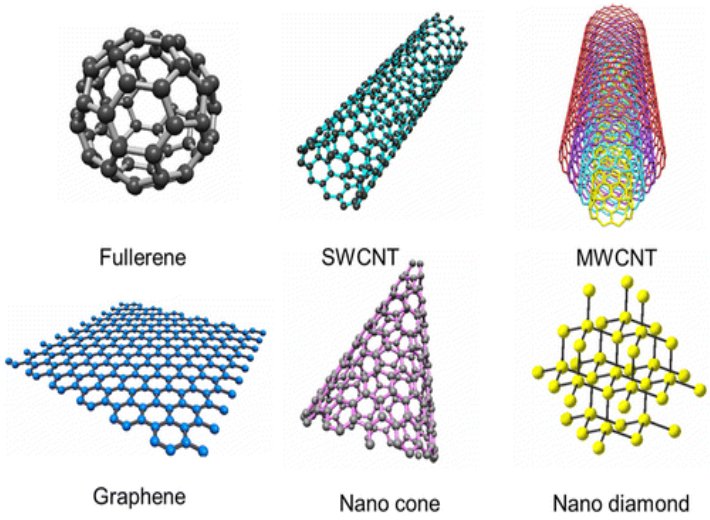

Figure 1 OD, 1D, 2D and 3D allotropes of carbon. (From ref. [7]).

Nanocarbons possess high electrical, thermal conductivity and large specific surface area along with the good mechanical strength that conventional material cannot match which makes their field of application large. Moreover, these characteristic properties can be achieved over broad range of conditions along with the diversity in their structure. Due to this reasons, nanocarbons are extensively studied in applications going from photonics and optoelectronics to biotech and nanomedicine.[1-4, 9, 15, 16] Recently, nanocarbons have gained increased focus as a catalyst in a variety of energy related applications such as Li-ion batteries, metal-air batteries, fuel cells, supercapacitors, water-splitting reactions and so on.[17, 18]

1.2: Fullerenes

The 0D form of carbon, fullerenes, contains a closed cage of carbon molecules with three-coordinate carbon atoms tiling spherical or nearly spherical surfaces. In 1970, Osawa envisioned soccer-ball shaped C_{60} molecule based on theoretical calculation.[19] In 1985, Smalley, Curl and Kroto observed a peak due to sixty carbon clusters in the mass spectrum of laser evaporated graphite with the next most abundant peak from seventy carbon cluster.[20] They proposed closed cage truncated-icosahedral structure to explain the unusual stability of C_{60} which leads to its high relative abundance in the vapour phase mass spectrum. For this novel discovery, they shared Nobel Prize in 1996. C_{60} has 20 six-membered and 12 five-membered rings with the latter providing the curvature necessary for forming a closed-cage molecule.

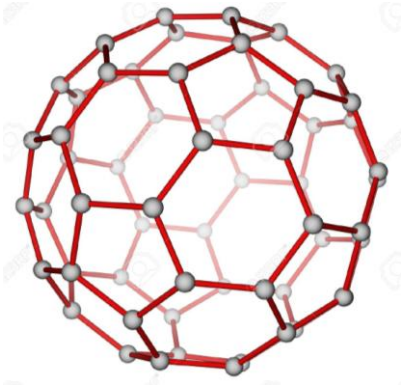

Figure 2. C_{60} Molecular Structure

Fullerenes are stable molecules. Theoretical calculations suggest that a single C_{60} molecule has a extremely high bulk modulus of 668 GPa. When compressed to 75 % of its size, it becomes harder than steel and diamond.[21] Fullerenes are the only carbon forms that

can be chemically hydrogenated and dehydrogenated reversibly due to their unique molecular structure.[22] The properties of C_{60} to accept electrons from photoexcited conjugated polymers like oligophenylenevinylene (OPV) has attracted fair attention in view of its potential application in photovoltaic devices.[23] C_{60} and other fullerenes are generally made by arc evaporation of graphite rods in inert atmosphere.[24]

1.3: Carbon nanotubes (CNTs)

In 1991, Iijima observed the carbon nanotubles deposited on the negative (cathode) electrode during direct current arcing of graphite electrodes while preparing fullerenes. Carbon nanotubes (CNTs) can be envisaged as rolled hexagonal carbon networks that are capped by pentagonal carbon rings which can be either single-walled (SWNTs) or multi-walled (MWNTs). CNTs have typical lengths of micron and are closed at either end due to the presence of five membered rings. The nanometre magnitude of the CNTs along with the characteristic electronic structure of a graphene, make these 1D form extremely unusual.[25] After Iijima's paper, growth mechanisms of CNTs has been studied and used in variety of application because of their high surface area, electronic conductivity and good mechanical strength. CNTs are extremely strong materials with the tensile strength ranges from 11 to 63 GPa, while Young's modulus is also very high, in the range of 270 to 950 GPa.[26] High thermal conductivity of CNTs (6000–3000 W/mK) arises because of the large phonon mean free path.

Synthesis

MWNTs have been traditionally prepared by the arc-evaporation of graphite.[27] A schematic diagram of the arc-discharge chamber is shown in Figure 3a. In this method, an electric arc is struck between two graphite electrodes, with a current of 60-100 A across a potential of 20-30 V in a helium atmosphere (approximately 500 torr). Carbon evaporates from the anode and gets deposited at the cathode, thereby yielding a cathodic stub. The cathodic stub contains a high yield of MWNTs. CNTs can be prepared in large quantities using plasma arc-jets, by optimizing the quenching process in an arc between a graphite anode and a cooled copper electrode.[28] SWNTs were first synthesized by metal-catalyzed DC-arcing of graphite electrodes.[29] The graphite anode is normally filled with metal powders such as Fe, Co or Ni and pure is used as the cathode. Large quantities of SWNTs as seen in Figure 4a can be obtained by using a mixture of 1 at.% of Y and 4.2 at.% of Ni.[30]

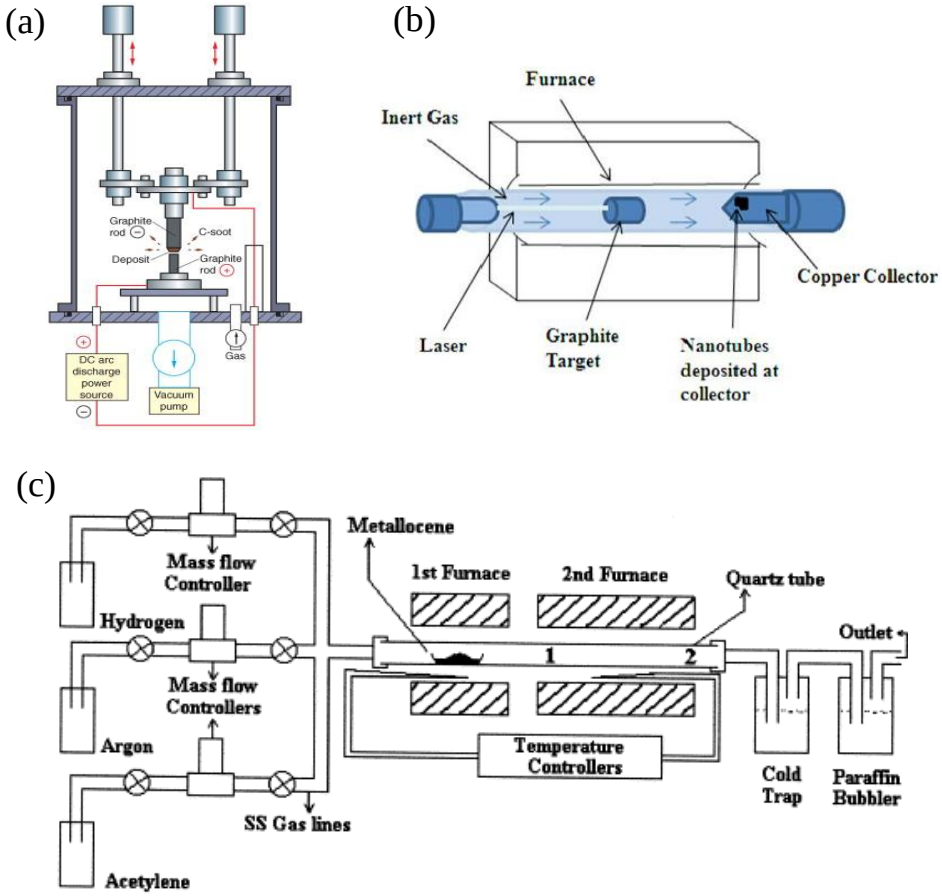

Figure 3. Schematic diagram of (a) arc discharge chamber, (b) high-temperature laser ablation and (c) organometallic pyrolysis experimental set-ups.

SWNTs have also been synthesized by the condensation of a laser-vaporized carbon-nickel-cobalt mixture at 1200 ^{o}C.[31] A sketch of the laser-ablation set-up is shown in Figure 3b.

The decomposition of hydrocarbons over small metal catalyst has been the focus area of research in the synthesis of CNTs due to their scalability and ease of synthesis [32]. MWNTs have been obtained by the decomposition of acetylene under inert conditions over Fe or Co/graphite[33a] and Fe/SiO_2.[33b] The presence of transition metal catalyst is essential for the formation of nanotubes and the diameter of the nanotube is determined by the size of the metal particles.[34] Aligned MWNT bundles have been obtained by chemical vapor deposition over transition metal catalyst embedded in the pores of mesoporous silica or in the channels of alumina membranes.[35] Plasma-enhanced chemical vapor deposition on nickel-coated glass using acetylene and ammonia has been employed by Ren *et al.*[36] to obtain aligned MWNT bundles.

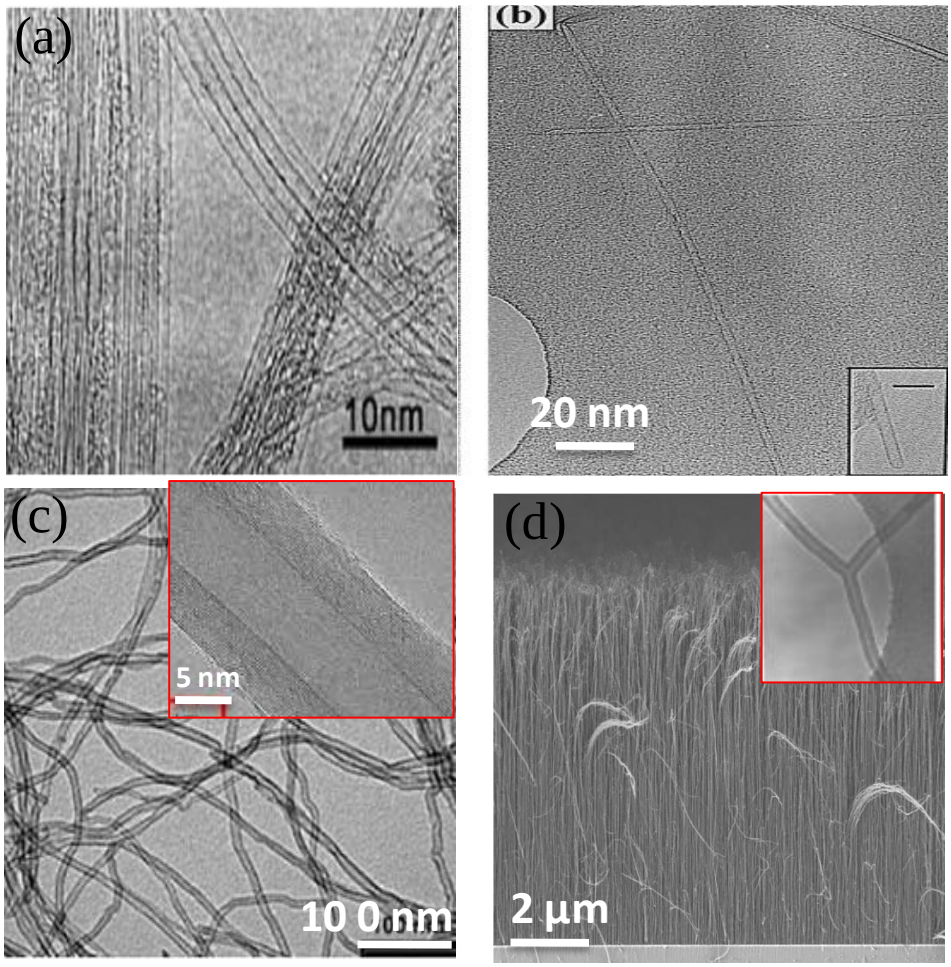

Figure 4. Electron microscope images of (a, b) SWNTs prepared by arc discharge process, (c) MWNTs, (d) aligned MWNT bundles (Inset: Y-junction nanotube).

Pyrolysis of organometallic compounds such as ferrocene, cobaltocene, nickel or iron pthalocyanine in a two stage furnace provides a straight forward procedure to prepare CNTs.[37] The organometallic compound acts as a source of carbon as well as metal catalyst nanoparticles. In a typical synthesis, a metalocene is slowly sublimed from furnace 1 to furnace 2 placed at a higher temperature in an inert atmosphere (Figure 3c). Additionally hydrocarbons such as acetylene, methane, etc can also be used as secondary carbon sources. The parameters that can be varied in these pyrolysis reactions are sublimation rate of the organometallic precursors, flow rate of the carrier gas and the pyrolysis temperature. This method has yielded MWNTs,[38a] aligned MWNT bundles,[38b] and aligned metal filled MWNTs,[38c] Y-junction MWNTs,[38d] as well as SWNTs under various experimental conditions.

Structure

A SWNT can be visualized by cutting C_{60} across the middle and adding a graphene cylinder of same diameter. If the C_{60} is bisected normal to a three-fold axis, a zigzag tube is formed and if it is bisected normal to a five-fold axis, an arm-chair tube is formed. However, a variety of chiral nanotubes can be obtained with the screw axis along the axis of the tube (armchair and zigzag nanotubes are achiral).

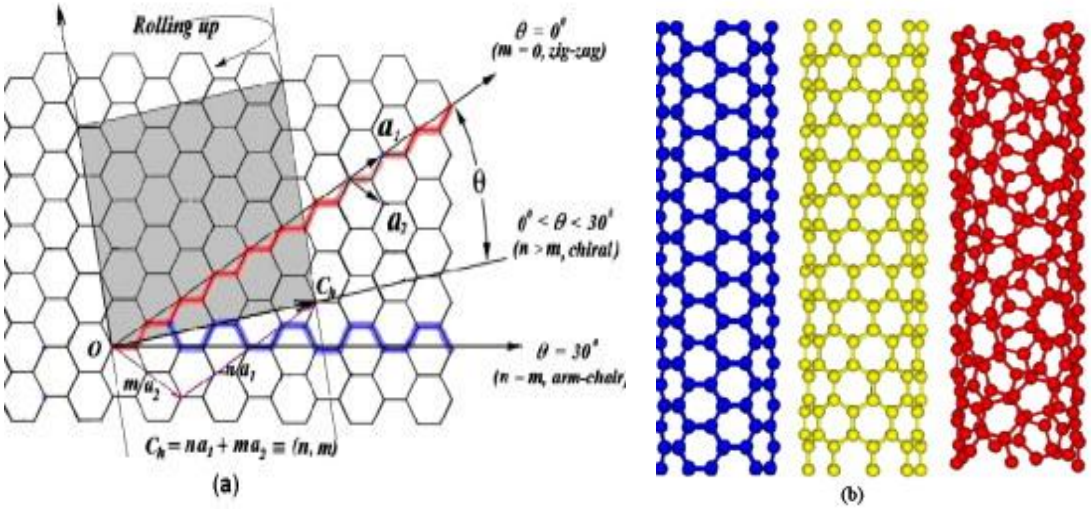

Figure 5. (a) 2D graphene sheet showing chiral vector C_h and chiral angle θ and (b) Schematic models of armchair, zigzag, chiral nanotubes (From ref. [27]).

Nanotubes can be defined by chiral vector C_h and chiral angle θ using the equation,

$$C_h = na_1 + ma_2 \quad (1)$$

Where a_1 and a_2 represent unit vectors in graphene 2D lattice and n, m are integers (Figure 5a).

The vector C_h connects two crystallographically equivalent sites on a 2D graphene sheet while the chiral angle is the angle it makes with respect to zigzag direction. A tube is formed by rolling up the graphene sheet that two points connected by the chiral vector coincide. The nanotube can be specified by the pair of integers (n, m), which have a wide range of values. For the armchair nanotubes, $n = m \neq 0$ while $n \neq 0$, $m = 0$ for the zigzag nanotubes. For a nanotube defined by the index (n, m), the diameter, d, and chiral angle, θ, are given by the equations 2 and 3, where a = 1.42 A^o and $0 \leq \theta \leq 30^o$.

$$d = a \cdot (m^2 + m \cdot n + n^2)^{1/2}/\pi \quad (2)$$

$$\theta = \arctan\left(-(3)^{1/2} \cdot m\right)/2n+m) \quad (3)$$

It should be noted that nanotubes having chiral numbers n = m (arm-chair) are metallic and quasi-metallic if n−m is divisible by 3, while all the other nanotubes are generally semiconducting. In conventional synthetic processes for SWNTs, metallic nanotubes constitute 33%, the remaining being semiconducting nanotubes.

1.4: Graphene

The 2D form of carbon, called graphene (or '2D graphite'), is the mother of all graphitic forms in which carbon atoms are tightly packed in a honeycomb lattice. These 2D sheets can either be wrapped up into 0D fullerenes, rolled into 1D nanotube or stacked into 3D graphite (Figure 6).

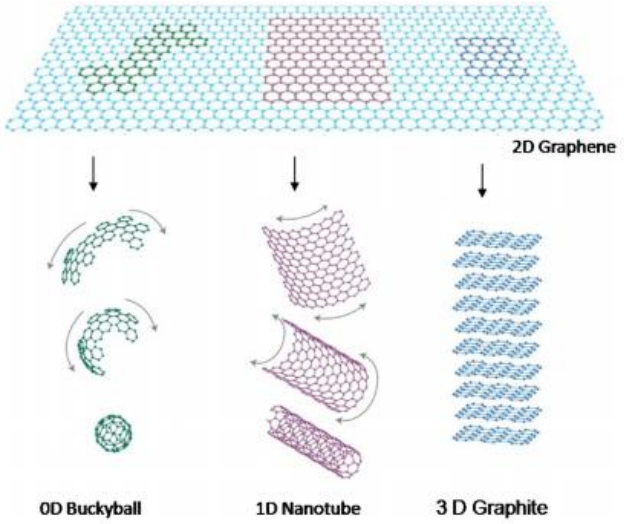

Figure 6. Mother of all graphitic forms. (From ref. [38]).

Graphene is the 2D counterpart of 3D graphite, displays good crystal quality and ballistic conduction. But some of the earlier reports indicated that, in the typical harmonic approximation, thermal fluctuations demolish the long-range order which leads to the melting of 2D lattice at any finite temperature and hence perfectly 2D crystal cannot exist.[39-42] However, a thorough investigation of the 2D crystal problem beyond the harmonic approximation has lead to the conclusion that the interaction between the bending and stretching of long-wavelength phonons could in principle steady atomically thin membranes through their deformation in the third dimension.[43-45] Theoretical investigations in 1940s[46] pointed out that the graphitic layers in their isolated form can display extraordinary characteristics. Latter, first experimental study on graphene by Novoselov *et.al*[47] showed it exhibits pronounced ambipolar electric field with a very high concentration of electrons and

holes, upto $10^{13}/cm^2$ and mobilities of ~10,000 cm^2/V at room temperature. Furthermore, other properties such has high elasticity,[48] unusual magnetic properties,[49, 50] extremely high surface area, gas adsorption[51] (H_2, CO_2 and CH_4) and charge-transfer interactions with electron-donor (-acceptor) molecules makes it more exciting for numerous applications.[52, 53] In general the term 'graphene' refers to a single-layer of sp^2 bonded carbon atoms while bi- and few-layer (3-4 layers) graphene also equally investigated due to dramatic changes in properties with the increase in number of layers.

1.4.1: Synthesis of single and few-layer graphenes

In graphite, overlapping of partially filled Pz or π orbitals perpendicular to the plane of 2D sheets causes stacking of layers (involve van der Waals forces). Attempts have been made to obtain monolayer graphene through exfoliation of bulk graphite due to the weak bonding and greater lattice spacing in the perpendicular direction as compared with small lattice spacing and stronger bonding in the hexagonal lattice plane. Graphene layers of variable thickness can be generated by micro mechanical exfoliation or peeling off layers from highly ordered pyrolytic graphite (HOPG). Manipulation and peeling of graphene layers from HOPG is carried by AFM and STM tips [54-59] while precise control over folding and unfolding of sheets could be achieved by modulating distance or bias between the tip and sample.[60] Zhang *et al.*[61] showed that by using graphitic islands attached to tip of micro-machined Si cantilever 10-100 nm thick graphene sheets can be obtained to scan over Si/SiO_2 surface. Novoselov *et al.*[47] obtained atomically thin graphene sheets from pressed patterned HOPG square meshes on a photo resist spun over a glass substrate by repeated peeling using scotch tape and were released in acetone. By dipping Si/SiO_2 wafer in acetone, monolayers of graphene can be captured. Even though mechanical exfoliation gives graphene layers of good quality (least defects), this method is not applicable for bulk scale preparations. Chemical exfoliation, on the other hand, has an added advantage of large scale productivity.

Exfoliation

During exfoliation, inter-layer spacing between stacked layers can be increased by intercalating guest molecule or by oxidizing the layers surface which are then sonicated or heated to get single-layer graphene (SGO). Classic example of chemical exfoliation involves the oxidation of graphite to graphite oxide (GO) by strong oxidizing agents like $KMnO_4$ and $NaNO_3$ in H_2SO_4/H_3PO_4 media which results in increased inter-layer spacing from 0.34 nm

to 0.95 nm.[62-66] The obtained product is ultrasonicated in DMF:water (9:1) mixture to get SGO. The SGO obtained by chemical exfoliation has a high density of carboxyl, aldehydic and hydroxyl functional groups on the surface. Chemical reduction with hydrazine hydrate is carried in order to achieve graphene-like properties.[60] The well dispersed graphene layers obtained from chemical oxidation followed by reduction are generally known as reduced graphene oxide (RGO).

Sudden heating of graphite oxide (GO) to 1050 ^{o}C causes evolution of CO_2 from functional groups which breaks GO sheets into individual layers and are known as exfoliated graphene (EG).[67, 68] Guoqing *et al.* used microwave source for thermal shock treatment to carry out exfoliation of acid intercalated graphite oxide.[69] HOPG exfoliation is also been carried out using a pulsed laser source (neodymium-doped yttrium aluminium garnet) which yields few-layer graphene (2-3 layers).[70]

Viculis *et al.*[71] obtained K^-, Cs^- and NaK_2^- intercalated graphite by treating acid intercalated/exfoliated graphite with that of alkali metals in a sealed Pyrex tube. Alkali metal intercalated graphite on vigorous reaction with ethanol gives exfoliated graphene. Schematic diagram illustrating intercalation and exfoliation of graphite is shown in Figure 7a.

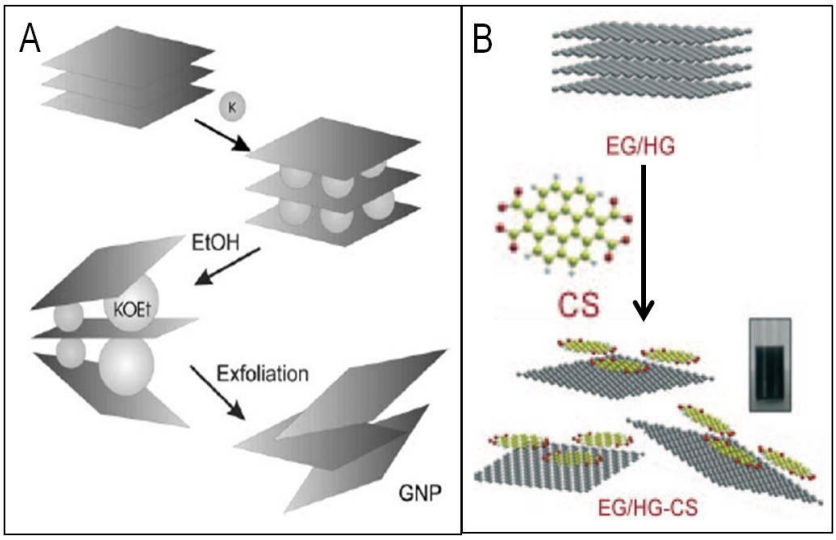

Figure 7. (A) Schematic diagram showing the intercalation of Potassium between layers followed by violent reaction with alcohol to produce exfoliated (~30 layers) thin slabs of graphite (From ref. [71]); (B) Schematic illustration of the exfoliation of few-layer graphene with Coronene tetracarboxylate (CS) to yield monolayer graphene–CS composites. (From ref. [73]).

K intercalated graphite is also been prepared by using ternary potassium salt to obtain $K(THF)_xC_{24}$ which readily get exfoliated in N-methyl-2-pyrolidine solvent resulting in single-layer graphene with negative charges on surface, and these layers can be easily deposited onto any substrate.[72] Ghosh *et al.*[73] showed that the treatment of exfoliated graphene (EG) with potassium salt of coronenetetracarboxylic acid (CS) followed by sonication results in simultaneous exfoliation and non-covalent functionalization of graphene (Figure 7b). These EG-CS complexes give stable dispersions even at higher concentrations in ionic liquids. The process of exfoliation-reintercalation-expansion of bulk graphite leads to the highly conducting graphene layers suspended in organic solvents.

Chemical vapor deposition

Chemical Vapor deposition (CVD) is the most promising, easily accessible and inexpensive route available for the deposition of high quality graphene on transition metal substrates. This technique based on the carbon-saturation of transition metals at relatively higher temperatures (1000-1500 ^oC) upon exposure to hydrocarbon gas. On cooling the substrate, thin carbon film get precipitated due to decreased solubility of carbon at low temperature. Different transition metal substrate such as Ni,[74] Pd,[75] Ru,[76] Ir,[77] and Cu,[78] have been used as substrates with various hydrocarbons like methane, ethylene, acetylene and benzene. Decomposition of various hydrocarbons on different transition metal substrates gave the conclusion that growth of graphene depends on the reaction conditions as well as on the hydrocarbon source. Methane (60-70 sccm) or ethylene (4-8 sccm) vapor diluted with hydrogen (500 sccm), and decomposed on a nickel foil at 1000 ^oC for 5-10 min results in single-layer graphene (SLG). Similarly, on a cobolt foil, acetylene (4-8 sccm) and methane (65 sccm) mixture diluted with hydrogen (500 sccm), decomposed at 800 and 1000 ^oC, respectively also yields SLG. In case of benzene, vapors diluted with hydrogen and argon was decomposed on a nickel foil at 1000 ^oC for 5 min to get SLG. In Figure 8 we show the AFM images and Raman spectra of graphene sheets prepared using methane-based CVD on nickel films deposited over complete Si/SiO_2 wafers. The relative high intensity and narrow line width of 2D (~ 2760 cm^{-1}) bands, confirms that the obtained samples mainly contain mono (or) bi-layer graphene. Moreover, graphene obtained by CVD is easily transferred to any other arbitrary substrate by etching of the underlying transition metal substrate.

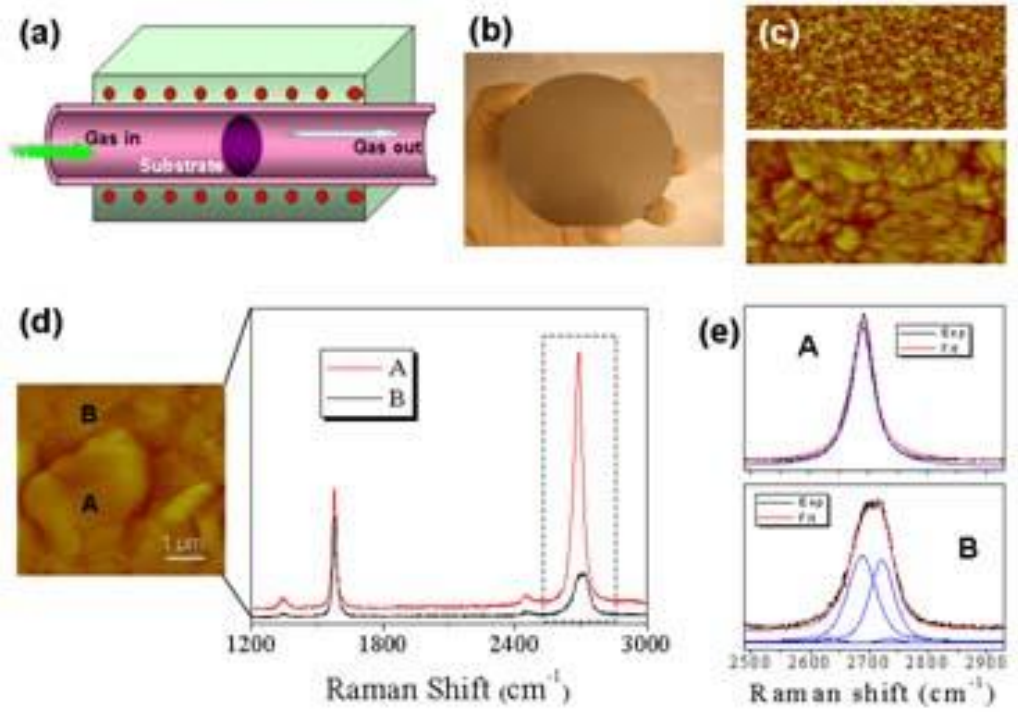

Figure 8. (a) Schematic of full-wafer scale deposition of graphene layers on polycrystalline nickel by CVD. (b) E-beam evaporated nickel film (100 nm) on a 4" Si/SiO_2 wafer. (c) AFM image of Ni film before (top) and after (bottom) thermal annealing. (d) AFM image of Graphene layers deposited on polycrystalline Ni. Raman spectra on the right were taken on locations marked as A and B. (e) G' band Lorentzian fits of the Raman spectra showed in (d) from monolayer (A) and bilayer (B) graphene. (From ref. [79]).

Arc discharge

Synthesis of graphene from arc evaporation of graphite rods in the presence of hydrogen gas is relatively new method which yields few-layer graphene (2-3 layers) with the flake size of ~100-200 nm.[80, 81] Existence of H_2 gas during arcing terminates the carbon dangling bonds, thereby avoiding the formation of closed structures. Graphene can be deposited on the inner walls of arcing chamber by employing the conditions of high current (above 100 A), large voltage (> 50V) and huge pressure of hydrogen (above 200 torr). By regulating gas pressure and currents during arc discharge, graphene with varying number of layers can be obtained. This method is also adequately employed to dope graphene with boron and/or nitrogen. Arc evaporation of graphite rod in a mixture of H_2+diborane and H_2+pyridine (ammonia) yield boron (B-HG) and nitrogen (N-HG) doped graphene,

respectively.[82] Li *et al.*[83] obtained multi-layered N-doped graphene by employing He and NH_3 atmosphere during arc discharge.

1.4.2: Doping of graphene

Molecular or atomic doping causes drastic changes in the electronic and electrochemical properties of graphene by means of opening up of intrinsic band gap.[82, 83] Therefore, doping of graphene to various extents is one of major area in graphene research and several synthetic strategies have been developed. Currently, atomic doping strategies can be sum up into two basic approaches. Firstly, methods such has chemical vapor deposition (CVD), ball milling, and bottom-up synthesis result in simultaneous synthesis and in-situ doping of graphene. Other kinds of approaches are post treatment methods such as thermal annealing of graphene oxide (GO) with heteroatom (N or B) containing precursors, wet chemical synthesis, plasma and arc discharge methods. CVD method has been widely used to get pure and high quality boron, nitrogen, phosphorous, sulfur doped graphene, even though it is expensive. Among these, boron and nitrogen doped samples are more interesting due to their similar size and valence electrons as that of carbon. During CVD, solid, liquid, or gaseous precursors containing desired foreign atoms were introduced into the growth furnace together with the carbon sources results in direct incorporation of heteroatoms into the graphene lattice.[84] Using boric acid and polystyrene as the B and C sources respectively, B-doped graphene with a doping amount of 4.3 at.% was grown on a copper (Cu) foil under the protection of H_2/Ar atmosphere at 1000 ^oC.[85] The carrier gas (Ar) transports the sublimated solid-phase feedstock towards the growth substrate. B-doped graphene can also be obtained by using boron powder as boron source and ethanol as carbon precursor, respectively.[86] N-doped graphene samples, where pyridinic N (as compared to the co-existing pyridinic and pyrrolic N) as the dominant species were prepared by using pyridine as the only precursor,[87] while acetonitrile sole source gives pyridinic and pyrrolic N-doped graphene.[88] The N-doped samples synthesized at 800 ^oC gives few-layer graphene with high nitrogen doped content (8.9 at%),[89] among which graphitic N is the dominant species, whereas at 1000 ^oC yields pyridinic and a small fraction of pyrrolic N as dominating content.[90] Ajayan *et al.*[91] reported the co-doping of graphene using methane and ammonia borane (NH_3–BH_3) as the carbon, and B (N) sources, respectively. In this method nickel foam was used as growth

template and the doping level can be tuned by adjusting the reaction parameters as well as by varying the amount of B (N) source.

In post treatment methods thermal annealing of GO with various heteroatom precursors has been realized as the most efficient approach because of the abundant oxygen functionalities and defects on GO which can act as reactive sites for doping. In addition, annealing of GO with appropriate precursors at high temperature results in regaining of its SP^2 carbon network along with the doping. For instance, annealing of RGO at 600 ^oC in NH_3 and Ar atmosphere or in BCl_3 and Ar atmosphere at 800 ^oC gives N-doped (3.06 at.%) or B-doped (0.88 at%) graphene.[92]

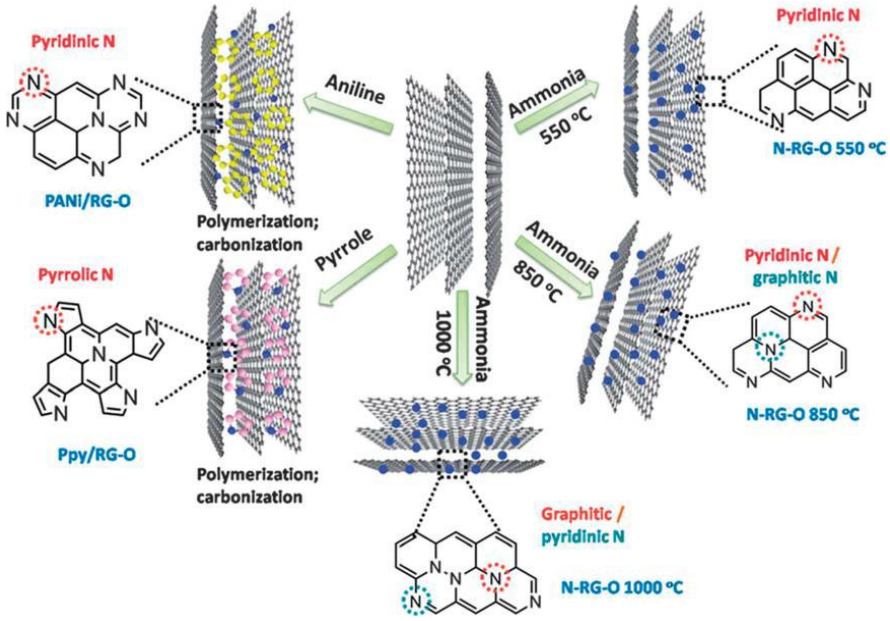

Figure 9. N-doping configuration depends on the precursor and temperature. (From ref. [92]).

Usually boron occurs in the form of BC_3 or BC_2O (due to high oxygen content of RGO) in the doped samples, whereas higher temperatures lead to the formation of more B–C bond rather than B–O bonding. In general, N-doped samples can also be obtained with high-purity ammonia gas (NH_3) which not only acts as nitrogen source but also more effective as reducing agent. Temperature appears to be a key factor in deciding N bonding configuration and doping efficiency with the 500–600 ^oC range is optimal for the overall stability of all the

N species (amino, pyrrolic, pyridinic, and possibly graphitic N) as reported in the literature.[93, 94]

Lower temperature of 300–500 ^{o}C yields N bonding configurations including amino, amide, and pyrrolic N, whereas high temperature of 800 ^{o}C gives pyridinic and pyrrolic N as the dominant species.[95-98] Temperatures higher than 800 ^{o}C gives graphitic N as dominant species due to burning of some pyridinic and pyrrolic N by oxygen released from GO which leads to reduced N content.[96] In doping graphene not only does the reaction conditions but also the heteroatom precursor are important, since the nature of heteroatom doped will vary for each precursor. Besides B and N, doping of halogens such as Cl, Br and F have also been reported to modify structure and properties of single and few-layered graphene.

1.4.3: Properties of graphene

Surface area and gas adsorption

Theoretical calculations predicted that the surface area of single-layer graphene can approach as high as 2600 m^2/g,[99] whereas that for few-layer graphene is 270-1550 m^2/g.[100] Patchkovskii *et al.*[101] by computational studies predicted that the H_2 adsorption capacities of graphene can approach the values that set by the US Department of Energy (DOE) (6.5 wt% and 62 kg of H_2 per m^3). Ghosh *et al.*[102] compared H_2 uptake of different few-layer graphene samples namely diamond graphene (DG), exfoliated graphene (EG) and hydrogenated graphene (HG) with surface area. DG, EG and HG showed an uptake of 1.2, 1.7 and 1.0 wt%, respectively at 77 K and 1 atm and adsorption is found to be directly proportional to the surface area of sample under study (Figure 10a). Maximum adsorption of 3 wt% was achieved at 298 K and 100 atm for EG. Kumar *et al.*[103] showed that CO_2 adsorption on graphene also depends on the surface area and they compared CO_2 uptake of different graphene samples with the activated charcoal. Four graphene samples, EG, HG, RGO, and SGO, were examined. Among the samples studied SGO has the lowest surface area of 5 m^2/g, EG shows high surface area of 640 m^2/g, whereas activated charcoal (AC) showed 1250 m^2/g. CO_2 uptake values range between the 5–45 wt% at 195 k and 0.1 MPa for the graphene samples, with EG exhibiting the highest uptake. Graphene samples showed lesser CO_2 uptake compared to AC because of huge number of surface functional groups in the latter. AC showed an uptake of 64 wt% at 195 K and 1 atm, whereas uptake of CO_2 by EG at

298 K and 50 bar was 51 wt%. Similarly, uptake of methane (CH_4) on graphene samples and activated charcoal was recorded at 273 and 298 K and at a constant pressure of 5MPa.

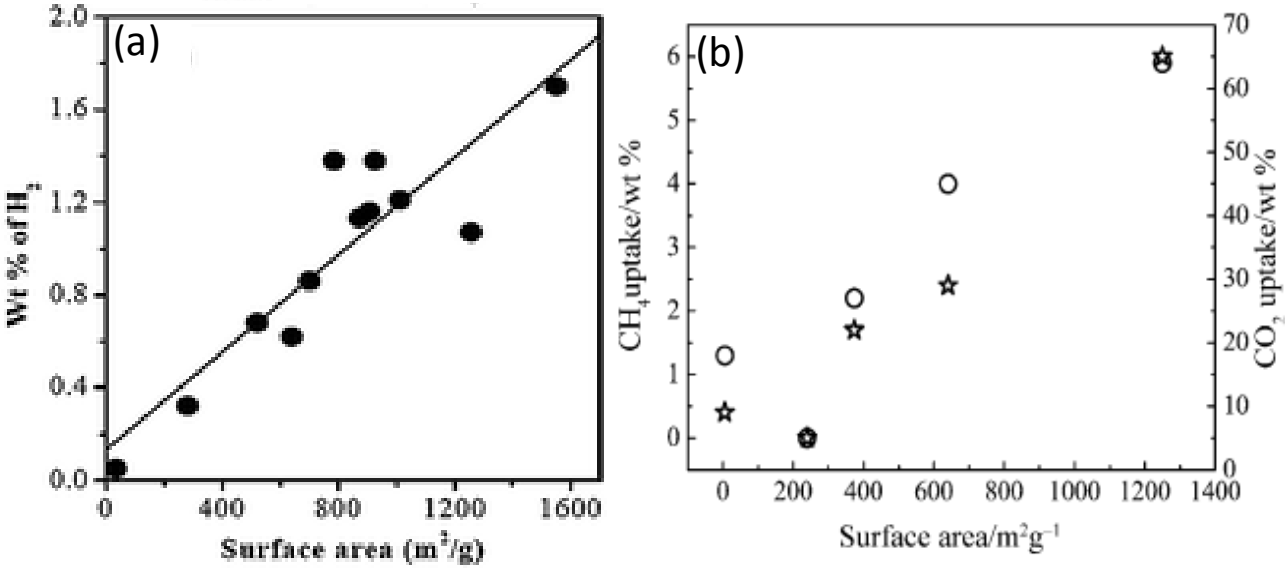

Figure 10. (a) Linear relationship between the BET surface area and weight percentage of hydrogen uptake at 77 K and 1 atm for various graphene samples and (b) Plot of weight percentage of CO_2 (at 195K and 1 atm) and methane (at 298K and 5MPa) uptake versus surface area for different graphene samples. (From ref. [102]).

The CH_4 adsorption of the different graphene samples varies between 0 and 3 wt % at 273 K while activated charcoal shows an uptake of 6 and 7 wt% at 298 K and 273 K, respectively. Figure 10b shows the CO_2 and methane uptake of graphene samples as well as activated charcoal with their surface areas.

Molecular Charge-Transfer

Carbon nanostructures display marked changes in their electronic structure and properties on interaction with electron-donor and –acceptor molecules.[104] For example, charge-transfer (CT) interaction of C_{60} with electron donating molecules like organic amines both in the ground and excited states is well documented.[104] Stiffening or softening of the G-band frequencies of single layer graphene films on interaction with various aromatic molecules has been studied by Dong *et al.*[105] The G-band of few-layer graphene progressively softens (i.e. shift to lower frequency) with the increasing concentration of electron donors molecules such as aniline and tetrathiafulvalene (TTF), while nitrobenzene

and tetracyanoethylene (TCNE), electron-acceptors, stiffen (i.e. shift to higher frequency) the G band (Figures 11a, b).[53, 104, 106] Furthermore, both electron-donor and –acceptor molecules with increase in concentration broadens the G-band along with decrease in intensity of the 2D-band. The ratio of intensities of the 2D and G bands, 'I(2D)/I(G)' is another sensitive probe which was used to examine the extent of doping of graphene by electron-donor and -acceptor molecules.

Detailed investigations of charge-transfer (CT) doping effect of Br_2 and I_2 vapors on single to multi-layer graphene (1-4 layers) pointed out that CT effect is more prominent in single and –bi layer graphene as compared to that of multi-layers (3-4 layers).[107] These complexes showed stiffening of the Raman G-band with the appearance of new bands in the electronic spectra indicating the molecular CT between the halogen molecules and nanocarbons. The extent of CT interactions in these complexes varies in the order of $ICl>Br_2>IBr>I_2$ which is consistent with the estimated range of electron affinities.[108] A quantitative approximation of the degree of CT in these doped samples is obtained from X-ray photo electron spectroscopy (XPS).

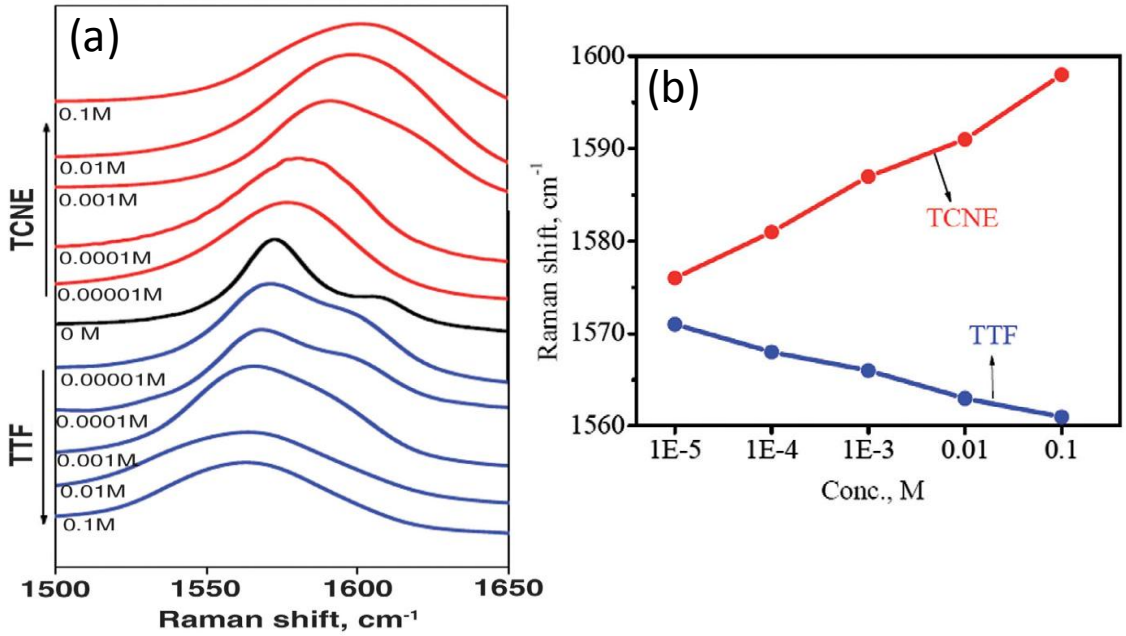

Figure 11. (a) Shifts of the Raman G-band of graphene caused by interaction with varying concentrations of TTF and TCNE, (b)Variation in the Raman G-band position of graphene on interaction with varying concentrations of electron-donor (TTF) and electron-acceptor (TCNE) molecules. (From ref.104).

Electrical resistivity of graphene films also found to be altered systematically with and without CT interactions. For instance, the electrical resistance is higher in presence of aniline (electron-donor), whereas lowest in the presence of nitrobenzene (electron-acceptor). Additionally, surface area of the graphene sample also influence the magnitude of CT interaction with electron-donor/acceptor molecules.[104]

Density functional theory (DFT) calculations showed that CT induced changes in graphene giving rise to mid-gap molecular levels with the tuning of band gap region near the Dirac point and elucidated how they different from the effects of electrochemical doping.[109] It has also been shown that the extent of doping depends on the coverage of organic molecules and predicted that CT interaction of graphene with donor and acceptor molecules result in n- and p-type graphene, respectively.

1.5: Raman Spectroscopy of Nanocarbons

Raman spectroscopy is an important non-destructive tool in the study and characterization of graphitic materials,[110-112] being extensively used in last four decades to characterize nanocarbons such as fullerenes, CNTs, nanohorns, -onions, graphitic fibers, -ribbons, and graphene.

The G-band: The stretching of C-C bond in graphitic materials gives rise to the so called G-band at ~1582 cm^{-1} which is common for all sp^2 carbon systems. For sp^2 carbons, Raman spectroscopy gives information regarding crystallite size, clustering of the sp^2 phase, presence of SP^2-SP^3 hybridization and chemical impurities. Raman spectroscopy is also used as successful tool for obtaining nanotube -diameter, -chirality, optical energy gap and metallic vs. semiconducting behaviour. The Raman G-band feature is similar for all sp^2 carbon systems but yet has properties capable of differentiating one carbon nanostructure from the other. The G-band is highly sensitive to strain effects in sp^2 carbons and can be used to probe any modifications to the flat geometric structure of graphene, due to strain induced by external forces, by one graphene layer on the other in few-layer graphene. G-band of SWNTs gives multiple peaks due to curvature effect,[113] whereas 2D graphene sheet generates single peak. This curvature dependence generates diameter dependence, hence making G-band as a probe for measuring the nanotube diameter. The Kohn anomaly is observed in both metallic and semiconducting systems. The real electron-hole pair creation

can occur by a phonon excitation process which strongly influences the G-band frequency and the spectral width of graphene and metallic SWNTs.

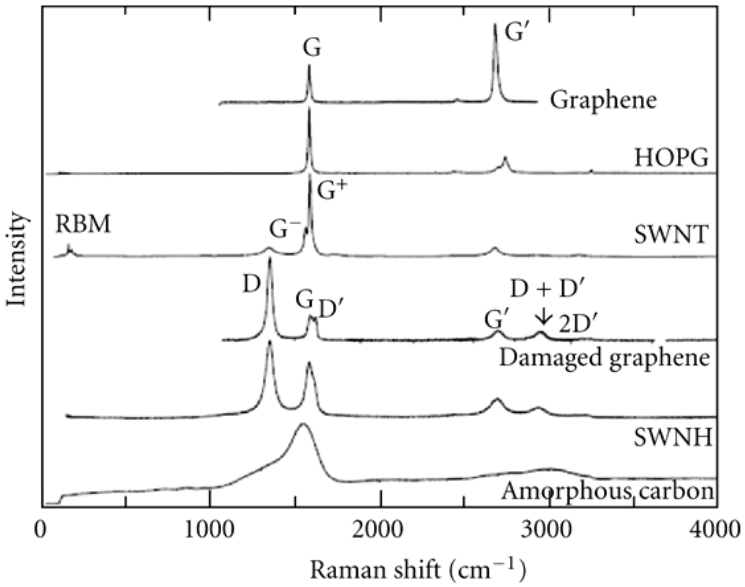

Figure 12. Raman spectra from different sp^2 nanostructures. From top to bottom: monolayer graphene, highly oriented pyrolytic graphite (HOPG), single-wall carbon nanotubes (SWNT) bundle sample (notice the presence of the RBMs at low frequencies), damaged graphene (notice the appearance of disorder-induced peaks), single wall carbon nanohorns (SWNHs), and hydrogenated amorphous carbon (Some Raman peaks are labelled in a few of the spectra).

These effects are more prominent in metallic SWNTs compared to graphene due to quantum confinement effect, and this process sensitively depends on nanotube diameter and chiral angle.[114] But these effects in graphene is strongly depends on the number of layers. Semiconducting SWNTs also show phonon energy renormalization because of electron-phonon coupling, but it is weaker than those in metallic SWNTs and for graphene.

Disorder-induced D band: The existence of disorder in SP^2 hybridized graphitic material leads to rich and intriguing phenomena in their resonance Raman spectra, thus making it more sensitive technique to characterize disorder in SP^2 carbon system. Raman spectroscopy has been widely used to identify disorder in SP^2 carbon nanostructures like nanodiamond, nanoonions, amorphous carbon, nanofibers, nanotubes and nanohorns.[115, 116]

Dispersive G' Band; Double Resonance Process: All sp^2 carbon nanostructures shows a dominant Raman feature which appears in the range of 2500-2800 cm^{-1}, as shown in Figure 12. Together with the G-band (1582 cm^{-1}), this feature is a Raman signature of graphitic sp^2 materials and termed as the G`-band to underline the fact that it is a Raman-allowed mode for $SP^2$ carbons. G`-band is a second-order two-phonon process, and interestingly shows strong frequency dependence on the excitation laser energy (E_{laser}).

The Radial Breathing Mode (RBM): The RBM mode is significant in two ways: (1) for the determination of the nanotube diameter (d_t) through the dependence of radial breathing mode frequency (ω_{RBM}) on d_t (2) for relating the ω_{RBM} and the resonant optical transition energies E_{ii} for a given tube.

Experimental data on the ω_{RBM} taken by many authors have been fit using the relation $\omega_{RBM} = A/d_t + B$. For the water-assisted super growth samples, values of A=227 $nm.cm^{-1}$ and B=0.3 cm^{-1} are obtained. This result is in remarkably good agreement with elasticity theory parameterized by the graphite elastic properties, thus directly connecting 1D nanotubes and their 2D counterpart graphene from which nanotubes are conceptually obtained.

1.1.6: Mechanical Properties of Nanocarbons

Among the several unique features of nanocarbons, especially noteworthy are high aspect ratio, huge surface area along with in plane strong C-C (δ) bonds. These features are tender spots for exciting areas of research as well as for technological advancements. Thus, a vital use of nanocarbons is in reinforcing polymer matrices considering the beneficial effects of the ultra-high stiffness and hardness shown by them. Lee *et al.*[119] measured the elastic properties and intrinsic breaking strength of free-standing monolayer graphene membranes by nanoindentation and found that it possess a excellent mechanical properties such as an elastic modulus of ~1 TPa, a strength of ~130 GPa and a breaking strength of 42 Nm^{-1}. Recent studies have shown that the addition of small amount (up to ≈1 wt%) of certain nanocarbons such as CNTs improve the mechanical properties noticeably, some cases by as much as 100%.[26, 120] Ramanthan *et al.* [121] reported that even as low as ~1 wt% graphene coupled to the poly(methyl methacrylate) (PMMA) matrix leads to huge enhancement in elastic modulus (80%) and tensile strength (20%). Although the exact mechanism accountable for this striking improvement is not exclusively understood, it is normally

considered that the large interface area accessible between the nanomaterials and polymer matrices play a major role. Additionally, nanoscale roughness results in increased mechanical interlocking with the polymer matrix which makes transfer of load easy between the matrix and filler. Prasad et al.[122] have reported that the inclusion of binary mixtures of nanocarbons causes extraordinary synergy in the mechanical properties of polyvinyl alcohol matrix (PVA).

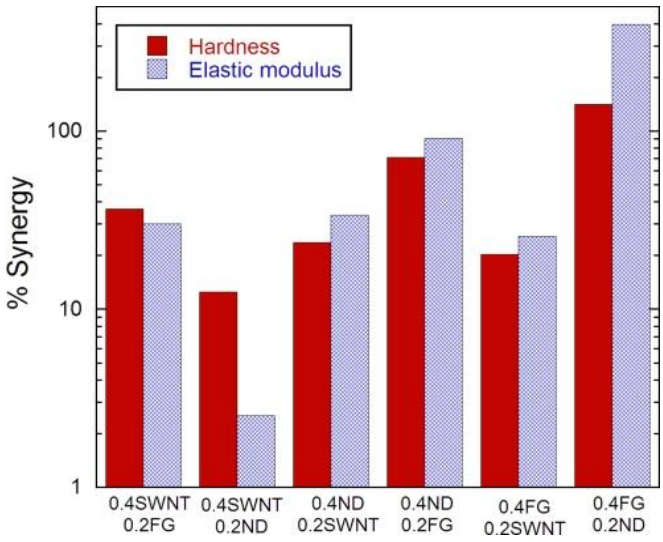

Figure 13. Percentage synergy in mechanical properties of different binary mixtures of nanodiamond, single walled nanotubes (SWNTs) and few-layer graphene.[122] *[reproduced from ref. 122]*

The synergistic effect is dramatic in the nanodiamomd (ND) plus few-layer graphene (FG) composites, with ~4- and 1.5-fold increase in elastic modulus and hardness, respectively, in PVA-0.4FG-0.2ND composite. Variation in the percent crystallinity (%) of the polymer matrix composites with 2 nanocarbons is ~2%, suggesting that increase in crystallinity is not the cause of the observed synergy.

1.7: Nanocarbon-Inorganic Nanoparticle Composites

Nanostructured metal oxide/chalcogenides have emerged as promising functional materials in applications such as energy storage and conversion technologies, including fuel cells, supercapacitors and lithium ion batteries. Using the inorganic nanoparticles in

combination with high surface area nanostructured carbon supports, such as carbon nanotubes or graphene, would be exceedingly beneficial. These nanocarbons underlying the inorganic nanoparticles offer an electrically conducting support, control the particle size, and enhance the catalytic activity of nanoparticles through strong electrochemical coupling.[123] Furthermore, structural, surface and electronic properties of nanocarbons can be modified through doping with various heteroatoms such as sulfur or nitrogen.

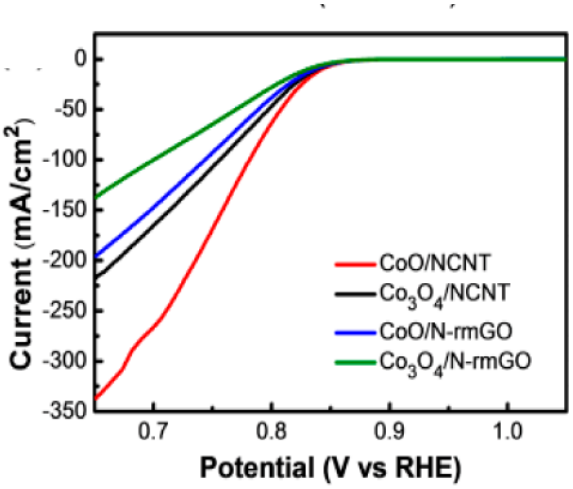

Figure 14. Oxygen reduction polarization curves recorded with the CoO/NCNT, CoO/nitrogen doped reduced GO (N-rmGO) hybrids, Co_3O_4/NCNT and Co_3O_4/NrmGO hybrids. (*Reproduced from ref. 126*).

Co_3O_4 nanocrystals grown on mildly oxidized graphene oxide (GO) showed superior oxygen reduction reaction (ORR) activity than bare Co_3O_4 nanoparticle, free GO, and their physical mixture.[124] Co_3O_4/RGO hybrid display high ORR performance in alkaline solutions as compared to commercial Pt/C catalyst (20 wt % Pt on Vulcan carbon black) while also exhibits good electrochemical stability. On the other hand, a $Co_{1-x}S$/RGO nanocomposite has also been reported which afford high ORR catalytic activity among all cobalt chalcogenide based ORR catalysts in acidic media.[125] Degree of oxidation of graphene surface has direct effect on performance of these hybrids since defect sites and functional groups on graphene can reduce its electronic-conductivity. In view of this, Co_3O_4/NCNT (MWNTs) hybrids have been developed where outermost wall of MWNTs are functionalized to afford chemical reactivity while inner graphitic walls stay intact to offer well conducting network.

Co_3O_4/NCNT composite shows improved ORR performance as compared to Co_3O_4/ nitrogen doped reduced GO (NrmGO) and their linear sweep voltammogram (LSV) curves are shown in Figure 14.

1.8: Boron Nitride

Boron nitride (BN) is the lightest among all group III-V compounds and draws resemblance with the graphite and diamond in terms of number of electrons between the neighbouring atoms. Hexagonal boron nitride (*h*-BN) crystallizes in graphite-like structure whereas cubic-BN (c-BN) is similar to diamond with sp^3 hybridized three dimensional networks of B and N. An *h*-BN layer is similar to graphene, in which C-C pair is completely replaced by isoelectronic B-N pair. The strong ionic character of the B–N bond because of the significant difference in electronegativity of nitrogen and boron atoms leads to a large band gap opening in *h*-BN while graphene is gapless conductor. According to Bader analysis there is a transfer of 2.19 electrons from boron to nitrogen in BN network.[127] Hence, single layer of h-BN is insulating with a theoretical band gap of 4.5 eV, unlike graphene, where two bands cross each other at Fermi energy to show semi-metallic property.[128] Layers of h-BN consists of hexagonal BN networks with lattice constants (a = 2.504 Å, c = 6.661 Å) similar to those of graphite (a = 2.458 Å, c = 6.696 Å). These h-BN layers are stacked on top of each other with an interlayer spacing of 3.331 Å in AA'AA'…. sequence, such that B atoms in each layer are bonded to N atoms in the neighbouring layer by electrostatic interaction. Even though BN show negligible electrical conductivity, the lattice thermal conductivity (K_L) values of single-layer BN approaches as high as 600 $Wm^{-1}K^{-1}$ at room temperature, one of the highest among non-carbon-based materials. However, observed K_L values for *h*-BN smaller than single-layer graphene (K_L = 1500-2500 $Wm^{-1}K^{-1}$) due to stronger phonon-phonon scattering in the former.[129]

Fascinating electronic and mechanical properties of carbon nanotubes (CNTs) and their applications in various fields attracted research attention in other analogous nanotubes. Boron nitride nanotubes (BNNTs) were first predicted theoretically in 1994[130, 131] soon after Chopra *et al.*[132] synthesized BNNTs in 1995. Unlike CNTs, BNNTs electronic properties and hence the band gap does not depends on their radii and helicities. Young's modulus of BNNTs (Y = 1.1–1.3 TPa) is comparable to that of CNTs (Y = 1.3–1.8 TPa) make them one

of the stiffest insulating nanofibres.[133] Furthermore, high stability of BN for thermal oxidation compared to carbon nanostructures makes them useful as coating material for devices operates at relatively high temperature.

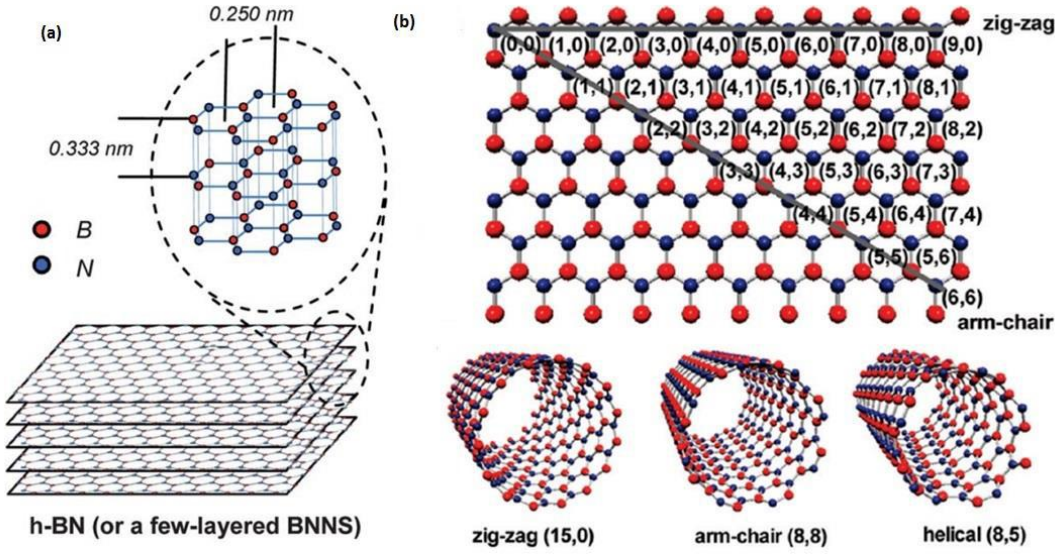

Figure 15. (a) Structural basis of BN,[134] (b) Plane BN sheet with possible wrapping fashions and the corresponding (n,m) indices, also including ball and stick structural models of three types of single-walled BNNTs made of a wrapped BN layer: zig-zag (15,0), arm-chair (8,8), and a helical (8,5) tube.[135] *[reproduced from ref. 134 and 135]*.

Li *et al.*[136] have reported that the monolayer BN showed high stability towards thermal oxidation and remained unchanged till 700 ^{o}C after which it started getting oxidized. However, monolayer graphene sheet started reacting with O_2 at 250 ^{o}C only.

W. H. Balmain obtained BN for the first time by the reaction of molten boric acid with potassium cyanide.[137] Various methods have been reported for the synthesis of 2D BN nanostructures which are similar to the familiar techniques employed for the synthesis of graphene layers with little modifications. Mono and few-layer BN sheets were obtained by mechanical exfoliation, chemical exfoliation and chemical vapor deposition techniques, whereas solid state approaches are used for bulk scale preparations. Flower shaped BN nanoflakes were obtained by the solid phase reaction of $NaBF_4$, NH_4Cl and NaN_3 reagents where powders are mixed, pressed into pellets and then heated in autoclave at 300 ^{o}C.

Reaction of boric acid with urea in nitrogen atmosphere at 900 ^{o}C is another interesting approach to obtain few-layer BN, where increasing urea concentration decreases layers thickness.[138]

1.9: Borocarbonitrides

Compositions formed between boron and carbon as well as carbon and nitrogen has been well studied and it is only recently that materials containing boron, carbon and nitrogen have received attention. Substitutional doping of graphene with nitrogen and/or boron causes metal-to-semiconductor transition due to modification in band structure.[139] On the other hand, lateral grouping of graphene and hexagonal boron nitride (insulator) allow tuning of the electronic characteristics as needed for a particular application. Solid solution of h-BN and graphene having domains of BN in a matrix of graphene are predicted to show exciting changes in electronic properties, with the properties depend on the size of BN domain as well as the type of interface with graphene (zigzag or arm chair) matrix.[140]

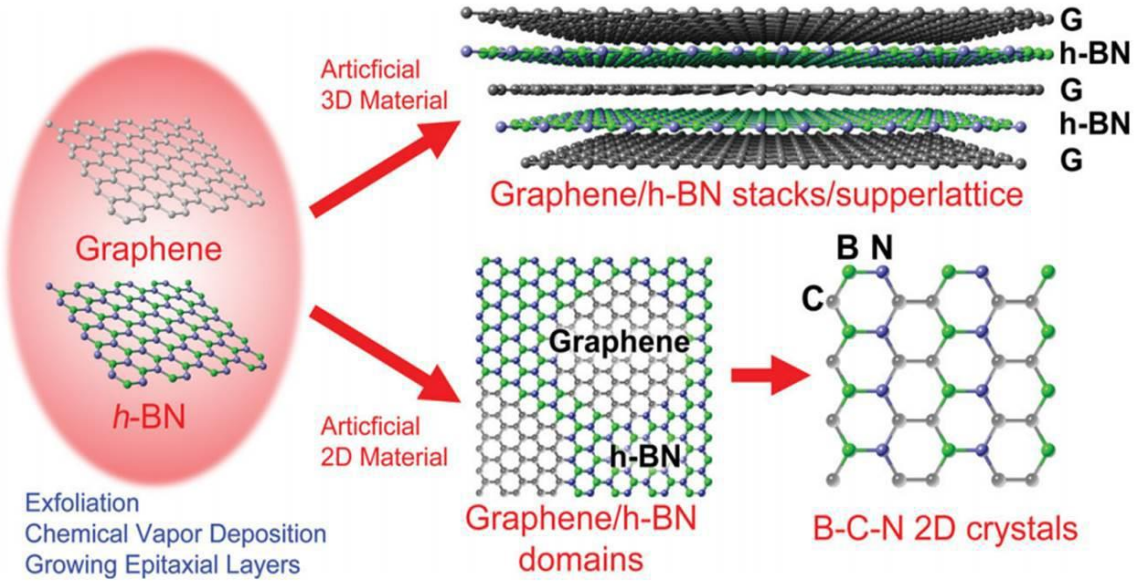

Figure 16. Schematics of possible approaches for artificial B–N–C layers. Exfoliation, chemical vapor deposition, and epitaxial growth are three common methods to synthesize carbon- and BN-based atomic layered structures such as graphene and h-BN. The B–N–C layers could be constructed vertically for G/h-BN stacks/superlattice, or in-plane for G/h-BN domains and finally B–C–N 2D crystals with a controllable stoichiometry. *[reproduced from ref. 141 with permission]*

Borocarbonitride nanosheets, containing hexagonal $B_xC_yN_z$ networks, can be prepared by the reaction of carbon (high surface-area activated charcoal), boric acid and urea.[142] These materials have high surface areas. In a typical synthesis, different ratios of the three starting materials were mixed in water and kept at 80 °C in order to obtain slurry. The slurry is then heated at 900–1000 °C in a nitrogen atmosphere followed by a heat treatment in an ammonia atmosphere at around 900 °C. The reactions involved in the synthesis were represented in the following chemical equations:

$$2H_3BO_3 \xrightarrow{\Delta} B_2O_3 + 3H_2O$$

$$CO(NH_2)_2 \xrightarrow{\Delta} NH_3 + HNCO$$

$$B_2O_3 + 2NH_3 + 2C \xrightarrow{\Delta} 2BCN + 3H_2O$$

$$B_2O_3 + 2NH_3 + 4C \xrightarrow{\Delta} 2BC_2N + 3H_2$$

The composition of the products can be varied by changing the molar ratio of the reactants as well as the temperature of the reaction. High temperature gas phase synthesis of BCN using BBr_3 with a mixture of ethylene and ammonia is also reported which yields spherical shaped particles with an average diameter of 100 nm.[142]

Generally, boroncarbonitride (BCN) nanosheets contain graphene and BN domains, possibly along with BCN rings, and if the ratio of carbon to boron is 1:1 then the composition would be BCN. Presence of covalent BN domains in the carbon matrix distinguishes $B_xC_yN_z$ from B and N-doped graphene. These nanosheets contain only hexagonal networks of B–C, B–N, C–N, and C–C bonds but no B–B or N–N bonds. Figure 16 presents the various ways in which graphene and BN components can be grouped to obtain borocarbonitrides with different properties. Gao *et al.* reported the artificially stacked layers of graphene and BN obtained by liquid phase exfoliation which display considerably different electrical, mechanical and optical properties than that of starting parent layers.[141]

Like CNTs which are considered as rolled forms of graphene, nanotubes of borocarbonitrides are also examined for their structural and electronic properties. Various methods have been reported for the preparation of both single-walled and multi-walled BxCyNz, among them the most studied being CVD method. Pyrolysis of single precursor molecule containing boron, carbon and nitrogen atom (or) combination of two/three precursors with nanoparticles of transition metal catalyst yields BCN nanotubes. For

example, pyrolysis of $CH_3CN.BCl_3$ precursor at 950-1000 ^oC using cobalt nanopowder as catalyst gives $B_xC_yN_z$ nanotubes of composition BC_2N.[144] Kim *et al.* demonstrated that the different structure variants of multiwalled borocarbonitride nanotubes can be synthesized in the CVD conditions just by changing C/B ratio.[145] When C:B is 1:1, BN nanotubes with outer layer of C were obtained while at lower value of C:B ratio (1:2), a mixture of carbon and BN nanotubes was obtained. At higher concentration of carbon (2:1), the entire product was carbon doped BN nanotubes.

1.10: References

1. J. J. Vilatela, D. Eder, *ChemSusChem* **2012**, *5*, 456.
2. F. D'Souza, O. Ito, *Chem. Soc. Rev.* **2012**, *41*, 86.
3. A. Rahman, I. Ali, S. M. Al Zahrani, R. H. Eleithy, *NANO* **2011**, *6*, 185.
4. S. Roth, H. J. Park, *Chem. Soc. Rev.* 2010, 39, 2477.
5. M.-Q. Zhao, Q. Zhang, J.-Q. Huang, F. Wei, *Adv. Funct. Mater.* **2012**, *22*, 675.
6. D. S. Su, *ChemSusChem* **2009**, *2*, 1009.
7. D. S. Su, S. Perathoner, G. Centi, *Chem. Rev.* **2013,** *113*, 5782.
8. C. N. R. Rao, K. Biswas, K. S. Subrahmanyam, A. Govindaraj, *J. Mater. Chem.* **2009**, *19*, 2457.
9. D. S. Su, R. Schlögl, *ChemSusChem* **2010**, *3*, 136.
10. B. C. Yadav, R. Kumar, *Int. J. Nanotechnol. Applications* **2008**, *2*, 15.
11. U. Maitra, A. Gomathi, C. N. R. Rao, *J. Exp. Nanosci.* **2008**, *3*, 271.
12. J. Bartelmess, S. Giordani, Beilstein, *J. Nanotechnol.* **2014,** *5*, 1980.
13. S. Iijima, M. Yudasaka, R. Yamada, S. Bandow, K. Suenaga, F. Kokai, K. Takahashi, *Chem. Phys. Lett*. **1999**, ***309,*** 165.
14. Z. Xu, C. Gao, *Mater. Today* **2015**, *18*, 480.
15. X. Hu, Z. Xu, Z. Liu, C. Gao, *Sci. Rep.* **2013**, *3*, 2374.
16. N. J. Komatsu, *Jpn. Petrol. Inst.* **2009**, *52*, 73.
17. D. A. C. Brownson, D. K. Kampouris, C. E. Banks, *J. Power Sources* **2011**, *196*, 4873.
18. J. P. Paraknowitsch and A. Thomas, *Energy Environ. Sci.* **2013**, *6*, 2839.
19. E. Osawa, *Kagaku (in Japanese)* **1970**, *25, 854.*
20. H. W. Kroto, J. R. Heath, S. C. O'Brien, R. F. Curl, R E. Smalley, *Nature*, **1985**, *318*, 162.
21. R. S Rouff, *App. Phy. Lett.* **1991**, *59*, 15553.
22. J. W. Withers, R. O. Laoufy, T. P. Lowe, **1997** 6BCF667CC63447AC275FDA4F421E5.tobacco03.
23. R. B. Ross, C. M. Cardona, D. M. Guldi, S. G. Sankaranarayanan, M. O. Reese, N. Kopidakis, J. Peet, B. Walker, G. C. Bazan, E. V. Keuren, B. C. Holloway and M. Drees, *Nat. Mater.*, **2009**, *8*, 208.

24. W. Krätschmer, L. D. Lamb, K. Fostiropoulos, D. R. Huffman, *Nature*, **1990**, *347*, 354.

25. B. I. Yakobson, R. E. Smalley, *Am. Sci*. **1997**, *85*, 234.

26. M. F. L. De Volder, S. H. Tawfick, R. H. Baughman, A. J. Hart, *Science* **2013**, *339*, 535**.**

27. S. Iijima, *Nature* **1991**, *354*, 56.

28. D. T. Colbert, J. Zhang, S. M. McClure, P. Nikolaev, Z. Chen, J. H. Hafner, D. W. Owens, P. G. Kotula, C. B. Carter, J. H. Weaver, A. G. Rinzler, R. E. Smalley, *Science*, **1994**, *266*, 1218.

29. S. Iijima, T. Ichihashi, *Nature* **1993**, *363*, 603.

30. C. Journet, W. K. Maser, P. Bernier, A. Loiseau, M. L. Delachapelle, S. Lefrant, P. Deniard, R. Lee, J. E. Fischer, *Nature* **1997**, *388*, 756.

31. A. Thess, *et al*. *Science* **1996**, *273*, 483.

32. C. N. R. Rao, A. Govindaraj, *Acc. Chem. Res.* **2002**, 35, 998.

33. a) M. Jose-Yacaman, M. Miki-Yoshida, L. Rendon, J. G. Santiesteban, *Appl. Phys. Lett.* **1993**, *62*, 657; b) K. Hernadi, A. Fonseca, J. B. Nagy, D. Bernaerts, J. Riga, A. Lucas, *Synth. Met.* **1996**, *77*, 1.

34. N. M. Rodriguez, *J. Mater. Res.* **1993**, *8*, 3233.

35. W. Z. Li , S. S. Xie , L. X. Qian , B. H. Chang , B. S. Zou , W. Y. Zhou , R. A. Zhao , G. Wang , *Science* **1996**, *274*, 1701.

36. Z. F. Ren, Z. P. Huang, *Science*, **1998**, *282*, 1105.

37. *a)* B. C. Satishkumar, A. Govindaraj, R. Sen, C. N. R. Rao, *Chem. Phys. Lett.* **1998,** *293*; b) B. C. Satishkumar , A. Govindaraj , M. Nath , C. N. R. Rao , *J. Mater. Chem***. 2000**, *10*, 2115.

38. a) M. Yudasaka, R. Kikuchi, Y. Ohki, S. Yoshimura, Carbon 1997, 35, 195; b) C. N. R. Rao, B. C. Satishkumar, A. Govindaraj, *Chem. Commun*. **1998**, 1525; C) B. C. Satishkumar, A. Govindaraj, P. V. Vanitha, A. K. Raychaudhuri, C. N. R. Rao, *Chem. Phys. Lett.* **2002,** *362*, 301; d) F. L. Deepak, A. Govindaraj, C. N. R. Rao, *Chem. Phys. Lett.* **2001**, *345*, 5.

39. R. E. Peierls, *Ann. Inst. Henri Poincare* **1935**, *5*, 177.

40. L. D. Landau, *Phys. Z. Sowjetunion* **1937,** *11*, 26.

41. C. Berger, Z. Song, X. Li, X. Wu, N. Brown, C. Naud, D. Mayou, J. H. T. Li, A. N. Marchenkov, E. H. Conrad, P. N. First, W. A. de Heer, *Science* **2006**, *312*, 1191.
42. K. H. M. Born, Oxford, Clarendon, 1954.
43. D. R. Nelson, L. Peliti, *J. Physique* **1987**, *48*, 1085.
44. P. Le Doussal, L. Radzihovsky, *Phys. Rev. Lett.* **1992**, *69*, 1209.
45. D. R. Nelson, T. Piran, S. Weinberg, *Statistical Mechanics of Membranes and Surfaces*, World Scientific, Singapore, 2004.
46. P. R. Wallace, *Phys. Rev.* **1947**, *71*, 622.
47. K. S. Novoselov, A. K. Geim, S. V. Morozov, D. Jiang, Y. Zhang, S. V. Dubonos, I. V. Grigorieva, A. A. Firsov, *Science* **2004**, *306*, 666.
48. C. Lee, X. Wei, J. W. Kysar, J. Hone, *Science*, **2008**, *321*, 385.
49. Y. Wang, Y. Huang, Y. Song, X. Y. Zhang, Y. F. Ma, J. J. Liang, Y. S. Chen, *Nano Lett.* **2009**, *9*, 220.
50. H. S. S. R. Matte, K. S. Subrahmanyam, C. N. R. Rao, *J. Phys. Chem. C* **2009**, *113*, 9982.
51. A. Peigney, C. Laurent, E. Flahaut, R. R. Bacsa, A. Rousset, *Carbon*, **2001**, *39*, 507.
52. C. N. R. Rao, A. K. Sood, R. Voggu, K. S. Subrahmanyam, *J. Phys. Chem. Lett.* **2010**, *1*, 572.
53. B. Das, R. Voggu, C. S. Rout, C. N. R. Rao, *Chem. Commun.* **2008**, 5155.
54. H. Hiura, T. W. Ebbesen, J. Fujita, K. Tanigaki, T. Takada, *Nature*, **1994**, *367*, 148.
55. T. W. Ebbesen, H. Hiura, *Adv. Mater. 7*, 582.
56. T. M. Bernhardt, B. Kaiser, K. Rademann, *Surf. Sci.* **1998**, *408*, 86.
57. H. Roy, *J. Appl. Phys.* **1998**, *83*, 4695.
58. X. Lu, M. Yu, H. Huang, R. S. Ruoff, *Nanotechnol.* **1999**, *10*, 269.
59. H. V. Roy, C. Kallinger, K. Sattler, *Surf. Sci.* **1998**, *407*, 1.
60. S. Park, J. An, I. Jung, R. D. Piner, S. J. An, X. Li, A. Velamakanni, R. S. Ruoff, *Nano Lett.* **2009**, *9*, 1593.
61. Y. Zhang, *Appl. Phys. Lett.* **2005**, *86*, 073104.
62. D. C. Marcano, D. V. Kosynkin, J. M. Berlin, A. Sinitskii, Z. Sun, A. Slesarev, L. B. Alemany, W. Lu, J. M. Tour, *ACS Nano* **2010**, *4*, 4806.
63. W. S. Hummers, R. E. Offeman, *J. Am. Chem. Soc.* **1958**, *80*, 1339.

64. M. J. Allen, V. C. Tung, R. B. Kaner, *Chem. Rev.* **2009**, *110*, 132.
65. V. C. Tung, M. J. Allen, Y. Yang, R. B. Kaner, *Nat. Nanotechnol* **2009**, *4*, 25.
66. J. I. Paredes, S. Villar-Rodil, A. Marti'nez-Alonso, J. M. D. Tasco'n, *Langmuir* **2008**, *24*, 10560.
67. H. C. Schniepp, J.L. Li, M. J. McAllister, H. Sai, M. Herrera-Alonso, D. H. Adamson, R. K. Prud'homme, R. Car, D. A. Saville, I. A. Aksay, *J. Phys. Chem. B*, **2006**, *110*, 8535.
68. M. J. McAllister, J.L. Li, D. H. Adamson, H. C. Schniepp, A. A. Abdala, J. Liu, M. Herrera-Alonso, D. L. Milius, R. Car, R. K. Prud'homme, I. A. Aksay, *Chem. Mater.* **2007**, *19*, 4396.
69. X. Guoqing, H. Wontae, K. Namhun, M. C. Sung, C. Heeyeop, *Nanotechnol.* **2010**, *21*, 405201.
70. M. Qian, *Appl. Phys. Lett.* **2011**, *98*, 173108.
71. L. M. Viculis, J. J. Mack, O. M. Mayer, H. T. Hahn and R. B. Kaner, *J. Mater. Chem.* **2005**, *15*, 974.
72. C. ValleÌs, C. Drummond, H. Saadaoui, C. A. Furtado, M. He, O. Roubeau, L. Ortolani, M. Monthioux, A. PeÌnicaud, *J. Am. Chem. Soc.* **2008**, *130*, 15802.
73. A. Ghosh, K. V. Rao, S. J. George, C. N. R. Rao, *Chem. Eur. J.* **2010**, *16*, 2700.
74. K. S. Kim, Y. Zhao, H. Jang, S. Y. Lee, J. M. Kim, K. S. Kim, J.H. Ahn, P. Kim, J. Y. Choi, B. H. Hong, *Nature* **2009**, *457*, 706.
75. S. Y. Kwon, C. V. Ciobanu, V. Petrova, V. B. Shenoy, J. Bareno, V. Gambin, I. Petrov, S. Kodambaka, *Nano Lett.* **2009**, *9*, 3985.
76. P. W. Sutter, J.I. Flege, E. A. Sutter, *Nat. Mater.* **2008**, *7*, 406.
77. J. Coraux, A. T. N`Diaye, C. Busse, T. Michely, *Nano Lett.* **2008**, *8*, 565.
78. Y. Xia, D. Qian, D. Hsieh, L. Wray, A. Pal, H. Lin, A. Bansil, D. Grauer, Y. S. Hor, R. J. Cava, M. Z. Hasan, *Nat. Phys.* **2009**, *5*, 398.
79. L. Gomez, Y. Zhang, A. Kumar, C**.** Zhou *IEEE Transactions on Nanotechnology*, **2009,** *8*, 135.

80. C. N. R. Rao, K. S. Subrahmanyam, H. S. S. Ramakrishna Matte, B. Abdulhakeem, A. Govindaraj, B. Das, P. Kumar, A. Ghosh, D. J. Late, *Sci. Tech. Adv. Mater.* **2010**, *11*, 054502.
81. K. S. Subrahmanyam, L. S. Panchakarla, A. Govindaraj, C. N. R. Rao, *J. Phys. Chem. C* **2009**, *113*, 4257.
82. L. S. Panchakarla, A. Govindaraj, C. N. R. Rao, *Inorg. Chem. Acta*, **2009**, *363*, 4163.
83. N. Li, Z. Wang, K. Zhao, Z. Shi, Z. Gu, S. Xu, *Carbon* **2010**, *48*, 255.
84. D. C. Wei, Y. Q. Liu, Y. Wang, H. L. Zhang, L. P. Huang, G. Yu, *Nano Lett.* **2009**, *9*, 1752.
85. T. R. Wu, H. L. Shen, L. Sun, B. Cheng, B. Liu, J. C. Shen, *New J. Chem.* **2012**, *36*, 1385.
86. X. Li, L. L. Fan, Z. Li, K. L. Wang, M. L. Zhong, J. Q. Wei, D. H. Wu, H. W. Zhu, *Adv. Energy Mater.* **2012**, *2*, 425.
87. Z. Jin, J. Yao, C. Kittrell, J. M. Tour, *ACS Nano* **2011**, *5*, 4112.
88. A. L. M. Reddy, A. Srivastava, S. R. Gowda, H. Gullapalli, M. Dubey, P. M. Ajayan, *ACS Nano* **2010**, *4*, 6337.
89. D. C. Wei, Y. Q. Liu, Y. Wang, H. L. Zhang, L. P. Huang, G. Yu, *Nano Lett.* **2009**, *9*, 1752.
90. L. T. Qu, Y. Liu, J. B. Baek, L. M. Dai, *ACS Nano*, **2010**, *4*, 1321.
91. L. Ci, L. Song, C. H. Jin, D. Jariwala, D. X. Wu, Y. J. Li, A. Srivastava, Z. F. Wang, K. Storr, L. Balicas, F. Liu, P. M. Ajayan, *Nat. Mater.* **2010**, *9*, 430.
92. Z. S. Wu, W. C. Ren, L. Xu, F. Li and H. M. Cheng, *Nano Lett.*, **2011**, *5*, 5463.
93. L. F. Lai, J. R. Potts, D. Zhan, L. Wang, C. K. Poh, C. H. Tang, H. Gong, Z. X. Shen, L. Y. Jianyi, R. S. Ruoff, *Energy Environ. Sci.* **2012**, *5*, 7936.
94. L. S. Zhang, X. Q. Liang, W. G. Song, Z. Y. Wu, *Phys.Chem. Chem. Phys.* **2010**, *12*, 12055.
95. D. S. Geng, Y. Chen, Y. G. Chen, Y. L. Li, R. Y. Li, X. L. Sun, S. Y. Ye, S. Knights, *Energy Environ. Sci.* **2011**, *4*, 760.
96. E. Yoo, J. Nakamura, H. S. Zhou, *Energy Environ. Sci.* **2012**, *5*, 6928.
97. T. V. Khai, H. G. Na, D. S. Kwak, Y. J. Kwon, H. Ham, K. B. Shim, H. W. Kim, *J. Mater. Chem.* **2012**, *22*, 17992.

98. H. B. Wang, C. J. Zhang, Z. H. Liu, L. Wang, P. X. Han, H. X. Xu, K. J. Zhang, S. M. Dong, J. H. Yao and G. L. Cui, *J. Mater. Chem.* **2011**, *21*, 5430.

99. A. Peigney, C. Laurent, E. Flahaut, R. R. Bacsa, A. Rousset, *Carbon* **2001**, *39*, 507.

100. C. N. R. Rao, A. K. Sood, R. Voggu, K. S. Subrahmanyam, *J. Phys. Chem Lett*. **2010**, *1*, 572.

101. S. Patchkovskii, J. S. Tse, S. N. Yurchenko, L. Zhechkov, T. Heine, G. Seifer, *Proc. Natl. Acad. Sci. U. S. A.* **2005**, *102*, 10439.

102. A. Ghosh, K. S. Subrahmanyam, K. S. Krishna, S. Datta, A. Govindaraj, S. K. Pati, C. N. R. Rao, *J. Phys. Chem. C* **2008**, *112*, 15704.

103. N. Kumar, K. S. Subrahmanyam, P. Chaturbedy, K. Raidongia, A. Govindaraj, K. P. S. S. Hembram, A. K. Mishra, U. V. Waghmare, C. N. R. Rao, *Chem. Sus. Chem.* **2011**, *4*, 1662.

104. C. N. R. Rao, R. Voggu, *Mater. Today* **2010**, *13*, 34.

105. X. Dong, D. Fu, W. Fang, Y. Shi, P. Chen, L.-J. Li, *Small* **2009**, *5*, 1422.

106. R. Seshadri, C. N. R. Rao, H. Pal, T. Mukherjee, J. P. Mittal, *Chem. Phys. Lett.* **1993**, *205*, 395.

107. N. Jung, N. Kim, S. Jockusch, N. J. Turro, P. Kim, L. Brus, *Nano Lett.* **2009**, *9*, 4133.

108. S. Ghosh, S. R. K. C. Sharma Yamijala, S. K. Pati, C. N. R. Rao, *RSC Adv.* **2012**, *2*, 1181.

109. S. K. Saha, R. C. Chandrakanth, H. R. Krishnamurthy, U. V. Waghmare, *Phys. Rev. B* **2009**, *80*, 6.

110. L. M. Malard, M. A. Pimenta, G. Dresselhaus, M. S. Dresselhaus, *Phys. Rep.* **2009**, *473*, 51.

111. M. S. Dresselhaus, A. Jorio, M. Hofmann, G. Dresselhaus, R. Saito, *Nano Lett.* **2010**, *10*, 751.

112. A. C. Ferrari, J. Robertson, *Philos. Trans. R. Soc. A* **2004**, *362*, 2477.

113. M. S. Dresselhaus, G. Dresselhaus, R. Saito, A. Jorio, *Phys. Rep.* **2005**, *409*, 47.

114. K. Sasaki, R. Saito, G. Dresselhaus, M. S. Dresselhaus, H. Farhat, J. Kong, *Phys. Rev. B* **2008**, *77*, 245441.

115. M. A. Pimenta, G. Dresselhaus, M. S. Dresselhaus, L. A. Cancado, A. Jorio, R. Sato, *Phys. Chem. Chem. Phys.* **2007**, *9*, 1276.

116. *Carbon Nanotubes: Advanced Topics in the Synthesis Structure, Properties and Applications* (Eds.: A. Jorio, G. Dresselhaus, M. S. Dresselhaus), Springer, Berlin, 2008.
117. R. Saito, A. Jorio, A. G. Souza Filho, G. Dresselhaus, M. S. Dresselhaus, M. A. Pimenta, *Phys. Rev. Lett.*, **2002**, *88*, 027401.
118. J. Jiang, R. Saito, G. G. Samsonidze, A. Jorio, S. G. Chou, G. Dresselhaus, M. S. Dresselhaus, *Phys. Rev. B* **2007**, *75*, 035407.
119. C. Lee, X. D. Wei, J. W. Kysar, J. Hone, *Science* **2008**, *321*, 385.
120. M. Cadek, J. N. Coleman, V. Barron, K. Hedicke, W. J. Blau, *Appl. Phys. Lett.* **2002**, *81*, 5123.
121. T. Ramanathan, A. A. Abdala, S. Stankovich, D. A. Dikin, M. Herrera-Alonso, R. D. Piner, D. H. Adamson, H. C. Schniepp, X. Chen, R. S. Ruoff, S. T. Nguyen, I. A. Aksay, R. K. Prud'homme, L. C. Brinson, *Nat. Nanotechnol.* **2008**, *3*, 327.
122. K. E. Prasad, B. Das, U. Maitra, U. Ramamurty, C. N. R. Rao, *Proc. Natl. Acad. Sci. U. S. A.* **2009**, *106*, 13186.
123. J. Feng, Y. Y. Liang, H. L. Wang, Y. G. Li, B. Zhang, J. G. Zhou, J. Wang, T. Regier, H. J. Dai, *Nano Res.* **2012**, *5*, 718.
124. Y. Y. Liang, Y. G. Li, H. L. Wang, J. G. Zhou, J. Wang, T. Regier, H. J. Dai, *Nat. Mater.* **2011**, *10*, 780.
125. H. L. Wang, Y. Y. Liang, Y. G. Li, H. J. Dai, *Angew. Chem., Int. Ed.*, **2011**, *50*, 10969.
126. Y. Liang, H. Wang, P. Diao, W. Chang, G. Hong, Y. Li, M. Gong, L. Xie, J. Zhou, J. Wang, T. Z. Regier, F. Wei, H. Dai, *J. Am. Chem. Soc.* **2012**, *134*, 15849.
127. X. Jiang, J. Zhao, R. Ahuja, *J. Phys. Condens. Matter* **2013,** *25*, 122204.
128. Y.-H. Kim, K. J. Chang, S. G. Louie, *Phys. Rev. B* **2001,** *63*, 205408.
129. L. Lindsay, D. A. Broido, *Phys. Rev. B* **2011,** *84*, 155421.
130. A. Rubio, J. L. Corkill, M. L. Cohen, *Phys. Rev. B* **1994,** *49*, 5081.
131. X. Blase, A. Rubio, S. G. Louie and M. L. Cohen, *Europhys. Lett.* **1994,** *28*, 335.
132. N. G. Chopra, R. J. Luyken, K. Cherrey, V. H. Crespi, M. L. Cohen, S. G. Louie, A. Zettl, *Science* **1995,** *269*, 966.
133. R. Arenal, M.-S. Wang, Z. Xu, A. Loiseau, D. Golberg, *Nanotechnology* **2011,** *22*, 265704.
134. Y. Lin, J. W. Connell, *Nanoscale* **2012,** *4*, 6908.

135. D. Golberg, Y. Bando, Y. Huang, T. Terao, M. Mitome, C. Tang, C. Zhi, *ACS Nano* **2010,** *4*, 2979.

136. L. H. Li, J. Cervenka, K. Watanabe, T. Taniguchi, Y. Chen, *ACS Nano* **2014.**

137. W. H. Balmain, *J. Prakt. Chem.* **1842**, *27*, 422.

138. A. Nag, K. Raidongia, K. P. S. S. Hembram, R. Datta, U. V. Waghmare, C. N. R. Rao, *ACS Nano* **2010**, *4*, 1.

139. C. N. R. Rao, K. Gopalakrishnan, A. Govindaraj, *Nano Today* **2014**, *9*, 324.

140. N. Kumar, K. Moses, K. Pramoda, S. N. Shirodkar, A. K. Mishra, U. V. Waghmare, A. Sundaresan, C. N. R. Rao, *J. Mater. Chem. A* **2013**, *1*, 5806.

141. G. Gao, W. Gao, E. Cannuccia, J. Taha-Tijerina, L. Balicas, A. Mathkar, T. N. Narayanan, Z. Liu, B. K. Gupta, J. Peng, Y. Yin, A. Rubio, P. M. Ajayan, *Nano Lett.* **2012,** *12*, 3518

142. N. Kumar, K. S. Subrahmanyam, P. Chaturbedy, K. Raidongia, A. Govindaraj, K. P. S. S. Hembram, A. K. Mishra, U. V. Waghmare, C. N. R. Rao, *ChemSusChem* **2011**, *4*, 1662.

143. N. Kumar, K. Raidongia, A. K. Mishra, U. V. Waghmare, A. Sundaresan, C. N. R. Rao, *J. Solid State Chem.* **2011**,*184*, 2902.

144. M. Terrones, A. M. Benito, C. Manteca-Diego, W. K. Hsu, O. I. Osman, J. P. Hare, D. G. Reid, H. Terrones, A. K. Cheetham, K. Prassides, H. W. Kroto, D. R. M. Walton, *Chem. Phys. Lett.* **1996,** *257*, 576.

145. S. Y. Kim, J. Park, H. C. Choi, J. P. Ahn, J. Q. Hou and H. S. Kang, *J. Am. Chem. Soc.* **2007,** *129*, 1705.

Part 2

Investigations of

Single-Walled Nanohorns

2.1: Arc-discharge Synthesis, Characterization and Functionalization of Single-Walled Nanohorns

Summary*

This chapter reports the synthesis of single-walled carbon nanohorns (SWNHs) by sub-merged arc discharge of graphite rods in liquid nitrogen medium, and their characterization using electron microscope, IR, Raman spectroscopy and by other means. Water-dispersible SWNHs has been produced by extensive acid treatment with nitric and sulfuric acid mixture. Furthermore, carboxyl functionalized SWNHs obtained by acidification are utilized for the covalent attachment of dodecylamine which results in enhanced dispersibility of SWNHs in organic solvents like carbon tetrachloride and tetrahydrofuran. Non-covalent modification is achieved with tetrapotassium salt of coronene tetracarboxylic acid through π-π interaction which yields stable dispersions in water. Wrapping of SWNHs with polyoxyethylene-40-nonylphenyl ether (IGPAL), sodium dodecyl sulfate (SDS) and cetyl-trimethyl-ammonium bromide (CTAB) surfactants results in aqueous dispersions stable over a period of 2 months.

Papers based on this work have appeared in *J. Clust. Sci. (2014), Chem. Eur. J. (2015).*

2.1.1: Introduction

Single-walled nanohorns (SWNHs) contain sheath aggregates of graphene with lengths in the 50-100 nm range. These nanocarbons are similar to nanotubes, but closed at one end with a conical cap open at the other end.[1] Since the synthesis of SWNHs, they have attracted scientific interest owing to their high surface area and porosity with reasonable gas storage capacity as well as possible biological applications like drug delivery.[2, 3] Large scale synthesis of SWNHs by laser ablation is first reported by Ijima *et al*.[1] Since SWNHs preparation involves only pure graphite rods, toxic responses from metal impurities can be excluded when they used as drug-delivery vehicles unlike other nanocarbons such as SWNTs.[4] In addition, the huge pore volume intrinsic to internal nanospaces and rough external surface makes SWNHs promising candidates for H_2 and CH_4 storage, supercapacitor electrode and as catalyst support materials.[5, 6] Unfortunately, pristine SWNHs are insoluble in water and in most of the solvents due to lack of surface functional groups.[7] In order to make SWNHs readily dispersible in different solvents, it is essential to chemically or physically attach some groups or molecules to the surface without varying their properties significantly.

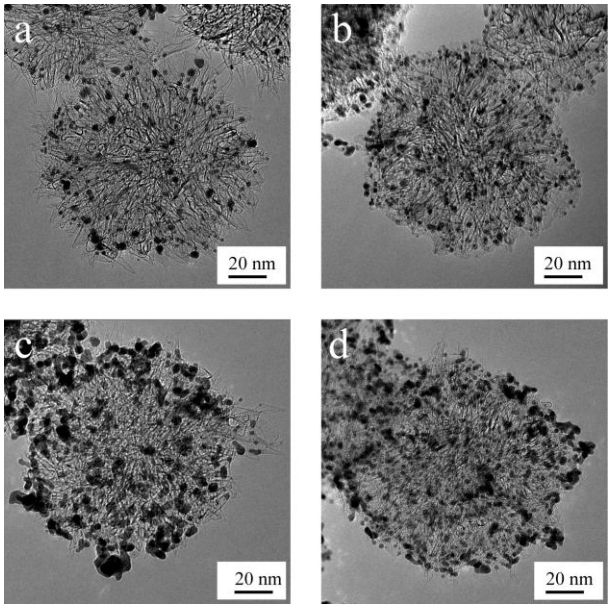

Figure 1. TEM images of the supported catalyst: (a) 20 wt % Pt on pristine SWNHs, (b) 20 wt % Pt on functionalized-SWNHs, (c) 60 wt % Pt on SWNHs, and (d) 60 wt % Pt on functionalized-SWNHs.

Surface functional groups apart from providing surface wettability would be helpful in making uniform composite with other components. For example, Pt nanocatalysts decorated on functionalized SWNHs surfaces show uniform distribution of metal particles and much improved performance in direct methanol fuel cells.[5] Pthalocyanin functionalized SWNHs can be used in dual-modality photothermal therapy and photodynamic therapy.[8]

Although there is not much advancement on functionalization of SWNHs, explorations for single-walled nanotubes (SWNTs) have been reported whose structure is considered as similar to SWNHs. SWNTs are few micrometers long and exist as ropes which are entangled together making complex network structure, and are highly resistant to wetting. These factors, together with the lack of surface functional groups make them much hard to soluble in organic solvents.[9] It is possible to disperse SWNTs by refluxing with HNO_3/H_2SO_4 mixture, whereby the end caps of the tubes are oxidized mainly as carboxylic acids.[10] These functionalized tubes are dispersible in amide group containing solvents such has N,N-dimethylformamide under the influence of ultrasonication. Covalent functionalization creates defect sites on nanotubes[11] along with the oxidation of the surface due to impurity states introduced at the Fermi level of nanotubes.[12] These defect sites helpful in shortening of nanotubes under similar oxidizing circumstances.[13, 14] The shortened tubes showed much better dispersibility in organic solvents compared to full-length SWNTs. Covalent functionalization considerably ruptures conjugation and makes tubes less conducting. On the other hand, functionalization of SWNTs by non-covalent modification strategies such as wrapping with surfactant or polymer results in enhanced surface wettability without much altering their electronic structure. It is possible to transfer nanotubes to aqueous phase in presence of surface active benzylalkonium chloride, where tubes are part of the hydrophobic interior of the formed micelles. [15-17]

We have carried out several experiments to carry out both covalent and non-covalent functionalizations of SWNHs are detailed below.

2.1.2: Scope of the present investigations

Synthesis of SWNHs:

Carbon nanohorns are the relatively new form of nanocarbons which may also become important from the application point of view.[18] Widely used methods for preparation of carbon nanostructures includes laser ablation[19], arc discharge[20] and chemical vapor

deposition[21] techniques. Large scale synthesis of SWNHs by laser ablation is first reported by Ijima *et al.* [1] Ishigami *et al.* showed an arc discharge generated between two carbon electrodes in liquid nitrogen gives multi-walled carbon nanotubes (MWNTs) with high yield which does not require any vacuum system.[22] Furthermore, vacuum system can also give amorphous carbon in addition to the desired material. Here we report the relatively simple and economically alternative method of arc discharge of graphite rods in liquid nitrogen for SWNHs preparation which does not require any expensive laser sources and vacuum equipments.

Functionalization of nanohorns:

Since pristine SWNHs are insoluble in aqueous or organic solvents, it is essential to prepare stable dispersions of SWNHs in various solvents for further modification which broadens their potential areas of applications. Appropriate functionalities apart from providing surface wettability would be helpful in covalent or non-covalent attachment of various other moieties to nanohorn. For example; porphyrin moieties covalently attached to SWNHs are explored in photo-electrochemical solar cell.[23] Carbon nanohorn/nanotube composite is used as electrode material for high-power supercapacitor.[24] Surface modification of SWNTs achieved by covalent or non-covalent modifications and their advantageous properties are well documented.[25] We felt that it would be worthwhile to functionalize SWNHs which is helpful in obtaining stable dispersions of SWNHs in various solvents and these functionalities may further assist the formation uniform mixtures of SWNHs with many other organic, inorganic and polymeric materials.

We have carried out surface functionalization of SWNHs by employing both covalent and non-covalent approaches. These samples were characterized by making use of Infrared (IR) spectroscopy, Raman spectroscopy and electron microscopy (SEM). Covalent modification is achieved through the following two independent routes (a) acidification and (b) amidation. Acidification makes SWNHs dispersible in aqueous media, whereas amidation gives stable dispersions in organic solvents like THF and CCl_4. On the other hand, non-covalent functionalization has been carried out through (a) π-π interaction with aromatic molecules and (b) supramolecular approaches using surfactants. Supramolecular approaches give aqueous dispersions which are stable for several days.

2.1.3: Experimental section

SWNHs Synthesis:

The submerged arc method was used for the preparation of SWNHs. Briefly DC-arc discharge was generated between two graphite electrodes submerged in liquid nitrogen in a stainless steel dewar. The arc discharge was initiated inside the liquid nitrogen by touching a 99.99% purity graphite anode (6 mm in diameter) with a graphite cathode (12 mm tip diameter) of similar purity. The applied DC-arc voltage and currents were 35 V and 65 A, respectively. The gap between the electrodes kept constant at around 1 mm by continuously translating the anode during the experiment in order to maintain a stable discharge. The arc discharge in liquid nitrogen was turbulent. After arcing, remaining liquid nitrogen was transferred from dewar to a glass beaker, and allowed it to evaporate. The product settled at the bottom of dewar was also collected. In Scheme 1, we show the schematic of the experimental set-up used for carrying out arc discharge of graphite electrodes in liquid nitrogen media.

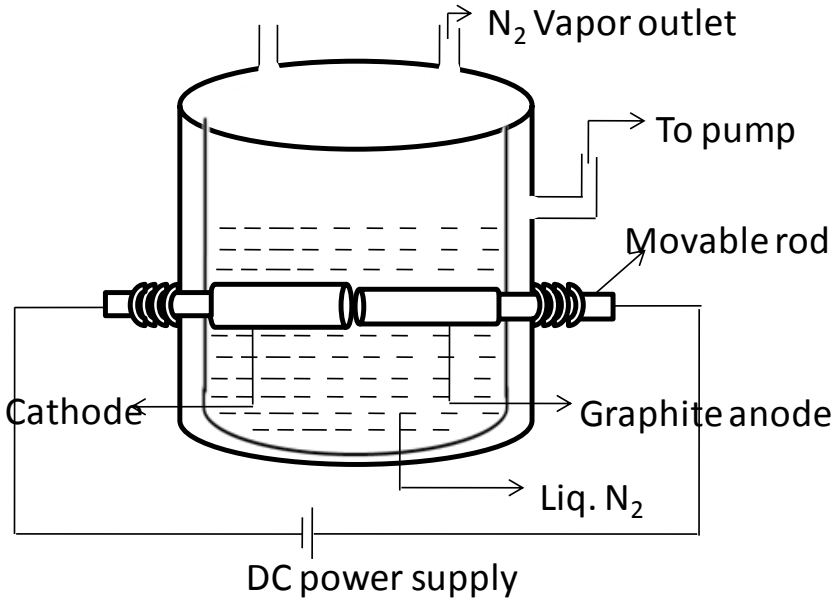

Scheme 1. Schematic diagram of the submerged arc discharge apparatus.

Functionalization

To prepare acid functionalized SWNHs, 50 mg of SWNHs were dispersed in water (15 ml) along with conc. nitric (2 ml) and sulphuric acids (2 ml). This mixture was heated in a microwave oven in a teflon-lined stain less steel autoclave for 10 min. The product was refluxed overnight and repeatedly washed with water and ethanol to remove traces of the acids.

To obtain amide functionalized SWNHs, acid functionalized nanohorns (10 mg) are refluxed at 70 °C with excess thionyl chloride and the unreacted solvent was removed under vacuum. The product is treated with dodecylamine (DDA) (5 ml) under microwave irradiation for 10 min in the presence of tri-ethyl amine as a base and refluxed overnight.

We have used the tetrapotassium salt of coronene carboxylic acid (CS) for non-covalent functionalization of SWNHs. SWNH-CS mixture was obtained by mixing aqueous dispersions of SWNHs and CS under sonication and then the product was refluxed for 24 h, followed by further sonication at 70 °C for 2 h.[26] The composite so obtained was centrifuged to remove insoluble SWNHs which were not fully exfoliated and the remaining aqueous dispersion obtained is black and it stable for several months.

We have also wrapped SWNHs with various surfactants to enhance their aqueous dispersibility. Typical procedure involves the sonication of SWNHs (5 mg) in aqueous media with different concentrations of surfactants like polyoxyethylene-40-nonylphenyl ether (IGPAL), sodium dodecyl sulfate (SDS) and cetyl-trimethyl-ammonium bromide (CTAB).

2.1.4: Results and Discussion

In Figures 2a, b, we show the FESEM images of the typical soot product obtained by the arc discharge of graphite electrodes in liquid nitrogen media. The product contains approximately uniform spherical aggregates and the diameter of individual aggregate is estimated to be 50-100 nm from direct observation of FESEM images. HRTEM images (Figure 2d) showed cone shaped tips are protruding from the spherical aggregates so that it resembled a dahlia flower. The environment formed during submerged arc discharge appeared to be assisting the formation of SWNHs. Particularly; the high density of nitrogen causes the drastic quenching of generated carbon species and low diffusion rate, thereby allowing the formation of graphene sheets. Kawai *et al.* from simulation studies showed that aggregates containing nanohorns could be generated from the graphene layers. [27]

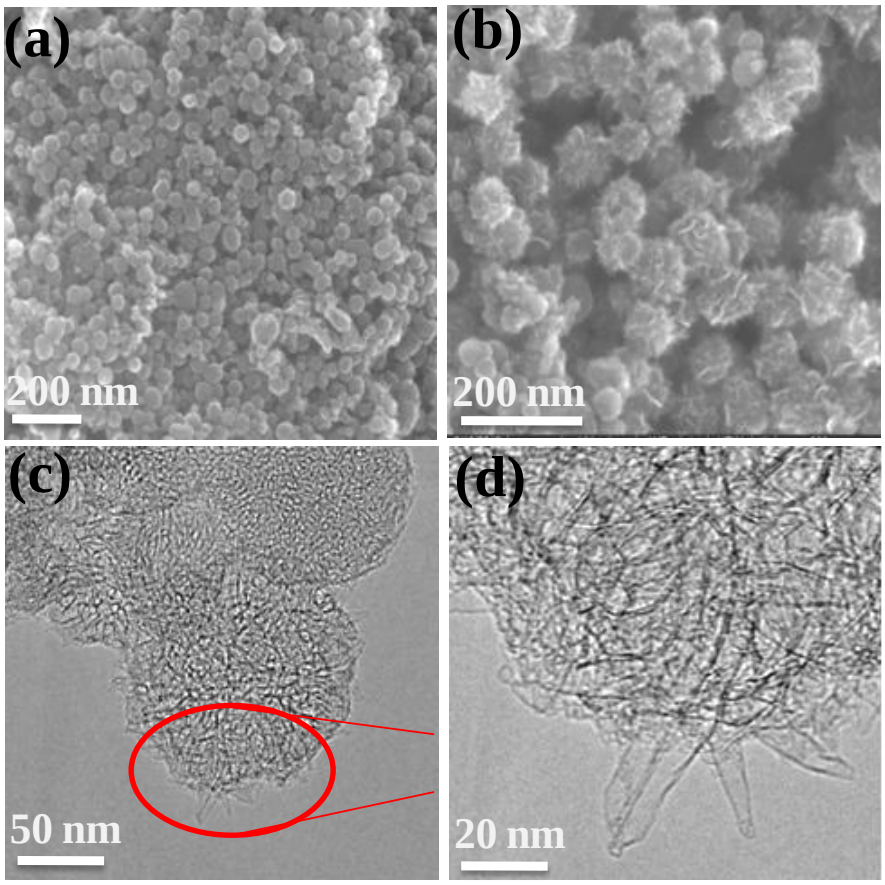

Figure 2. (a, b) FESEM, (c) TEM and (d) HRTEM images of SWNHs obtained by submerged arc discharge in liquid N_2.

Raman spectroscopy has emerged an important tool for the characterization of carbon nanostructures.[28] The Raman spectrum of pristine SWNHs excited at 633 nm is shown in Figure 3a which shows peaks from the defect induced D-band (SP^3 carbon), SP^2 bonded carbon G-band and the 2D-bands at 1343, 1,580 and 2,700 cm^{-1}, respectively, similar to graphene. [28] The FT-IR spectrum of SWNHs shows prominent peaks in the region between 1,600–1,200 cm^{-1} as can be seen in Figure 3b. The peaks at 1,510 and 1,210 cm^{-1} are assigned to the stretching modes of the sp^2 bonded carbon network (C=C) and C–O bonds, respectively. The UV–Vis spectrum of SWNHs displays a maximum at 270 nm corresponding to the π–π^* transition as shown in Figure 3c.

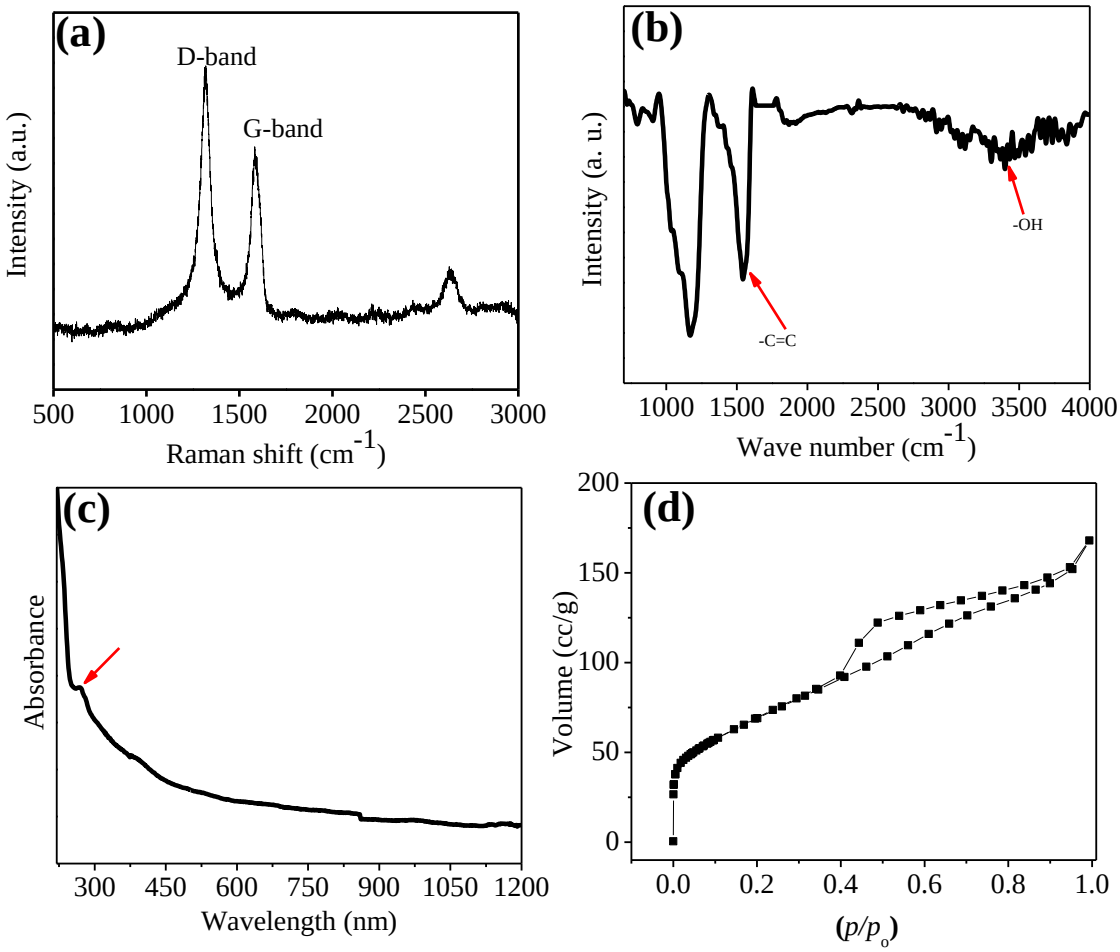

Figure 3. (a) Raman spectrum, (b) IR spectrum, (c) UV-Vis absorption spectrum and (d) N_2 adsorption–desorption curves (at 77 K and 1 atm) of SWNHs samples obtained by submerged arc discharge in liquid N_2.

Surface area and porosity of SWNHs are calculated from N_2 adsorption–desorption measurements *at* 77 K and 1 atm. SWNHs displays type IV adsorption behaviour with contribution from both micro and meso pores. Furthermore, Brunauer–Emmett–Teller (BET) surface area of SWNHs prepared by us is 320 m^2/g, which is comparable with the samples obtained from laser ablation methods.[29]

Although as prepared SWNHs have residual hydroxyl groups on their surface, they are not helpful in making stable dispersions. After treating SWNHs with a mixture of nitric and sulphuric acids, we obtain a water soluble SWNHs, along with some water insoluble portion which settles down (Figure 4a). The aqueous dispersion obtained after acid functionalization is stable for several hours. The infrared spectrum obtained for the soluble

part after drying shows a prominent band at 1720 cm^{-1} due to carboxylic groups as shown in Figure 4b.

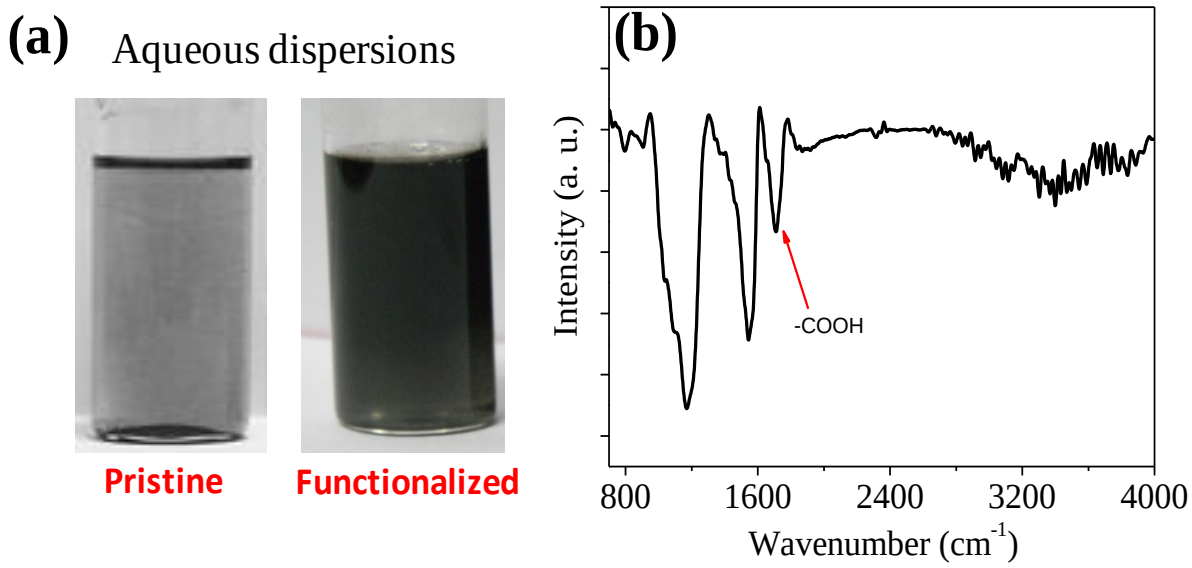

Figure 4. (a) Aqueous dispersions of pristine and acid-functionalized SWNHs and (b) IR spectrum of acid functionalized SWNHs

In order to enhance dispersibility of SWNHs in non-polar solvents we covalently attached long chain hydrocarbons to the acid functionalized nanohorns (SWNH-COOH). Typical synthesis involves treating of SWNH-COOH with DDA (dodecyl amine), where the carboxylic functional groups of nanohorns forms amide bond with the DDA (see experimental procedure). The formation of amide bond between SWNH-COOH and DDA is confirmed by infrared (IR) spectroscopy (Figure 5a). The IR spectrum of SWNH-COOH shows a band at 1,720 cm^{-1}corresponds to the C=O stretching of the carboxyl group. On the other hand, SWNH-DDA composite show characteristic amide I and II bands at 1665 and 1625 cm^{-1}, respectively due to conversion of carboxylic groups of SWNHs in to amide. After amide functionalization, stable dispersions of SWNHs are obtained in non-polar solvents just as in the case of SWNTs. In Figure 5b we show the photographs of the dispersions of SWNH-DDA composite in THF and CCl_4 solvents.

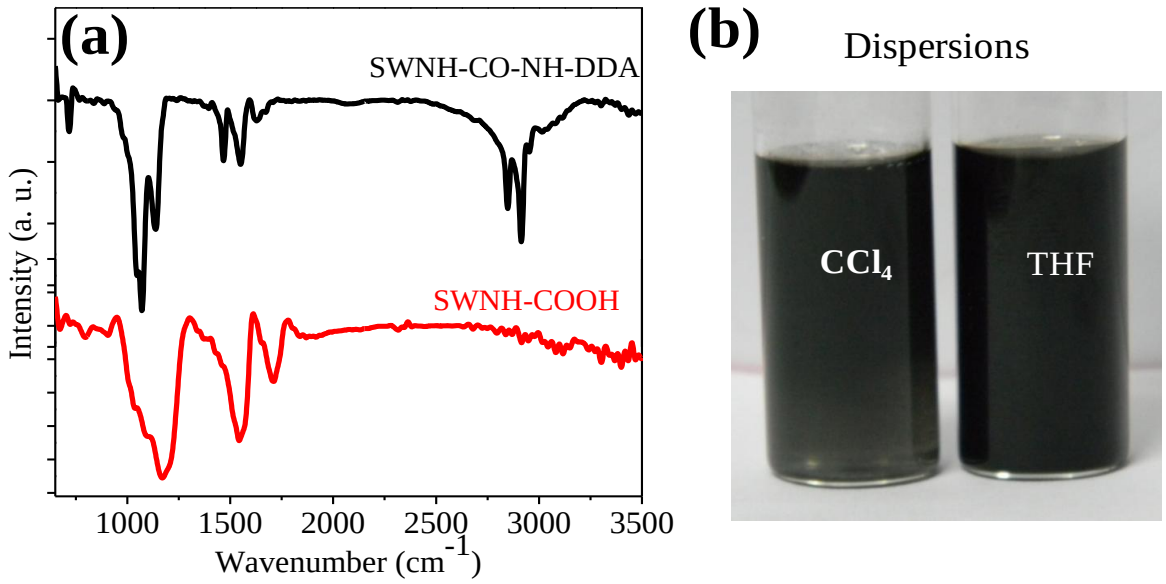

Figure 5. (a) IR Spectra of acid (red), amide functionalized SWNHs (black) and (b) Dispersions of amide functionalized SWNHs in carbon tetrachloride (CCl4) and tetra hydro furan (THF).

We have used tetrapotassium salt of coronene tetracarboxylic acid (CS) for non-covalent functionalization of SWNHs because of its π conjugated network. The large planar aromatic surface of CS permits strong interaction with SWNHs through π–π stacking.[26] Even though coronene is electron rich; its imide and carboxylate derivatives are electron deficient. Derivatives of coronene are fluorescent in solution as well as in solid state. Typical synthesis of SWNHs-CS composite involves the treatment of aqueous dispersion of SWNHs with CS under refluxing conditions (see experimental section). The resultant SWNHs-CS dispersions obtained are black and they are stable up to several months (Inset of Figure 6a). The presence of SWNHs in the aqueous phase is confirmed by Raman spectroscopy. In order to investigate the charge-transfer (CT) interaction of SWNHs-CS composite we have carried out UV-Vis absorption and fluorescence studies. UV–Vis absorption spectra of aqueous CS show characteristic absorption bands at 330 and 360 nm, respectively (Figure 6a). We did not see any change in intensity of absorption peaks of CS with the addition of SWNHs, indicates the absence of ground state CT interaction between two entities.

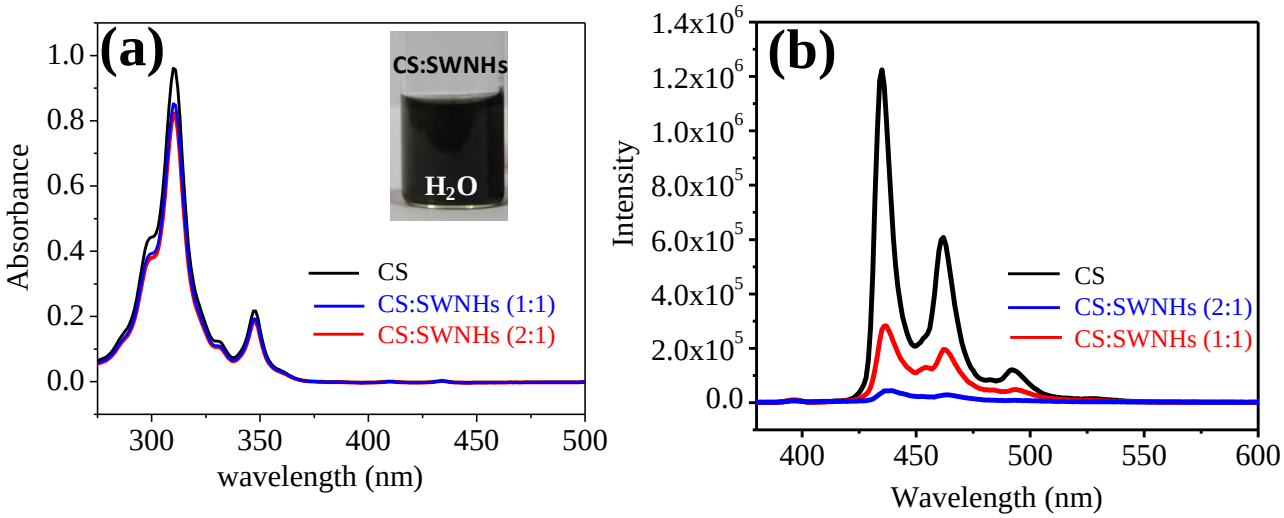

Figure 6. (a, b) UV-Vis absorption (Inset: aqueous dispersions) and Photoluminescence spectra of coronene salt functionalized SWNHs. (tetrapotassium salt of coronene tetracarboxylic acid (CS, black), CS:SWNHs (2:1, red) and CS:SWNHs (1:1, blue).

Unlike absorption spectra, we observed remarkable changes in the fluorescence spectra of CS upon addition of SWNHs. The fluorescence intensity of CS signal decreases drastically with increase in amount of SWNHs as shown in Figure 6b. The quenching of fluorescence intensity of CS signal confirms the excited state CT between CS and SWNHs in the formed composite.

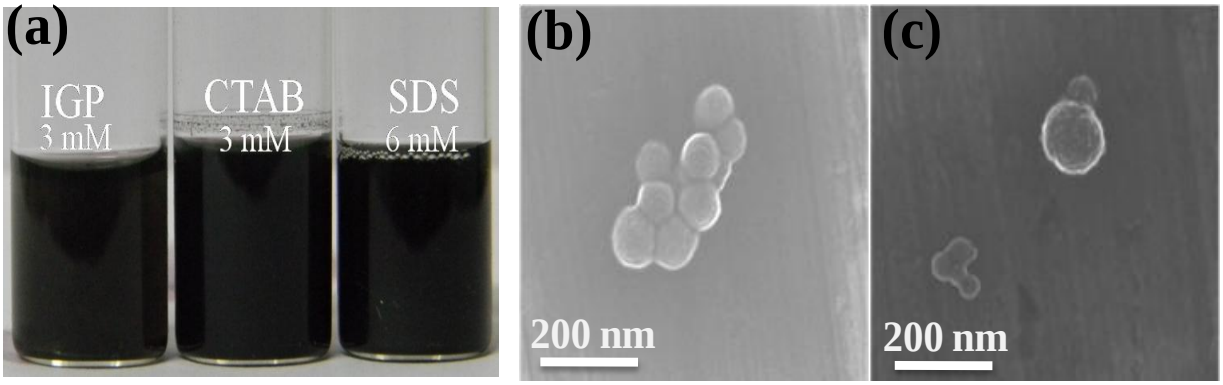

Figure 7. (a) Aqueous dispersions of SWNHs treated with surfactants and (b) FESEM images of SWNHs treated with SDS and IGEPAL.

Wrapping of nanocarbons with various surfactants such has SDS, CTAB and IGEPAL is another most common approach for non-covalent functionalization, where electronic structure of nanocarbons remains unaltered. We have treated SWNHs with various surfactants and examined their dispersibility in aqueous solvents. In case of CTAB and IGEPAL best dispersions were obtained at 3 mM, whereas with SDS we obtained stable dispersions at slightly higher concentration of 6 mM (Figure 7a). SWNH dispersions obtained with surfactants are stable for several months. In case of IGEPAL based dispersions we obtained isolated aggregates of SWNHs (Figure 7c).

2.1.5: Conclusions

We have successfully prepared SWNHs by submerged arc discharge of graphite rods in a liquid nitrogen medium. This method is relatively simple and economically alternative to the laser ablation method which requires high vacuum systems and expensive laser sources. The obtained SWNHs are characterized by using electron microscopy, Infrared, Raman spectroscopy and by other means. We have been able to functionalize and solubilize SWNHs by employing both covalent and non-covalent modifications. Acidification makes SWNHs dispersible in aqueous media, whereas solubilization in non-polar solvents such as THF and CCl_4 has been accomplished by attaching long chain amide, dodecylamine, through amide bond. On the other hand, solubilization in water has been attained by means of π-π interaction between graphene and coronene derivative as well as with surfactants such as IGEPAL, SDS and CTAB. The fluorescence intensity of coronene derivative decreases drastically with SWNHs, indicating the excited state charge-transfer between two components.

2.1.6: References

1. S. Iijima, M. Yudasaka, R. Yamada, S. Bandow, K. Suenaga, F. Kokai, K. Takahashi, *Chem. Phys. Lett*. **1999**, ***309,*** 165.
2. T. Ohba, K. Kaneko, M. Yudasaka, S. Iijima, A. Takase, H. Kanoh, *J. Phys. Chem. C* **2012**, ***116***, 21870.
3. T. Murakami, K. Ajima, J. Miyawaki, M. Yudasaka, S. Iijima, K. Shiba, *Mol. Pharm*. **2004**, ***1***, 399.
4. J. Miyawaki, M. Yudasaka, T. Azami, Y. Kubo, S. Iijima, *ACS Nano* **2008,** *2*, 213.
5. M. Kosaka, S. Kuroshima, K. Kobayashi, S. Sekino, T. Ichihashi, S. Nakamura, T. Yoshitake, Y. Kubo, *J. Phys. Chem. C* **2009,** *113*, 8660.
6. K. Murata, K. Kaneko, H. Kanoh, D. Kasuya, K. Takahashi, F. Kokai, M. Yudasaka, S. Iijima, *J. Phys. Chem. B **2006**, 106, 1136.*
7. N. Karousis, I. S.-Martinez, C. P. Ewels, N. Tagmatarchis, *Chem. Rev.* **2016**, 116, 4850.
8. B. Jiang, L. Hu, X. Shen, S. Ji, Z. Shi, C. Liu, L. Zhang, H. Liang *ACS Appl. Mater. Interfaces* **2014**, *6*, 18008.
9. Y. Chen, R. C. Haddon, S. Fang, A. M. Rao, P. C. Eklund, W. H. Lee, E. C. Dickey, E. A. Grulke, J. C. Pendergrass, A. Chavan, B. E. Haley, R. E. Smalley, *J. Mater. Res.* **1998**, *13*, 2423.
10. T. W. Ebbesen, *ACC. Chem. Res.* **1998**, *31*, 558.
11. M. Monthioux, B.W. Smith, B. Burteaux, A. Claye, J.E. Fischer, D.E. Luzzi, *Carbon*, **2001**, *39*, 1251.
12. K. Tohji, H. Takahashi, Y. Shinoda, N. Shimizu, B. Jeyadevan, I. Matsuoka, Y. Saito, A. Kasuya, S. Ito, Y. Nishina, *J. Phys. Chem B* **1997**, *101*, 1974.
13. S. Bandow, S. Asaka, X. Zhao, Y. Ando, *Appl. Phys. A* **1998**, *67*, 23.
14. E. Dujardin, T. W. Ebbesen, A. Krishnan, M. M. J. Treacy, *Adv. Mater*. **1998**, *10*, 611.
15. S. Bandow, A. M. Rao, K. A. Williams, A. Thess, R. E. Smalley, P. C. Eklund, *J. Phys. Chem. B* **1997**, *101*, 8839.
16. G. S. Duesberg, M. Burghard, J. Muster, G. Philipp, S. Roth, *Chem. Commun*. **1998**, 435.

17. R. J. Chen, Y. G. Zhang, D. W. Wang, H. J. Dai, *J. Am. Chem. Soc*. **2001**, *123*, 3838.
18. C. N. R. Rao, A. Govindaraj, Nanotubes and Nanowires, *Royal Society of Chemistry*, **2011**, 2nd edition.
19. C. D. Scott, S. Arepalli, P. Nikolaev, R. E. Smalley, Appl. Phys. A **2001**,*72*, 573.
20. 20. Y. Ando, X. Zhao, S. Inoue, S. Iijima S, *J. Cryst. Growth*. **2002,** *237*, 1926.
21. J. Cumings, W. Mickelson, A. Zettl, *Chem. Commun.* ***2003,*** *126*, 359.
22. M. Ishigami, J. Cumings, A. Zettl, S. Chen, *Chem. Phys. Lett*. **2000**, *319*, 457.
23. G. Pagona, A. S. D. Sandanayaka, T. Hasobe, G. Charalambidis, A. G. Coutsolelos, M. Yudasaka, S. Iijima, N. Tagmatarchis. *J. Phys. Chem. C* **2008**, *112*, 15735.
24. A. Izadi-Najafabadi, T. Yamada, D. N. Futaba, M. Yudasaka, H. Takagi, H. Hatori, S. Iijima, K. Hata, *ACS Nano* **2011**, 5, 811.
25. Y.-P. Sun, K. Fu, Y. Lin, W. Huang, *Acc. Chem. Res.* **2002**, *35*, 1096.
26. A. Ghosh, K. V. Rao, S. J. George, C. N. R. Rao, *Chem.–Eur. J.* **2010**, 16, 2700.
27. T. Kawai, Y. Miyamoto, O. Sugino, Y. Koga, *Phys. Rev. B* **2002**, *66*, 033404.
28. L. S. Panchakarla, K. S. Subrahmanyam, S. K. Saha, A. Govindaraj, H. R. Krishnamurthy, U. V. Waghmare, C. N. R. Rao *Adv. Mater*. **2009**, ***21***, 4726.
29. K. Murata, K. Kaneko, F. Kokai, K. Takahashi, M. Yudasaka, S. Iijima, *Chem. Phys. Lett.*, **2000**, *331*, 14.

2.2: Nitrogen Doped Single-walled Nanohorns and Other Nanocarbons Generated by Arc-discharge in Liquid Argon and Other Media.

Summary*

Synthesis of SWNHs by arc discharge between graphite electrodes submerged in liquid nitrogen medium yields nanohorns with some amount of nitrogen (1.5 at %) incorporated in them. If one has to obtain pure nanohorns by submerged arc discharge, it would be necessary to do so in a completely inert liquid medium. For this purpose, we have carried out arc discharge between graphite electrodes in liquid argon and compared them with that of samples obtained in liquid nitrogen. Nitrogen-doped SWNHs (N-SWNHs, 4.5 at %) are prepared in liquid argon medium by arc evaporation of the graphite electrodes suitably stuffed with nitrogen rich precursor (melamine). N-SWNHs show reduced electrical resistance compared to pristine SWNHs as indicated by I-V measurements. The N doping causes stiffening of the Raman G-band and intensifications of the defect related D-band.

Having prepared pure SWNHs by arc discharge in liquid argon, we have explored nanocarbon structures generated by arc discharge in different liquid media such as water, N,N-dimethylformamide (DMF) and *N*-methyl-2-pyrrolidone (NMP). Depending on the liquid medium, we obtained different forms of nanocarbons which include MWNTs and graphene nanosheets.

A paper based on this work has appeared in *Mater. Res. Express (2014).*

2.2.1: Introduction

Tuning physiochemical properties of materials by chemical modifications becomes essential in numerous applications.[1] One way of realizing this control is by elemental doping, a technique successfully adapted in semiconductor silicon technology.[2, 3] For instance, nitrogen atoms doped in silicon lock dislocations to enhance mechanical strength. Effects of subustitutional doping of silicon with phosphorous or other various elements with different oxidation state have been well documented in the literature. Heteroatom doping brings dramatic changes in the electronic properties of carbon based materials as well. Particularly, subustitution of carbon atoms of nanocarbons with boron or nitrogen renders them in to p- or n-type, respectively. In addition, subustitutional doping also causes changes in the Raman spectra and other properties of nanocarbons.

In the literature, different routes have been reported for doping of carbon nanotubes (CNTs) with heteroatoms such has nitrogen. In as early as 1997, carbon atoms of multi-walled nanotubes (MWNTs) were substituted with nitrogen by the pyrolysis of aza aromatics (pyridine, triazine).[4] MWNTs showed 5, 3.5 and 3 at.% nitrogen content at pyrolysis temperatures of 973, 1123 and 1273 K, respectively when pyridine was used for pyrolysis. Pyrolysis of mixture of a pyrirdine and $Fe(CO)_5$ in flowing $Ar+H_2$ yields good amount of nitrogen doped MWNTs.[4] Iron particles formed by the decomposition of $Fe(CO)_5$ acts as nucleation centers for the growth of CNTs. Nitrogen doped MWNTs were also synthesized by pyrolizing pyridine over Co catalyst at 1000 ^oC while pyrolysis of organic precursors in presence of pyridine yields bundles of aligned N-MWNTs. [5] High nitrogen doping content of 3 at.% has been achieved with iron catalyst rather than Co catalysts.[6] Pyrolysis of ferrocene and melamine mixture at 900-1000 ^oC yields bundles of aligned CN_x nanotubes and the nitrogen doping amount of 2-10 at.% is achieved by this strategy.[7] Using scanning tunneling spectroscopy (STS) experiments the electronic density of states of aligned CN_x tubes was obtained, they show strong features in the band close to Fermi level (0.18 eV). Tight-binding and ab initio calculations suggested that donor states close to Fermi level are arises from the pyridine-like nitrogen.

Nitrogen doped single walled nanotubes SWNTs (N-SWNTs) with nitrogen content up to 1 at.% have been prepared by the arc evaporation of graphite electrodes (anode) stuffed with nitrogen rich precursors along with the metal catalysts.[8] In this procedure, melamine or

boron nitride is used as nitrogen sources. Chemical vapor deposition (CVD) of xylene and acetonitrile over transition metal coated substrates is also reported for the preparation of N-SWNTs.[9] On the other hand, CVD of methane and ammonia over bi metallic catalyst $Mo_{0.1}Fe_{0.9}Mg_{13}O$ yields nitrogen doped double walled nanotubes (N-DWNTs). [10, 11]

2.2.2: Scope of the present investigations

Heteroatom doping in carbon nanotubes causes alterations in the electronic structure by tuning the position of Fermi level which is of great value in nanocarbon based devices. Nanotubes can be chemically doped by two means; (1) adsorption of organic or gas molecule to the nanocarbon surface (2) subustitutional doping where carbon atom is replaced with heteroatoms such as nitrogen and boron.

Like SWNTs, SWNHs are expected to display changes in electronic properties on subustitutional doping of carbon atoms with nitrogen due to similarity in their structures. In view of this, we considered it is worthwhile to investigate the effect of nitrogen doping on nanohorns. To prepare nitrogen doped SWNHs (N-SWNHs), graphite electrodes suitably stuffed with nitrogen rich precursor (melamine) are arc evaporated in liquid argon medium. Use of inert medium (liquid argon) is crucial in the synthesis, since SWNHs generated in liquid nitrogen medium themselves contain some amount of incorporated nitrogen. Then, we have compared N doping amounts of N-SWNHs obtained in liquid argon with pure SWNHs as well as with samples obtained in liquid nitrogen using X-ray photoelectron spectroscopy.

2.2.3: Experimental section

We synthesized pure and N-doped single-walled nanohorns (N-SWNHs) by arc discharge between graphite electrodes submerged in a liquid argon medium. For the synthesis of pure (un-doped) SWNHs, two graphite rods (99.999% purity) of 5 mm in diameter were set at the cathode and at a movable anode and then submerged in liquid argon. DC arc discharge (plasma) was generated between the graphite electrodes by touching each other. During arc discharge, current and voltage between the electrodes were maintained at 80 A and 38 V, respectively, A 10 cm long anode graphite rod was consumed in a period of 15 min. After arc discharge, the obtained product was collected and used for further characterization and analysis.

Nitrogen-doped SWNHs were also prepared under similar conditions by suitably modifying the graphite rod with a nitrogen source. A cylindrical hole with 3 mm diameter was made at the center of a 5 mm diameter graphite rod. Melamine (20 wt.%) containing graphite powder was stuffed into the graphite rod and preheated at 250 °C for 2 h in an inert atmosphere before arc discharge. Arc discharge is started between the pure and melamine-containing graphite rod submerged in liquid argon media by touching each other. In addition, we also carried out submerged arc discharge in water, ethanol, N,N-Dimethylformamide, and N-Methyl-2-pyrrolidinone solvents.

2.2.4: Results and Discussion

In Figures 1a and b we show the FESEM and HRTEM images of the arc soot obtained during submerged arc discharge of graphite rods in liquid argon. FESEM image infers that the product consists of spherical shaped particles with diameters in the range 80–100 nm. HRTEM image indicates that the particles are aggregates of horn-shaped nanostructures with closed tips. White arrows in HRTEM image shows the individual nanohorns protruding from spherical (dahlia-like) aggregates.

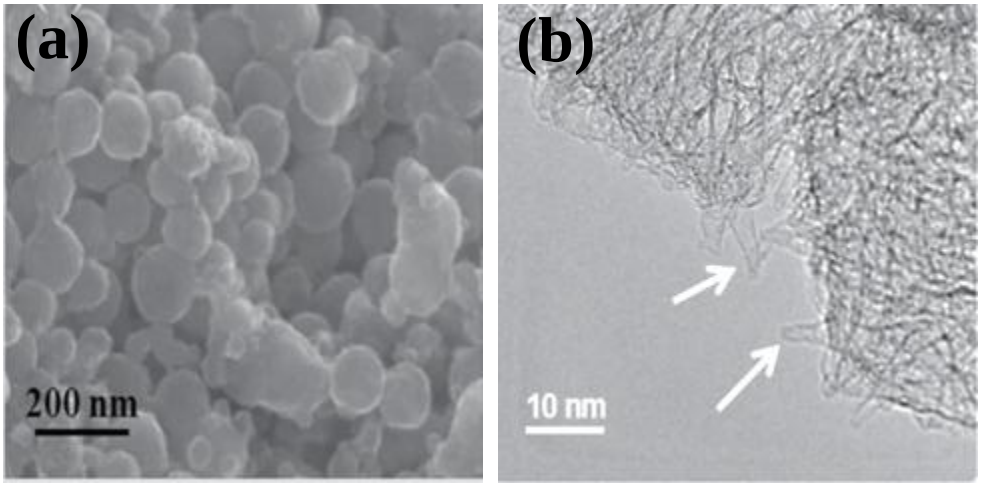

Figure 1. (a) FESEM and (b) HRTEM images of SWNHs obtained by submerged arc discharge in liquid argon.

In Figure 2b, we show the N1*s* core-level spectra of SWNHs obtained by arc discharge in liquid nitrogen and argon medium. SWNHs obtained in liquid nitrogen shows strong N1*s*

signal due to the incorporated nitrogen in the nanohorn structure while arc discharge. On the other hand, absence of N1*s* signal in case of SWNHs produced in liquid argon medium implies that the nanohorns produced are free of N impurities.

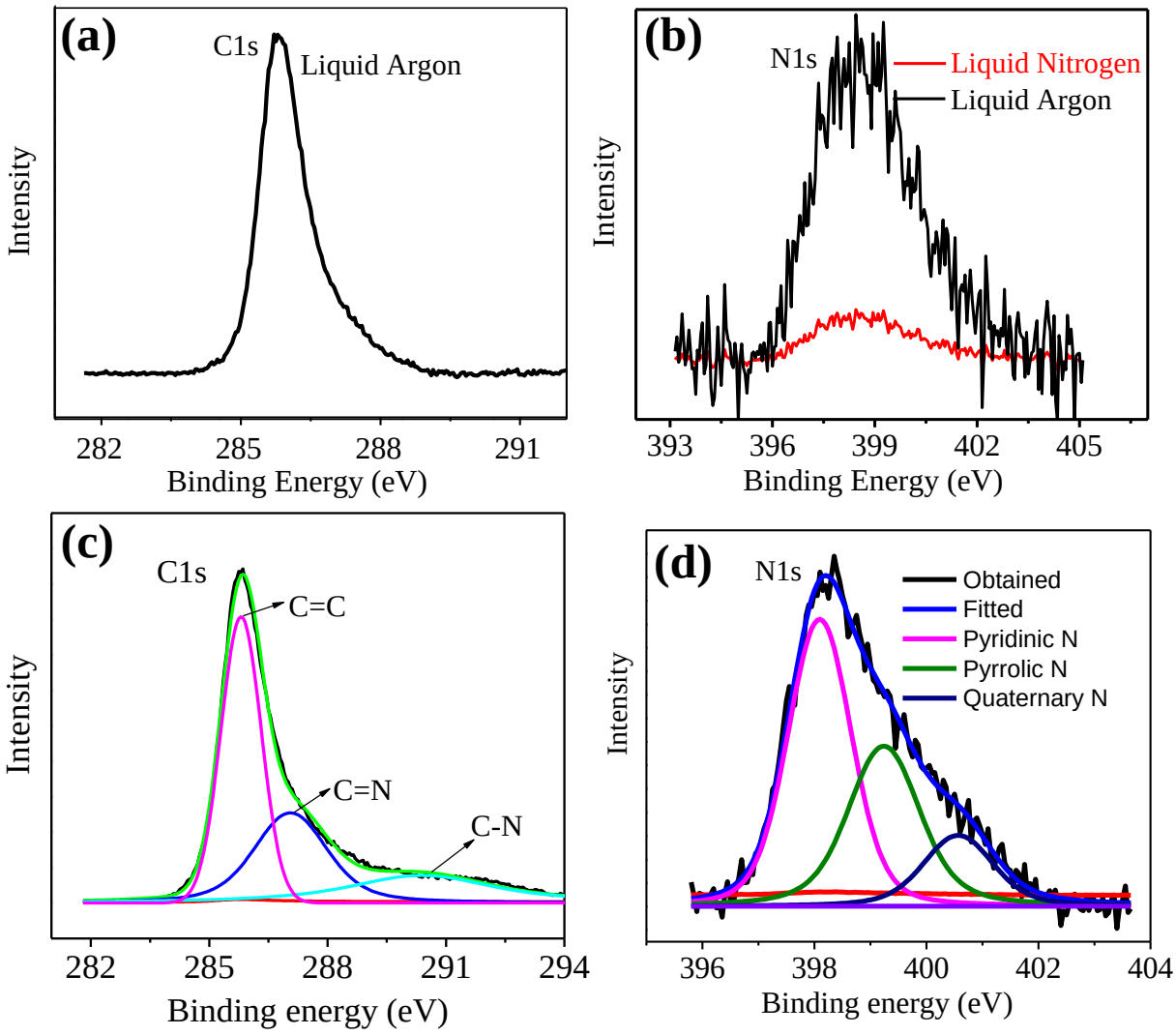

Figure 2. (a) C1*s* XPS core-level spectra of SWNHs obtained in liquid argon; (b) N1*s* XPS core-level spectra of SWNHs obtained in liquid argon and nitrogen, respectively and (c) C1*s* and (d) N1*s* XPS core-level spectra of N-doped SWNHs obtained in liquid argon medium.

The C1*s* and N1*s* core-level spectra of N-SWNHs prepared in liquid argon medium were shown in Figures 2c and d, respectively. The C1*s* signal is deconvoluted to three features

with a main peak at 285. 4 eV corresponds to the C–C bonds originating from the sp^2 like graphite structure. The small peaks at 285.4 and 288 eV are arises due to the C= N and C-N bonds, respectively. Similarly, N1*s* signal deconvoluted into three features with a peak at 398.4 eV corresponds to pyridinic nitrogen. The peak at 399.2 eV corresponds to pyrrolic nitrogen and the peak at 401.1 eV to graphitic nitrogen. These results are similar to that of reported for the substitutional doping of carbon with nitrogen in SWNTs or graphene.[12, 13] The nitrogen content in N-SWNHs as estimated from N1*s* spectrum is 4.5.at % while nanohorns generated in liquid nitrogen gives 1.5.at%.

We have investigated the Raman spectra of pure and N-SWNHs obtained by arc discharge in liquid argon along with that of nanohorns obtained from liquid nitrogen and they are shown in Figure 3a. Raman spectra of theses samples show an intense defect-induced D band (1337 cm^{-1}) and the SP^2 hybridized carbon G band (1583 cm^{-1}). It is noted that G-band stiffens in case of N-SWNHs as can be seen in Figure 3a.

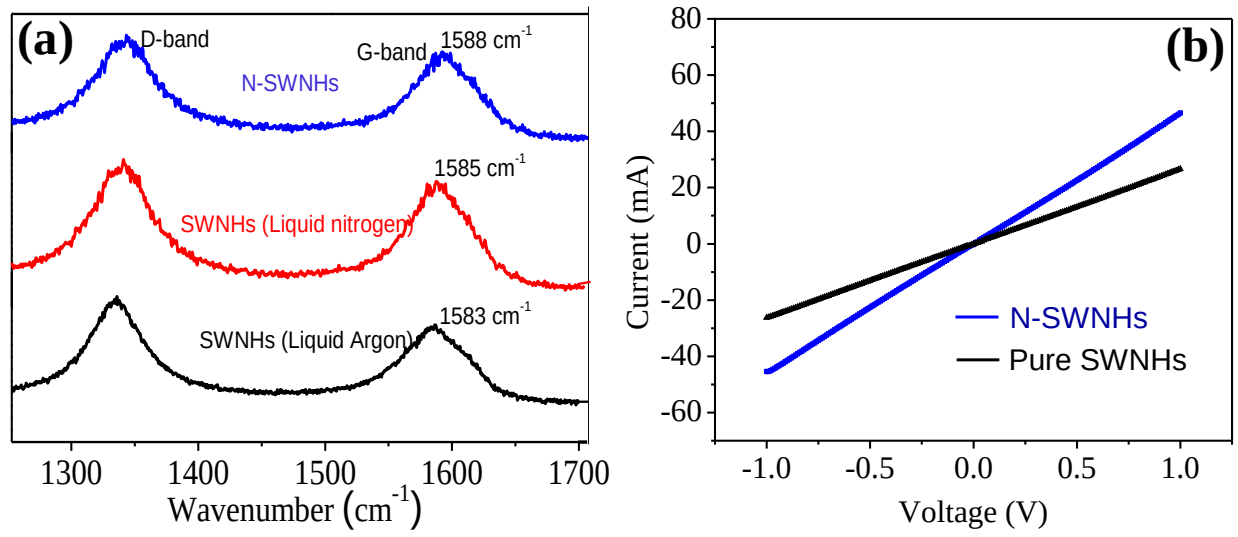

Figure 3. (a) Raman spectra of SWNHs obtained in liquid argon (black), liquid nitrogen (red) and N-SWNHs (blue). (b) I–V characteristics of pure and N-doped SWNHs obtained in liquid argon.

This is similar to the results obtained with nitrogen doped graphene.[13] Moreover, magnitude of G-band shift with liquid nitrogen sample is less in comparison to N-SWNHs, probably due to the more doped nitrogen content in the latter case. Figure 3b shows the I–V characteristics

of pure and N-SWNHs obtained by arc discharge in liquid argon. N-SWNHs showed slightly decreased electrical resistance compared to pure SWNHs (25 Ω). on the other hand, SWNHs obtained in liquid nitrogen did not show any changes in electrical resistance in comparison to N-SWNHs, except the slight non-linear behavior in case of N-SWNHs.

We have carried out submerged arc discharge between graphite electrodes in several liquid media and obtained different nanocarbon structures which include graphene and MWCNTs.

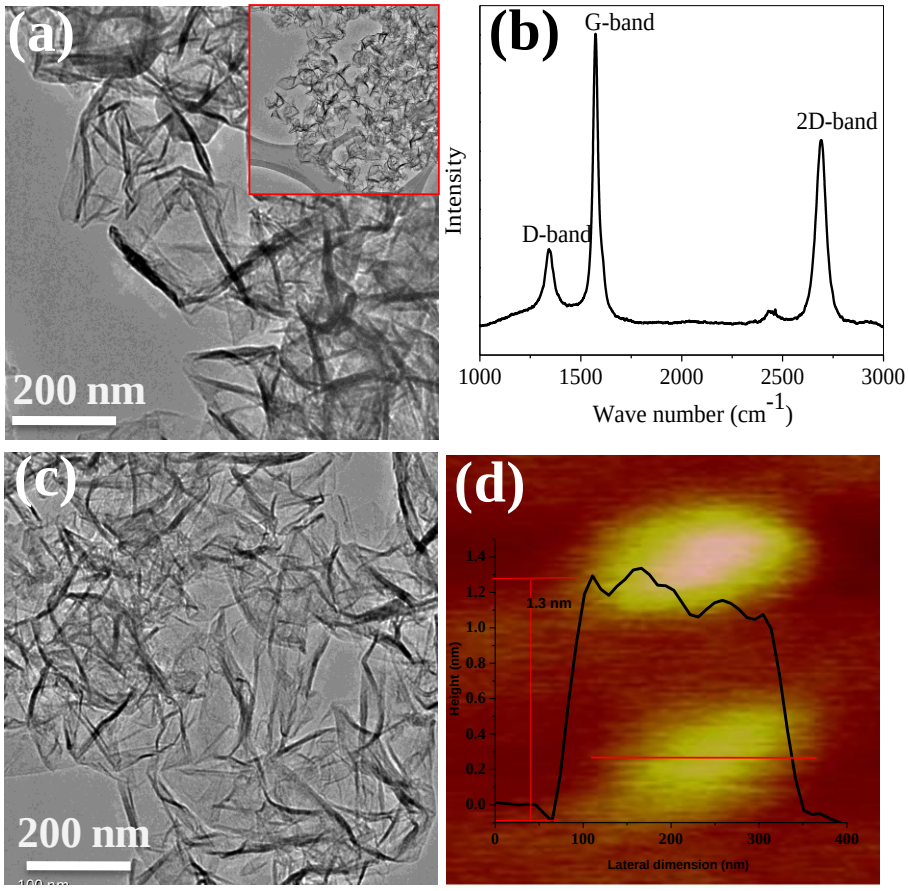

Figure 4. (a, b) TEM image and Raman spectra of few-layer graphene sheets obtained in DMF and (c, d) TEM and AFM images of few-layer graphene sheets obtained in NMP.

In each case, the applied current between the electrodes during arc discharge was optimized to get the best quality morphology. We obtained few-layer graphene sheets by arc discharge of graphite rods in both DMF and NMP solvents. TEM images of the graphene sheets obtained in DMF are shown in Figures 4a and c which shows the presence of well spread

graphene sheets. Figure 4b shows the Raman spectra of graphene sheets obtained by arc discharge in NMP. We see a weak band due to the defect induced D-band at 1343 cm^{-1}, an intense G-band at 1574 cm^{-1} along with the 2D band at 2690 cm^{-1}. The high intensity of the 2D band clearly indicates that the graphene sheets obtained are few-layer in nature. The thickness of graphene sheets as obtained by AFM measurements implies sheets are 4-5 layers thick. The formation of graphene sheets in DMF and NMP is due the formation reactive hydrogen species which terminate dangling carbon bonds, and do not allow nanosheets to form closed structures.[14]

Submerged arc discharge in a water medium yields a black fluffy product floating on the surface. TEM images show that the product contains multi-walled carbon nanotubes (MWNTs) as can be seen from Figure 5. The average outer diameter of the MWNTs is ~10 nm and the inner diameter is ~5 nm as obtained from HRTEM images. Arc discharge in water releases CO and H_2 gases and creates a quasi-inert gas atmosphere around the discharge zone. This process generates free carbon vapor to undergo nucleation and tubular growth results in the formation of MWCNTs.[15]

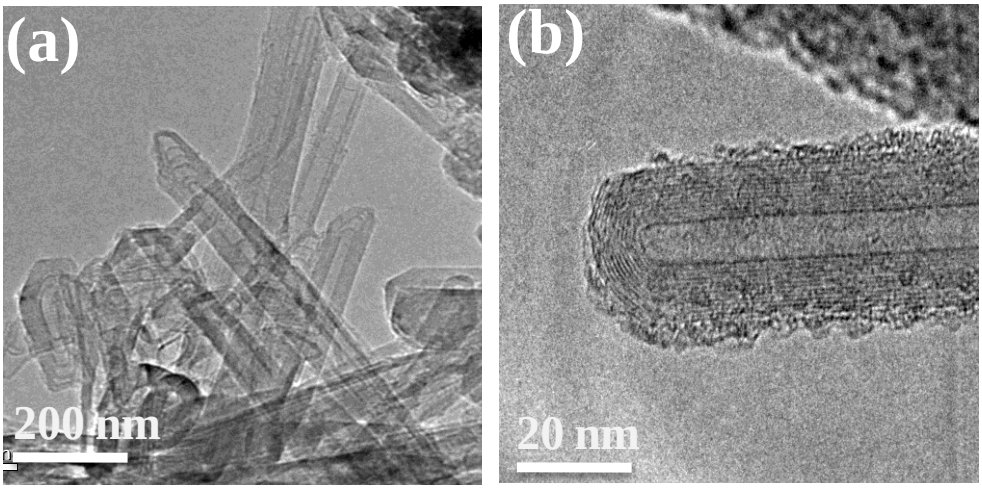

Figure 5. (a, b) TEM and HRTEM images of multi-walled carbon nanotubes obtained in water.

2.2.5: Conclusions

Here, we report the synthesis of pure and nitrogen-doped SWNHs obtained by submerged arc discharge of graphite rods in a liquid argon medium. The absence of an XPS N 1*s* signal, which is present in nanohorns obtained in liquid nitrogen, indicate that the nanohorns are free from nitrogen impurities. Stiffening of Raman G-band and decrease in electrical resistance is observed in case of N-SWNHs compared to pure SWNHs. Arc discharge in other liquid media such as water, ethanol, dimethylformamide (DMF), *n*-methyl pyrrolidone (NMP), yield different nanocarbon structures including multi-walled carbon nanotubes (MWNTs), and few-layer graphene.

2.2.6: References

1. C. N. R. Rao, A. Govindaraj, in *Nanotubes and Nanowires, RSC nanoscience & Nanotechnology Series*, RSC, Cambridge, UK, **2005**.
2. K. Sumino, M. Imai, *Philos. Mag. A.* **1983**, *47*, 753.
3. K. Sumino, I. Yonenaga, M. Imai, T. Abe, *J. Appl. Phys.* **1983**, *54*, 5016.
4. R. Sen, B. C. Satishkumar, A. Govindaraj, K. R. Harikumar, M. K. Renganathan, C. N. R. Rao, *J. Mater. Chem.* **1997**, *7*, 2335.
5. R. Sen, B. C. Satishkumar, A. Govindaraj, K. R. Harikumar, G. Raina, J.-P. Zhang, A. K. Cheetham, C. N. R. Rao, *Chem. Phys. Lett.* **1998**, *287*, 671.
6. M. Nath, B. C. Satishkumar, A. Govindaraj, C. P. Vinod, C. N. R. Rao, *Chem. Phys. Lett.* **2000**, *322*, 333.
7. M. Terrones, P. M. Ajayan, F. Banhart, X. Blase, D. L. Carroll, J. C. Charlier, R. Czerw, B. Foley, N. Grobert, R. Kamalakaran, P. Kohler-Redlich, M. Ruhle, T. Seeger, H. Terrones, *Applied Physics a-Materials Science & Processing* **2002**, *74*, 355.
8. M. Glerup, J. Steinmetz, D. Samaille, O. Stéphan, S. Enouz, A. Loiseau, S. Roth, P. Bernier, *Chem. Phys. Lett.* **2004**, *387*, 193.
9. G. Keskar, R. Rao, J. Luo, J. Hudson, J. Chen, A. M. Rao, *Chem. Phys. Lett.* **2005**, *412*, 269.
10. L. S. Panchalkarla, A. Govindaraj, C. N. R. Rao, *ACS Nano* **2007**, *1*, 494.
11. S. Y. Kim, J. Lee, C. W. Na, J. Park, K. Seo, B. Kim, *Chem. Phys. Lett.* **2005**, *413*, 300.
12. C. Morant, J. Andrey, P. Prieto, D. Mendiola, J. M. Sanz, E. Elizalde, *Phys. Status Solidi A* **2006**, *6*, 1069.
13. *L.* S. Panchakarla, K. S. Subrahmanyam, S. K. Saha, A. Govindaraj, H. R. Krishnamurthy, U. V. Waghmare, C. N. R. Rao, *Adv. Mater.* **2009**, *21*, 4726.
14. *V.* Scuderi, C. Bongiorno ,G. Faraci, S. Scalese, *Carbon* **2012,** *50,* 2365.
15. *Y. L. Hsin, K. C. Hwang, F. R. Chen, J. J. Kai, Adv. Mater.* **2001, *13,*** 830.

2.3: Mechanical properties of PVA-SWNHs composites

2.3: Carbon-Nanohorn-Reinforced Polymer Matrix Composites: Synergetic Benefits in Mechanical Properties

Summary*

Mechanical properties of single-walled carbon nanohorns (SWNH) and SWNH plus few-layer graphene (EG)-reinforced poly(vinyl alcohol) (PVA) matrix composites have been measured using the nanoindentation technique. The elastic modulus (E) and hardness (H) of PVA were found to improve by ~315% and ~135%, respectively, upon the addition of just 0.4 wt.% SWNH. These properties were found to be comparable to those obtained upon the addition of 0.2 wt.% single-walled nanotubes (SWNT) to PVA. Furthermore, upon binary addition of 0.2 wt.% EG and 0.4 wt % SWNH to PVA, benefits in the form of ~400% and ~330% synergy in E and H, respectively, were observed, along with an increased resistance to viscoelastic deformation. The reasons for these improvements are discussed in terms of the dimensionality of nanocarbon, the effectiveness of nanocarbon and polymer matrix interaction, and the influence of nanocarbon on the degree of crystallinity of the polymer. The results from SWNH reinforcement in this study demonstrate the scope for a novel and, in contrast to SWNT composites, a commercially feasible opportunity for strengthening polymer matrices.

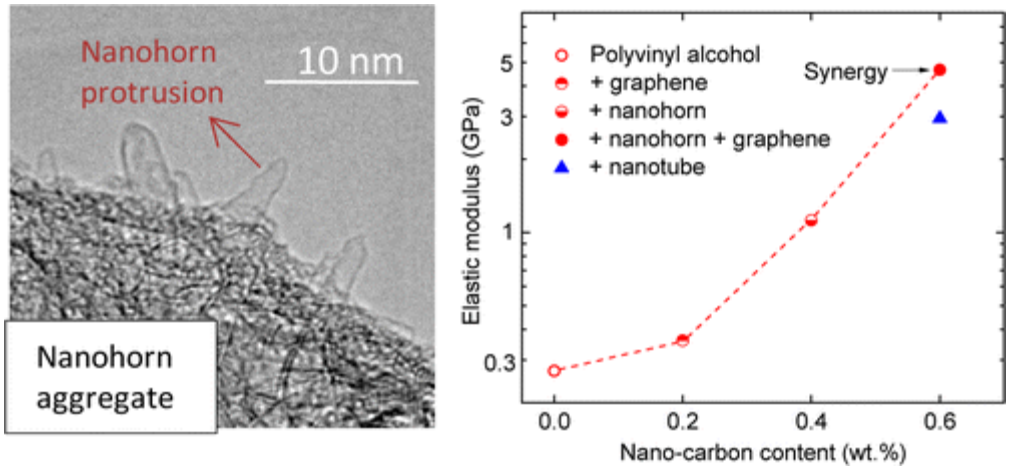

A paper based on this work has appeared in ACS Appl. Mater. Interfaces, *(2015).*

2.3.3: Experimental section

Synthesis and characterization:

SWNHs were prepared by DC-arc discharge of graphite rods in liquid nitrogen and were then functionalized by treating with a mixture of sulfuric acid and nitric acid at 80 °C for 2 h. The functionalized SWNHs were dispersed in distilled water by sonication. SWNH-PVA composites were then prepared as follows: First, a PVA solution was prepared by adding PVA to water at 60 °C while continuously stirring. The dispersed SWNHs, with weight fractions of 0.2, 0.4 and 0.6, were added to this and sonicated for further 900 s. The obtained dispersion was dried in a Petri dish at 40–50 °C under vacuum over a period of 4–5 days and subsequently desiccated in $CaCl_2$ for seven days to ensure complete removal of moisture from the composite. Pure PVA without nanocarbon addition and binary PVA composites with 0.4 wt.% SWNH and 0.2, 0.4 and 0.6 wt.% EG were prepared following the above steps.

Graphene (EG) with 3–4 layers were obtained by thermal exfoliation of graphite oxide; the latter prepared by the modified Hummer's method.[31] SWNTs with 98% purity were acquired from Comocat (Sigma Aldrich). Both of them were functionalized by acid treatment using the following procedure: EG (50 mg) and SWNTs (50 mg) were separately taken in a solution of conc. nitric acid (2 ml), sulphuric acid (2 ml) and distilled water (16 ml), and were heated in a microwave oven for 5–8 min under hydrothermal conditions to obtain a dispersed mixture. This mixture was then heated in an oven for 12 hrs at 100 °C and later filtered through a sintered glass funnel by repeatedly washing with distilled water to ensure complete removal of acid. The obtained fuctionalized nanocarbons showed good dispersion in water compared to their pristine form. EG- and SWNT-PVA composites were obtained using the same procedure mentioned for SWNH-PVA.

Infrared (IR) spectroscopy was performed on the functionalized SWNHs to confirm the introduction of hydroxyl (−OH) and carboxyl ($-CO_2H$) groups. Differential scanning calorimetry (DSC) was performed on all of the composite samples (10 mg each) in a Mettler-Toledo system using a scan rate of 0.08 K/s in the temperature range of 40–250 °C. SWNHs

were characterized by scanning and transmission electron microscopes following our previous study.[11]

Nanoindentation:

All nanoindentation tests were carried out using a TriboIndenter (Hysitron Inc., Minneapolis, MN, USA) system. A minimum of 25 indentations each was performed on PVA and PVA-nanocomposite films using a peak load, P_{max}, of 500 μN and a loading rate of 0.5 mN/s. Penetration depths (< 4 μm) corresponding to this load, despite being large, are significantly smaller than 5% of the film thickness (0.5 mm or more), thus ensuring negligible effect of the substrate on measured properties.[32] To reduce/eliminate artifacts in E and H estimation due to the viscoelastic behavior of PVA, the following procedure was utilized: A spheroconical tip (1 μm radius) was used to reduce large creep displacements produced by commonly used sharp tips;[33, 34] the unload curves from these preliminary indentations and E and H obtained from them are shown in Figure 1a. A prolonged hold-period of 250 s was found necessary to allow time for viscoelastic relaxation, and subsequently to avoid the effect of creep on unload curve, which otherwise results in an overestimation of E (Figure 1b). A relatively high unload rate of 2 mN/s was used to minimize viscoelastic recovery and to obtain a convergent solution to the power-law fit. These load function parameters were also used for the composites as they showed a similar or a more dampened viscoelastic response. E was extracted from the unloading curve by fitting it to a power-law relation given by Oliver & Pharr. [35] H was taken as the instantaneous value, obtained as P_{max} divided by the contact area at the end of loading. To ensure precise estimations, the tip area function was calibrated in a high depth range (0.5–4.5 μm) prior to testing. For this, optically clear polycarbonate (PC) with a modulus of 2.44 GPa was used.

PC was preferred to the conventionally used fused quartz as the latter does not facilitate large displacements required here, and has also been found unsuitable as a calibration standard for polymers for various reasons. [36]

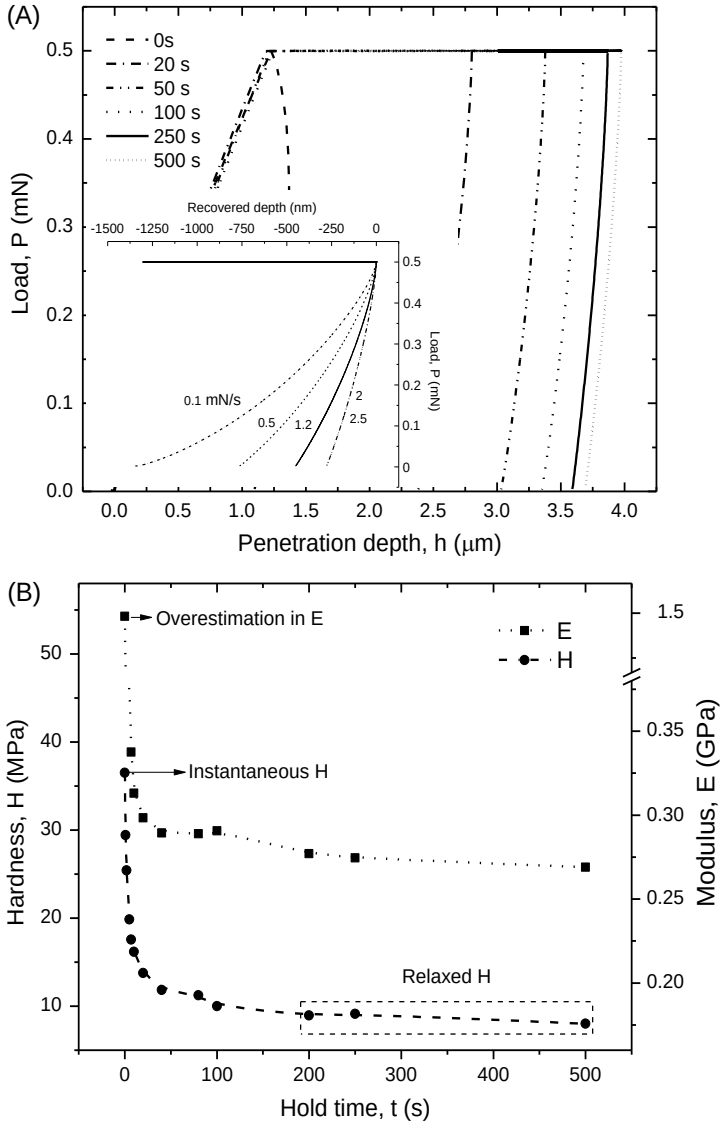

Figure 1: (a) Load-displacement, P-h, curves obtained from nanoindentation on PVA at varying hold times. Inset shows the rate dependent viscoelastic recovery of unload curves. An unload rate of 2 mN/s was chosen to minimize the effect of viscoelastic displacements on the Oliver-Pharr modulus estimation and to obtain a convergent solution (b). Shows the effect of hold-time creep on modulus, E, and hardness, H, estimates. A hold of at least 250s is found to be necessary to prevent the overestimations in E due to creep.

2.3.4: Results

In Figures 2a and b we present the scanning and transmission electron micrographs of SWNHs, which indicate nanohorns are aggregated and have spherical morphology. Some of these aggregates show outward protrusions of individual SWNHs as shown in HRTEM images. We have functionalized nanohorns by covalent modification (see experimental section) in order to enhance their dispersibility in polymer matrix.

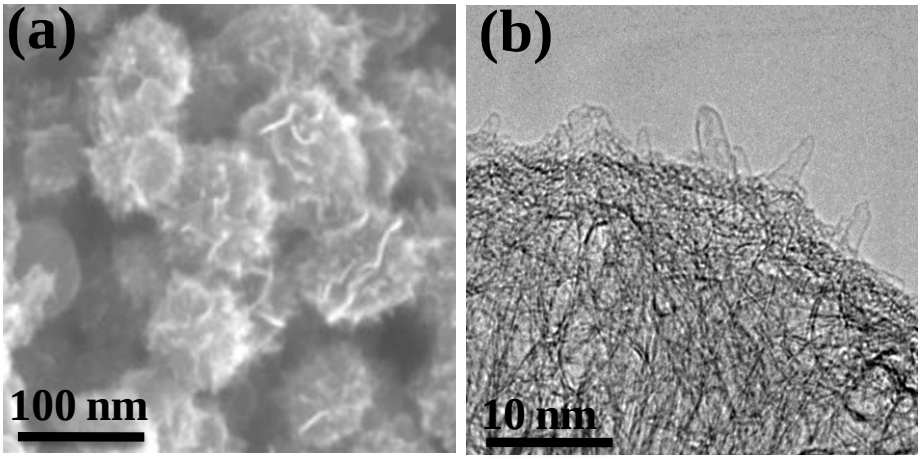

Figure 2. (a) FESEM and (b) HRTEM images of SWNHs.

Figure 3a shows the IR spectra of pristine SWNHs and acid-functionalized SWNHs. The new peak at 1720 cm^{-1} in functionalized sample confirm the successful introduction of carboxyl ($–CO_2H$) groups on SWNHs by acidification. Similarly, we also functionalized other nanocarbons such as graphene and SWNTs and their respective IR spectra are shown in Figure 3a. Degree of crystallinity (χ) of polymer matrix can have significant impact on the mechanical property of SWNH-PVA composites therefore we calculated change in χ of polymer upon addition of different weight ratios of nanohorn by differential scanning colorimetric method (DSC). Figure 3b shows the DSC curves obtained for SWNH-PVA composites. Note that the increase in area of the peak upon nanohorn addition indicates that enhanced crystalline content of the reinforced PVA.

2.3: Mechanical properties of PVA-SWNHs composites

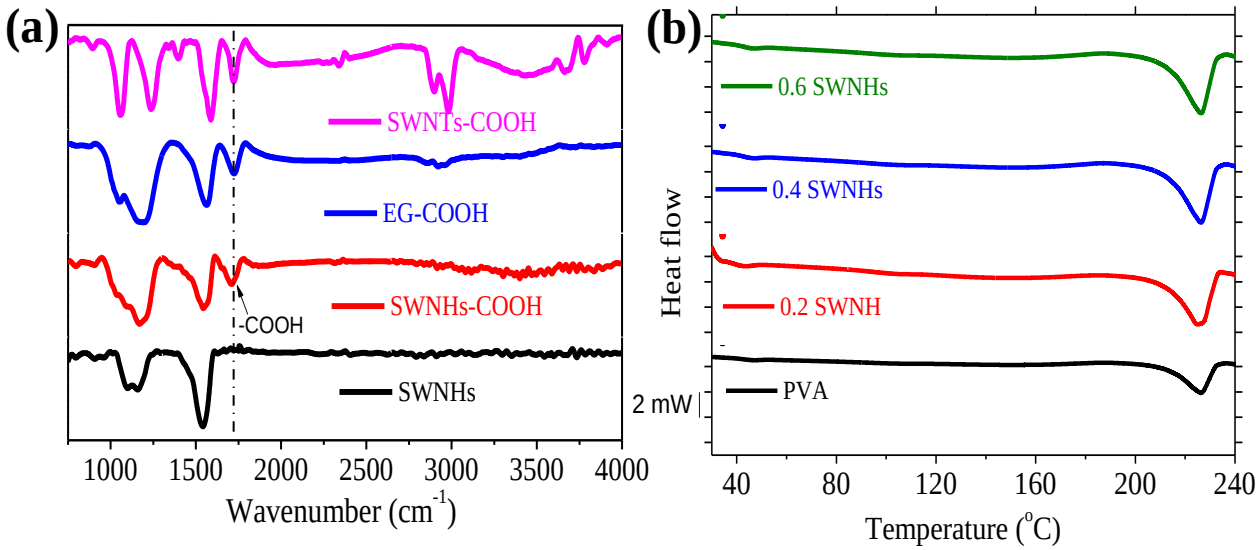

Figure 3. (a) The infrared spectra of pristine SWNHs and acid-functionalized SWNHs, SWNTs and EG. Peak at 1720 $cm^{-1}$for the functionalized nanocarbons confirm the presence of carboxyl groups. (d) DSC scans of PVA-SWNH composites showing endothermic peaks in the temperature range of 230–240 °C.

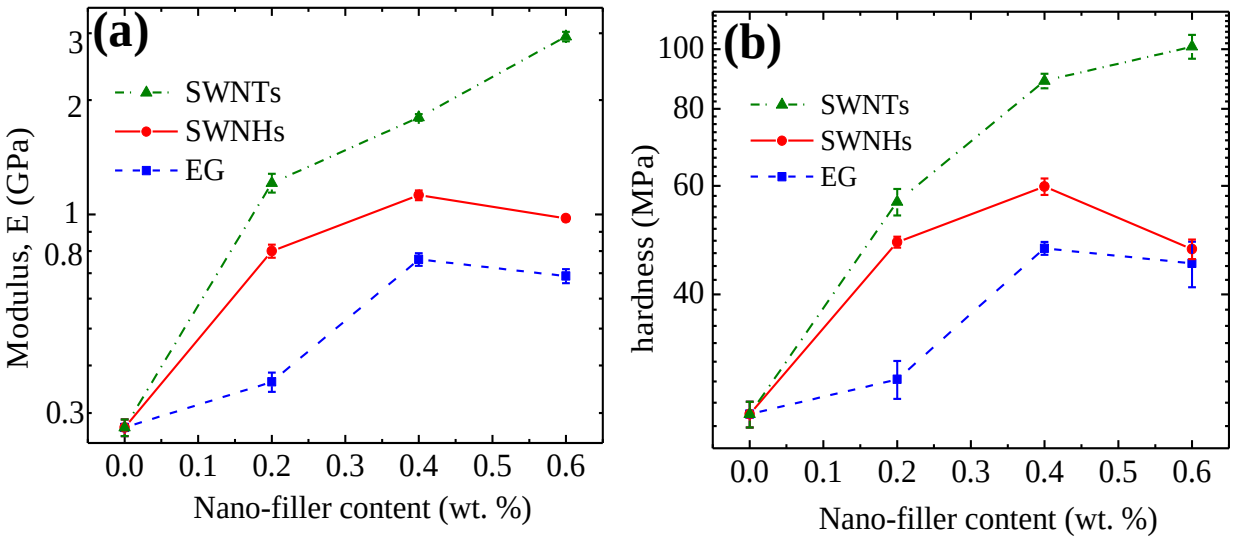

Figure 4. (a) Elastic modulus, E, of PVA and its nanocomposites for different nanocarbons and weight fractions, obtained from nanoindentation unloading response. (b) Variation of instantaneous hardness, H, for the same, calculated as the maximum applied load divided by the contact area at the end of loading. Note that y-axis for both (a) and (b) are in log scale.

2.3: Mechanical properties of PVA-SWNHs composites

The mechanical properties, elastic modulus, E, and hardness, H, of PVA and its composites with SWNHs, SWNTs and EG are presented in Table 1 and are plotted as functions of the filler concentration in Figure 4. From these, an enhancement in E and H is seen upon addition of SWNHs to PVA, with a maximum occurring at 0.4 wt.%; this amounts to an increase of ~315% and ~135% in E and H respectively over that of the unreinforced polymer. A decrease in E and H is seen with further increase in the concentration of SWNHs.

Table 1. Summary of mechanical properties and degree of crystallinity of single nanocarbon PVA composite

Nanofiller (wt.%)	Elastic modulus, E (GPa)	Hardness, H (MPa)	Viscosity parameters from Maxwell-Voigt fit		Degree of crystallinity, χ (%)
			η_1 (GPa s)	η_2 (GPa s)	
0	0.27 ± 0.01	25.6 ± 1.23	241	4.5	38.1
0.2 EG	0.36 ± 0.02	29.1 ± 2.07	278	4.6	41.8
0.4 EG	0.76 ± 0.03	47.5 ± 1.14	172	7.4	41.9
0.6 EG	0.69 ± 0.03	44.9 ± 3.80	301	5.3	42.4
0.2 SWNH	0.80 ± 0.03	48.6 ± 0.99	165	6.7	42.0
0.4 SWNH	1.12 ± 0.03	59.8 ± 1.84	160	9.0	44.4
0.6 SWNH	0.98 ± 0.02	47.3 ± 1.72	171	6.1	44.8
0.2 SWNT	1.21 ± 0.07	56.5 ± 2.80	586	12.3	46.3
0.4 SWNT	1.80 ± 0.04	88.8 ± 2.40	356	28.6	46.3
0.6 SWNT	2.94 ± 0.08	101.0 ± 4.50	760	48.9	48.0

In comparison, upon addition of SWNTs, a maximum increment of ~990% in E and ~295% in H is observed at 0.6 wt.%, while with addition of EG, a maximum improvement of ~180% in E and ~85% in H is seen at 0.4 wt.%. The observed increment in E for the case of SWNT is consistent with that (~1080%) reported by Eswar *et al*.[22] As a general observation, for a certain filler composition, SWNHs provide better strengthening compared to EG, and lower compared to SWNTs. However, note that E and H for 0.4SWNH-PVA and 0.2SWNT-PVA are similar.

Since 0.4 wt.% addition is most effective with SWNHs, this composition was considered as the base for examining its synergistic effect with EG. The results for these binary nanofiller composites are presented in Figure 5 and Table 2. Upon an addition of just 0.2 wt.% of EG to 0.4 wt.% SWNH, a jump in E and H values, corresponding to an increment of more than 4 and 2.5 times respectively, is observed. With further additions, a slight decrease is noticed.

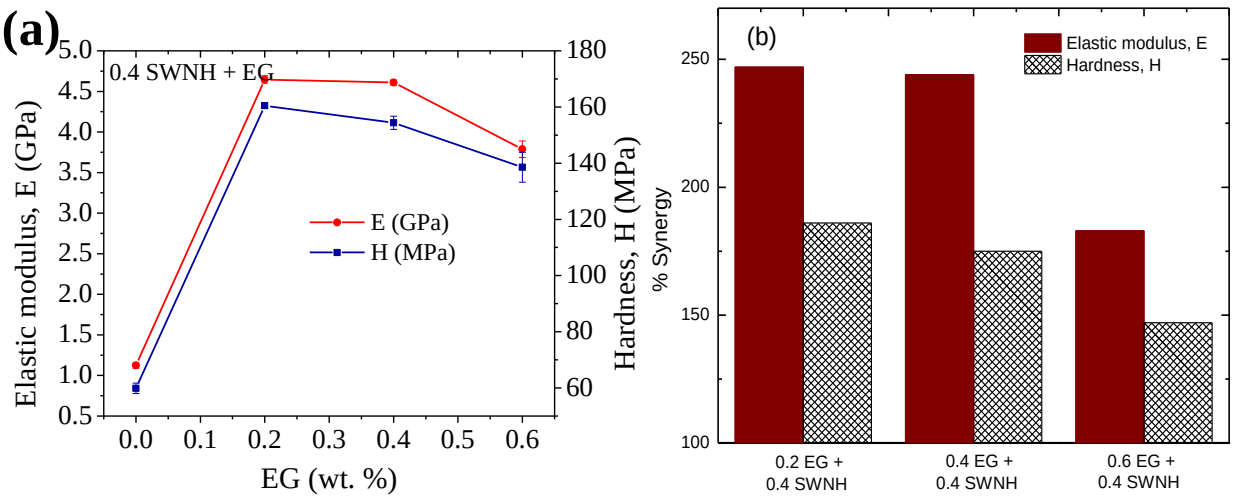

Figure 5. (a) Variation of elastic modulus, E, and hardness, H, for binary nanocomposites, with 0.2, 0.4 and 0.6 wt.% EG in PVA added in combination with 0.4 wt.% SWNH. (b) % Synergy in elastic modulus, E, and hardness, H, upon binary addition of SWNH and EG, estimated (Equation 1) with respect to the total mechanical property improvement upon individual nanocarbon additions. Average values of E and H were used for this calculation.

Table 2. Summary of mechanical properties and degree of crystallinity of binary nanocarbon PVA composite

EG (wt.%) + 0.4 NH	Elastic modulus, E (GPa)	Hardness, H (MPa)	% Synergy		Viscosity parameters from Maxwell-Voigt fit		Degree of crystallinity, χ (%)
			Elastic modulus	Hardness	η_1 (GPa s)	η_2 (GPa s)	
0	1.12 ± 0.03	59.8 ± 1.84	0	0	160	9.0	44.4
0.2	4.65 ± 0.04	160.5 ± 0.89	395	326	4555	152	45.3
0.4	4.61 ± 0.03	154.4 ± 2.32	244	175	1990	149	45.2
0.6	3.79 ± 0.10	138.6 ± 5.30	198	159	906	97	45.7

However, the properties remain significantly higher than those of SWNH-PVA composites. The synergistic effect resulting thus is evaluated using the following expression and are presented in Figure 5b.

$$\%\, Synergy = \frac{P_{SWNH\ +EG} - (\Delta P_{SWNH\ } + \Delta P_{EG})}{\Delta P_{SWNH\ } + \Delta P_{EG}} \times 100 \qquad (1)$$

Here, $P_{SWN\ H+EG}$ is the average mechanical property, E or H, of the binary composite and ΔP is the change in average mechanical property upon the addition of a single nanofiller, either SWNH or EG, to PVA. The results show a maximum synergy of ~400% in E and ~330% in H.

The degree of crystallinity, χ, for PVA and its composites, was calculated from DSC scans as the ratio of the heat required to melt 1 g of dry sample (area of the peak between 230–240 °C) to that of the standard enthalpy of pure crystalline PVA (ΔH ≈ 138.6 J/g). The values obtained for single and binary nanocarbon composites are tabulated in Table 1 and Table 2, respectively. The effectiveness of single nanocarbons in increasing χ is seen to take the order:

SWNT > SWNH > EG. The correspondence between the enhancement in E and the increase in χ, are shown in Figure 6. A parabolic relation is seen to hold for the single nanocarbon composite, while the binary nanocarbon composite deviates from this trend. While the increase in χ for 0.4SWNH-0.2EG-PVA is just ~2% over that of 0.4SWNH-PVA, the increment of E and H for the same is ~315% and ~170% respectively.

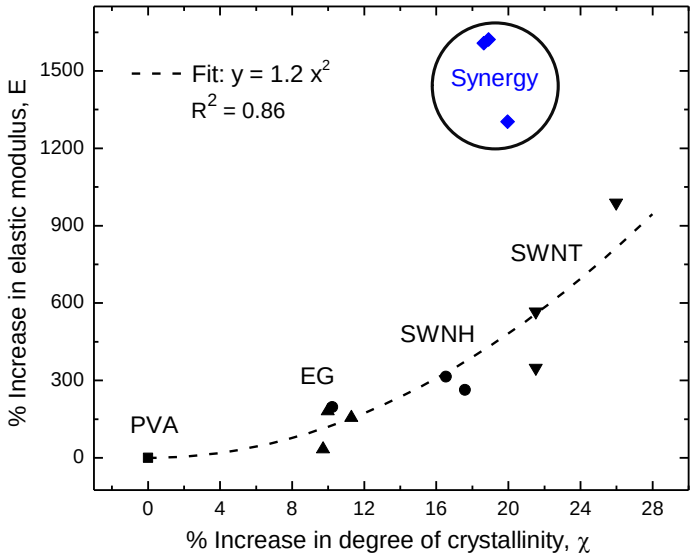

Figure 6. Shows the increase in elastic modulus, E, with respect to increase in the degree of crystallinity, χ, for single and binary PVA composite. EG-, SWNH- and SWNT-PVA composites show dependence between the change in χ and change in E. The binary composite is seen to deviate from this trend.

Next, to evaluate the effect of nanocarbon type and content on the polymer's viscous properties, a representative hold-time curve obtained from nanoindentation on PVA and its composites were empirically fit to a four-element Maxwell-Voigt model. The model, modified for the case of a conical indenter with semi-cone angle, α, is given by Fischer-Cripps[33] as:

$$h^2 = \frac{\pi}{2} P_0 \cot\alpha \left[\frac{1}{E_1} + \frac{1}{E_2}\left(1 - e^{-tE_2/\eta_2}\right) + \frac{1}{\eta_1} t\right]. \qquad (2)$$

Here, E_1 and E_2 are the spring constants representing the instantaneous and relaxation modulus respectively, and η_1 and η_2 are the viscosity terms representing the time-dependent

behavior. Since E has been obtained accurately from the Oliver-Pharr method, E_1 and E_2 obtained from the fit are of little importance and hence not considered for discussion in this study. α was found to be 35° from the area function calibration on PC. The empirical fit to a few of the hold-time curves are shown in Figure 7a.

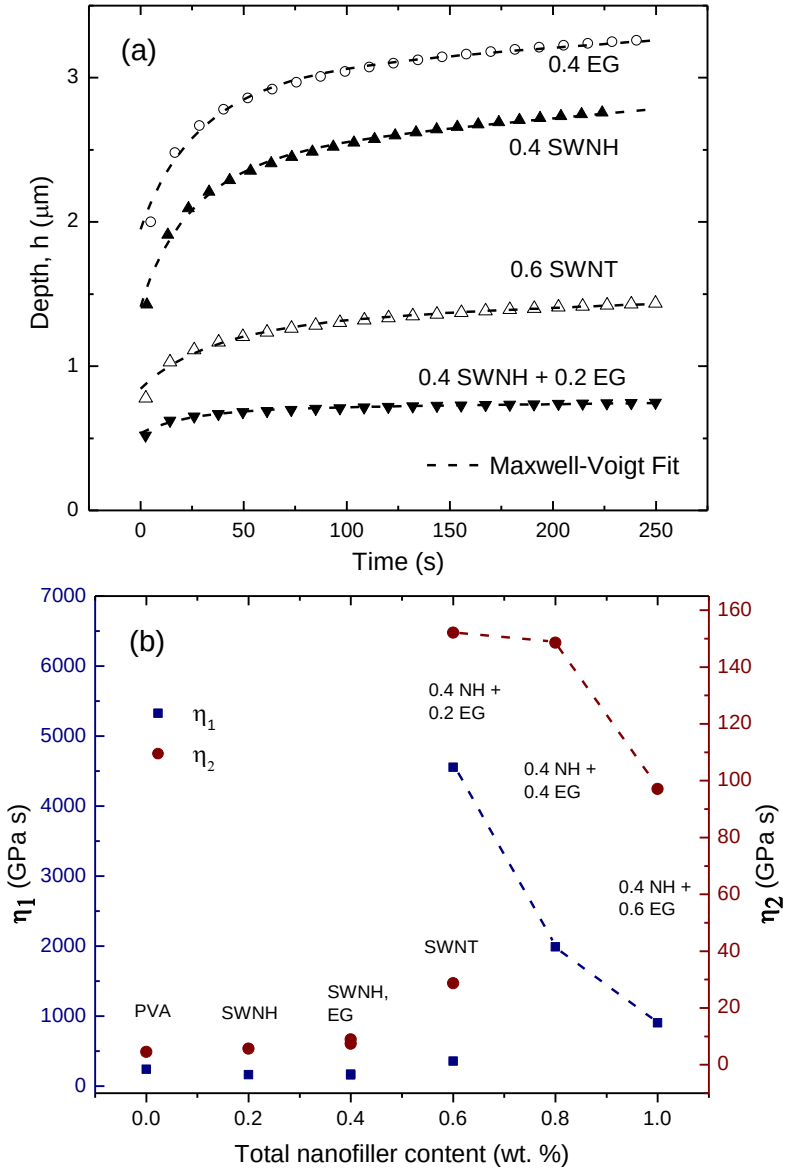

Figure 7. (a) Hold-time responses of some of the PVA nanocomposites are shown. The experimental creep curves are empirically fit to a four-element Maxwell-Voigt model (Goodness of fit, $R^2 > 0.85$ for all). (b) The viscosity terms, η_1 and η_2, obtained from the fit in (a) are plotted against their filler composition. Note the high resistance to creep or hold-time deformation of the SWNH-EG-PVA composites.

It has to be noted that the fit does not fully reflect the experimental conditions as the model assumes a step load to P_{max} and moreover does not account for any plastic displacement. Variations of η_1 and η_2, presented in Figure 7b, show minor changes upon EG and SWNH addition to PVA, while, a noticeable increase is observed for the case of SWNT. Prior studies, investigating the effect of nanocarbons on the time-dependent deformation of polymers, have shown either a substantial or a minor reduction in creep response upon addition of graphene,[37, 38] and a significant reduction upon addition of SWNTs,[39] both of which agree well with the present results. For the binary filler addition, EG plus SWNH, a substantial increment is seen, signifying a very high resistance to creep.

2.3.5: Discussion

The substantial improvement in mechanical properties obtained through nanocarbon additions to polymer matrix is due to the fact that the functionalized nanocarbons containing $–CO_2H$ and –OH groups (Figure 3a) act to bridge the weak van der Waals interaction between the polymer chains by forming stronger hydrogen bonds. In addition, the nanocarbons nucleate crystalline phases in the polymer as indicated by χ obtained from the DSC curves. In this context, the following factors hold the key in strengthening the polymer: the availability of a large surface area for interaction and the uniformity of nanocarbon dispersion.

For SWNH addition, experimental results (Figure 6) indicate that the enhancement in E and H are due, in part, to the formation of crystalline phases in PVA. Among the nanocarbons studied here, SWNTs are seen to induce the largest change in χ. This is attributed to its one-dimensionality and small size which allows good interaction of the polymer chains and the nanotubes, inducing nucleation of crystalline phases in the polymer.[19, 22] For SWNHs, however, the fact that they occur as three-dimensional aggregates (as seen in Figures 2a and b) with aggregate diameters of 50−100 nm,[29] and not as individual, one-dimensional SWNHs, results in a relatively low interaction area in comparison to SWNTs. Note here that individual SWNHs belong to the family of SWNTs and have tube length and diameter of 10−70 nm and 2−10 nm respectively.[40] While the measured BET surface areas are ~340 m^2/g for SWNTs and ~320 m^2/g for SWNHs, the

surface area available for interaction with polymer chains, will differ significantly from the measured values, which include the pore area present in the nanocarbons. For SWNTs, the dispersion from bundles during chemical functionalization and the use of water soluble PVA for composite preparation enhances the interaction area. On the other hand, SWNH aggregates are not dispersed into individual nanohorns. Chemical functionalization and the use of water soluble polymer only aids to separate one SWNH aggregate from another. Still, the reasonable change in χ (18%) induced by SWNH aggregates is probably due to the benefit of the interaction area provided by its spherical geometry, and also due to the outward protrusions of SWNH's conical ends (see 'dahlia-shaped' aggregate in the inset in Figure 2b), which act in a one-dimensional manner akin to SWNTs. The reason for EG effecting a small change in χ is due to the limited locations at the edges of graphene sheet where functional groups can be induced [41] and also the multi-layered nature (3–4 layers), which reduce the availability of the effective interfacial area.[42] Altogether, the effect of dimensionality on χ and on the mechanical properties is seen to increase as: EG (2D), SWNHs (1 and 3D), and SWNTs (1D).

The experimental results presented in this work show that combined addition of SWNHs and EG results in synergistic improvements (Figure 5b) in E and H of the composites. It appears that the synergy, which is quite substantial, is mediated by a mechanism other than crystalline-phase nucleation (Figure 6). Also, the binary addition is observed to significantly suppress the hold-time creep (Figure 7a). Quantitatively, this is reflected by the large increment in the viscosity parameters, η_1 and η_2, which signifies a transition from the fluid-like response of PVA (η_1 = 241 GPa s, η_2 = 4.5 GPa s) and the single nanofiller composites to a more solid-like response of the binary composite (η_1 = 4555 GPa s, η_2 = 152 GPa s). With no significant increase in χ, the enhanced resistance to viscoelastic creep is likely due to the hindered mobility of the molecular chains during deformation, which is possibly a result of strong interaction of the fillers with the amorphous regions in the polymer. Interestingly, in a previous study,[22] the synergistic benefit obtained with the binary combinations of SWNT, EG and ND were found to be independent of the crystallinity of the polymer and was attributed to an improved interaction between the nanocarbons and the polymer chains. With regards to practical applicability, the observation of an increase in the resistance to time-dependent deformation of PVA with SWNH and EG

addition (Figure 7) provides possibility for design of polymer composites for applications where dimensional stability is of importance.

The reduction or constancy in the mechanical properties (except for SWNT-PVA) of the composites at high filler concentration (Figure 4) is due to the problem of agglomeration. Among SWNHs, there is likely to be local clustering of SWNH aggregates. This is confirmed by the increase in scatter in H values and P-h responses, which is inferred to the increased inhomogeneity within the composite film. Also, the concurrent decrease in η_1 and η_2 reflects the higher mobility of polymer chains, which signifies weakening of filler-matrix interaction as a consequence of agglomeration. Such agglomeration could not be detected by optical microscopy or through Raman spectra. The latter, collected at different locations of the composite, showed peaks corresponding to both PVA and nanocarbon, signifying a generally good distribution of the nanocarbon. The local concentration of the nanocarbon however could not be assessed due to the high intensity of the obtained nanocarbon signal. With PVA being of limited use in engineering and structural applications, of concern is whether the results obtained in this study using PVA as the matrix material could translate to a similar performance in other polymers of practical importance. As the mechanical property enhancement here is believed to be governed by the amount of crystalline phase and the nucleation of the same upon SWNH addition, this strengthening mechanism would seem applicable to other polymers that are semi-crystalline in nature. In an earlier study, Cadek *et al*.[43] reasoned the greater increment in the mechanical properties of PVA—over an amorphous polymer—to the additional crystalline component formed upon carbon nanotube addition to the semi-crystalline PVA matrix. Thus the strengthening behavior of nanocarbon reinforced polymers is likely to depend on the amorphous/crystalline nature of the polymer, the nature of SWNHs' functionalization, and the ease of SWNH dispersion within the polymer, with the latter two factors influencing the interaction potential.

While excellent improvements in E and H are observed upon SWNH addition and SWNH plus EG binary addition, SWNHs occur in the form of spherically aggregated entities. As with SWNTs, in which well dispersed individual nanotubes provide a larger surface area for interaction as compared to the cylindrically bundled nanotubes, individual SWNHs separated from spherical aggregates can be expected to substantially improve the surface area available for interaction due to its one-dimensionality. The study by Zhang *et*

al.[40] which describes a process for such a separation of SWNH aggregates into individual entities, offers interesting possibility for further study of SWNH reinforced polymer matrix composites.

2.3.6: Conclusions

The potential offered by SWNHs to strengthen a semi-crystalline polymer (PVA) has been explored. Upon SWNH addition, substantial improvements in the elastic modulus and hardness are observed, the cause of which is the increase in the degree of crystallinity of the polymer. The properties obtained with SWNHs are better than those offered by the graphene (EG), and at a certain composition comparable to those obtained with SWNTs. The combined addition of SWNH and EG to PVA, results in extraordinary synergy in the mechanical properties and a high resistance to viscoelastic creep. Both of these are attributed (at low filler concentration) to a high degree of interaction between the filler and the matrix, but are found to be independent of the degree of crystallinity. The results of this study, in view of the commercial difficulty in producing SWNT composites, offer a new scope as SWNH composites can be produced economically. Further studies to determine properties such as ductility and toughness and to understand the mechanism of synergistic improvements in mechanical properties would be beneficial.

2.3.7: References

1. L. H. Baekeland, *Sci. Am.* **1909**, *68*, 322.

2. C. Goodyear, *Dinglers Polytechnisches J.* **1856**, *139*, 376 .

3. A. Usuki, M. Kojima, A. Okada, Y. Fukushima, O. Kamigaito, *J. Mater. Res.* **1993**, *8*, 1179.

4. Y. Kojma et al. *J. Mater. Res.* **1993**, *8*, 1185.

5. M. Cadek, J. N. Coleman, V. Barron, K. Hedicke, W. J. Blau, *Appl. Phys. Lett.* **2002**, *81*, 1523.

6. S.R.C. Vivekchand, U. Ramamurty, C.N.R. Rao, *Nanotechnol.* **2006**, *17*, 344.

7. B. Das, K.E. Prasad, U. Ramamurty, C.N.R. Rao, *Nanotechnol.* **2009**, *20*, 125705.

8. T. Ramanathan, A. A. Abdala, S. Stankovich, D. A. Dikin, M. Herrera-Alonso, R. D. Piner, D. H. Adamson, H. C. Schniepp, X. Chen, R. S. Ruoff, S. T. Nguyen, I. A. Aksay, R. K. Prud'Homme, L. C. Brinson, *Nature Nanotechnol.* **2008**, *3*, 327.

9. K.P. Ryan, M. Cadek, V. Nicolosi, S. Walker, M. Ruether, A. Fonseca, J.B. Nagy, W.J. Blau, J.N. Coleman, *Synthetic Metals* **2006**, *156*, 332.

10. T. Ramanathan, et al., *J. Polym. Sci. B* **2007,** *45*, 2097.

11. P. M. Ajayan, L. S. Schadler, C. Giannaris, A. Rubio, *Adv. Mater*. **2000**, *12*, 750.

12. B. Das, K. E. Prasad, U. Ramamurty, C. N. R. Rao, *Nanotechnology* **2009**, *20*, 125705.

13. D. Qian, E. C. Dickey, R. Andrews, T. Rantell, *Appl. Phys. Lett.* **2000**, *76*, 2868.

14. T. K. Gupta, B. P. Singh, R. K. Tripathi, S. R. Dhakate, V. N. Singh, O. S. Panwar, R. B. Mathur, *RSC Adv.* **2015**, *5*, 16921.

15. X. Wang, Y Hu, L. Song, H. Yang, W. Xing, H. Lu, *J. Mater. Chem.* **2011**, *21*, 4222.

16. S. Ansari, E. P. Giannelis, *J. Polym. Sci. Part B Polym. Phys.* **2009**, *47*, 888.

17. S. Lee, B. G. Choi, D. Choi, H. S. Park, *J. Memb. Sci.* **2014**, *451*, 40.

18. M. Li, Y. G. Jeong, *Compos. Part A Appl. Sci. Manuf.* **2011**, *42*, 560–566.

19. J. N. Coleman, U. Khan, W. J. Blau, Y. K. Gun'ko, *Carbon* **2006**, *44*, 1624.

20. T. Ramanathan, A. A. Abdala, S. Stankovich, D. A. Dikin, M. Herrera-Alonso, R. D. Piner, D. H. Adamson, H. C. Schniepp, X. Chen, R. S. Ruoff, S.T. Nguyen, I. A. Aksay, R. K. Prud'Homme, L.C. Brinson, *Nat. Nanotechnol.* **2008**, *3*, 327.

21. U. Maitra, K. E. Prasad, U. Ramamurty, C. N. R. Rao, *Solid State Commun.* **2009**, *149*, 1693.

22. K. E. Prasad, B. Das, U. Maitra, U. Ramamurty, C. N. R. Rao, *Proc. Natl. Acad. Sci. U. S. A.* **2009**, *106*, 13186.

23. M. S. Dresselhaus, G. Dresselhaus, P. Avouris, Eds.; Topics in Applied Physics; Springer Berlin Heidelberg: Berlin, Heidelberg, 2001; Vol. 80, pp. 391.

24. Y. Liu, S. Kumar, *ACS Appl. Mater. Interfaces* **2014**, *6*, 6069.

25. P. J. F. Harris, *Int. Mater. Rev.* **2004**, *49*, 31.

26. S. R. C. Vivekchand, R. Jayakanth, A. Govindaraj C. N. R. Rao, *Small* **2005**, *1*, 920.

27. T. Azami, D. Kasuya, R.Yuge, M. Yudasaka, S. Iijima, T. Yoshitake, Y. Kubo, *J. Phys. Chem. C* **2008**, *112*, 1330.

28. S. Iijima, M. Yudasaka, R. Yamada, S. Bandow, K. Suenaga, F. Kokai, K. Takahashi, *Chem. Phys. Lett.* **1999**, *309*, 165.

29. K. Pramoda, K. Moses, M. Ikram, K. Vasu, A. Govindaraj, C. N. R. Rao, *J. Cluster Sci.* **2014**, *25*, 173.

30. C. Cioffi, S. Campidelli, C. Sooambar, M. Marcaccio, G. Marcolongo, M. Meneghetti, D. Paolucci, F. Paolucci, C. Ehli, G. M. A. Rahman, V. Sgobba, D.M. Guldi, P. Prato, *J. Am. Chem. Soc.* **2007**, *129*, 3938.

31. S. William, J. Hummers, R. E. Offeman, *J. Am. Chem. Soc* **1958**, *80*, 1339.

32. U. Ramamurty, J. Jang, *Cryst. Eng. Commun.* **2014**, *16*, 12.

33. A. C. Fischer-Cripps, *Mater. Sci. Eng. A* **2004**, *385*, 74–82.

34. C. Klapperich, K. Komvopoulos, L. Pruitt, *J. Tribol.* **2001**, *123*, 624.

35. W. C. Oliver, G. M. Pharr, *J. Mater. Res.* **2011**, *7*, 1564.

36. B. J. Briscoe, L. Fiori, E. Pelillo, *J. Phys. D. Appl. Phys.* **1998**, *31*, 2395.

37. J. Chen, X. Guo, Q. Tang, C. Zhuang, J. Liu, S. Wu, B. D. Beake, *Carbon* **2013**, *55*, 144.

38. J. A. King, D. R. Klimek, I. Miskioglu, G. M. Odegard, *J. Appl. Polym. Sci.* **2013**, *128*, 4217.

39. M. Tehrani, M. Safdari, M. S. Al-Haik, Nanocomposite. *Int. J. Plast.* **2011**, *27*, 887.

40. M. Zhang, T. Yamaguchi, S. Iijima, M. Yudasaka, *J. Phys. Chem. C* **2009**, *113*, 11184.

41. H. K. F. Cheng, N. G. Sahoo, Y. P. Tan, Y. Pan, H. Bao, L. Li, S. H. Chan, J. Zhao, *ACS Appl. Mater. Interfaces* **2012**, *4*, 2387.

42. M. S. R. N. Kiran, K. Raidongia, U. Ramamurty, C. N. R. Rao, *Scr. Mater.* **2011**, *64*, 592.

43. M. Cadek, J. N. Coleman, V. Barron, K. Hedicke, W. J. Blau, *Appl. Phys. Lett.* **2002**, *81*, 5123.

Part 3

Covalently-linked Nanocomposites-based on graphene

3.1: Covalently Cross-Linked Graphene-SWNTs Composites

3.1: Nanocomposites Generated by Covalent Cross-Linking of Graphene and Single-Walled Carbon Nanotubes

Summary*

Composites of graphene and single-walled carbon nanotubes (SWNT) have been generated by covalent cross-linking through two different coupling strategies, namely Sonogashira and EDC (1-ethyl-3-(3-dimethylaminopropyl)carbodiimide) coupling reactions. The obtained assemblies have been characterized by various microscopic and spectroscopic techniques. The assemblies obtained by Sonogashira coupling exhibit high surface area, the value increasing with the graphene content. The highest surface area obtained is 1260 $m^2 g^{-1}$ in the composition with highest graphene content (graphene:SWNT 4:1). These composites show a uniform slit-shaped porous network with pores of approximately 1–2 nm. CO_2 uptake of this assemblies is in the range 11–15 wt % at 273 K (1 atm) and 9–11 wt % at 298 K (1 atm), whereas the H_2 uptake is in the 1–1.3 wt % range at 77 K (1 atm). The composites generated by Sonogashira coupling show superhydrophobicity with high contact angles in the range from 159–163°. The EDC-coupled composites show less surface area than the composites from Sonogashira coupling.

A paper based on this work has been published in *Chem. Asian J. (2015).*

3.1.3: Experimental section

Reagents and precursors: Chemicals used in synthesis were of high purity and obtained from commercial sources. Solvents were pre dried before synthesis. 4,4′-diethynylbiphenyl (DEBP) was synthesized using previously reported procedure.[18]

Synthesis of graphite oxide (GO): Graphite oxide was prepared using a modified Hummers method. In an ice bath 1 g graphite powder was mixed properly with 50 ml conc. H_2SO_4 and 1 g $NaNO_3$under constant stirring. In the uniform mixture 6.5 g $KMnO_4$ was added slowly. The reactants were transferred to an oil bath maintained at 40 °C, allowed for 30 min followed by slow addition of 50 ml water and temperature raised to 70 °C. After 15 min 10 ml H_2O_2 (30 %) in 100 ml warm water (~ 70 °C) was added to the reaction mixture. Obtained brown dispersion was centrifuged, washed with copious amount of water followed by dialysis and freeze dried.

Reduction of graphite Oxide (RGO): 500 mg graphite oxide was dispersed in 500 ml H_2O by sonication, pH raised to ~ 10 by adding aqueous Na_2CO_3 solution and stirred at 95 °C for 12 h. 5 g $NaBH_4$ dissolved in 50 ml water was added to the reaction mixture with pH maintained at ~ 10 and the resultant solution stirred for 4 h at 80 °C. Obtained product was filtered (0.45 μm, PTFE) washed with copious amount of water and dried in vacuum oven at 90 °C.

Iodobenzene functionalization (RGO-IBz): Thediazonium salt of 4-iodoaniline was prepared *in situ*. 4-Iodoaniline (9 mmol) was dissolved in 150 ml water by adding minimum amount of conc. HCl. In an ice bath $NaNO_2$ (15 mmol) and 8 ml 20% HCl (6.4 M) was added to the solution and allowed to stir for 45 min. Color of the solution changed from transparent to yellow due to the formation of diazonium salt. RGO (250 mg) dispersed in 250 ml 1 wt% sodium dodecylbenzenesulfonate (NaDDBS) surfactant was added to diazonium salt solution and allowed at 0 °C for 2 h, followed by stirring at room temperature for next 4 h. Obtained product was filtered and washed with copious amount of water to remove the surfactant properly and dried in vacuum at 60 °C.

Iodobenzene functionalization of SWNTs (SWNT-IBz): Purified CoMoCAT SWNTs (150 mg) was functionalized with 7.5 mmol 4- iodoaniline using the same procedure as for RGO.

Synthesis of Graphene@SWNTs assemblies using Sonogashira coupling: In a schlenk flask iodobenzene functionalized SWNTs and graphene (20 mg) was mixed in four different

ratios (SWNT:graphene = 2:1, 1:1, 1:2 and 1:4), purged with nitrogen and sealed with septum. *N*,*N*-Dimethylformamide (DMF) (4ml) and triethylamine (4 ml) was added and sonicated for 3 h. In the uniform dispersion $Pd(PPh_3)_4$ (10 mg) and CuI (5 mg) was added under constant stirring and temperature raised to 80 °C. In a separate vial 1,4-diethynylbenzene (65 mg) dissolved in 1.5 ml DMF was added dropwise to the reaction mixture, subsequently temperature raised to 140 °C and allowed for 24 h. Nitrogen atmosphere was maintained during the reaction. Precipitates were collected by filtration (0.45 μm, nylon) and washed properly with DMF and hexane. Further purification was carried out using Soxhlet extractor with methanol for 48 h. Yield: between 71 – 76%. The product is designated as.

Carboxylate functionalization of SWNTs: In a Teflon microwave reactor 50 mg SWNTs, 2 ml conc. HNO_3, 2 ml conc. H_2SO_4 and 16 ml H_2O was added, irradiated with microwave for 10 min (450 W) followed by heating at 100 °C for 12 h under hydrothermal condition. Obtained product was filtered (0.45 μm, PTFE), washed with copious amount of water and dried at 60 °C under vacuum.

Amine functionalized graphene: Graphite oxide (120 mg) was dispersed in 20 ml water by sonication. In the uniform dispersion 70 ml ammonia solution (30 %) was added followed by sonication and stirring to make a uniform dispersion. Uniform dispersion was transferred to Teflon lined autoclave and heated in 200 °C oven for 16 h. Obtained product was filtered (0.45 μm, PTFE), washed with water and dried at 60 °C under vacuum.

Synthesis of Graphene@SWNTs assemblies using EDC coupling: In a Schlenck flask carboxylated SWNTs (25 mg) and aminatedgraphene (25 mg) was mixed, purged with N_2, sealed using septum and 5 ml DMF was added. Uniform dispersion was obtained by sonication. In the uniform dispersion *N*-(3-Dimethylaminopropyl)-*N'*-ethylcarbodiimidehydrochloride (EDC.HCl) 20 mg, 1-Hydroxybenzotriazole (HOBt) 20 mg and *N*,*N*-Diisopropylethylamine (DIPEA) 300 μl was added under constant stirring and allowed for 48 h. Nitrogen atmosphere was maintained during the reaction. Obtained product was filtered using 0.45 μm PTFE membrane, washed with copious amount of DMF and water. The solid product was further washed with methanol in a Soxhlet extractor for 48 h and dried at 60 °C under vacuum.

Characterization and instrumentation: Solid state ^{13}C magic angle spinning (MAS) NMR spectra was collected on a Bruker 400 MHz spectrometer. Morphological studies were carried out using Nova Nano SEM 600, FEI Company. Transmission Electron Microscope (TEM) images were recorded using the FEI Tecnai with an accelerating voltage of 200 kV. Thermogravimetric analysis (TGA) was carried out using Mettler Toledo TGA 850 instrument in nitrogen atmosphere with a heating rate of 3 °C/ min. XPS spectra were recorded in an Omicron Nanotechnology Spectrometer with Mg Kα as the X-ray source.

Adsorption measurement: The adsorption isotherm N_2 (77 K), CO_2 (195 K, 273 K and 298 K) and H_2 (77 K) were obtained using QUANTACHROME QUADRASORB-*SI* analyzer. The samples were heated at 433 K under vacuum for about 12 h. The adsorbate was charged into the sample tube and change in pressure was monitored. The degree of adsorption was determined by monitoring the decrease in pressure at the equilibrium state. All the operations were computer controlled and automatic.

Contact angle measurement: The samples were dispersed in 1:1 Water: ethanol mixture and resultant ink was coated on the glass substrate. The obtained film was used for the contact angle measurement using a goniometer. A total volume of 4 µl deionized water was placed on the sample by micropipette, images were recorded using a digital camera attached to goniometer.

3.1.4: Results and discussion

Sonogashira coupling has been widely employed in synthetic organic chemistry.[19] Recently this strategy has been used to grow conjugated microporous polymers (CMPs) on the surface of different dimensional nanocarbons with interesting morphological and functional properties. The CMPs and nanocarbon composites (graphene, SWNT and carbon spheres) have promising optical and electrochemical properties.[20] Scheme 1 shows the steps involved in the synthesis of covalently cross-linked graphene@SWNT assemblies using Sonogashira coupling, designated as G-SWNT (1).[19a, 21] This strategy involves iodobenzene (IBz) functionalization of reduced graphene oxide (RGO-IBz) as well as SWNT (SWNT-IBz) using *in-situ* prepared diazonium salt of 4-iodoaniline. The RGO-IBz and SWNT-IBz was mixed in four different ratios (graphene:SWNT=1:2, 1:1, 2:1 and 4:1) and dispersed in *N*,*N*-dimethylformamide (DMF). The resultant dispersion was cross-linked with 4,4′-

diethynylbiphenyl (DEBP) linker in the presence of Pd^0 and Cu^1 catalysts (see experimental section).

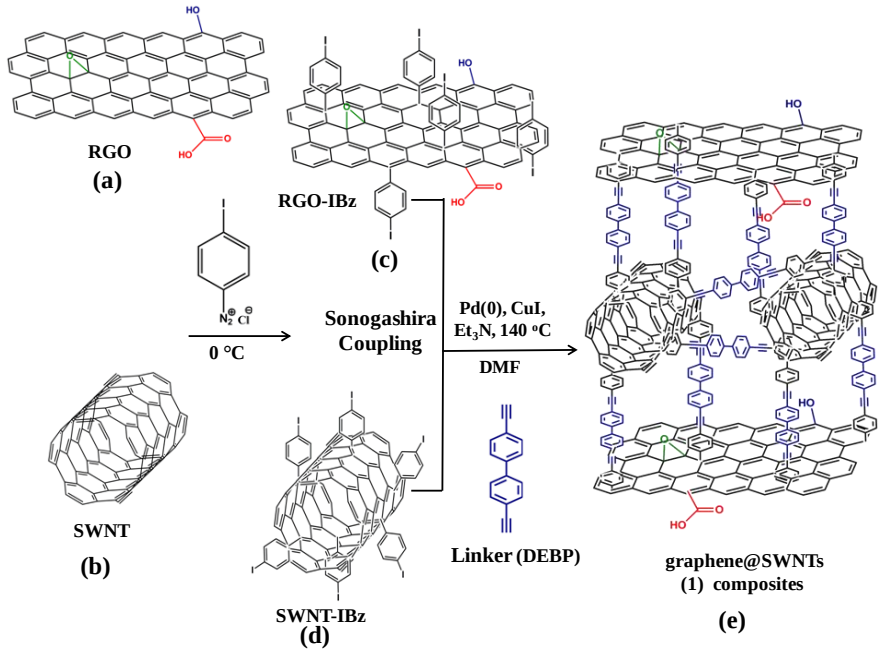

Scheme 1. Schematic representation of the synthesis of graphene@SWNTs (1), using Sonogashira coupling. (a, b) Reaction of reduced graphene oxide (RGO) and SWNT with 4-iodobenzenediazonium chloride. (c, d) Iodobenzene-functionalized RGO and SWNT (RGO-IBz, SWNT-IBz). (e) Graphene@SWNT (1) assemblies

The mechanism involves the oxidative addition of Pd^0 to the C−I bond of iodobenzene to form Pd^{II} intermediate, followed by elimination of iodine (I) during transmetallation with copper acetylide. The Subsequent step involves reductive elimination of iodine followed by C−C bond formation.[22] Pd^0 catalyzed coupling strategies may have promising uses in nanocarbon chemistry for the design of functional materials.[23]

Scheme 2 shows the synthesis of graphene@SWNT assemblies by the EDC coupling reaction through amide bond formation.[24] The synthesis of these composites designated as G-SWNT (2), involves the amine and carboxyl functionalization of graphene and SWNT respectively, followed by the activation of carboxylate groups using EDC. The subsequent step involves the cross-coupling of amine groups on graphene with activated carboxylate groups on SWNT. The advantage of EDC based activation over $SOCl_2$ is that, no HCl is liberated; obtained urea by-product is water soluble. And this reaction is carried out at room

temperature (see experimental section). Graphene and SWNT assemblies obtained by Sonogashira and EDC coupling are named as G-SWNT (1) and G-SWNT (2) respectively.

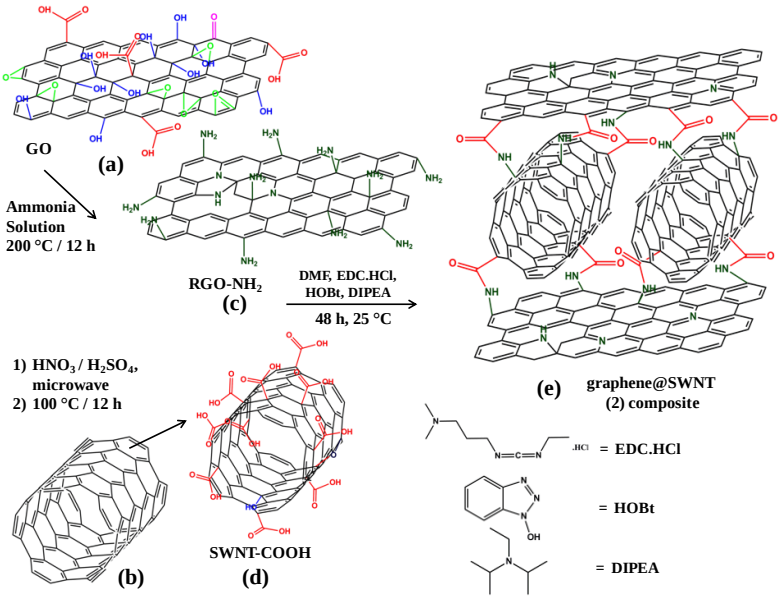

Scheme 2. Schematic representation of the synthesis of graphene@SWNT (2) using EDC coupling. a) Hydrothermal amination of graphene oxide (GO). b) Carboxylate functionalization of SWNT. c) Aminated graphene (RGO-NH_2). d) Carboxylated SWNT (SWNT-COOH). e) graphene@SWNT (2) assembly.

Figure 1a displays the infrared (IR) spectra of G-SWNT (1) assemblies prepared by Sonogashira coupling. The IR bands at 1500 and 1604 cm^{-1} are due to C=C stretching modes of benzene, whereas the bands at 3030 and 3064 cm^{-1} corresponds to the aromatic C−H stretching. The 2200 cm^{-1} band results from C≡C stretching of the linker, indicates the cross-linking of graphene and SWNT.[25] Figure 1b displays the Raman spectra of G-SWNTs (1), SWNT and RGO, collected using 632.84 nm He-Ne lasers. The D-band is observed at 1300 cm^{-1} for SWNT and 1330 cm^{-1} in graphene. The G-band for both SWNT and graphene occurs at around 1590 cm^{-1}. The radial breathing modes (RBM) in SWNT are in the 100-400 cm^{-1} region.[3a] Raman spectra of G-SWNTs (1) show combined characteristics of SWNT and graphene. The D-band region of assemblies shows shoulder at 1330 cm^{-1} due to contribution from graphene, whereas the G-band region merges with that of SWNT. The G-band broadens with the increase in graphene content.

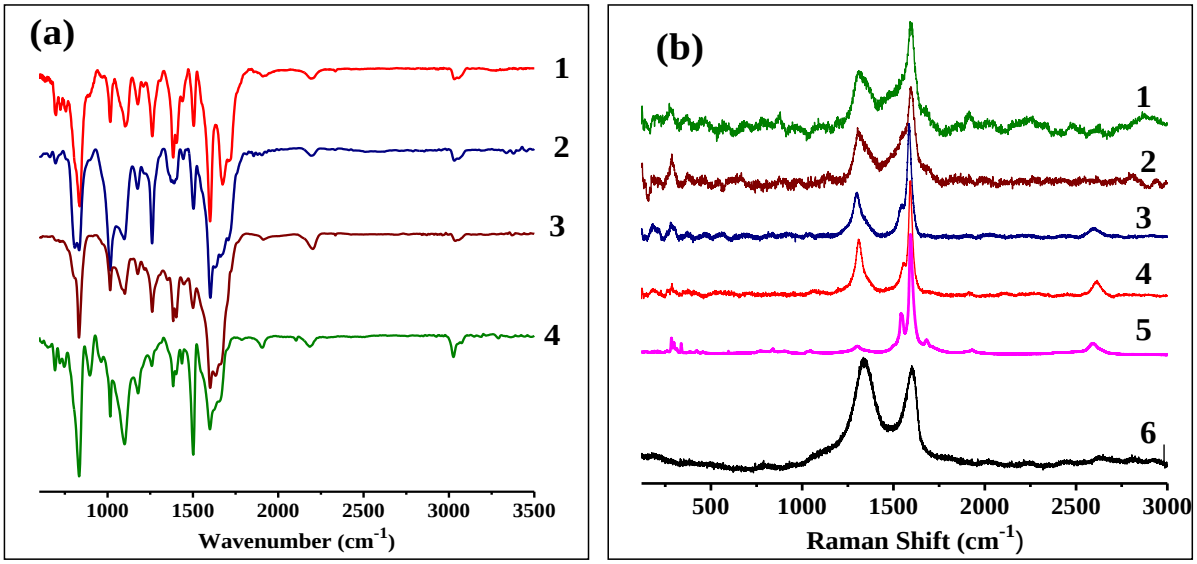

Figure 1. (a) ATR-FTIR spectra of graphene@SWNTs (1) [graphene:SWNT 1 (1:2), 2 (1:1), 3 (2:1), and 4 (4:1)]; (b) Raman spectra of [graphene:SWNT 1 (4:1), 2 (2:1), 3 (1:1), 4 (1:2), 5 (SWNT), and 6 (RGO)].

Sonogashira cross-linking (Scheme 1) involves the formation of C−C bond and breaking of C−I bond.[22] Monitoring the intensity of I 3d (iodine) signal in X-ray photoelectron spectroscopy (XPS) is an effective method to follow the extent of cross-linking. Figures 2a, b and c display the I 3d signals of RGO-IBz, SWNT-IBz and G-SWNTs (1). RGO-IBz and SWNT-IBz show strong I 3d signal due to iodobenzene functional groups. The G-SWNTs (1), composite does not exhibit a significant signal of I 3d, confirming that cross coupling of SWNT and graphene has occurred through C−C bond formation.

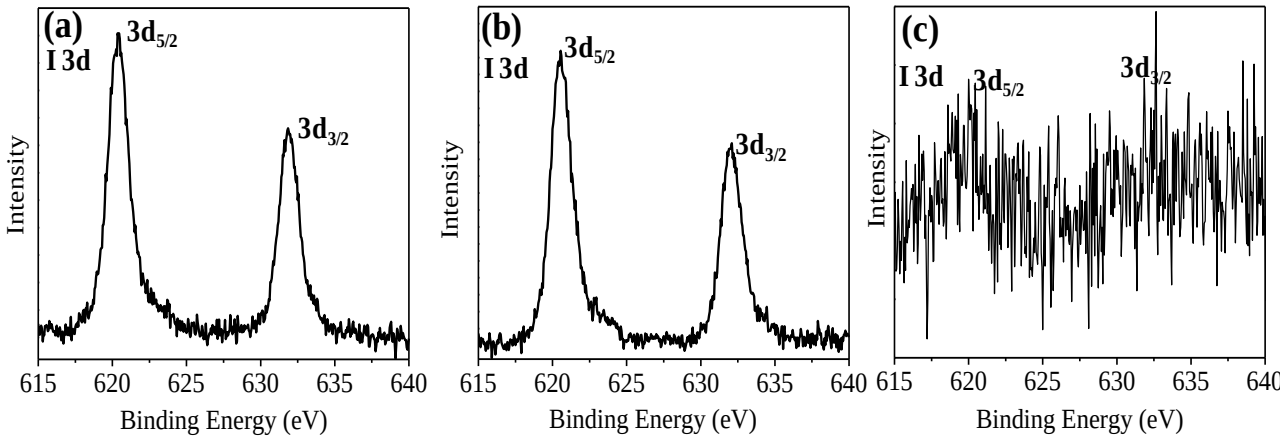

Figure 2. High resolution I 3d X-ray photoelectron spectrum (XPS) of (a, b) Iodobenzene functionalized RGO, SWNTs and (c) graphene@SWNT (1) (present spectrum for Graphene:SWNT: 1:1)

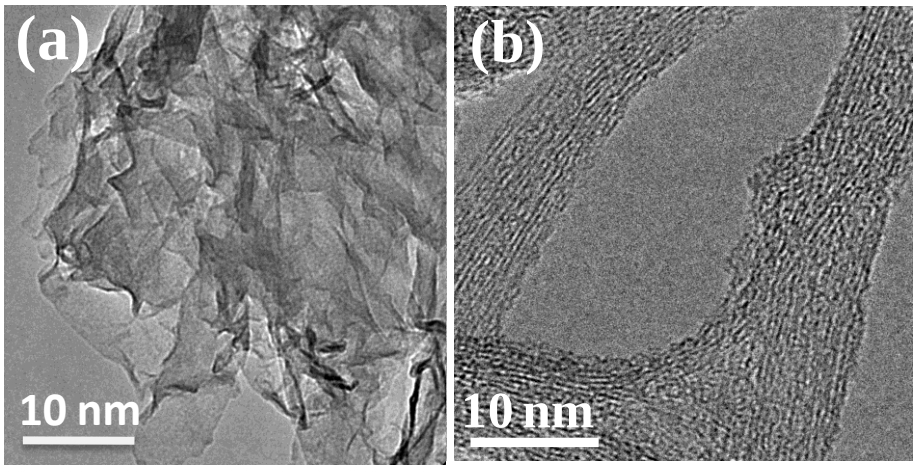

Figure 3. TEM image of a) Reduced graphene oxide (RGO); b) SWNT

We would expect interesting morphological features on cross-linking 1D SWNT with 2D graphene through organic linkers, resulting in the formation of 3D-monoliths.

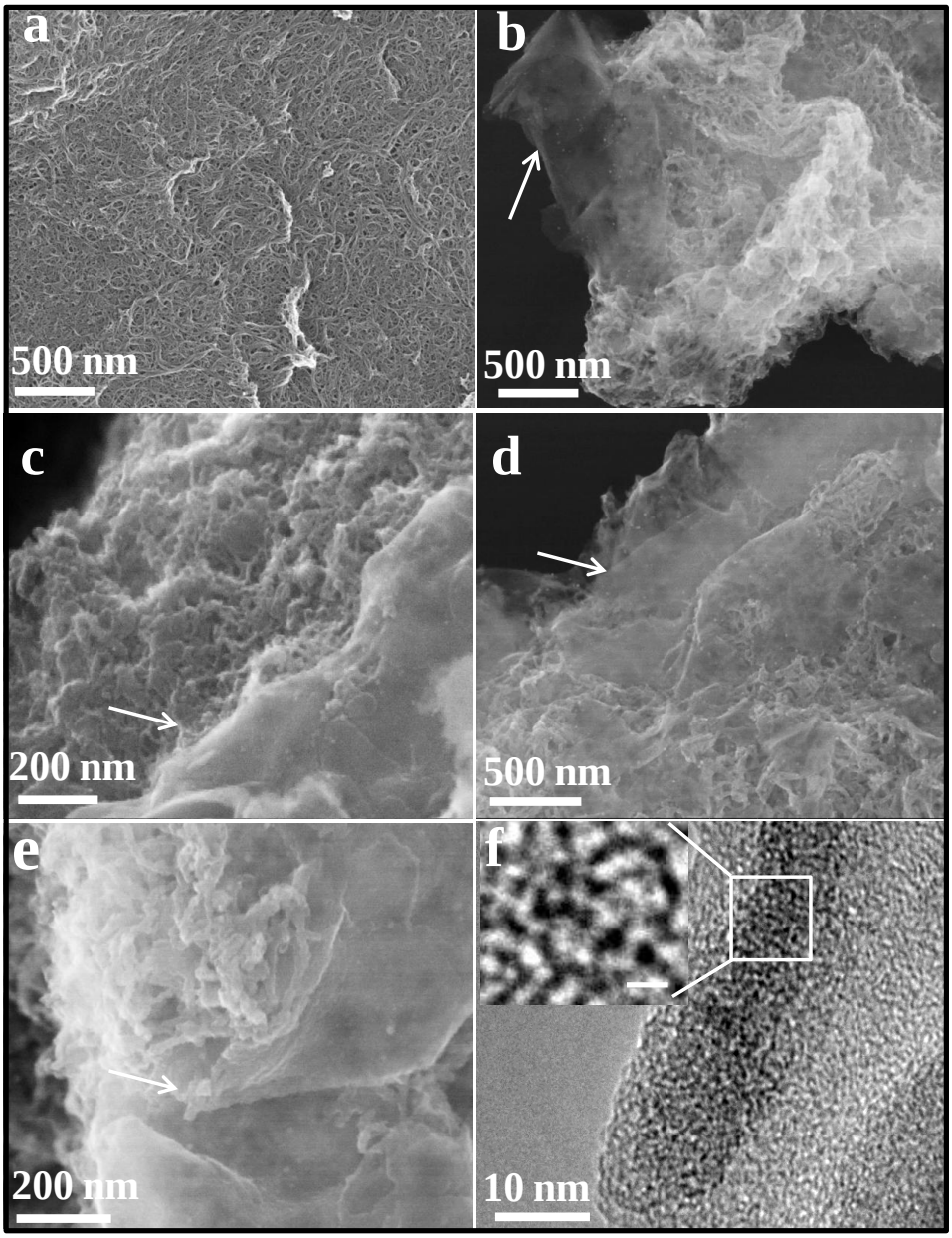

Figure 4. a) SEM image of SWNT. b–e) SEM images of graphene@SWNTs (1) with increasing graphene content [arrows indicate the cross-linked graphene sheet; graphene:SWNT b (1:2), c (1:1), d (2:1), e (4:1)]. f) HRTEM image of graphene@SWNT (1); inset shows 1–2 nm slit pores arising from covalent cross-linking (inset scale bar 2 nm).

Figures 3a, b display the transmission electron microscope images (TEM) of graphene and SWNTs used for cross-linking. Agglomerated few-layer graphene sheets with lateral dimensions of 3–5 μm are observed in electron microscopy. SWNTs have ~10 nm thick, micron length bundles. Figure 4 shows the SEM image of G-SWNT (1) with varying graphene content. It is evident from FESEM images that the SWNT are sandwiched between the graphene sheets. And also we observed high content of cross-linked SWNT at the surface of G-SWNTs (1), in case of less graphene containing assemblies (Figures 4b, c). Figure 4f shows the high resolution transmission electron microscope (HRTEM) image of G-SWNTs (1). The inset in Figure 4f shows the formation of uniform slit shaped porous network with dimensions of 1–2 nm. The length of linker cross-linking SWNT and graphene is ~2 nm.

Prompted by the micro and nanoscale surface roughness observed in SEM imaging of G-SWNTs (1), we carried out surface wettability experiments using water contact angle measurements. Figure 5 shows the typical optical images of water droplets on G-SWNTs (1),

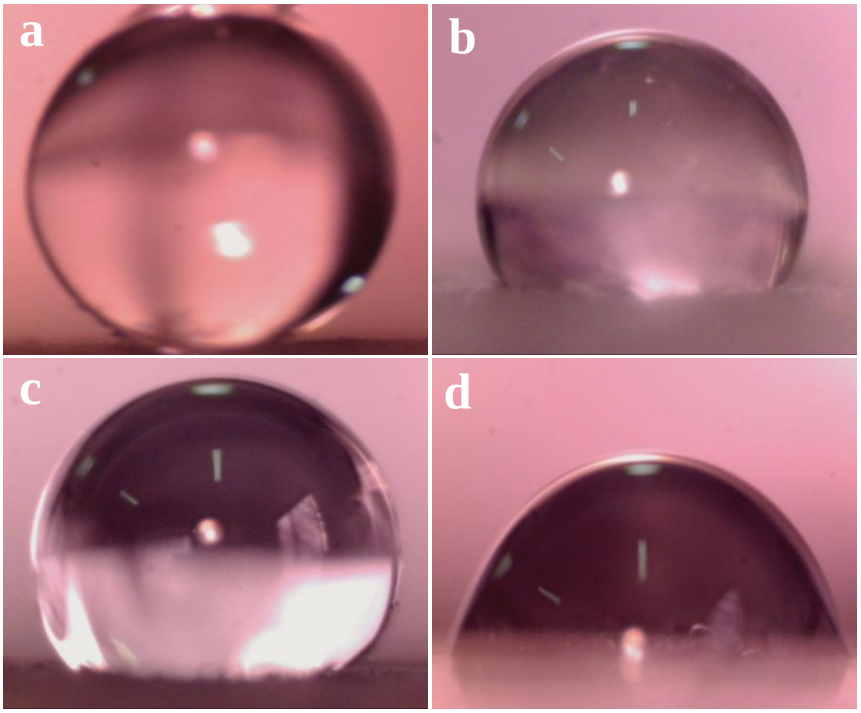

Figure 5. Optical images of a 4 μL water droplet on a) 1:1 graphene@SWNT (1); b) diethynylbiphenyl (DEBP) linker; c) RGO; and d) SWNT.

DEBP linker, RGO and SWNT respectively. The assemblies show contact angle in the range from 159 to 163°, whereas DEBP, reduced graphene oxide (RGO) and SWNT exhibit contact angles of 110°, 122° and 68° respectively. The superhydrophobic nature of assemblies is attributed to micro and nanoscale surface roughness. The surface contact area available to water droplet is reduced due to trapped air, as proposed by the Cassie model.[26] Additionally, the hydrophobic DEBP linker prevents penetration of water into the pore surface.

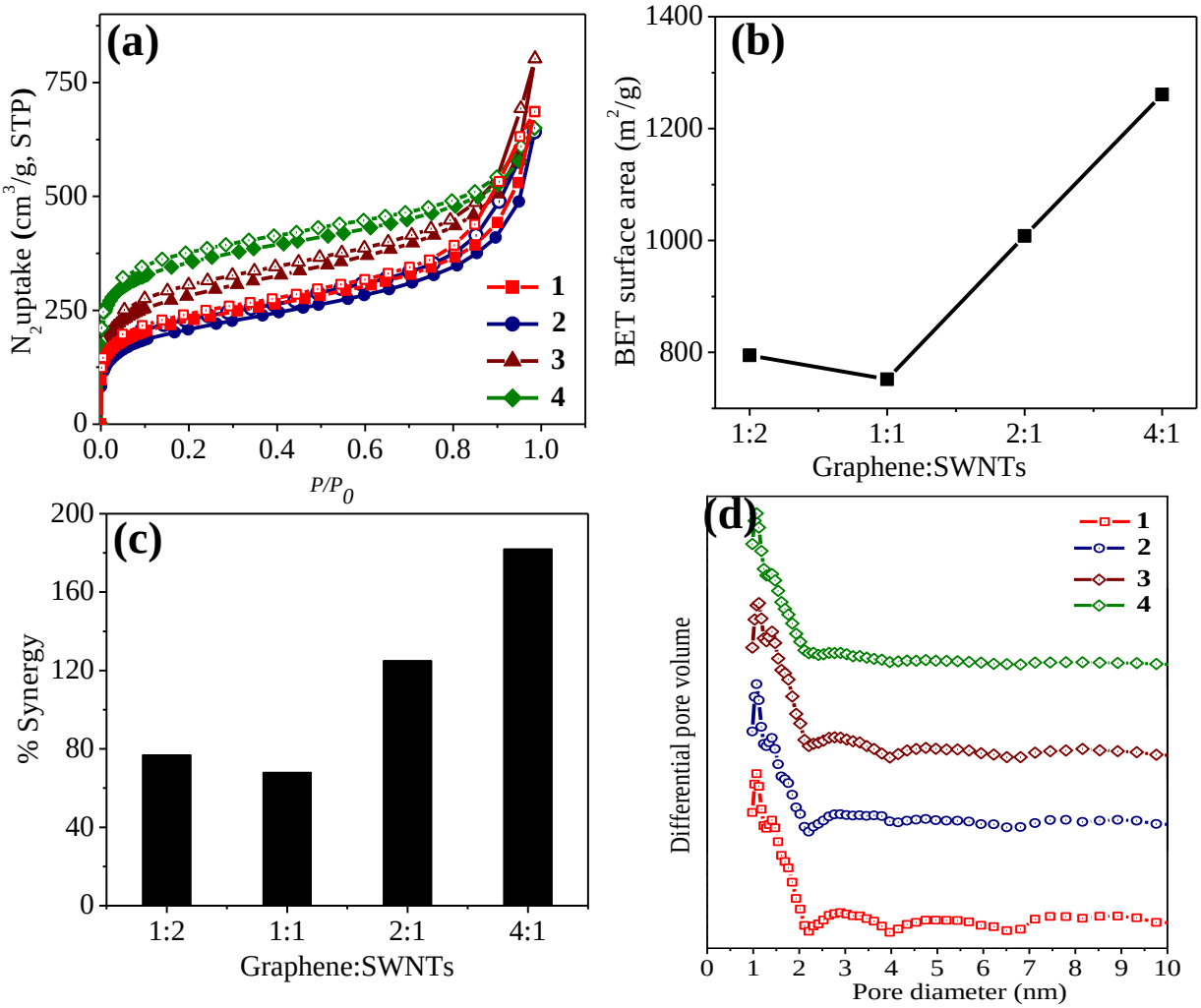

Figure 6. a) Nitrogen adsorption profiles at 77 K. b) Variation in surface area with increase in graphene content. c) Synergy (%) in surface area exhibited by assemblies in comparison to the pristine SWNT and graphene. d) Pore size distribution of graphene@SWNTs (1) [graphene:SWNT 1 (1:2), 2 (1:1), 3 (2:1), 4 (4:1).

3.1: Covalently Cross-Linked Graphene-SWNTs Composites

The presence of a uniform porous network, high thermal stability, along with superhydrophobic nature, prompted us to investigate the potential of G-SWNTs (1) for gas storage and separation. The porosity of G-SWNTs (1) was investigated by nitrogen adsorption at 77 K (Figure 6). The adsorption profile has combined features of type-I in low and type-II in high pressure regions according to the IUPAC classification (Figure 6a).[27] The type-I feature is due to adsorption in micropores (1–2 nm), whereas the type-II is from macropores, as evident from TEM and SEM images. The Brunauer-Emmet-Teller (BET) surface areas of different G-SWNTs (1), with varying graphene content are given in Table 1. The surface areas are in the range from ~750-1260 $m^2 g^{-1}$. The BET surface area of SWNT is 415 $m^2 g^{-1}$, whereas RGO prepared by sodium borohydride reduction of graphene oxide (GO) is nonporous with a low surface area of 32 $m^2 g^{-1}$. The enhanced surface area of G-SWNTs (1) assemblies is due to the pillaring of individual graphene sheets and SWNTs with DEBP. Figures 6b and c show the effect of graphene content on the surface area and % synergy in the G-SWNTs (1) assemblies. Figure 6d shows the pore size distribution of G-SWNTs (1) calculated using non-local density functional theory (NLDFT). The pore size distribution of G-SWNTs (1), in 1–10 nm range have two major contributions at 1 and 1.6 nm, with other minor contributions in 2–4 nm range. The SWNT have a pore of ~1 nm corresponding to its diameter. The additional contribution of ~1.6 nm pores in G-SWNTs (1) is due to new adsorption spaces generated by cross-linking. This pore size distribution is further confirmed by HRTEM images.

Table 1. Surface area, pore volume, CO_2 and H_2 uptake of graphene@SWNTs (1) assemblies

Sample (Gr:SWNT)	BET surface Area (m^2/g)	CO_2 uptake (wt%) 273K (1atm)	CO_2 uptake (wt%) 298 K (1atm)	H_2 Uptake (wt%) 77 K, (1 atm)	Pore volume (cc/g) at P/P_o ~ 0.9
1;2	795	10.9	9	1.1	0.68
1:1	752	11.6	7	1	0.63
2:1	1008	13	10.6	1.16	0.78
4:1	1261	15.7	10.8	1.3	0.8

The pore volume of SWNT is 0.48 $cm^3 g^{-1}$, whereas that of G-SWNTs (1) is in the range of 0.68–0.8 $cm^3 g^{-1}$ calculated at P/P_0~0.9 (Table 1). The pore volume increases with increase in graphene content in G-SWNTs (1), just as the surface area. The above studies confirm that, graphene provides more surface area and adsorbate accessible space in comparison to SWNT.G-SWNTs (1) composites show a CO_2 uptake of ~11 to 15.7 wt % at 273 K and 1 atm, and ~9 to 11 wt % at 298 K and 1 atm (Figure 7a, Table 1). The high uptake efficiency is due to interaction of CO_2 with π electron cloud of SWNT, graphene and DEBP.[28] Residual functional groups like carboxyl and hydroxyl groups also facilitate CO_2 adsorption.[29] The magnitudes of adsorption obtained are comparable to some of the high surface area metal organic frameworks (MOFs).[30] Although the uptake capacity is less than zeolite 13 X and the highest reported MOFs,[30, 31] additional properties like superhydrophobicity, high thermal and chemical stability makes G-SWNTs (1) composites promising. There is drastic decrease in CO_2 uptake of MOFs and zeolites in moisture (flue gas contains 5–7 % by volume).[30] The G-SWNTs (1) show a hydrogen uptake between 1 to 1.3 wt % at 77 K and 1 atm, which is comparable to MOFs (Figure 7b and Table 1).[32] Under similar conditions, SWNT shows a H_2 uptake of 0.35 wt %.

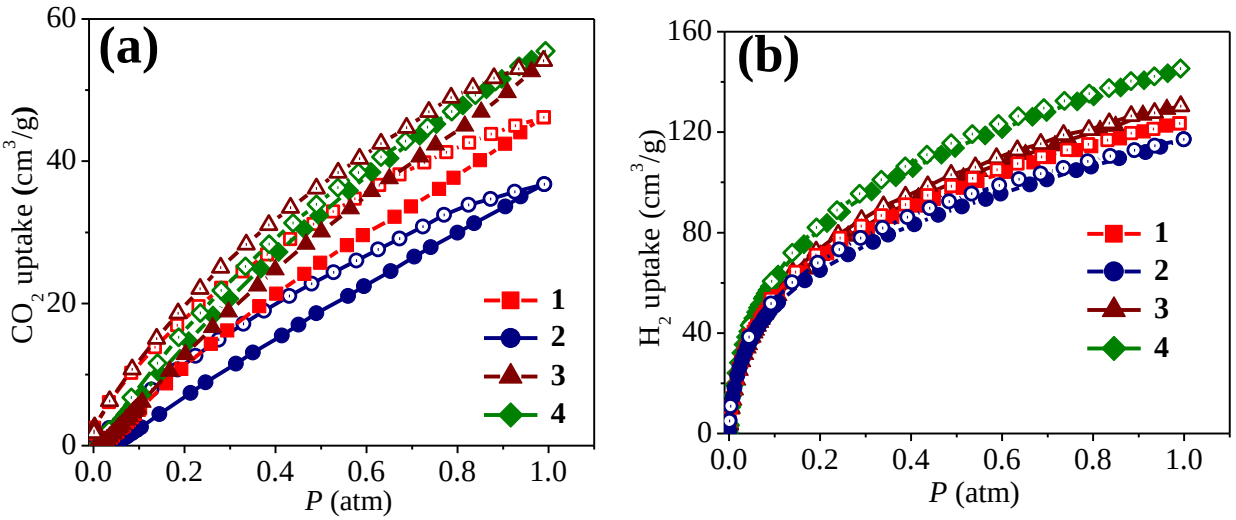

Figure 7. a) CO_2 adsorption profiles of graphene@SWNTs (1) at 298 K. b) Hydrogen adsorption profile of graphene@SWNTs (1) at 77 K. [graphene:SWNT 1 (1:2), 2 (1:1), 3 (2:1), 4 (4:1)].

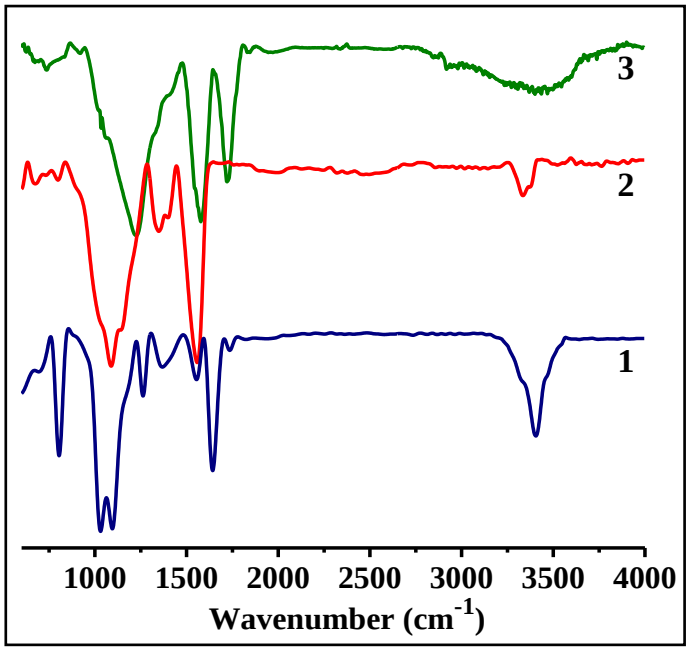

Figure 8. ATR-FTIR spectra of (1) Aminated graphene, (2) Carboxylated SWNT and (3) graphene@SWNT (2)

We have been able to generate graphene-SWNT assemblies, G-SWNT (2), by direct cross-linking of aminated graphene (RGO-NH_2) with carboxylated SWNT (SWNT-COOH) by the amide bond using EDC coupling (Scheme 2). Figure 8a shows the IR spectra of RGO-NH_2, SWNT-COOH and G-SWNT (2). SWNT-COOH shows bands at 1577, 1724 due to C=C and C=O of aromatic domains and carboxylate groups respectively.[25] The band at 1724 cm^{-1} confirms carboxyl functionalization of SWNT. RGO-NH_2 exhibits the N−H bending band at 1544 cm^{-1}, which merges with aromatic C=C stretching band.[33] The bands at 3336 and 3384 cm^{-1} correspond to N−H stretching of primary amines. The IR spectrum of G-SWNT (2) shows a strong band at 1650 cm^{-1} corresponding to the amide C=O stretching band, confirming the successful cross-linking of graphene and SWNT.[25] The weak band in G-SWNT (2) at 1726 cm^{-1} is due to residual carboxylate groups of SWNT. The high relative intensity of the 1650 cm^{-1} band compare to 1726 cm^{-1} band, confirms the effective amide bond formation. An additional band at 3408 cm^{-1} is due to N−H stretching of the amide involved in cross-linking.

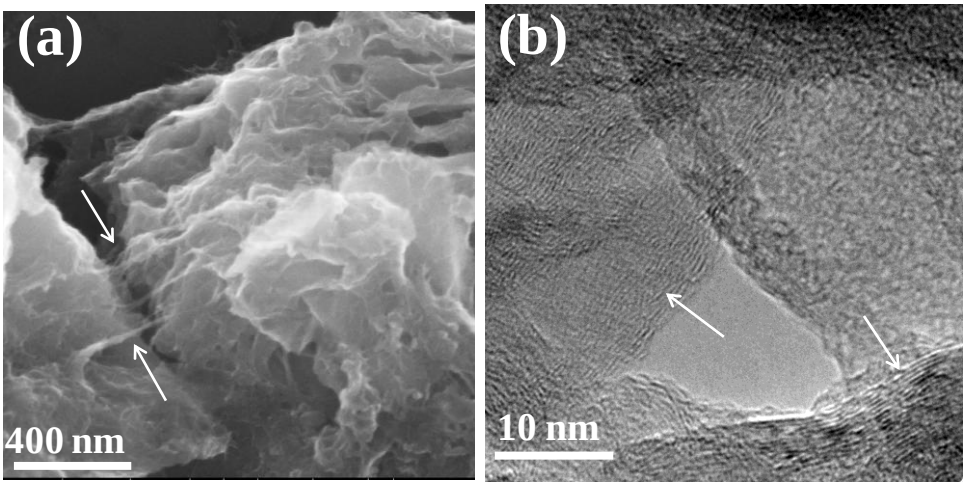

Figure 9. a, b) FEEM and TEM images of graphene@SWNT (2) synthesized by EDC coupling (arrows indicate the cross-linked nanotube bundles).

Figures 9a, b shows FESEM and TEM images of G-SWNT (2) synthesized using EDC coupling. These images confirm the presence of nanotube bundle strands connected and sandwiched between graphene sheets. Although uniformly connected SWNT strands with graphene are observed, no uniform porous architecture as in G-SWNT (1) is found here. Cross-linked nanotube strands protruding out and connecting graphene sheets are observed in the G-SWNT (2) assembly.

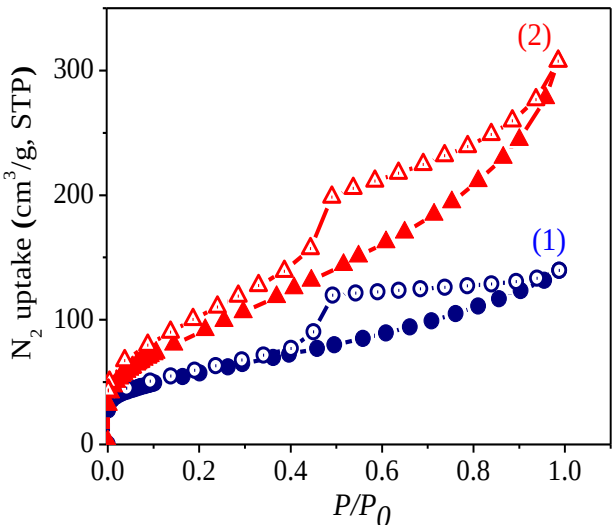

Figure 10. Nitrogen adsorption profile at 77 K of (1) aminated graphene and (2) graphene@ SWNT (2).

Nitrogen adsorption and porosity analysis show that G-SWNT (2) has a BET surface area of 337 $m^2 g^{-1}$ with a type-IV mesoporous adsorption profile as shown in Figure 10.[27] The observed mesoporous behaviour is likely due to the sheet wrinkling and agglomeration. RGO-NH_2 shows a relatively low surface area of 202 $m^2 g^{-1}$. The enhanced surface area of ~130 $m^2 g^{-1}$ in assembly is due to additional space in the interstices.

3.1.5: Conclusions

In conclusion, we have been able to synthesize graphene-SWNT assemblies using two different synthetic protocols, namely Sonogashira coupling and EDC coupling. The Sonogashira coupling makes use of Pd^0 catalyzed C−C cross-coupling of SWNT and graphene using DEBP linker. The assemblies obtained by Sonogashira coupling exhibit high surface areas comparable to MOFs, the surface area increasing with graphene content in the composites. Electron microscopy confirms the formation of uniform slit-shaped pores on cross-linking graphene and SWNT with the DEBP linker. Additionally, they have good CO_2 storage capacity under ambient conditions. H_2 uptake of the Sonogashira coupled assemblies is comparable with that of MOFs. They also have superhydrophobic surfaces. The assembly obtained by EDC coupling has a lower surface area than that of the assemblies from Sonogashira coupling.

3.1.6: References.

1. a) A. K. Geim, K. S. Novoselov, *Nat Mater.* **2007**, *6*, 183; b) C. N. R. Rao, A. K. Sood, K. S. Subrahmanyam, A. Govindaraj, *Angew. Chem. Int. Ed.* **2009**, *48*, 7752; c) H. Kataura, Y. Kumazawa, Y. Maniwa, I. Umezu, S. Suzuki, Y. Ohtsuka, Y. Achiba, *Synth. Met.* **1999**, *103*, 2555; d) H. Dai, *Acc. Chem. Res.* **2002**, *35*, 1035; e) R. S. Ruoff , D. C. Lorents, *Carbon* **1995**, *33*, 925.
2. F. Su, C. Lu, H. S. Chen, *Langmuir 27,* 8090.
3. A. K. Mishra, S. Ramaprabhu, *J. Mater. Chem.* **2011,** *21*, 7467.
4. N. Kumar, K. S. Subrahmanyam, P. Chaturbedy, K. Raidongia, A. Govindaraj, K. P. S. S. Hembram, A. K. Mishra, U. V. Waghmare , C. N. R. Rao, *Chem Sus Chem* **2011,** *4,* 1662.
5. a) R. Kumar, V. M. Suresh, T. K. Maji, C. N. R. Rao, *Chem. Commun.* **2014**, *50*, 2015; b) G. Garberoglio, N. M. Pugno, S. Taioli, *J. Phys. Chem. C* **2015**, *119*, 1980.
6. R. Kumar, C. N. R. Rao, *J. Mater. Chem. A* **2015**, *3*, 6747.
7. a) K. Pramoda, K. Moses, U. Maitra and C. N. R. Rao, *Electroanalysis* **2015**, DOI: 10.1002/elan.201500021; b) K. Zhang, F. L. Yap, K. Li, C. T. Ng, L. J. Li and K. P. Loh, *Adv. Funct. Mater.* **2014**, *24*, 731; c) K. Gopalakrishnan, K. Pramoda, U. Maitra, U. Mahima, M. A. Shah, C. N. R. Rao *Nanomat and Energy* **2014**, DOI:0.1680/nme.14.00024.
8. a) D. Yu, L. Dai, *J. Phys. Chem. Lett.* **2010**, *1*, 467; b) C. H. Choi, M. W. Chung, H. C. Kwon, J. H. Chung, S. I. Woo, *Appl. Catal. B* **2014**, *144*, 760.
9. a) N. Yousefi, X. Lin, Q. Zheng, X. Shen, J. R. Pothnis, J. Jia, E. Zussman J.-K. Kim, *Carbon* **2013**, *59*, 406; b) C.-H. Tseng, C.-C. Wang and C.-Y. Chen, *Chem. Mater.* **2007**, *19*, 308.
10. G. K. Dimitrakakis, E. Tylianakis, G. E. Froudakis, *Nano Lett.* **2008**, *8*, 3166.
11. F. Du, D. Yu, L. Dai, S. Ganguli, V. Varshney, A. K. Roy, *Chem. Mater.* **2011,** *23*, 4810.
12. C. N. R. Rao, A. K. Sood, K. S. Subrahmanyam, A. Govindaraj, *Angew. Chem., Int. Ed.* 2009, 48**,** 7752.
13. A. K. Geim, K. S. Novoselov, *Nat. Mater.* **2007**, *6*, 183.

14. A. Ghosh, K. S. Subrahmanyam, K. S. Krishna, S. Dutta, A. Govindaraj, S. K. Pati, C. N. R. Rao, *J. Phys. Chem.* **2008**, *112*, 15704.
15. M. Herrera-Alonso, A. A. Abdala, M. J. McAllister, I. A. Aksay, R. K. Prud'homme, *Langmuir*, **2007**, *23*, 10644.
16. K. Zhang, L. Mao, L. L. Zhang, H. S. O. Chan, X. S. Zhao, J. Wu, *J. Mater. Chem.* **2011**, *21*, 7302.
17. J. W. Burress, S. Gandipelli, J. Ford, J. M. Simmons, W. Zhou, T. Yildirim, *Angew. Chem., Int. Ed.* **2010,** *49*, 8902.
18. R. Kumar, C. N. R. Rao, *J. Mater. Chem. A* **2015**, *3*, 6747.
19. a) R. Chinchilla and C. Nájera, *Chem. Rev.* **2007**, *107*, 874; b) M. J. Mio, L. C. Kopel, J. B. Braun, T. L. Gadzikwa, K. L. Hull, R. G. Brisbois, C. J. Markworth and P. A. Grieco, *Org. Lett.* **2002**, *4*, 3199.
20. a) X. Zhuang, F. Zhang, D. Wu, N. Forler, H. Liang, M. Wagner, D. Gehrig, M. R. Hansen, F. Laquai, X. Feng, *Angew. Chem. Int. Ed.* **2013**, *52*, 9668; b) X. Zhuang, D. Gehrig, N. Forler, H. Liang, M. Wagner, M. R. Hansen, F. Laquai, F. Zhang, X. Feng, *Adv. Mater.* **2015**, *27*, 3789.
21. K. Sonogashira, Y. Tohda, N. Hagihara, *Tetrahedron Lett.* **1975**, *16*, 4467.
22. K. Sonogashira, *J. Organomet. Chem.* **2002**, *653*, 46.
23. a) F. Cheng, A. Adronov, *Chem. Mater.* **2006**, *18*, 5389; b) E.-i. Negishi, *J. Organomet. Chem.* **2002**, *653*, 34.
24. a) S.-Y. Han, Y.-A. Kim, *Tetrahedron* **2004**, *60*, 2447; b) E. Valeur, M. Bradley, *Chem. Soc. Rev.* **2009**, *38*, 606.
25. D. W. Mayo, F. A. Miller, R. W. Hannah in *Course Notes on the Interpretation of Infrared and Raman Spectra*, *Vol.* John Wiley & Sons, Inc., **2003** DOI:10.1002/0471690082.
26. a) K. K. S. Lau, J. Bico, K. B. K. Teo, M. Chhowalla, G. A. J. Amaratunga, W. I. Milne, G. H. McKinley, K. K. Gleason, *Nano Lett.* **2003**, *3*, 1701; b) X. Dong, J. Chen, Y. Ma, J. Wang, M. B. Chan-Park, X. Liu, L. Wang, W. Huang, P. Chen, *Chem. Commun.* **2012**, *48*, 10660.
27. K. S. W. Sing, D. H. Everett, R. A. W. Haul, L. Moscou, R. A. Pierotti, J. Rouquerol, T. Siemieniewska, *Pure Appl. Chem.* **1984**, *57*, 603.

28. A. M. Plonka, D. Banerjee, W. R. Woerner, Z. Zhang, N. Nijem, Y. J. Chabal, J. Li, J. B. Parise, *Angew. Chem. Int. Ed.* **2013**, *52*, 1692.

29. a) R. Vaidhyanathan, S. S. Iremonger, G. K. H. Shimizu, P. G. Boyd, S. Alavi, T. K. Woo, *Science* **2010**, *330*, 650; b) R. Dawson, A. I. Cooper, D. J. Adams, *Polym. Int.* **2013**, *62*, 345.

30. K. Sumida, D. L. Rogow, J. A. Mason, T. M. McDonald, E. D. Bloch, Z. R. Herm, T.-H. Bae, J. R. Long, *Chem. Rev.* **2012**, *112*, 724.

31. a) A. Ö. Yazaydın, R. Q. Snurr, T.-H. Park, K. Koh, J. Liu, M. D. LeVan, A. I. Benin, P. Jakubczak, M. Lanuza, D. B. Galloway, J. J. Low, R. R. Willis, *J. Am. Chem. Soc.* **2009**, *131*, 18198; b) Y. Wang and M. D. LeVan, *J. Chem. Eng. Data* **2009**, *54*, 2839; c) J.-S. Lee, J.-H. Kim, J.-T. Kim, J.-K. Suh, J.-M. Lee, C.-H. Lee, *J. Chem. Eng. Data* **2002**, *47*, 1237.

32. a) K. S. Park, Z. Ni, A. P. Côté, J. Y. Choi, R. Huang, F. J. Uribe-Romo, H. K. Chae, M. O'Keeffe, O. M. Yaghi, *Proc. Natl. Acad. Sci.U.S.A* **2006**, *103*, 10186; b) M. Dincă, A. Dailly, Y. Liu, C. M. Brown, D. A. Neumann, J. R. Long, *J. Am. Chem. Soc.* **2006**, *128*, 16876.

33. Y. Cao, J. Feng, P. Wu, *Carbon* **2010**, *48*, 1683.

3.1: Covalently Cross-Linked Graphene-SWNTs Composites

3.2: Graphene Composites Containing Chemically Bonded Metal Oxides

Summary*

Composites of graphene containing chemically bonded nano films of metal oxides such as TiO_2 or SiO_2 have been prepared by reacting graphene containing surface oxygen functionalities with metal halide vapors ($TiCl_4$ or $SiCl_4$) followed by exposure to water vapor. These composites have been characterized by electron microscopy, atomic force microscopy and other techniques. On calcining graphene-metal oxide composite in air at higher temperature of 600 ^oC we obtained thin metal-oxide films of TiO_2 and/or SiO_2 due to removal of underlying graphene template.

Papers based on this work have been published in *Bull. Mater. Sci. (2013), Z. Anorg. Allg. Chem. (2012).*

3.2.3: Experimental section

Graphite oxide (GO) was synthesized by the modified Hummer's method.[24] Exfoliated graphene [EG] samples were obtained from graphite oxide by the thermal exfoliation in a furnace preheated to 250 °C. Figure 1 shows the schematic diagram of experimental set-up used for coating of metal oxides on to graphene.[25] It consists of three glass chambers, one to contain the metal halide ($TiCl_4$, $SiCl_4$, etc), the second for graphene and the third for water. High-vacuum stopcocks interconnect the chambers, which are connected to a vacuum pump.

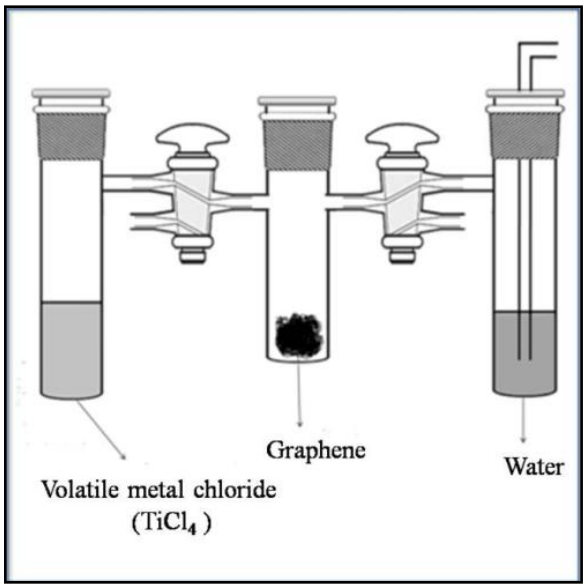

Figure 1. Schematic diagram of the experimental set-up used for metal-oxide coating on graphene.

In a typical preparation, the sample chamber is evacuated for 15 min and the metal halide vapor from first chamber is allowed to enter the reaction chamber and allowed to react for 10 min. The unreacted metal halide vapor is removed by evacuation. In this step, the metal halide reacts with the oxygen functionalities on graphene giving out HCl. Water vapor from the third chamber is then passed on to the sample chamber for hydrolyzing the remaining unreacted chlorines of the metal halide. These two procedures are repeated several times. The graphene samples so obtained were heated to 350 °C to produce metal oxide coatings. In the

case of TiO_2, samples obtained after calcination at 350 and 600 °C for 12 h are designated as G-TiO_2-350 and G-TiO_2-600, respectively. The sample is heated to 600 °C to burn off the carbon giving only a thin free-standing film of TiO_2. It should be noted that coating obtained on the graphene would not be of the oxide at room temperature, but of the same oxidic/hydroxidic species. It is only after the calcination that an oxide coating was forms. For purpose of brevity, we have called the products obtained at room temperature as oxide coated nanostructures.

3.2.4: Results and Discussion

For our present work graphitic oxide was synthesized by modified Hummers method[24] and exfoliated at low temperature of 350 ^{O}C (EG) to ensure enough residual functional groups are left on graphene surface for further modification. On reaction of EG with the vapor of a metal halide such as $TiCl_4$, the surface hydroxyl groups on EG can form metal–oxygen bonds by eliminating HCl leaving extra metal–chlorine bonds. The metal–chlorine bond is hydrolyzed by treatment with water and the hydroxide layer again reacted with the metal chloride. On repeating the process several times followed by calcination, we obtained a graphene with a chemically bonded ceramic coating of the desired thickness. Thus, in the case of $TiCl_4$ we obtain a coating of a TiO_2 film on graphene by this means. The thickness of the oxide layer depends on the number of times we carry out the reaction with the metal halide. In Figure 2, we show the FESEM images of TiO_2 coated graphene (G-TiO_2) samples obtained after the reaction of $TiCl_4$ with EG at room temperature. The energy-dispersive X-ray analysis (EDX) pattern given in the inset of the Figure 2a indicates the presence of Ti, O and Cl in the G-TiO_2 samples.

]

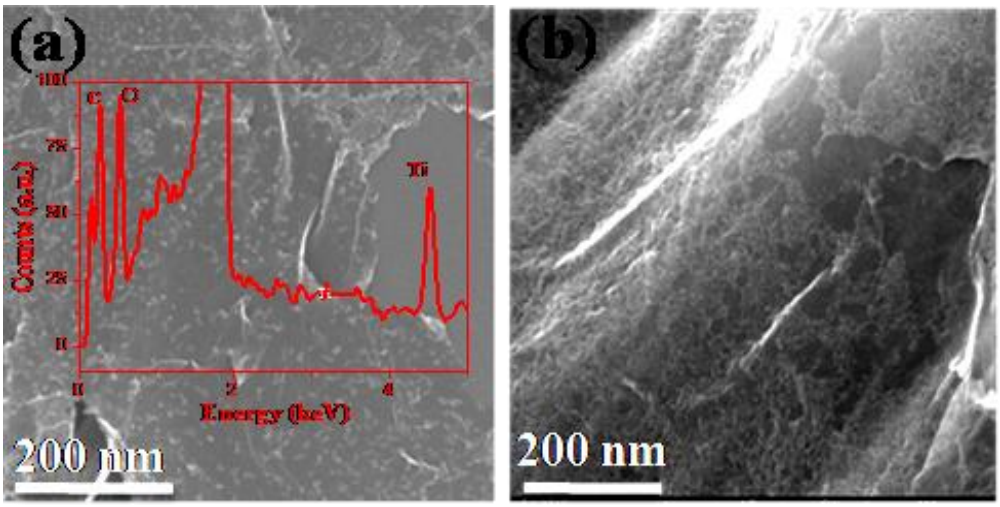

Figure 2. FESEM images of TiO_2-bonded graphene prepared at room temperature (a) after 3 cycles (b) after 12 cycles.

Raman spectra of G-TiO_2 samples shows only D (1345 cm^{-1}) and G (1590 cm^{-1}) band peaks corresponding to graphene, whereas signals from TiO_2 are absent which indicates TiO_2 coated on graphene at room temperature is amorphous in nature (Figure 3a). In view of this, we calcined our G-TiO_2 samples at different temperatures.

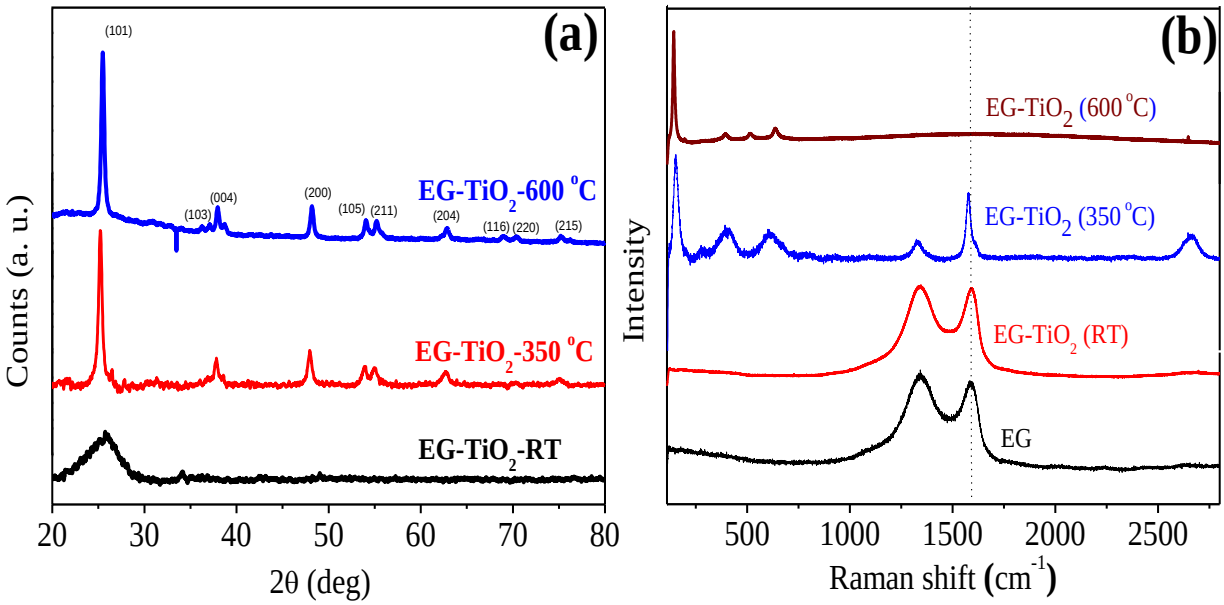

Figure 3. (a) PXRD pattern of TiO_2-bonded graphene prepared at room temperature (black), same sample after calcination at 350 °C (red), TiO_2 nanosheets after removal of graphene at 600 °C (blue); (b) Raman spectra of exfoliated graphene (black), TiO_2-bonded graphene

prepared at room temperature (red), same sample after calcination at 350 °C (blue), TiO_2 nanosheets after removal of graphene at 600 °C (wine).

G-TiO_2 sample heated at 350 ^oC (G-TiO_2-350) gives peaks from both graphene and TiO_2 with significant reduction in the D-band intensity of graphene. Furthermore, appearance of new 2D-band in the G-TiO_2-350 composites implies that coated sheets are further exfoliated during calcination. PXRD patterns of G-TiO_2 and G-TiO_2-350 also corroborate Raman spectra (Figure 3b). Interestingly, on heating G-TiO_2 samples at 600 ^oC for 12 h we obtained thin TiO_2 layers due to complete removal of underlying graphene template. Raman spectra of G-TiO_2-600 show the absence of G and D bands, indicating the complete removal of graphene template after calciniation at 600 ^oC. PXRD pattern confirms that the TiO_2 layers obtained after calcination are anatase in structure as shown in Figure 3b. G-TiO_2-600 displays layered nature as confirmed from HRTEM images (Figure 4a) and EDAX pattern shows the presence of only Ti and O. This indicates that in G-TiO_2-600, coated TiO_2 particles are condensed themselves during calcination along with the removal of grapheme template. The AFM image of G-TiO_2-600 shows that thickness of the oxide film obtained is ~1.5 nm (Figure 4b).

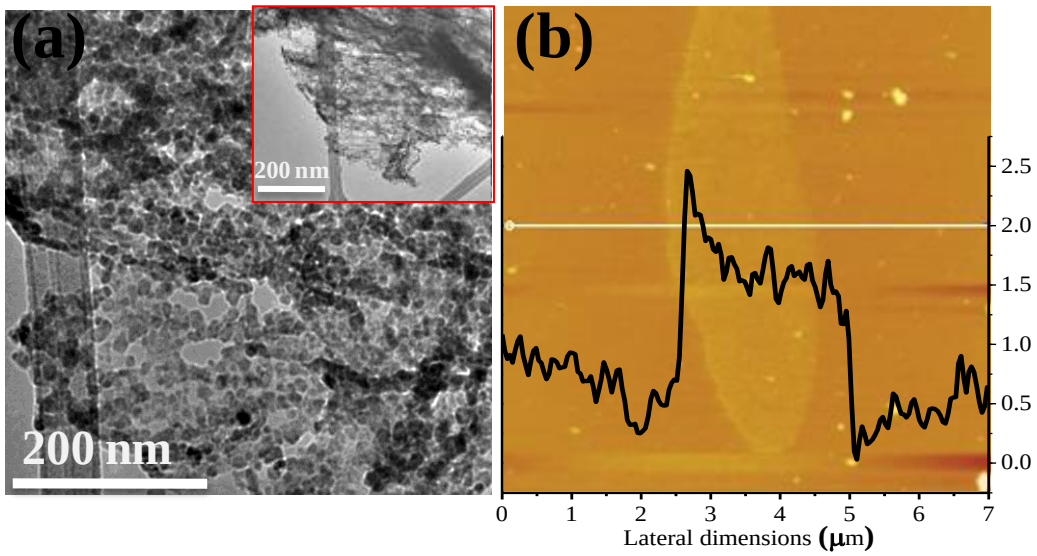

Figure 4. (a) TEM, (b) AFM images of TiO_2 nanosheets after removal of graphene at 600 °C.

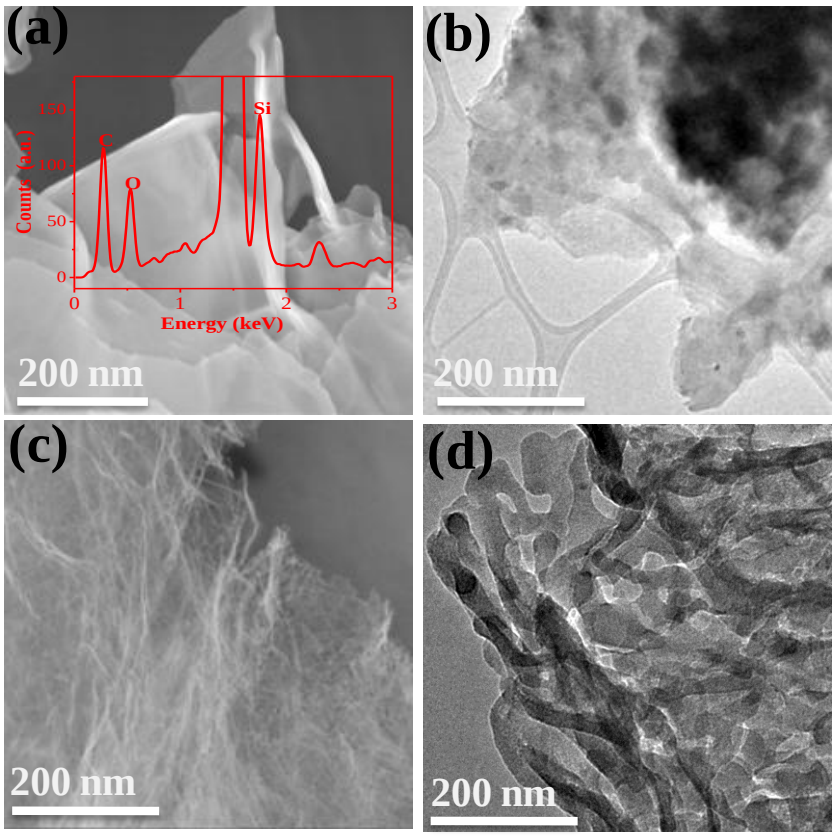

Figure 5. **a, c**) FESEM and TEM images of SiO_2-bonded graphene obtained at room temperature (Inset: EDAX pattern); **b, d**) FESEM and TEM image of SiO_2 nanosheets obtained after calcination of SiO_2-bonded graphene at 600 °C.

Encouraged by the success of preparing TiO_2-bonded graphene, we prepared graphene bonded to SiO_2 films by using $SiCl_4$ as the reagent. In Figures 5a, c we show the SEM and TEM image of SiO_2-bonded to graphene prepared after 10 cycles of coating. A TEM image of SiO_2 nanosheets obtained after calcination of SiO_2-bonded graphene sheets at 600 °C is shown in Figure 5d.

TiO_2 is a well known dielectric material with the bulk sample having dielectric constant of 20–30. TiO_2 nanosheets obtained by us have a much higher dielectric constant as shown in Figure 6.

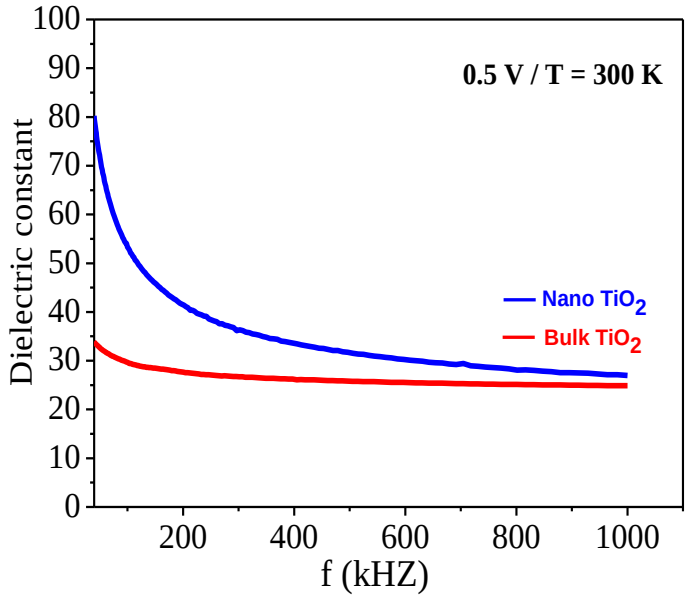

Figure 6. Frequency-dependent dielectric constant of TiO_2 nanosheets compared to bulk TiO_2.

3.2.5: Conclusions

Thin films of SiO_2 or TiO_2 have been prepared using acidified graphene layers as templates. The procedure involves the reaction of graphene surface with $TiCl_4$ or $SiCl_4$ vapors then hydrolysis followed by calcination and heating at higher temperatures in air to oxidize the carbon. Thin layers of TiO_2 or SiO_2 prepared by this procedure may be useful in catalysis. Thin metal oxide layers obtained are characterized by Raman spectroscopy, PXRD and electron microscopy.

3.2.6: References

1. P. M. Ajayan, O. Stephan, Ph. Redlich and C. Colliex, *Nature* **1995**, *375*, 564.
2. W. Q. Han, A. Zettl, *Nano Lett.* **2003**, *3*, 681.
3. L. Fu, Z. Liu, Y. Liu, B. Han, J. Wang, P. Hu, L. Cao, D. Zhu, *Adv. Mater*. **2004**, *16*, 350.
4. H. Dai, E. W. Wong, Y. Z. Lu, S. Fan, C. M. Lieber, *Nature* **1995**, *375*, 769.
5. W. Han, S. Fan, Q. Li, Y. Hu, *Science*, **1997**, *277*, 1287.
6. W. Han, S. Fan, Q. Li, B. Gu, X. Zhang, D. Yu, *Appl. Phys. Lett.* **1997**, *7*, 2271.

7. B. B. Lakshmi, C. J. Patrissi, C. R. Martin, *Chem. Mater.* **1997**, *9*, 2544.
8. B. C. Satishkumar, A. Govindaraj, E. M. Vogl, L. Basumallick, C. N. R. Rao, *J. Mater. Res.* **1997**, *12*, 604.
9. C. N. R. Rao, B. C. Satishkumar, A. Govindaraj, *Chem. Commun*. **1997**, 1581.
10. B. C. Satishkumar , A. Govindaraj , M. Nath , C. N. R. Rao , *J. Mater. Chem***. 2000**, *10*, 2115.
11. Y.-S. Min, E. J. Bae, K. S. Jeong, Y. J. Cho, J.-H. Lee, W. B. Choi, G.-S. Park, *Adv. Mater.* **2003**, *15*, 1019.
12. A. K. Geim, *Science* **2009**, *324*, 1530.
13. D. J. Late, B. Liu, H. S. S. R. Matte, C. N. R. Rao, V. P. Dravid, *Adv. Funct. Mater.* **2012**, 22, 1894.
14. C. N. R. Rao, B. Raveau, *Transition Metal Oxides*, Wiley-VCH, *Weinheim, 1998.*
15. K. S. Novoselov, D. Jiang, F. Schedin, T. J. Booth, V. V. Khotkevich, S. V. Morozov, A. K. Geim, *Proc. Natl. Acad. Sci. USA* **2005**, *102*, 10451.
16. T. Sasaki, M. Watanabe, *J. Am. Chem. Soc*. 1998, *120*, 4682.
17. M. Osada, T. Sasaki, *Adv. Mater*. **2012**, 24, 210.
18. A. K. Geim K. S. Novoselov, *Nat. Mater.* **2007,** *6*, 183.
19. J. N. Coleman *et al.*, *Science* **2011,** 331568.
20. H. S. S. R. Matte, A. Gomathi, A. K. Manna, D. J. Latte, R. Datta, S. K. Pati, C. N. R. Rao, *Angew. Chem. Int. Ed.* **2010**, *49***,** 4059.
21. H. Cao, B. Li, J. Zhang, F. Lian, X. Kong, M. Qu, *J. Mater. Chem.* **2012**, *22*, 9759.
22. X .Wang, S. M. Tabakman, H. Dai, *J. Am. Chem. Soc.* **2008**, ***130,*** 8152.
23. H. Zhang, X. Lv, Y. Li, Y. Wang, J. Li, *ACS Nano* **2010**, *4***,** 380.
24. W. S. Hummers, R E Offeman, *J. Am. Chem. Soc.* 1958, **80,** 1339.
25. A. Gomathi, S. R. C. Vivekchand, A. Govindaraj, C. N. R. Rao, *Adv. Mater.* **2005**, *17* 2757.

Part 4

Covalently Cross-linked MoS_2-based Nanocomposites

4.1: Overview of Molybdenum Disulfide Nanosheets

4.1.1: Introduction

The discovery of graphene, the two-dimensional network of sp^2 carbon atoms created sensation because of its amazing properties.[1, 2] This discovery has given impetus to the study of other two-dimensional structures based on layered inorganic materials. In the last few years, it has been possible to synthesize two-dimensional nanosheets of a variety of inorganic layered materials such as MoS_2 (Figure 1) and other metal chalcogenides.[3, 4] Single- and few-layered MoS_2 exhibits novel properties that are distinctly different from those of graphene.[5, 6] Whereas graphene is a gapless material, the stable 2H form of single-layered MoS_2 is a direct band gap semiconductor.[5, 6] Some properties of single-layer MoS_2 (2H) arise from valley polarization arising from spin–orbit splitting and transformation of the 2H form to the 1T form with entirely different properties.

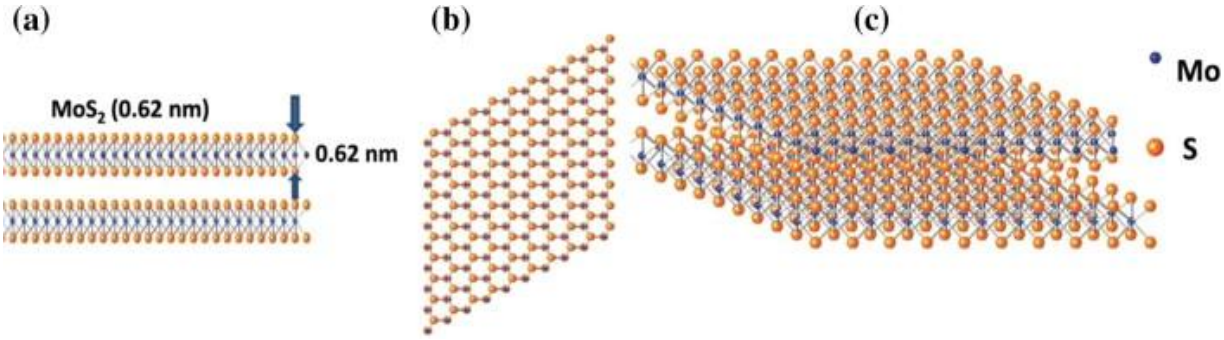

Figure 1. Structure of MoS_2: (a) side view and (b, c) top view. (Reproduced from Ref. [5])

Coleman *et al.*[8] have reported the synthesis of defect free graphene dispersions from bulk graphite by ultrasonication in NMP and other solvents for several hours. Later the same technique has been employed to obtain single- and multi-layers of transition metal dichalcogenides such as MoS_2, WS_2 in various organic solvents via sonication (Figure 2).[9] The concentrations of the resulting MoS_2 and WS_2 suspensions are 0.30 and 0.15 mg/mL respectively. The important factor for choosing the appropriate solvent for given material is that solvent and the exfoliating material should have the similar surface energy.

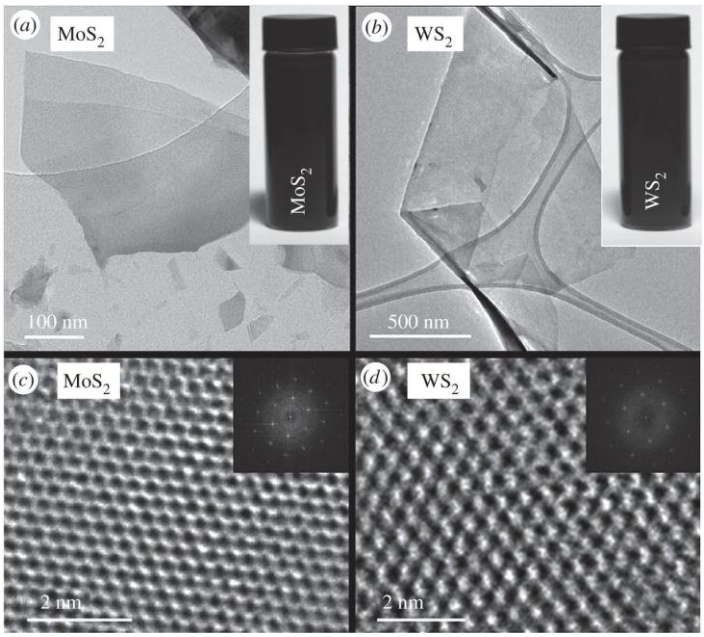

Figure 2. (a, b) Low resolution TEM images of MoS_2 and WS_2, (d, f) HRTEM images of MoS_2 and WS_2 monolayers. (Insets) Fast Fourier transforms of the images. (Reproduced from Ref. [8]).

Laser irradiation has been used to obtain single-layer MoS_2 with a defined shape and size. Laser thinning does not alter the semiconducting properties of MoS_2 compared with those of pristine single-layer samples.[10] Laser irradiation of dispersions of bulk metal dichalcogenides (MoS_2, WS_2, $MoSe_2$, and WSe_2) in DMF by a KrF excimer laser was used to produce single- and few-layer materials. Laser exfoliation was followed by centrifugation to collect the supernatant containing dispersions.[21] As early as 1986, Frindt and coauthors[12] successfully demonstrated exfoliation of MoS_2 into single- to few-layer nanosheets by Li intercalation, using *n*-butyl Li dissolved in hexane followed by reaction with water. This process leads to the transition of the stable 2H form of MoS_2 to the less stable 1T form. Of the commonly found polymorphs of TMDs (1T, 2H, and 3R), the 2H form has the trigonal prismatic coordination of the metal and chalcogen atoms, whereas the 1T form has an octahedral or trigonal antiprismatic coordination.[13] The 1T form obtained by intercalation of Li into MoS_2 is retained even after exfoliation.[14, 15] An electron diffraction pattern of the 2H phase shows the usual hexagonal spot pattern, whereas the 1T phase shows an extra hexagonal spot at $30^{\mathbf{o}}$ angular spacing between the spots of the 2H structure (Figure 3*a*, ***b***).[16] Thus, the 1T phase has AbC-AbC type of stacking, whereas the 2H phase has AbA-BaB type of stacking (Figure 3*c*).

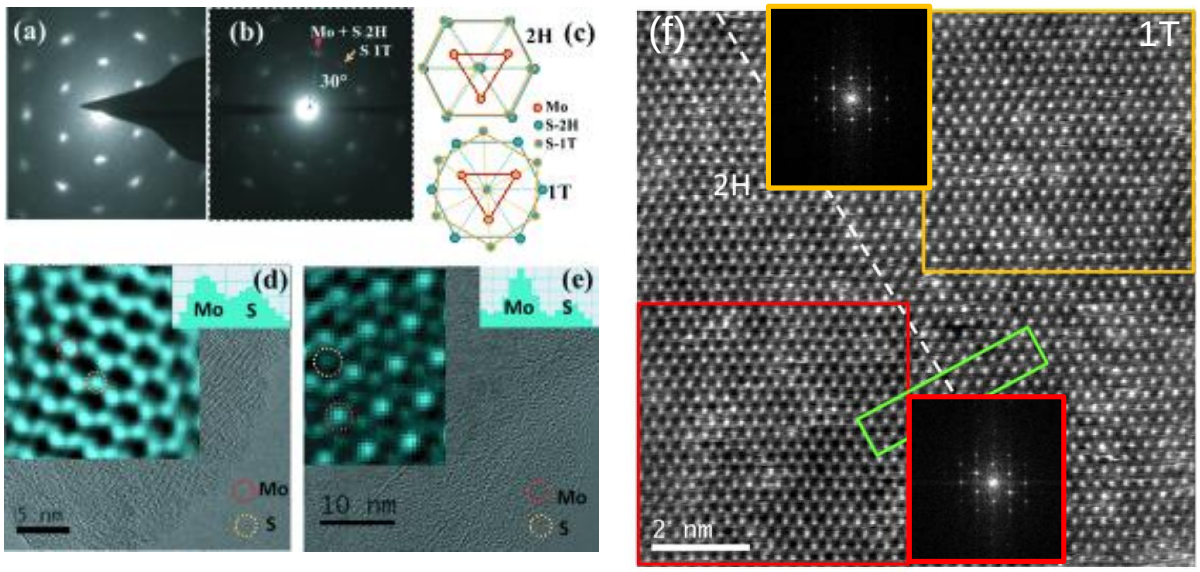

Figure 3. (*a*, *b*) SAED pattern from single-layer MoS_2 with (*a*) 2H and (*b*) 1T structures. (*c*) Schematic structural model corresponding to the 2H and 1T structures. (*d*, *e*) HRTEM images of the single-layer MoS_2 with (*d*) 2H and (*e*) 1T structures. The insets in panels *d* and *e* show magnified images of Mo and S atomic arrangements in 2H and 1T structures as well as intensity line scans through Mo and S atoms. (*f*) HRTEM image of the heterojunction of 1T- and 2H-MoS_2 obtained by Li intercalation and exfoliation. The white dashed line represents the transition from the 1T to the 2H structure. Panel *a* adapted with permission from Reference 16; panel *b* adapted with permission from Reference 15.

HRTEM images of the 2H and 1T samples are shown in panels *d* and *e* of Figure 3, respectively. Chhowalla and coworkers[13, 15] carried out high resolution scanning transmission electron microscope (STEM) imaging to identify the 2H and 1T phases of MoS_2 and showed that the samples prepared by Li intercalation and exfoliation exist as coherent heterostructures of the 1T and 2H phases (Figure 3*f*). Because 1T- and 2H-MoS_2 are metallic and semiconducting, respectively, their heterojunctions represent a chemically homogeneous layer with possible use in molecular electronic devices.

4.1.2: Properties

Bulk MoS_2 is an indirect band gap semiconductor with an energy gap of 1.2 eV, and has attracted interest as photovoltaic and photocatalytic material.

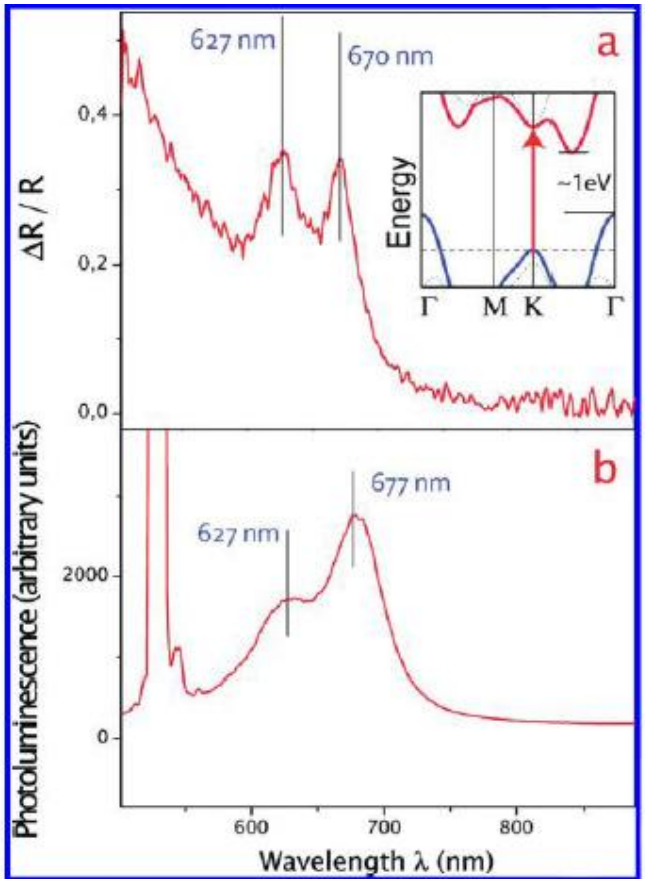

Figure 4. Reflection and photoluminescence spectra of ultrathin MoS_2 layers. (a) Reflection difference due to an ultrathin MoS_2 layer on a quartz substrate, which is proportional to the MoS_2 absorption constant. The observed absorption peaks at 1.85 eV (670 nm) and 1.98 eV (627 nm) correspond to the A_1 and B_1 direct excitonic transitions with the energy split from valence band spin-orbital coupling. The inset shows the bulk MoS_2 band structure neglecting the relatively weak spin-orbital coupling, which has an indirect bandgap around 1 eV and a single higher energy direct excitonic transition at the K point denoted by an arrow. (b) A strong photoluminescence is observed at the direct excitonic transitions energies in a monolayer MoS_2. Such luminescence is absent in the indirect bandgap bulk MoS_2 sample [from ref 9].

It is of recent interest to investigate the various properties of inorganic layered materials chalcogenides when they exfoliated to single and few-layers. Mak *et al.* studied the optical properties and electronic structure of ultrathin MoS_2 films as a function of number of layers N= 1; 2; 3: . ; 6. It is found that with decreasing N, there is a progressive confinement-induced shift in the indirect gap from the bulk value of 1.29 to 1.90 eV and transforming it from a indirect band gap semiconductor to direct band gap semiconductor with emerging photoluminescence of greater than 10^4 of its bulk counterpart.[17] Photoluminescence in MoS_2 obtained by mechanical exfoliation was also reported by Splendiani *et al.* and they observed that there is an increase in photoluminescence intensity with decreasing layer thickness, and it is maximum for a monolayer (Figure 4).[18] Later, Eda *et al.* has also observed the emerging photoluminescence from the SL-MoS_2 obtained by Li-intercalation of bulk MoS_2, indicating that SL-MoS_2 retains the structural integrity with low density of critical defects.[19] Few-layer

MoS_2 obtained by the liquid phase exfoliation of bulk MoS_2 is shown to emit at 440 nm and the fluorescence intensity was further increased by making composites with $Ag@SiO_2$ and explained on the basis of metal-enhanced fluorescence.[20]

4.1.3: Applications

Two-dimensional materials have attracted significant attention in the scientific community in the last few years due to their potential transport physics and prospects for technological applications in various fields.

Transistors

The main advantage of graphene based field-effect transistors (FET) is the associated carrier high mobility of up to 106 $cm^2V^{-1}s^{-1}$.[21] However, several problems remain with graphene due to absence of a bandgap, which is essential for transistor applications.

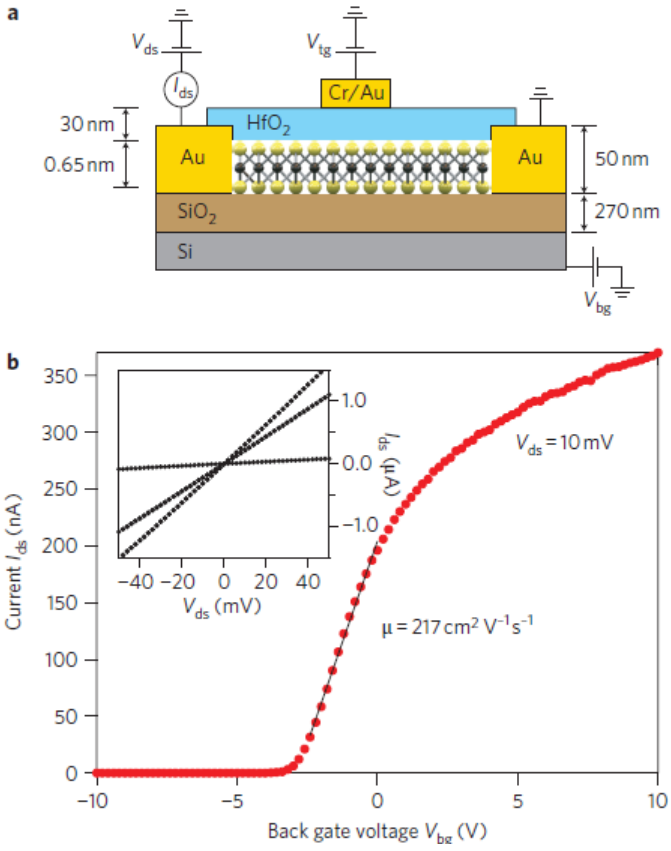

Figure 5: (a) Cross sectional view of the structure of a monolayer MoS_2 FET together with electrical connections used to characterize the device. A single layer of MoS_2 (thickness, 6.5 Å) is deposited on a degenerately doped silicon substrate with 270-nm-thick SiO_2. The substrate acts a back gate. One of the gold electrodes acts as drain and the other source electrode is grounded. The monolayer is separated from the top gate by 30 nm of ALD-grown HfO_2. The top gate width for the device is 4 mm and the top gate length, source–gate and gate–drain spacing are each 500 nm. (b) Room-temperature transfer characteristic for the FET with 10 mV applied bias voltage Vds. Backgate voltage Vbg is applied to the substrate and the top gate is disconnected. Inset: Ids–Vds curve acquired for Vbg values of 0, 1 and 5 V [From ref 24].

Subsequently, considerable efforts have been made to "open" the bandgap of graphene, such as changing the dimensions to form graphene nanoribbons.[22] In this context, there has been an extensive search for other layered materials that are analogous to graphene but with semiconducting characteristics. Recently Novoselov *et al.* has fabricated a FET on single-layer of MoS_2 obtained by mechanical exfoliation using back gate device fabrication mode and reported that the mobilities are in the range of 0.5–3 $cm^2V^{-1}s^{-1}$.[23] Later, Radisavljevic *et al.* has modified the fabrication procedure by using top gate using HfO_2 as dielectric and found that at room temperature single-layer MoS_2 has mobilities of at least 200 $cm^2V^{-1}s^{-1}$, with current on/off ratios of 10^8 with ultralow standby power dissipation (Figure 5).[24] Soon after this work there are plenty of reports appeared in the literature by modifying various important parameters.

Li-ion Batteries

Layered transition metal dichalcogenides MX_2 (M = Mo, Ti, V, and W, X = S or Se) can intercalate and de-intercalate the Li-ions into their structure between the layers along with the fast-ion conductivity. These features, have led them to consider a host materials for application in the field of primary or rechargeable batteries.

The first lithium ion battery using MoS_2 as the electrode material gave impressive results which has led to further investigate the different morphologies of MoS_2.[25] MoS_2 with enlarged c-lattice parameter and high surface area obtained by exfoliation and restacking of commercially available MoS_2, showed the first charge capacity of 800 mAh/g and maintained a capacity of 750 mAh/g after 20 cycles at current density of 50 mA/g.[26] Bulk MoS_2 electrodes exhibited decrease in the charge capacity from 800 to 226 mh/g after 50 cycles. Feng *et al.*[27] synthesized MoS_2 nanoflakes by a hydrothermal method and found that the MoS_2 nanoflake electrodes exhibit a capacity of 1000 mAh/g. Hierarchical spheres composed of ultrathin MoS_2 nanosheets prepared by polystyrene microsphere-assisted hydrothermal method show lithium storage capacity of 672 mAh/g.[28] MoS_2 nanoflowers synthesized using ionic liquid assisted hydrothermal method showed a reversible capacity of 900 mAh/g.[29] Recently, a simple, one-pot synthesis of graphene-like MoS_2 nanoplates obtained by solvothermal method using molybdenum carbonyl and sulphur showed the first

discharge and charge capacities of 1062 and 917 mAh/g, respectively at current density of 1.06 A/g (see Figure 6).[30]

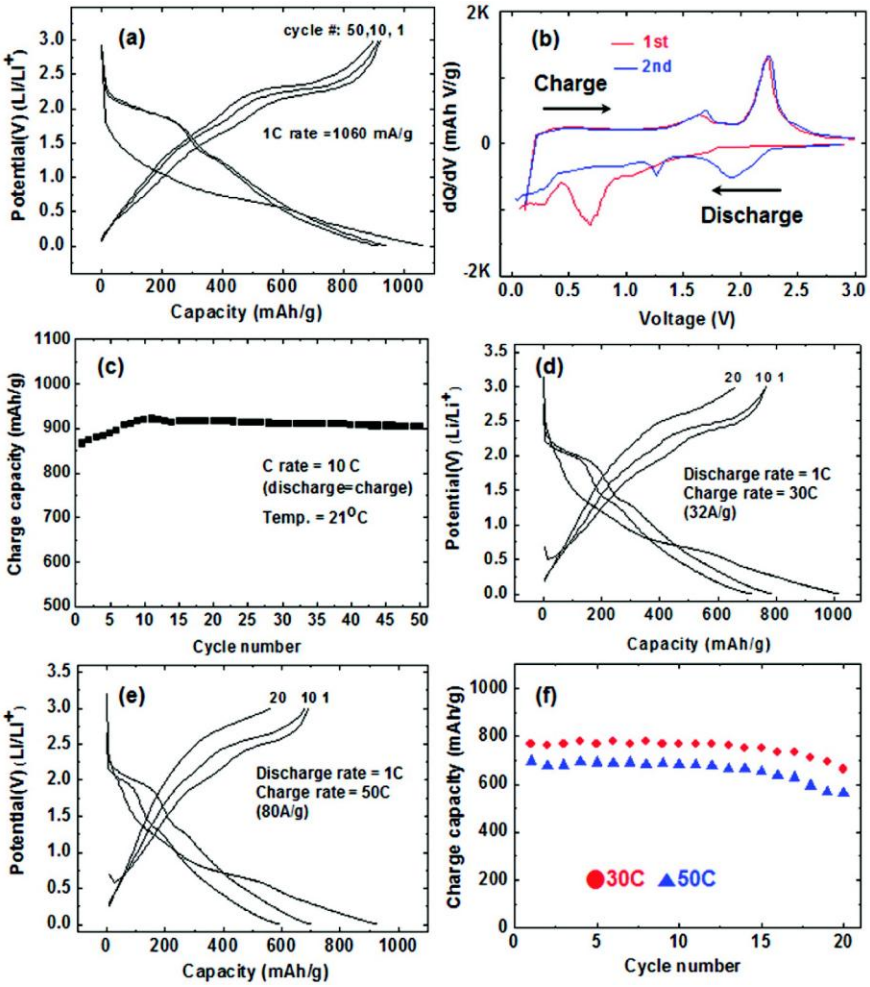

Figure 6. (a) Voltage profiles of MoS_2 nanoplates in coin-type lithium half cells between 0 and 3 V at a rate of 1C (=1062 mA/g) (charge and discharge rates were the same) at room temperature. (b) Differential curves of MoS_2 nanoplates during the first and second cycles. (c) Plot of charge capacity vs cycle number in coin-type lithium half cells between 0 and 3 V at a rate of 10C rates (charge and discharge rates were the same) at room temperature. (d, e) Voltage profiles of MoS_2 nanoplates in coin-type lithium half cells between 0 and 3 V at a rate of 20 and 50C rates (discharge rates to 0 V were 1C) at room temperature. (f) Plot of charge capacity vs cycle number obtained from (d) and (e)

Hydrogen evolution reactions

The necessary condition for any catalyst to act as a hydrogen-evolving catalyst is that the bottom of the conduction band of the catalyst should be more negative than the redox potential of H^+/H_2 (0 V vs NHE at pH 0). Efficiency of a HER catalyst is determined by the efficiency of the three steps of HER: (i) photogeneration of electrons and holes, (ii) separation of photogenerated electrons from holes, and (iii) reduction of H^+ to H_2 using the photogenerated electrons.[6] Hinnemenn et al. first showed that nanoparticles of MoS_2 can be used for electrochemical HER with an overpotential as low as 0.1-0.2 V.[31] Theoretical studies have shown that edge sites of MoS_2[32] and vacancy defects[33] are active in HER. Because edges seem to be the catalytically active sites of HER, several studies have been carried out to prepare nanoparticles,[34] nanosheets,[35] and other morphologies[36] with a large density of exposed edges and have been shown to improve both the Tafel slope and the overpotential. An improvement in the electrochemical activity is achieved by increasing the surface area of MoS_2 along with the edge sites.[37] The addition of graphene to MoS_2 increases the electronic conductivity of the electrode, thereby improving the overall activity.[38] On the basis of the importance of edges in the catalytic activity of MoS_2, several studies have been carried out to understand the nature of edges in MoS_2, and it has been found that edge states in MoS_2 are metallic in nature.[39, 40]

It has been recently found that monolayers of metallic 1T phases of MoS_2 and WS_2 prepared by chemical exfoliation exhibit superior catalytic activity in electrochemical HER relative to that of the 2H analogue.[41- 43] Density functional calculations on the 1T phase of WS_2 has shown that the strained form of 1T state facilitates hydrogen binding and thereby brings the free energy of hydrogen binding close to zero. A hydrogen binding energy of $\Delta G \sim 0$ for a catalyst implies that binding and release of hydrogen by the catalyst are equally easily achieved.[41] Deliberate oxidation of edges of chemically exfoliated MoS_2 has shown that the basal plane of 1T-MoS_2 nanosheets, not the edges, are active in H_2 evolution.[42] Figure 7 compares the electrocatalytic HER activity of 2H- and 1T-MoS_2 with and without edge oxidation. Whereas the catalytic activity of 2H-MoS_2 is mostly dependent on its edges, the basal plane of 1T-MoS_2 determines its catalytic activity.

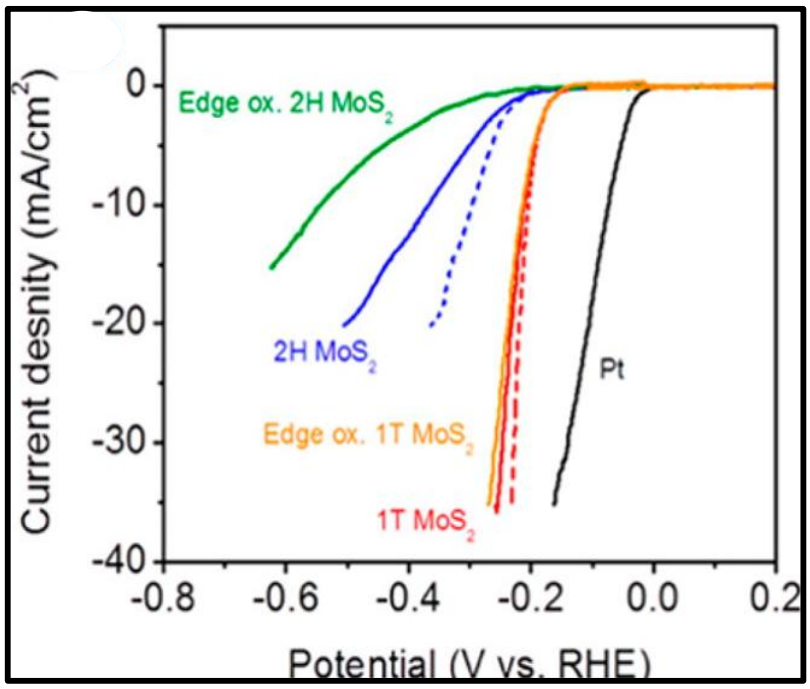

Figure 7. Hydrogen evolution with MoS_2 nanosheets: (a) electrochemical HER with polarization curves of 1T- and 2H-MoS_2 nanosheet electrodes before and after edge oxidation (*iR*-corrected polarization curves from 1T- and 2H-MoS_2 are shown by dashed lines). Reprinted with permission from ref 43.

4.1.4: References

1. A.K. Geim, K.S. Novoselov, Nat. Mater. **2007,** 6, 183.
2. C.N.R. Rao, A.K. Sood, Graphene: synthesis, properties, and phenomena *Wiley-VCH, Verlag GmbH, Weinheim* **2013**.
3. K.S. Novoselov, D. Jiang, F. Schedin, T.J. Booth, V.V. Khotkevich, S.V. Morozov, A.K. Geim, *Proc. Natl. Acad. Sci. U.S.A.* **2005**, *102*, 10451.
4. C.N.R. Rao, H.S.S. Ramakrishna, *Angew. Chem. Int. Ed*. **2013**, *52*, 13162.
5. C. N. R. Rao, U. Maitra, U. *Annu. Rev. Mater. Res*. **2015**, *45*, 29.
6. C. N. R. Rao, K. Gopalakrishna, U. Maitra, *ACS Appl. Mater. Interfaces*, 2015, 7, 7809.
7. D.J. Late, B. Liu, H.S.S.R. Matte, C.N.R. Rao, V.P. Dravid *Adv. Funct. Mater*. **2012**, *22*, 1894
8. J. N. Coleman, M. Lotya, A. O'Neill, S. D. Bergin, P. J. King, U. Khan, K. Young, A. Gaucher, S. De, R. J. Smith, I. V. Shvets, S. K. Arora, G. Stanton, H.-Y. Kim, K. Lee, G. T. Kim, G. S. Duesberg, T. Hallam, J. J. Boland, J. J. Wang, J. F. Donegan, J. C. Grunlan, G. Moriarty, A. Shmeliov, R. J. Nicholls, J. M. Perkins, E. M. Grieveson, K. Theuwissen, D. W. McComb, P. D. Nellist, V. Nicolosi, *Science* **2011**, *331*, 568.
9. Y. Hernandez, V. Nicolosi, M. Lotya, F. M. Blighe, Z. Sun, S. De, I. T. McGovern, B. Holland, M. Byrne, Y. K. Gun'Ko, J. J. Boland, P. Niraj, G. Duesberg, S. Krishnamurthy, R. Goodhue, J. Hutchison, V. Scardaci, A. C. Ferrari, J. N.Coleman, *Nat. Nanotechnol.* **2008**, *3*, 563.
10. Gomez , M. Barkelid, A. M. Goossens, V. E. Calado, H. S. J. van der Zant, G. A. Steele, *Nano Lett.* **2012**, *12*, 3187.
11. H. S. S. R. Matte, U. Maitra, P. Kumar, B. G. Rao, K. Pramoda, C. N. R. Rao, *Z. Anorg. Allg. Chem*. **2012,** *638*, 2617.
12. P. Joensen, R. F. Frindt, S. R. Morrison, *Mater. Res. Bull.* **1986,** *21*, 457.
13. M. Chhowalla, H. S. Shin, G. Eda, L. Li, K. P. Loh, H. Zhang H, *Nat. Chem.* **2013,** 5, 263.
14. G. Eda, H. Yamaguchi, D. Voiry, T. Fujita, M. Chen, M. Chhowalla, *Nano Lett.* **2011**, *11*, 5111.

15. G. Eda, T. Fujita, H. Yamaguchi, D. Voiry, M. Chen, M. Chhowalla, *ACS Nano* **2012,** *6*, 7311.
16. U. Maitra, U. Gupta, M. De, R, Datta, A. Govindaraj, C. N. R. Rao, *Angew. Chem., Int. Ed.* **2013**, *52*, 13057.
17. K. F. Mak, C. Lee, J. Hone, J. Shan, T. F. Heinz, *Phys. Rev. Lett.* **2010**, *105*, 136805.
18. A. Splendiani, L. Sun, Y. Zhang, T. Li, J. Kim, C.-Y. Chim, G. Galli, F. Wang, *Nano Lett.* **2010**, *10*, 1271.
19. G. Eda, H. Yamaguchi, D. Voiry, T. Fujita, M. Chen, M. Chhowalla, *Nano Lett.* **2011**, *11*, 5111.
20. K. Zhou, Y. Zhu, X. Yang, J. Zhou, C. Li, *Chem Phys Chem* **2012**, *13*, 699.
21. F. Schwierz, *Nat Nanotechnol.* **2012**, *5* 487.
22. X. W. Li, L. Zhang, S. Lee, H., , Dai, *Science* **2008**, *319*, 1229
23. K. S. Novoselov et al. *Proc. Natl. Acad. Sci. USA* **2005** *102*, 10451.
24. B. Radisavljevic, A. Radenovic J. Brivio, V. Giacometti. A. Kis, *Nat. Nanotecnol.* **2011**, *6*, 147.
25. R. R. Haering, J. A. R. Stiles, K. Brandt, (Ed.: US Patent 4224390), **1980.**
26. G. Du, Z. Guo, S. Wang, R. Zeng, Z. Chen, H. Liu, *Chem. Comm.* **2010**, *46*, 1106.
27. C. Feng, J. Ma, H. Li, R. Zeng, Z. Guo, H. Liu, *Mater. Res. Bull.* **2009**, *44*, 1811.
28. S. Ding, D. Zhang, J. S. Chen, X. W. Lou, *Nanoscale* **2012**, *4*, 95.
29. H. Li, W. Li, L. Ma, W. Chen, J. Wang, *J. Alloys Compd.* **2009**, *471*, 442.
30. H. Hwang, H. Kim, J. Cho, *Nano Lett.* **2011**, *11*, 4826.
31. B. Hinnemann, P. G. Moses, J. Bonde, K. P. Jørgensen, J. H. Nielsen, S. Horch, I. Chorkendorff, J. K. Nørskov, *J. Am. Chem. Soc.* **2005,** *127*, 5308.
32. T. F. Jaramillo, K. P. Jørgensen, J. Bonde, J. H. Nielsen, S. Horch, I. Chorkendorff, *Science* **2007**, *317*, 100.
33. C. Ataca, S. Ciraci, *Phys. Rev. B* **2012**, *85*, 195410.
34. D. Wang, Z. Wang, C. Wang, P. Zhou, Z. Wu and Z. Liu, *Electrochem. Commun.*, **2013**, *34*, 219.
35. C. Ataca, S. Ciraci, *Phys. Rev. B: Condens. Matter Mater. Phys*. **2012**, *85*, 195410.
36. J. Kibsgaard, Z. Chen, B. N. Reinecke, T. F. Jaramillo, *Nat. Mater.* **2012**, *11*, 963.

37. a) D. Merki, X. Hu, *Energy Environ. Sci.* **2011**, 167; b) V. Lau, V. A. F. Masters, A. M. Bond, T. Maschmeyer, *Chem. Eur. J*. **2012,** *18*, 8230.
38. E. G. S. Firmiano, M. A. L. Cordeiro, A. C. Rabelo, C. J. Dalmaschio, A. N. Pinheiro, E. C. Pereira, E. R. Leite, *Chem. Commun.* **2012,** 48, 7687.
39. J. V. Lauritsen, M. Nyberg, T. R. Vang, M. V. Bollinger, B. S. Clausen, H. Topsøe, K. W. Jacobsen, E. Lægsgaard, J. K. Nørskov, F. Besenbacher, *Nanotechnology* **2003**, *14*, 385.
40. L. P. Hansen, Q. M. Ramasse, C. Kisielowski, M. Brorson, E. Johnson, H. Topsøe, S. Helveg, *Angew. Chem., Int. Ed.* **2011**, *50*, 10153.
41. M. A. Lukowski, A. S. Daniel, F. Meng, A. Forticaux, L. Li, S. Jin, *J. Am. Chem. Soc*. **2013**, 135, 10274.
42. D. Voiry, H. Yamaguchi, J. Li, R. Silva, D. C. B. Alves, T. Fujita, M. Chen, T. Asefa, V. B. Shenoy, G. Eda, M. Chhowalla, *Nat. Mater*. **2013**, *12*, 850.
43. D. Voiry, M. Salehi, R. Silva, T. Fujita, M. Chen, T. Asefa, V. B. Shenoy, G. Eda, M. Chhowalla, *Nano Lett*. **2013**, *13*, 6222.

4.2: Nanocomposites of 2D-MoS_2 Nanosheets with the Metal–Organic Framework, ZIF-8

Summary*

Nanocomposites of MoS_2 nanosheets with the metal–organic framework, ZIF-8, have been synthesized starting with the layers of 1T-MoS_2 generated by Li intercalation of bulk MoS_2, followed by exfoliation. One can visualize excess negative charges on the 1T-MoS_2 template as structure-directing agents for the ZIF-8 precursor (eg; zinc nitrate). The nanocomposites contain the Zn–S bond and exhibit reasonably high surface areas. They exhibit CO_2 uptake higher than ZIF-8. Heating the nanocomposites to 900 °C under a N_2 atmosphere yields MoS_2–ZnS nanocomposites which show good activity for the visible-light induced hydrogen evolution reaction.

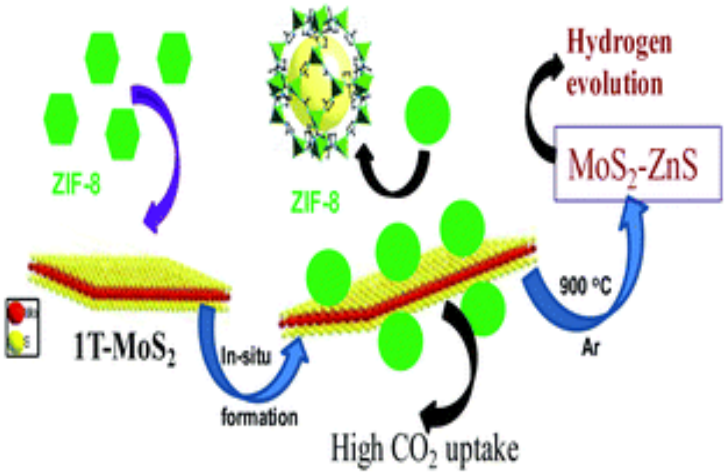

A Paper based on this work has been appeared in *Dalton Trans. (2016).*

4.2.1: Introduction

Carbon dioxide and methane are the main greenhouse gases of concern. Greenhouse effect refers to the entrapment of heat radiation by infrared absorbing gases, which is in other words difference in energy that escapes to space and the energy emitted from the earth's surface. In the last few decades there has been an unprecedented increase in the CO_2 emission in the atmosphere. Main sources of this increment are deforestation, factory exhausts, vehicular emission *etc*. Role of CO_2 in climate change over other natural variability is a much debated topic. However, some recent studies have suggested increased amount of CO_2 to be an important contributor towards global warming. According to a study, (1) energy related CO_2 emission over a period of 2005-2030 would cause CO_2 emission jump of 57 %, (2) fossil fuel will still be the most important energy source covering 83 % of the total increase in the demand and (3) considering that the policies by governments around the world to stabilize global emissions achieve their goals there would still be an increase of 3 % in average global temperature by 2030. One way to tackle this problem is to convert CO_2 into fuels and various other useful products by chemical reactions also known as chemical fixation. CO_2 has been converted into methanol, formic acid, dimethyl carbonate, methyl formate, higher hydrocarbons, pharmaceutical products *etc*. Another strategy to capture excess CO_2 in the environment is to capture it in porous materials like activated carbon, zeolited, metal-organic frameworks (MOFs) *etc.* by physical adsorption. Recently, varieties of metal-organic frameworks (MOFs) have been studied which can selectively adsorb CO_2 inside the pores. One main advantage of these materials is that the pore size can easily be tuned by proper modifications of linkers. For example, Yaghi *et al.* showed huge CO_2 uptake in MOF-210 which is based on $Zn_4O(CO_2)_6$ units .[1] More recently, polyethyleneimine incorporated MIL-101 which is a chromium based MOF, is tested with an unprecedented CO_2 uptake selectivity of 770 over N_2 at room temperature and 1200 at 50 ^oC.[2] Despite such outstanding performances, factors like very high cost, poor thermal and chemical stability limit the large scale use of MOFs to trap CO_2. A class of carbon based materials, activated carbon and cabon nanotubes in particular are potential candidates for CO_2 sequestration. There are several reports of CO_2 adsorption on the ammine functionalized carbon nanotubes. Dillon *et al.*[3] studied the effect of polyethyleneimine (PEI) functionalization on fluorinated SWNTs (FSWNTs). Lu and co-workers[4, 5] compared the adsorption properties of pure and 3-

aminopropyl-triethoxysilane (APTS) functionalized multiwalled carbon nanotubes (MWNTs) at a temperature range of 293 to 373 K. They showed an increase of more than 40 % of CO_2 adsorption at 293 K and influent flow of 50 mg/L.

Growing MOFs on 2D layered materials such as graphene and boron nitride is another attractive strategy where one can expect enhanced thermal and chemical stabilities of MOFs along with the increased CO_2 uptake. Hybrid nanocomposites of MOFs, namely zeolitic imidazolate frameworks (ZIFs), covalently linked with graphene and few-layer boron nitride enabled the integration of the unique properties of the layered materials with the ZIF-8.[9-12] It is to be noted that ZIFs constitute a new class of zeolite-like MOFs with a high degree of microporosity, which can be exploited to obtain thin films and good gas separation.[13-15] Recently, Co, Ni, and Cu based metal–organic frameworks (MOFs) with good gas adsorption properties covalently linked with graphene are reported to exhibit improved CO_2 uptake as well as mechanical properties.[16] Frameworks generated by cross-linking the layers of graphene and other 2D materials have also been examined recently due to their tunable surface areas and gas storage properties with high thermal stabilities.[6-8] Thus, graphene layers covalently cross-linked to one-another generates an all-carbon porous material with significant CO_2 uptake under ambient conditions.[6] Assemblies of covalently cross-linked nanosheets of MoS_2 and of MoS_2 with reduced graphene oxide where the 2D layers are covalently pillared by rigid organic linkers have also been studied.[8] These composites are porous and show substantial CO_2 storage capacity and enhanced visible-light induced hydrogen evolution characteristics.

In the case of graphene or BN, functional groups in the basal-plane favour the nucleation of ZIF-8, which allows one to design nanoscale MOFs which have potential applications in bioimaging, biosensing and other areas.[17] Furthermore, nanoscale MOFs provide solution-based processability and exhibit increased gas uptake.[18] Huang et al. recently have reported ZIF-8 coated MoS_2 as a material for memory devices,[19a] while Weng et al. described microporous carbon wrapped MoS_2, generated by heating the MoS_2–ZIF-8 composite, as the electrode material for supercapacitors.[19b] There are no reports on in-situ growth of ZIF-8 crystals on MoS_2 due to the limited number of functionalization approaches for MoS_2 owing to the inert nature of its basal-plane.[20]

4.2.2: Scope of the present investigations

Growth of MOF nanoparticles of different morphologies on 2D layered materials such as graphene and boron nitride has enabled integration of the unique properties of the layered materials with ZIF-8. One can visualize 2D layers as structure-directing agents for the growth and stabilization of MOF nanocrystals, where coordination modulation occurs through the various residual functional groups on the 2D surface. In this perspective, making use of ZIFs, a novel class of zeolite-like MOFs, possessing exceptional thermal and chemical stabilities and a high degree of microporosity, to prepare composites with MoS_2, appears to be attractive strategy. In the present study, we have generated single layers of metallic octahedral phase (1T) MoS_2 by lithium-ion intercalation followed by exfoliation and reacted the 1T-MoS_2 sheets with the precursors of ZIF-8 to form nanocomposites with the Zn–S bond. These metallic sheets contain excess negative charge on the sulfur atoms of the basal-plane.[21] One can envisage negative charges on the 1T-MoS_2 template as structure-directing agents for the ZIF-8 precursor (eg; zinc nitrate). 1T-MoS_2 is known to react with organic halides giving rise to the covalent C–S bonds.[21, 22] Furthermore, the nanocomposite obtained through a covalent strategy allows the intercalation and stabilization of ZIF-8 nanocrystals between the nanosheets, thereby retaining thin-layer characteristics.[9-12, 16] The MoS_2–ZIF-8 nanocomposites prepared by us exhibit good CO_2 uptake. Interestingly, on heating the nanocomposite at 900 °C under an inert atmosphere, we obtained an adduct of zinc sulphide (ZnS) nanoparticles with MoS_2 sheets which exhibits good visible-light induced hydrogen evolution activity.

4.2.3: Experimental section

Synthesis of 1T-MoS_2, ZiF-8 and MoS_2-ZiF-8 nanocomposites:

To synthesize 1T-MoS_2, 300 mg of bulk MoS_2 powder was stirred in a solution of 3 ml n-butyllithium (n-BuLi in 1.6 M hexane) at 70 °C over a period of two days under an argon atmosphere.[23] The resultant black Li_xMoS_2 was collected by vacuum filtration, and washed extensively with hexane. Ultrasonication of the Li-intercalated sample was performed in water (1 mg ml^{-1}) for an hour, and the resulting solution was centrifuged at a high speed (8000 rpm) to settle LiOH, and any remaining unexfoliated material. The final concentration

of MoS_2 in water was obtained from inductively coupled plasma (ICP) analysis, and it was found to be ~0.7 mg ml^{-1}.

ZIF-8 nanocrystals were synthesized by adding an aqueous solution of zinc nitrate hexahydrate ($Zn(NO_3)_2 \cdot 6H_2O$) (5 ml) (0.75 mmol) to 2-methylimidazole (10 ml) (34 mmol) dropwise under constant stirring conditions. The product was collected by centrifugation and washed with deionized water and methanol a number of times to remove any unreacted material, and the product yield was 65%. For the synthesis of MoS_2–ZIF-8 nanocomposites, a solution containing different wt% of exfoliated MoS_2 was added during the synthesis of ZIF-8. The nanocomposites obtained with different MoS_2 contents are designated as ZM, where M indicates wt% (5, 10, 20) of 1T-MoS_2 in comparison to the Zn(II) metal. These materials are designated as ZM (ZM-0, ZM-5, ZM-10 and ZM-20) based on the different MoS_2 loadings.

Hydrogen evolution measurements:

For hydrogen evolution measurements, few-layer MoS_2, ZnS and the MoS_2–ZnS composites were dispersed in a solution of water and triethanolamine (TEAO) (15% v/v) by sonication; to this 14 μmol of eosin Y dye was added. The vessel containing the above solution was purged with N_2, and illuminated with a 100 W halogen lamp under constant stirring conditions. The evolved gases were collected from the headspace and analyzed with a gas chromatograph fitted with a thermal conductivity detector (TCD) (PerkinElmer Clarus ARNEL 580GC).

Characterization

Powder X-ray diffraction (PXRD) patterns of the ZM nanocomposites were recorded with a PANalytical Empyrean with Cu Kα radiation. X-ray photoelectron spectra (XPS) were obtained with an Omicron Nanotechnology Spectrometer using Mg Kα as the X-ray source. TEM (Technai T20, FEI) operating at an accelerating voltage of 200 kV was used for morphological analysis of the sample. Raman spectra were recorded at several different spots with back scattering arrangement using a HORIBA LabRam HR800. Adsorption isotherms of N_2 (77 K), and CO_2 (275 K, 1 atm) were obtained using a QUANTACHROME QUADRASORB-SI analyzer.

4.2.4: Results and Discussion

In Scheme 1, we show the steps involved in synthesizing ZIF-8 nanocomposites (designated as ZM) with varying MoS_2 content (0, 5, 10 and 20 wt% of 1T-MoS_2), yielding ZM-0, ZM-5, ZM-10 and ZM-20, respectively. Exfoliation of MoS_2 was achieved with n-butyllithium leading to the formation of layers of 1T-MoS_2.[23] The formation of ZIF-8 nanoparticles on the 1T-MoS_2 basal-plane is favored by the negative charges on the sulfur atoms through the formation of Zn–S bonds. The excess negative charges on the sulfur atoms of 1T-MoS_2 can undergo coordination modulation with the metal precursor leading to nucleation and growth of ZIF-8 nanocrystals on the basal-plane. It is important to note that in the final ZM nanocomposites, 1T-MoS_2 eventually transforms to the trigonal (2H) structure.

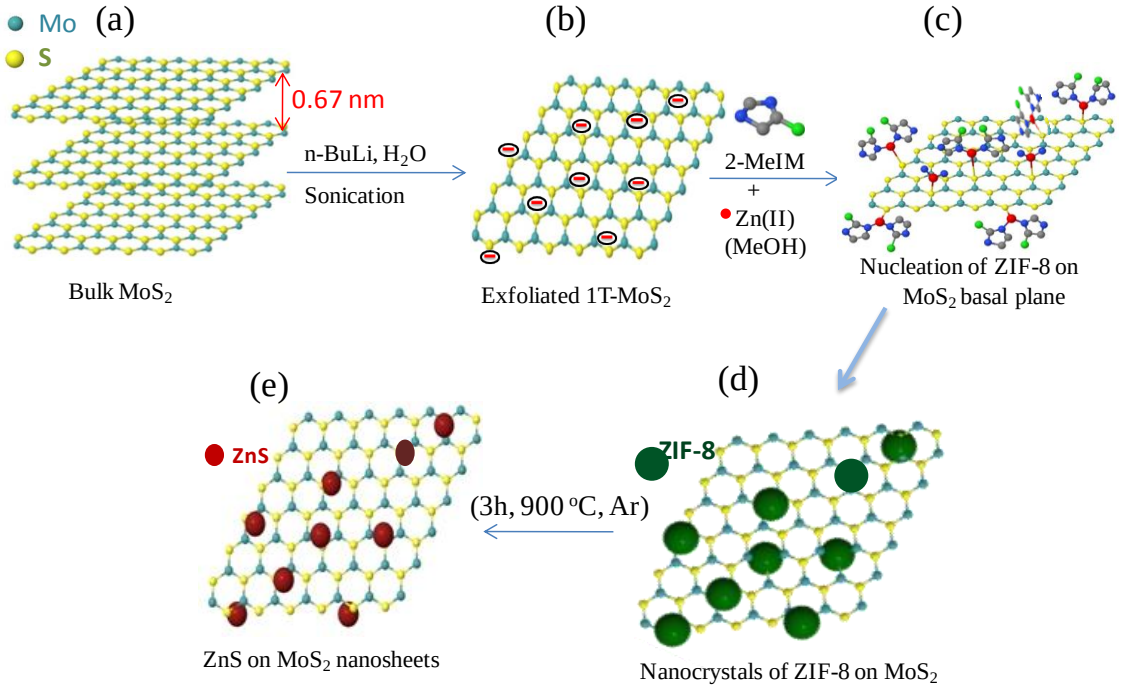

Scheme 1 Schematic of the in-situ synthesis of MoS_2–ZIF-8 nanocomposites (a) MoS_2, (b) exfoliation of bulk MoS_2 with n-butyllithium, (c and d) nucleation and formation of ZIF-8 on the 1T-MoS_2 basal plane, (e) formation of ZnS nanoparticles on MoS_2.

Elemental mapping images of a typical nanocomposite of ZIF-8 with MoS_2, ZM-10 (MoS_2–ZIF-8 containing 10 wt% MoS_2), using energy-dispersive X-ray spectroscopy (EDAX) show homogeneous distribution of Mo, S, Zn, N and C confirming the uniform nature of the nanocomposite (Figure 1).

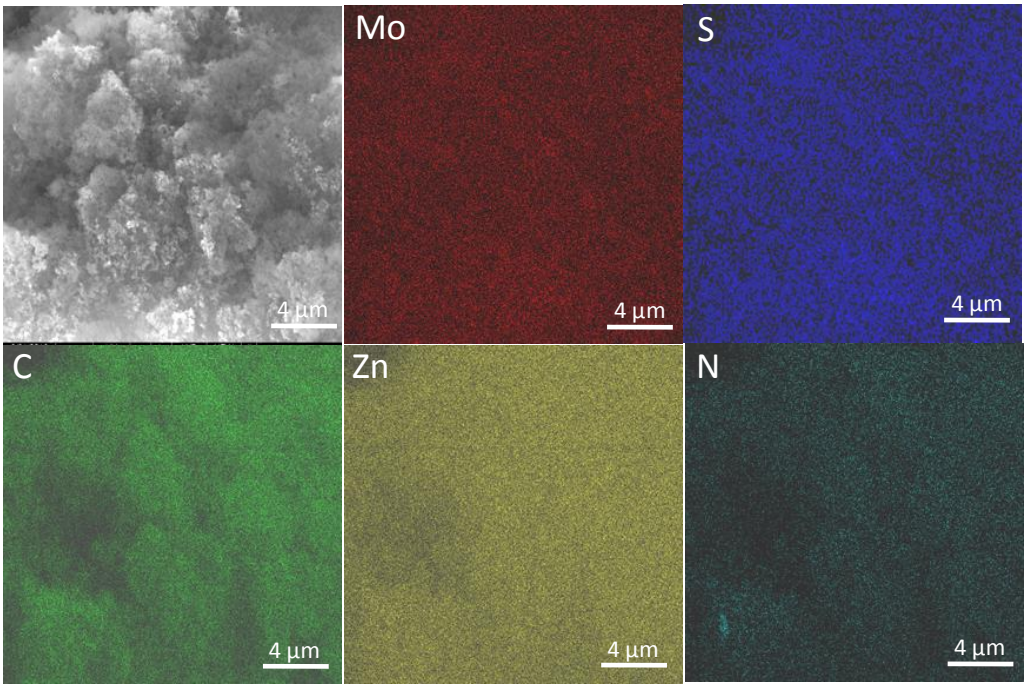

Figure 1. Elemental mapping of the ZM-10 nanocomposites displaying the phase purity with homogeneously distributed MoS_2 throughout the sample.

The PXRD patterns of the ZM nanocomposites along with ZIF-8 are shown in Figure 2. The patterns of the nanocomposites are consistent with the cubic space group of ZIF-8 with an additional reflection at $2\theta = 12.9°$, the intensity of which increases with the MoS_2 content.

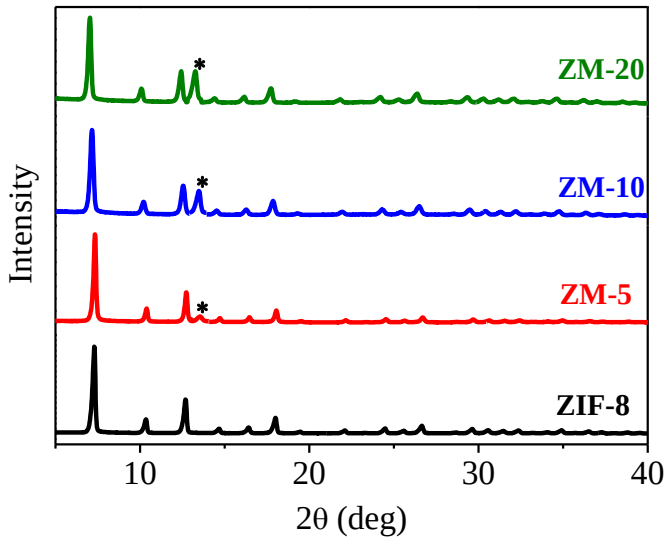

Figure 2. PXRD patterns of ZIF-8 (black), ZM-5 (red), ZM-10 (blue) and ZM-20 (olive) (asterisks indicate the (002) reflection due to MoS_2).

MoS_2 itself exhibits a strong (002) reflection (2θ = 14.8°) corresponding to an inter-layer spacing (~0.67 nm) between the sheets and there is no significant signal in the 2θ range of ~10 to 14°. The additional reflection at 2θ = 12.9° can only arise from the (002) reflection of MoS_2 due to the enhanced inter-layer spacing of the nanosheets caused by the growth of ZIF-8 nanoparticles on the basal-planes.

Evidence for the adsorption of ZIF-8 precursors on the 1T-MoS_2 surface was obtained from zeta potential measurements. Exfoliated 1T-MoS_2 solution shows a negative zeta potential value of −37 mV due to the negatively charged sulfur which increases to +10 mV on addition of the ZIF-8 precursors (zinc nitrate and 2-methylimidazole). The zeta potential was recorded after washing the as obtained sample extensively with methanol and water through vacuum filtration to get rid of any physisorbed species. The increased zeta potential value reveals the adsorption of metal precursors on the MoS_2 basal-plane by forming Zn–S bonds. Figure 3a presents the Raman spectra of 1T-MoS_2 along with those of ZM-0 (ZIF-8), ZM-5 (MoS_2–ZIF-8 containing 5 wt% MoS_2), ZM-10 and ZM-20 nanocomposites. Exfoliated MoS_2 shows bands due to J_1, J_2, and J_3 modes at 156, 236 and 330 cm^{-1}, respectively, and the E^1_{2g} and A_{1g} bands from the 2H-phase are observed at 384 and 405 cm^{-1}, respectively.[24] The ZM nanocomposites show only the bands due to 2H-MoS_2 in addition to bands due to ZIF-8. This is because 1T-MoS_2 which is unstable transforms to 2H-MoS_2 in the case of the formation of the nanocomposite.

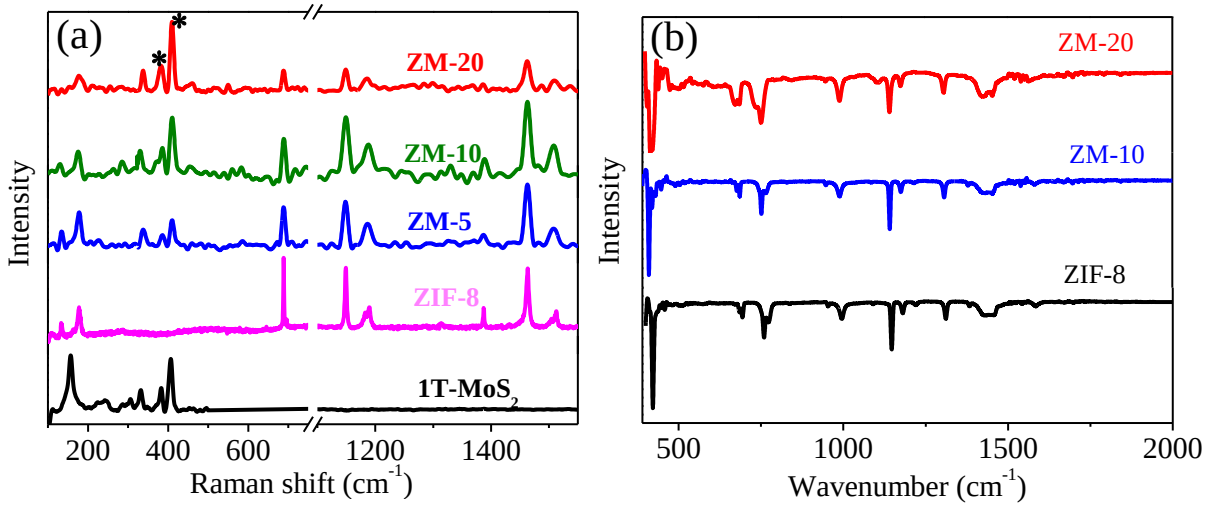

Figure 3. (a) Raman spectra of 1T-MoS_2, ZIF-8, ZM-5, ZM-10 and ZM-20 (black asterisks indicate 2H-MoS_2 bands); (b) Infrared spectra of ZIF-8, ZM-10 and ZM-20.

This behaviour is similar to that reported for the reaction of 1T-MoS_2 with organic halides.[21] Intensities of the bands due to 2H-MoS_2 increase with the MoS_2 content. Attenuated total-reflectance infrared spectra of ZIF-8 and nanocomposites show a strong band at 421 cm^{-1} corresponding to the Zn–N stretching. The bands at 1584 and 1170 cm^{-1} are attributed to the –C=N and –C–N stretching of methyl imidazole.[25] The ZIF-8 bands in the nanocomposites are shifted to slightly lower frequencies due to the interaction between the Zn(II) and sulfur atoms of MoS_2.

Evidence for bonding of sulfur atoms of MoS_2 to the Zn(II) in the nanocomposites is obtained from XPS. The S (2p) core level spectrum of MoS_2 shows a single peak centered at 162.2 eV (Figure 4a). On the other hand, the nanocomposites exhibit an additional band at a higher binding energy of 165.3 eV due to the sulfur coordinated to Zn(II) as shown in Figure 4b in the case of ZM-10.[26] The degree of surface functionalization can be obtained by calculating the ratio of the integrated signal intensity of the S2p component at high energy to the total integrated S 2p core level signal. The ratio was found to be 42% in the case of ZM-10 indicating that 42% sulfur atoms of MoS_2 are covalently linked with ZIF-8. Thus, XPS as well as Raman and IR spectra along with PXRD data establish the growth of ZIF-8 nanocrystals on MoS_2 basal planes by forming the Zn–S bond.

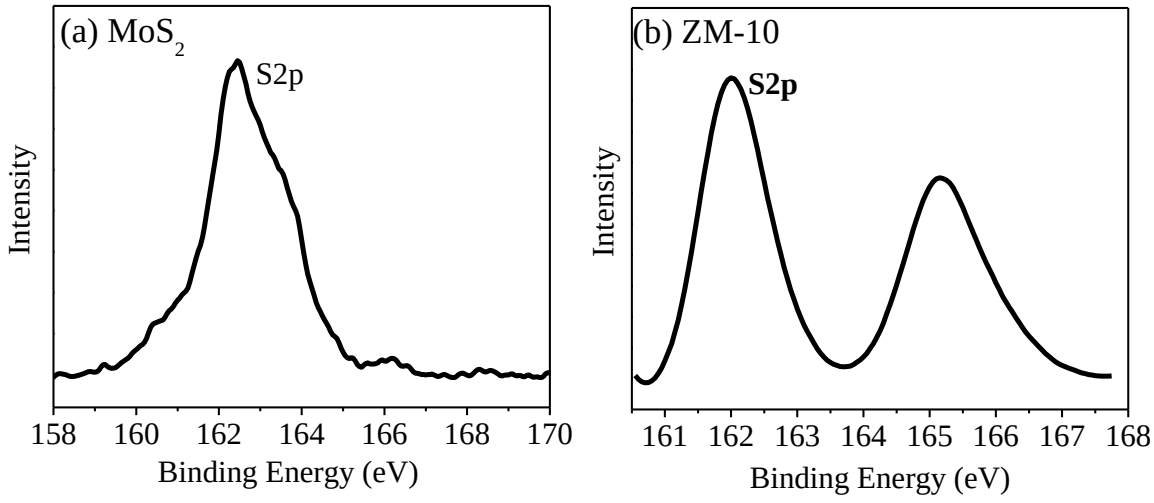

Figure 4. High resolution S (2p) X-ray photoelectron spectrum of (a) MoS_2 and (b) ZM-10.

The homogeneity and morphology of the nanocomposites were examined using field emission scanning electron microscopy (FESEM) and transmission electron microscopy (TEM) images (Figure 5). ZIF-8 nanocrystals have rhombic dodecahedral morphology with an average particle size of 100–150 nm, whereas exfoliated MoS_2 has a wrinkled morphology due to the thin-layers (Inset of Figure 5a). Figure 5a shows a FESEM image of ZIF-8 while Figure 5b shows the FESEM image of the ZM-5 nanocomposite. We see that the MoS_2 sheets are embedded between the ZIF-8 nanocrystals.

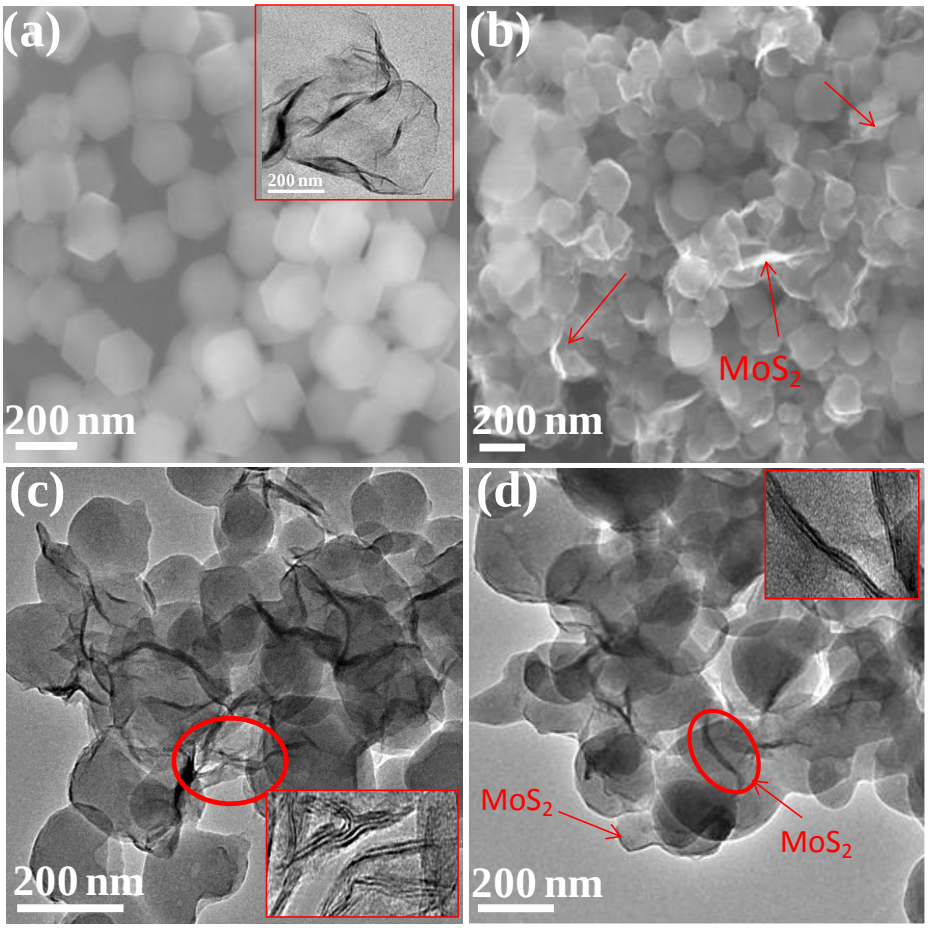

Figure 5. FESEM images of (a) ZIF-8 (Inset: TEM Image of MoS_2) and (b) ZM-5, TEM images of (c) ZM-5 (inset HRTEM) and (d) ZM-20 (inset HRTEM showing the (002) fringes of MoS_2).

Figure 5c shows a TEM image of ZM-5, demonstrating that the ZIF-8 nanocrystals grow on the basal plane of MoS_2 sheets, and the particle morphology changes from rhombic dodecahedral to spherical. The ZM-20 nanocomposite with a high MoS_2 content displays wrapping of ZIF-8 nanocrystals by thin sheets of MoS_2 (Figure 5d). Thus, electron microscopy images provide evidence for the growth of ZIF-8 nanocrystals on the MoS_2 basal-plane. A change in the morphology of ZIF-8 (rhombic dodecahedral to spherical) in the nanocomposites is an indication that there is an interaction between the components. A similar modification in the morphology is observed in the case of carbon nanotubes (CNTs) and graphene nancomposites with ZIF-8.[9, 27]

Surface areas of MoS_2, ZIF-8 and ZM nanocomposites were determined by using N_2 adsorption–desorption measurements at 77 K. The N_2 isotherms of ZIF-8 and ZM nanocomposites show microporous type-1 adsorption behaviour (Figure 6a) with the Brunauer–Emmet–Teller (BET) surface areas of ZM-5, ZM-10, and ZM-20 being 1045, 990 and 825 $m^2\ g^{-1}$, respectively. MoS_2 has a low surface area of 90 $m^2\ g^{-1}$ while ZIF-8 shows a surface area of 1180 $m^2\ g^{-1}$. There is a decrease in surface area with the increasing MoS_2 content in the ZM nanocomposites as expected. We have measured the CO_2 uptake of the ZM nanocomposites at 275 K and 1 atm.

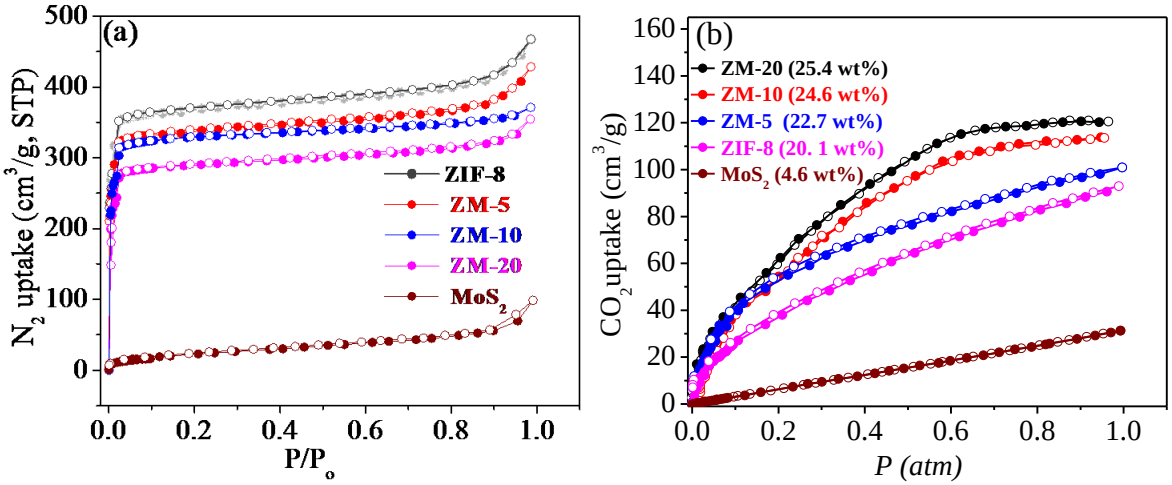

Figure 6. (a) N_2 adsorption profile of MoS_2, ZM-20, ZM-10, ZM-5 and ZIF-8 at 77 K; (b) CO_2 adsorption profile of MoS_2, ZIF-8, ZM-5, ZM-10 and ZM-20 at 275 K, 1 atm.

Interestingly, the uptake of the nanocomposites is higher than that of ZIF-8, the actual values for ZM-5, 10, and 20 being 22.7, 24.6 and 25.4 wt% respectively, compared to 20.1 wt% in the case of ZIF-8 (Figure 6b). MoS_2 shows a CO_2 uptake of only 4.6 wt%. The enhancement in CO_2 uptake is attributed to the combined effect of ZIF-8 and MoS_2 with the latter providing additional interaction sites for CO_2. In the literature, edge and defect sites of MoS_2 are depicted as potential sites for CO_2 adsorption.[28] In the nanocomposites one would expect an enhanced interaction from MoS_2 nanosheets due to the more exposed edge sites and increased inter-layer spacing caused by the intercalation of ZIF-8.

On heating the ZM nanocomposites at 900 °C in an inert atmosphere, we obtain ZnS nanoparticles along with MoS_2. The MoS_2–ZnS composite derived by burning ZM-20 exhibits XRD reflections of ZnS in the wurtzite structure along with the MoS_2 reflections (Figure 7a). TEM images reveal the presence of ZnS nanoparticles of ~20–30 nm diameters on the nanosheets (Figure 7c). The elemental composition of the MoS_2–ZnS composites was estimated from energy-dispersive X-ray spectroscopy (EDAX) and XPS analysis. The inset of Figure 7b shows an EDAX spectrum of MoS_2–ZnS obtained by heating ZM-20 confirming the presence of Mo (23 at%), Zn (11 at%), and S (62 at%) with a low content of carbon (4 at%).

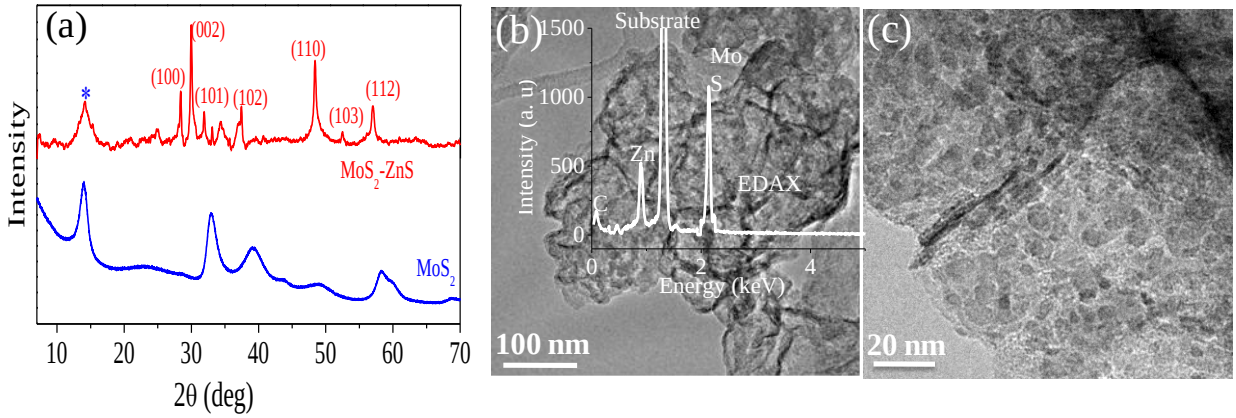

Figure 7. (a) PXRD patterns of MoS_2 and MoS_2–ZnS nanocomposites obtained after heating ZM-20 under an argon atmosphere at 900 °C (asterisks indicate peaks due to MoS_2); (b, c) TEM (inset: EDAX) and HRTEM images showing ZnS nanoparticles on the MoS_2 nanosheet.

The Zn–S covalent bonds in the ZM nanocomposite favors the formation of the MoS_2–ZnS adduct on heating. The high thermal stability of ZnS is another factor that may influence the formation of ZnS on MoS_2 at high temperature.

ZnS is a wide band gap (~3.7 eV) semiconductor exhibiting novel electrical and optical properties. The composites of ZnS with CdS, graphene and other layered materials are reported, which are expected to display enhanced hydrogen evolution characteristics and are known as good electrode materials for lithium-ion batteries.[29, 30] MoS_2 is a promising catalyst for visible-light induced photocatalytic hydrogen generation from water.[31] Considering these properties of MoS_2 and ZnS, we have studied the hydrogen evolution reactions of MoS_2–ZnS composites in the presence of the Eosin Y (EY) dye under visible light illumination. The mechanism of photochemical hydrogen evolution of MoS_2 in the presence of the eosin dye has been reported.[24] While the dye acts as the electron source, the MoS_2–ZnS composite provides active sites for hydrogen generation. Figure 8 shows the yield of H_2 evolved by using ZnS nanoparticles, few-layer MoS_2, and the MoS_2–ZnS nanocomposite obtained by burning ZM-20 (MoS_2–ZIF-8 containing 20 wt% MoS_2). The MoS_2–ZnS composite shows an H_2 evolution rate of 411 μmol h^{-1} g^{-1}, whereas the activities of individual ZnS and MoS_2 are 42 μmol h^{-1} g^{-1} and 68 μmol h^{-1} g^{-1}, respectively. The composite MoS_2–ZnS exhibits an enhancement of 10 and 7 times higher H_2 evolution rates than the individual ZnS and MoS_2 components, respectively. From the above study, it is clear that both MoS_2 and ZnS provide active sites for hydrogen evolution. The energy diagram of hydrogen evolution on the MoS_2–ZnS surface is shown in Scheme 2. Since there is an energy gradient between the conduction band (CB) of ZnS and MoS_2, there is a possibility of electrons moving from the CB of ZnS to MoS_2 (green arrow).[32] Furthermore, the CB energy gradient between ZNS and MoS_2 is less compared to the water reduction potential, and chances of electrons moving from the CB of ZnS to MoS_2 are favored resulting in charge separation.[33] In the case of individual ZnS and MoS_2, there are more chances of electron quenching on the surface which occurs at a high rate compared to the red-ox reaction, and hence exhibit lower activity.[23, 34] Additionally, in the MoS_2–ZnS composites due to the intimate contact between ZnS and MoS_2 particles the possibility of electron quenching on individual components decreases greatly, thereby giving higher yields.

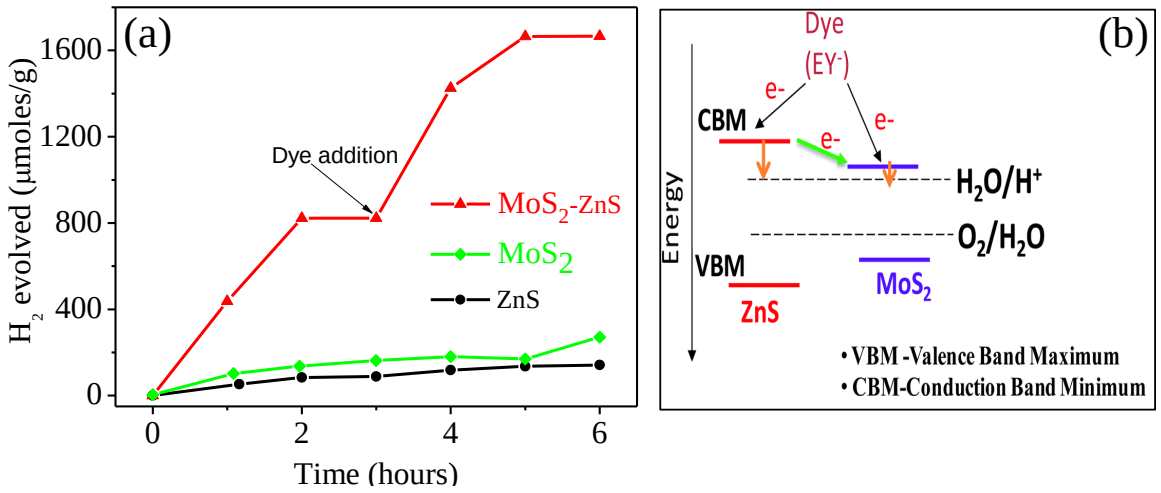

Figure 8. (a) H_2 evolved per gram of the catalyst by ZnS nanoparticles, few-layer MoS_2 and MoS_2–ZnS nanocomposite obtained after heating ZM-20 in argon at 900 °C (arrow indicates the dye addition point); (b) **Scheme 2** Schematic illustration of the possible pathways of electron transfer from the dye to the hydrogen evolution sites on the MoS_2–ZnS surface (green arrow indicates charge transfer at the MoS_2–ZnS interface).

4.2.5: Conclusions

We have successfully prepared MoS_2–ZIF-8 nanocomposites wherein ZIF-8 is chemically bonded to MoS_2 nanosheets by forming Zn–S bonds. The use of metallic 1T-MoS_2 nanosheets is crucial for the synthesis of nanocomposites since they contain excess negative charges on sulfur atoms which undergo coordination modulation with the ZIF-8 metal precursors. The change in the morphology of ZIF-8 nanocrystals from rhombic dodecahedral to spherical in nanocomposites indicates that there is an interaction between the individual components. Interestingly, CO_2 uptake by the MoS_2–ZIF-8 nanocomposites is higher than that of ZIF-8. On heating MoS_2–ZIF-8 nanocomposites at high temperatures, we obtained MoS_2–ZnS adducts, where ZIF-8 and MoS_2 act as sacrificial sources of sulfur and zinc, respectively. MoS_2–ZnS exhibits enhanced hydrogen evolution activity compared to individual MoS_2 and ZnS nanoparticles. The enhanced activity is attributed to the MoS_2–ZnS

interface which acts as the charge separating layer, thereby increasing the chances of electron transfer from the dye to water through hydrogen evolution sites.

4.2.6: References

1. H. Furukawa, N. Ko, Y. B. Go, N. Aratani, S. B. Choi, E. Choi, A. Ö. Yazaydin, R. Q. Snurr, M. O'Keeffe, J. Kim, O. M. Yaghi, *Science* **2010,** *329,* 424.
2. Y. Lin, Q. Yan, C. Kong, L. Chen, *Sci. Rep.* **2013,** *3.*
3. E. P. Dillon, C. A. Crouse, A. R. Barron, *ACS Nano* **2008,** *2,* 156.
4. F. Su, C. Lu, W. Cnen, H. Bai, J. F. Hwang, *Sci. Total Environ.* **2009,** *407,* 3017.
5. F. Su, C. Lu, H.-S. Chen, *Langmuir* **2011**, *27,* 8090.
6. R. Kumar, V. M. Suresh, T. K. Maji, C. N. R. Rao, *Chem. Commun.* **2014**, *50*, 2015.
7. R. Kumar, K. Gopalakrishnan, I. Ahmad, C. N. R. Rao, *Adv. Funct. Mater*. **2015**, *25*, 5910.
8. K. Pramoda, U. Gupta, I. Ahmad, R. Kumar, C. N. R. Rao, *J. Mater. Chem. A*, **2016**, *4*, 8989.
9. R. Kumar, K. Jayaramulu, T. K. Maji, C. N. R. Rao, *Chem. Commun*. **2013**, *49*, 4947.
10. D. Kim, D. W. Kim, W. G. Hong, A. Coskun, *J. Mater. Chem. A* **2016**, *4*, 7710.
11. A. Huang, Q. Liu, N. Wang, Y. Zhu, J. Caro, *J. Am. Chem. Soc.* **2014**, *136***,** 14686.
12. R. Kumar, D. Raut, I. Ahmad, U. Ramamurty, T. K. Maji, C. N. R. Rao, *Mater. Horiz.* **2014**, *1,* 513.
13. K. S. Park, Z. Ni, A. P. Cote, J. Y. Choi, R. Huang, F. J. Uribe-romo, H. K. Chae, M. O'Keeffe, O. M. Yaghi, *Proc. Natl. Acad. Sci. U. S. A.* **2006**, *103*, 10186.
14. Z. Jiang, H. Sun, Z. Qin, X. Jiao, D. Chen, *Chem. Commun.* **2012**, *48*, 3620.
15. J. Cravillion, S. Munzer, S, -J. Lohmeier, A. Feldhoff, K. Huber, M. Wiebeke, *Chem. Mater.* **2009**, *21*, 1410.
16. R. Kumar, D. Raut, U. Ramamurty, C. N. R. Rao, *Angew. Chem. Int. Ed*. **2016**, *55*, 7857.
17. (a) W. Lin, W. J. Rieter, K. M. L. Taylor, *Angew. Chem. Int. Ed.* **2009**, *48*, 650; (b) M. Spokoyny, D. Kim, A. Sumrein and C. A. Mirkin, *Chem. Soc. Rev.*, 2009, **38,** 1218; (c) D. Kim, D. W. Kim, W. G. Hong, *J. Mater. Chem. A* **2016**, *4*, 7710; (d) Y. Wang, Y. Zhang, C. Hou, M. Liu, *RSC Adv.* **2015**, *5***,** 98260.

18. (a) H. J. Lee, W. Cho, S. Jung, M. Oh, Adv. Mater. **2009**, *21*, 674; (b) O. K. Farha, A. M. Spokoyny, K. L. Mulfort, S. Galli, J. T. Hupp, C. A. Mirkin, *Small* **2009**, *5*, 1727; (c) T. Tsuruoka, S. Furukawa, Y. Takashima, K. Yoshida, S. Isoda, S. Kitagawa, *Angew. Chem. Int. Ed.* **2009**, *48***,** 4739.
19. (a) X. Huang, B. Zheng, Z. Liu, C. Tan, J. Liu, H. Li, J. Chen, X. Zhang, Z. Fan, W. Zhang, Z. Guo, F. Huo, Y. Yang, L. Xie, W. Huang, H. Zhang *ACS Nano* **2014**, *8*, 8695; (b) Q. Weng, X. Wang, C. Zhang, X. Jiang, Y. Bando, D. Goldberg *J. Mater. Chem. A* **2015**, *3***,** 3097.
20. X. Chen, A. R. McDonald, *Adv. Mater*. **2016**, DOI:10.1002/adma.201505345.
21. D. Voiry, A. Goswami, R. Kappera, C. Carvalho C. Silva, D. Kaplan, T. Fujita, M. Chen, T. Asefa, M. Chhowalla, *Nat. Chem.* **2015**, *7*, 45.
22. K. C. Knirsch, N. C. Berner, H. C. Nerl, C. S. Cucinott, Z. Gholamvand, N. McEvoy, Z. Wang, I. Abramovic, P. Vecera, M. Halik, S. Sanvito, G. S. Duesberg, V. Nicolosi, F. Hauke, A. Hirsch, J. N. Coleman, C. Backes, *ACS Nano* **2015**, *9***,** 6018.
23. G. Eda, H. Yamaguchi, D. Voiry, T. Fujita, M. Chen, M. Chhowalla, *Nano Lett.* **2011**, *11*, 5111.
24. U. Gupta, B. S. Naidu, U. Maitra, A. Singh, S. N. Shirodkar, U. V. Waghmare, C. N. R. Rao, *APL Mater.* **2014**, *2*, 092802.
25. M. Jian, B. Liu, R. Liu, J. Qu, H. Wang, X. Zhang, *RSC Adv.* **2015**, *5*, 48433.
26. C. Backes, N. C. Berner, X. Chen, P. Lafargue, P. Laplace, M. Freeley, G. S. Duesberg, J. N. Coleman, A. R. McDonald, *Angew. Chem. Int. Ed.* **2015**, *54*, 2638.
27. Y. Yang, L. Ge, V. Rudolph, Z. Zhu *Dalton Trans.* **2014**, *43***,** 7028.
28. (a) N. Yu, L. Wang, M. Li, X. Sun, T. Hou, Y. Li, *Phys. Chem. Chem. Phys.* **2015**, *17*, 11700; (b) L. Wang, Z. Xu, W. Wang, X. Bai, *J. Am. Chem. Soc.* **2014**, *136***,** 6693; (c) S. Zhao, J. Xue, W. Kang, *Chem. Phy. Lett*. **2014**, *595*, 35.
29. D. Jiang, Z. Sun, H. Jia, D. Lu, P. Du, *J. Mater. Chem. A* **2016**, ***4***, 675.
30. G. D. Park, S. H. Choi, J. Lee, Y. C. Kang, *Chem. Eur. J* **2014**, *20*, 12183.
31. A. B. Laursen, S. Kegnaes, S. Dahl, I. Chorkendorff, *Energy Environ. Sci.* **2012**, *5*, 5577.

32. J. Li and N. Wu, *Catal. Sci. Technol.*, 2015, **5**, 1360.

33. B. Zhu, B. Lin, Y. Zhou, P. Sun, Q. Yao, Y. Chen, B. Gao, *J. Mater. Chem. A* **2014**, *2*, 3819.

34. Y. Zhu, Q. Ling, Y. Liu, H. Wang, Y. Zhu, *Phys. Chem. Chem. Phys.* **2015,** *17*, 933.

4.3: Nanocomposites of MoS_2 with Reduced Graphene Oxide for the Oxygen Reduction Reaction

Summary*

The present study demonstrates the use of MoS_2-RGO composites as non-Pt cathode catalysts for the oxygen reduction reaction (ORR) in alkaline medium. To assess the ORR activity, cyclic voltammetry and rotating disk electrode measurements have been carried out at different MoS_2-RGO electrodes (2 : 1 and 1 : 2). The best results are obtained with the MoS_2-RGO (1:2) composite with the number of electron transferred being ~ 3.8. The excellent performance of the MoS_2-RGO (1:2) composite is attributed to the combined effect of good electrical conductivity of RGO, and unique surface properties of MoS_2 as well as of RGO.

A papers based on this work has been published *in Nanomater. Energy (2014).*

4.3.1: Introduction

The oxygen reduction reaction (ORR) is one of the important processes dictating the performance of fuel cells and metal-air batteries [1-3] besides several biological reactions. One of the limitations in the commercialization of fuel cells is the sluggish ORR kinetics found with various electrode materials.[3-5] It has been reported that the kinetics of ORR is 6 orders slower than fuel oxidation in several cases.[6, 7] The ORR proceeds through different mechanisms depending on the nature of the catalyst, pH of the electrolyte, temperature etc. A direct, four-electron ORR to water is considered efficient as compared to the two-electron reduction to H_2O_2. This necessitates the development of highly active catalysts which reduce oxygen in an efficient $4e^-$ pathway. Platinum (Pt) has been widely used as the cathode catalyst in many electrochemical devices. However, the high cost and the limited abundance of Pt restricts its use. Furthermore, when Pt is supported on conductive carbon, the catalyst leaches out due to the corrosion of carbon support in aggressive environments. This has prompted a search for Pt-free catalysts for ORR. The non-Pt based materials reported for ORR include transition metal carbides,[8, 9] transition metal nitrides,[10-12] transition metal oxides[13-15] and transition metal chalcogenides.[16, 17]

Graphene–like two–dimensional (2D) transition–metal dichalcogenides (TMDs) have been widely studied for various energy storage and conversion applications due to their intriguing properties.[18-20] Among 2D layered TMDs, molybdenum disulfide (MoS_2) is one of the most promising semiconductors due to its inherent, thickness–dependent band gap, and abundance in nature as molybdenite.[21-23] MoS_2 monolayer is formed by a stack of hexagonal layers of molybdenum atoms sandwiched between two layers of sulfur atoms (S–Mo–S) through weak van der Waals forces. Various techniques have been developed to synthesize the ultrathin MoS_2 nanosheets, such as chemical vapor deposition[24] and hydrothermal synthesis.[25] The unique properties render MoS_2 nanomaterials promising in various applications such as catalysis, sensing, energy storage and conversion devices.[26, 27] Compared with the extensive research on HER performance of MoS_2 nanosheets, only few experimental studies have explored the potential applications of MoS_2 nanosheets for ORR due to their low electronic conductivity.

Construction of hybrid structure between MoS_2 and conductive carbonaceous materials is considered as an effective strategy for improving the conductivity and stability of the MoS_2-based electrode materials.[28-32] In general, carbonaceous materials in nanocomposite electrode materials are anticipated to serve dual functions as conducting agents to promote the electron transport in the poorly conductive MoS_2, and probably more importantly as structure directing agents to enhance the stability of high-surface-energy MoS_2 (e.g. ultrathin MoS_2 nanosheets) by curbing restacking and overgrowth. In these regards, hybrid nanocomposites of MoS_2 with carbonaceous supports, in which the nanostructured MoS_2 are assembled onto or embedded into the conductive carbon matrix, such as amorphous carbon, carbon spheres, carbon nanotubes, graphene oxide (GO) and interconnected three dimensional (3D) graphene networks[33-37] were fabricated to improve the activity and stability of MoS_2-based materials. Among the conductive carbon matrices, graphene is believed as one of the most promising candidates due to its high electric conductivity, high adsorption of photo-irradiation, good flexibility and high chemical stability. In addition, graphene with unique 2D microstructure and surface chemistry is capable of restraining the over growth of guest species for preparation of ultrathin/ultra-tiny nanostructures, beneficial to more active sites and enhanced reaction kinetics. For example, Chen and coworkers reported a facile in-situ solution-phase reduction method for growing MoS_2 layers on graphene nanosheets to form face-to-face packed hybrid nanosheets, which exhibited extraordinary capacity, excellent rate capability and cycling stability as an anode material for LIBs.[28] Ajayan and coworkers reported a hydrothermal approach to grow MoS_2 atomic layers in situ onto the surface of GO, forming 3D graphene-backboned hybrid architectures.[29] Zhang and coworkers synthesized MoS_2 flakes-coated 3D graphene network by a facile chemical-vapor-deposition method.[30] As a proof of concept, all these hybrid 3D MoS_2-graphene architectures show excellent electrochemical performance.[29, 30]

4.3.2: Scope of the present investigations

Oxygen-reduction reaction (ORR) has great importance in energy storage applications as it dictates the operation of fuel cells and Li-air batteries. The slow rate of ORR is the major challenge in commercialization of fuel cells and there is real need for catalysts that reduce oxygen efficiently via the $4e^-$ pathway. Despite the tremendous efforts

dedicated to graphene based electrocatalyst for ORR, the research on 2D MoS_2 is still limited due to lower electronic conductivity. Stacking of MoS_2 layers on conductive graphene surface leads to decrease in resistance connection for the electrons transfer from the substrate to the active sites. We considered that composites of MoS_2 with RGO could show superior ORR activity by virtue of their enhanced surface area and higher electrical conductivity. In view of this, we have examined the ORR activity of the MoS_2-RGO hybrid modified glassy carbon electrode in basic media.

4.3.3: Experimental section

Preparation of Graphene Oxide: Graphite flakes were dispersed in a mixture of sulfuric and $NaNO_3$, subsequently cooled to ice cold temperature. To this $KMnO_4$ was added after 10 min. The obtained mixture was stirred in room temperature for 10 min. Distilled water (150 mL and 420 mL) was added in sequential steps followed by the addition of H_2O_2.

Preparation of MoS_2 Nanosheets: In a typical synthesis, 0.1 g $(NH_4)_6Mo_7O_{24}{\cdot}6H_2O$ (ammonium heptamolybdate) and 0.3 g NH_2CSNH_2 (thiourea) mixture was dissolved in 17 mL distilled water. The resultant solution was transferred into a stainless steel autoclave and heated in an oven at 200 °C for 72 hours. The product was washed with excess water and dried at 70 °C. The obtained nanosheets consisted of 3–7 layers.

Preparation of MoS_2-RGO Composites: MoS_2-RGO composites of different compositions were prepared by varying the weight ratios of Mo and graphene. To prepare MoS_2-RGO (1 : 2), 6 mL of (20 mg/mL) GO solution was ultrasonicated with 100 mL distilled water for half an hour. To this, '0.63' mg of $(NH_4)_6Mo_7O_{24}{\cdot}6H_2O$ and 0.2 g of NH_2CSNH_2 were added and stirred for an hour. The mixture was heated in an oven at 200 °C for 24 hours in a stainless steel autoclave. The product was washed and dried. Under the conditions of experiments, GO gets reduced to RGO. RGO had 3–5 layers on average. The specific surface area of graphene and the MoS_2-RGO composites calculated by the BET method are 120 and 147 m^2/g respectively.

Preparation of Catalyst Ink and Electrode Modification: 1 mg of MoS_2-RGO was dispersed in 1 mL of 1 : 1 water-ethanol mixture along with 5 µL of Nafion and sonicated for 60 min. Glassy carbon electrode (precleaned) was modified by drop casting the catalyst ink 5 µL and air dried, used for different measurements.

4.3.4: Results and Discussion

The morphology of the MoS_2-RGO composite was examined by electron microscopy.

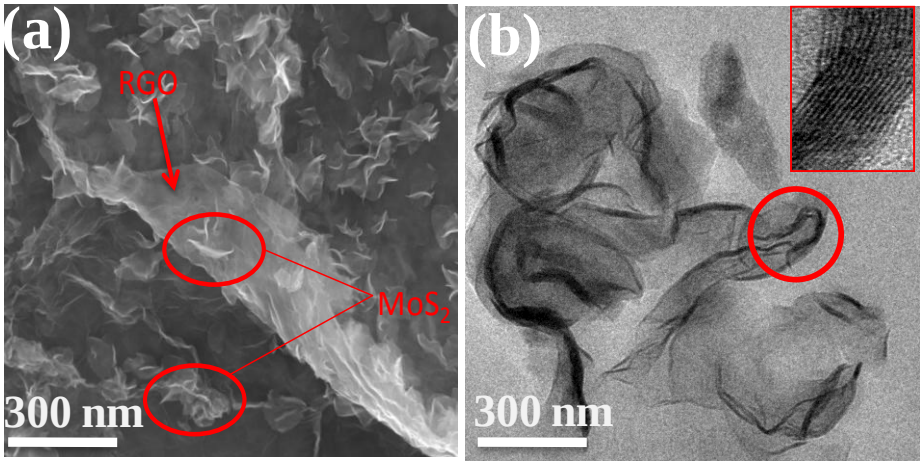

Figure 1. a) FEEM and (b) TEM image (Inset: HRTEM image) of MoS_2–RGO composite.

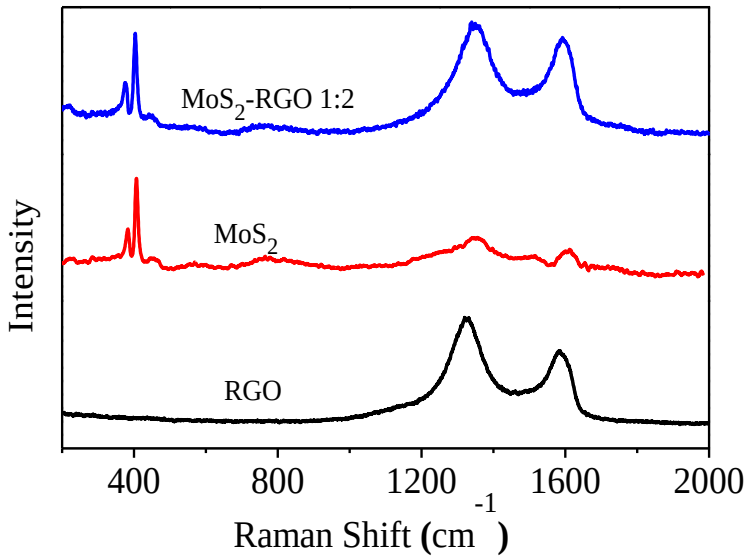

Figure 2. Raman spectra of RGO, MoS_2 and MoS_2-RGO (1:2) composite.

FESEM image of MoS_2-RGO indicates vertically aligned MoS_2 nanosheets were grown on RGO (Figure 1a) while TEM images show MoS_2 sheets embedded in RGO matrix with an interlayer spacing of ~ 0.62 nm (Figure 1b). The Raman spectrum of the MoS_2-RGO composite shows the G-band at 1594 cm^{-1} and D-band at 1350 cm^{-1}. The characteristic bands due to the E^1_{2g} and A_{1g} modes of MoS_2 are clearly observed in the MoS_2-RGO (1:2) composite as shown in Figure 2.

To evaluate the oxygen reduction reaction activity of MoS_2, RGO and MoS_2-RGO composite, CV measurements were performed in 0.1 M KOH saturated with O_2 and N_2 as shown in Figure 3a. In KOH solutions saturated with O_2, MoS_2-RGO and RGO modified electrodes shows a pronounced ORR peaks indicating the reduction of oxygen, whereas no response was observed in N_2 saturated KOH solutions. The ORR onset peak potential of MoS_2-RGO is more positive than that of pristine RGO or MoS_2.

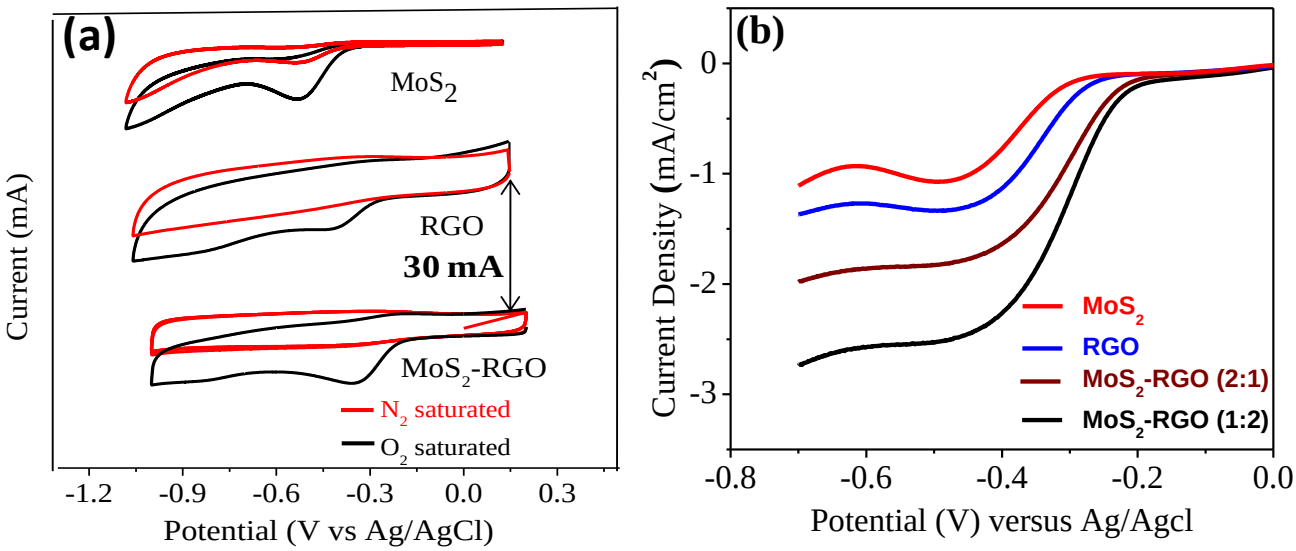

Figure 3. (a) Cyclic voltammograms of MoS_2, RGO and MoS_2-RGO (1:2) in nitrogen and oxygen purged 0.1 KOH solutions. (b) Linear sweep voltammograms of RGO and MoS_2-RGO composites measured at 1600 rpm (5 mV s^{-1}).

Rotating disk electrode (RDE) measurements were performed in linear sweep voltammetry (LSV) mode to gain insights into the ORR mechanism and reaction kinetics. Figure 3b shows LSV voltammograms of MoS_2, RGO, MoS_2-RGO (1:2 and 2:1) composites.

LSV polarization curves of MoS_2-RGO composites (1:2 and 2:1) demonstrate better ORR activities than either RGO or MoS_2 alone. Such enhanced performance is attributed to the synergistic effect between RGO and MoS_2. More interestingly, MoS_2-RGO (1:2) shows the most positive onset potential when compared with MoS_2-RGO (2:1). Just the right proportion of MoS_2 growing on RGO gives the optimum efficiency of electron transfer from MoS_2 to RGO thereby enhances ORR activity. Figure 4a shows that ORR current density of MoS_2-RGO (1:2) modified GCE increases with the rotation speed due to high availability of oxygen at the electrode interface. The Koutechy-Levich (K-L) plots for MoS_2-RGO (1:2) modified GCE at various potentials is shown in Figure 4b. The electron transfer number MoS_2-RGO (1:2) is ~ 3.8, confirming the 4 e- pathway for the ORR on MoS_2-RGO modified GCE.

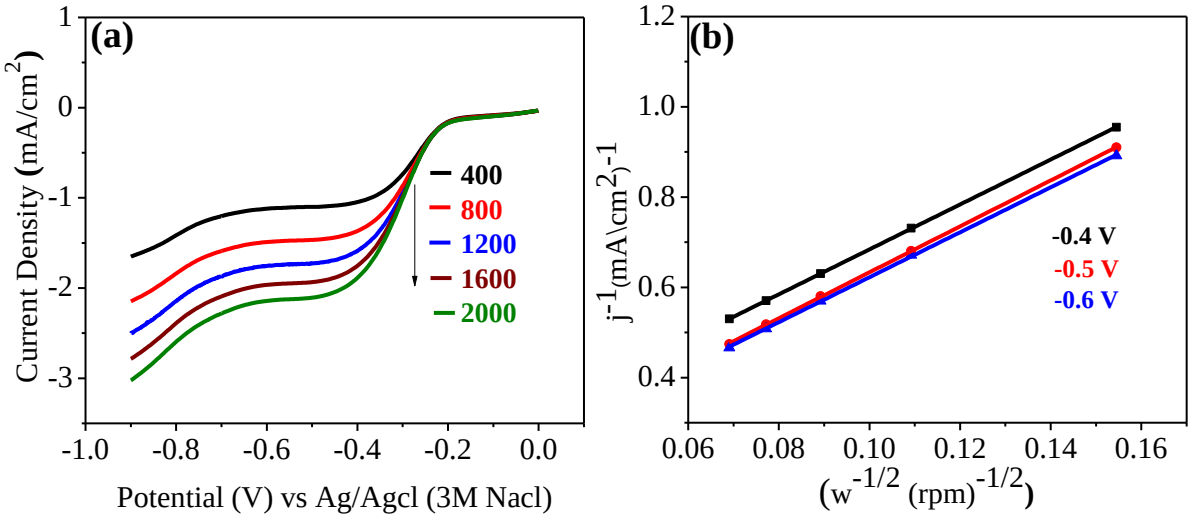

Figure 4. (a) Linear sweep voltammograms at different rotation speeds and (b) Koutechy-Levich plots of MoS_2-RGO (1:2) composite.

4.3.5: Conclusions

The MoS_2-RGO composites have been successfully prepared and used for the oxygen reduction reaction (ORR). MoS_2–RGO composite with the MoS_2:RGO ratio of 1:2 exhibits superior ORR activity compared to 2:1. The high electrocatalytic activity of MoS_2-RGO (1:2) composite is attributed to the enhanced electronic conductivity, large surface area and available edges which can facilitate electron transfer. It is noteworthy that MoS_2 provides a good reducing surface for the reduction of protons to hydrogen.

4.3.6: References

1. H. A. Gasteiger, N. M. Marković, *Science* **2009**, *324*, 48.
2. V. R. Stamenkovic, B. Fowler, B. S. Mun, G. Wang, P. N. Ross, C. A. Lucas, N. M. Marković, *Science* **2007**, *315*, 493.
3. P. G. Bruce, S. A. Freunberger, L. J. Hardwick, J.-M. Tarascon, *Nat. Mater.* **2012**, *11*, 19.
4. M. K. Debe, *Nature* **2012**, *486*, 43.
5. S. Y. Wang, S. P. Jiang, T. J. White, J. Guo, X. Wang, *J. Phys. Chem. C* **2009**, *113*, 18935.
6. W. Xiong, F. Du, Y. Liu, A. Perez, M. Supp, T. S. Ramakrishnan, L. Dai, L. Jiang, *J. Am. Chem. Soc.* **2010**, *132*, 15839.
7. A. J. Appleby, F. R. Foulkes, Fuel cell handbook, an Nostrand, New York, 1989.
8. H. Meng, P. K. Shen, *Electrochem. Commun.* **2006**, *8*, 588.
9. V. Kiran, K. Srinivasu, S. Sampath, *Phys. Chem. Chem. Phys.* **2013**, *15*, 8744.
10. J. Giner, L. Swette, *Nature* **1966**, *211*, 1291.
11. S. Isogai, R. Ohnishi, M. Katayama, J. Kubota, D. Y. Kim, S. Noda, D. Cha, K. Takanabe, K. Domen, *Chem. Asian J.* **2012**, *7*, 286.
12. J. Chen, K. Takanabe, R. Ohnishi, D. Lu, S. Okada, H. Hatasawa, H. Morioka, M. Antonietti, J. Kubota, K. Domen, *Chem. Commun.* **2010**, *46*, 7492.
13. Y. Gorlin, C.-J. Chung, D. Nordlund, B. M. Clemens, T. F. Jaramillo, *ACS Catal.* **2012**, *2*, 2687.
14. F. Cheng, J. Shen, B. Peng, Y. Pan, Z. Tao, J. Chen, *Nat. Chem.* **2011**, *3*, 79.
15. J. Xu, P. Gao, T. S. Zhao, *Energy Environ. Sci.* **2012**, *5*, 5333.
16. Alonso-Vante, Nicolas, *Chem. Phys. Chem*. **2010**, *11*, 2732.
17. H. Wang, Y. Liang, Y. Li, H. Dai, *Angew. Chem., Int. Ed.* **2011**, *50*, 10969.
18. R. R. Haering, J. A. R. Stiles, K. Brandt, (Ed.: US Patent 4224390), **1980.**
19. G. Du, Z. Guo, S. Wang, R. Zeng, Z. Chen, H. Liu, *Chem. Commun.* **2010**, *46*, 1106.
20. C. Feng, J. Ma, H. Li, R. Zeng, Z. Guo, H. Liu, *Mater. Res. Bull.* **2009**, *44*, 1811.
21. J. M. Soon, K. P. Loh, *ECS Solid State Lett.* **2007**, *10*, A250.

22. A. Ramadoss, G. S. Kim, S. J. Kim, *New J. Chem.* **2014**, *38*, 2379.
23. H. Li, W. Li, L. Ma, W. Chen, J. Wang, *J. Alloys Compd.* **2009**, *471*, 442.
24. H. F. Liu, S. L. Wong and D. Z. Chi, *Chem. Vap. Deposition* **2015**, *21*, 241.
25. X. Liang, X. Zhang, W. Liu, *J. Mater. Chem. C* **2016**, *4*, 6816.
26. C. N. R. Rao, U. Maitra, U. *Annu. Rev. Mater. Res*. **2015**, *45*, 29.
27. C. N. R. Rao, K. Gopalakrishna, U. Maitra, *ACS Appl. Mater. Interfaces*, 2015, *7*, 7809.
28. K. Chang, W.X. Chen, *Chem. Commun.* **2011,** *47*, 4252.
29. Y.J. Gong, S.B. Yang, Z. Liu, L. Ma, R. Vajtai, P.M. Ajayan, *Adv. Mater*. **2013**, *25*, 3979.
30. X.H. Cao, Y.M. Shi, W.H. Shi, X.H. Rui, Q.Y. Yan, J. Kong, H. Zhang, *Small* **2013,** *9*, 3433.
31. X. Huang, Z.Y. Zeng, H. Zhang, *Chem. Soc. Rev.* **2013**, 42, 1934.
32. T. Stephenson, Z. Li, B. Olsen, D. Mitlin, *Energy Environ. Sci.* **2014**, *7*, 209.
33. K. Bindumadhavan, S.K. Srivastava, S. Mahanty, *Chem. Commun.* **2013**, *49*, 1823.
34. K. Chang, W.X. Chen, *ACS Nano* **2011**, *5*, 4720.
35. S.J. Ding, J.S. Chen, X.W. Lou, *Chem. Eur. J.* **2011,** *17*, 13142.
36. S.K. Park, S.H. Yu, S. Woo, B. Quan, D.C. Lee, M.K. Kim, Y.E. Sung, Y. Piao, *Dalton Trans.* **2013**, *42*, 2399.
37. Y.M. Shi, Y. Wang, J.I. Wong, A.Y.S. Tan, C.L. Hsu, L.J. Li, Y.C. Lu, H.Y. Yang, *Sci. Rep.* **2013,** *3*, 2169.

4.4: Assemblies of Covalently Cross-linked Nanosheets of MoS_2 and of MoS_2–RGO

Summary*

We report the design and synthesis of porous MoS_2 frameworks (PGFs) prepared via covalent functionalization of 1T-MoS_2 with iodobenzene followed by Sonogashira coupling reaction. On the other hand, MoS_2-RGO framework is prepared by iodobenzene functionalization of both MoS_2 and RGO followed by Sonogashira coupling. In contrast to few-layer MoS_2 and RGO, these 3D frameworks show high surface area due to the effect of pillaring. Interestingly, both the frameworks show high CO_2 uptake (11.4 wt% for MoS_2 and 12.8 wt% for MoS_2-RGO assemblies at 298 K up to 1 atm). The hydrogen uptake efficiency values of MoS_2 and MoS_2–RGO assemblies are 0.78 and 0.94 wt%, respectively, at 77 K and 1 atm. The MoS_2 assemblies show superior hydrogen evolution activity over few-layer 2H-MoS_2 possibly due to more exposed edges.

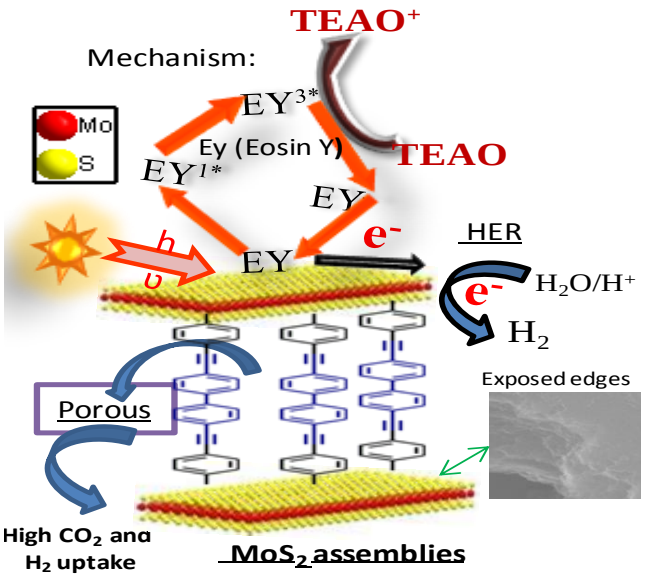

Paper based on this work has been appeared in *J. Mater. Chem. A, (2016).*

4.4.1: Introduction

The functionalization of two-dimensional (2D) materials such as graphene and boron nitride (BN) has received considerable attention and has been used for solubilization and other purposes.[1, 2] Many of the transition-metal chalcogenides (TMDCs) such as MoS_2 and $MoSe_2$ require chemical modifications to make them suitable for a wide variety of applications. Unlike graphene and BN, efforts in the functionalization of 2D sheets of TMDCs materials have been limited owing to the inert nature of their basal-plane.[3-5] Among the chalcogenide family, MoS_2 is special with its unique electronic and optical properties, field-effect transistor characteristics and gas sensing properties.[6, 7] MoS_2 has been found to be a promising catalyst for visible-light induced photocatalytic and photoelectrocatalytic hydrogen generation from water, replacing traditionally used catalysts.[8, 9] Theoretical and experimental studies indicated that the edges sites of MoS_2 are catalytically active while the basal plane remains inert.[5a] Chemical modifications of TMDCs surface is necessary in order to improve their versatility, for example, enhancing solubility in common organic solvents keeps thin-layer characteristics intact by way of avoiding restacking of layers due to van der Waals interactions.

Various surface modification strategies have been reported to enhance the processability as well as the chemical reactivity of MoS_2. For example, covalent functionalization of 2D MoS_2 can be achieved at sulfur defect sites through thiol-terminated ligands.[10, 11] A single-step reaction to exfoliate and functionalize MoS_2 by an organosulfur reaction has been carried out.[12] Thiol groups as in thiophenol chemically grafted to MoS_2 alter the electronic properties significantly.[13] Covalently cross-linked MoS_2–polymer composites have been explored, while surface modification of MoS_2 has been achieved with metal acetates.[14, 15] Nylon-6 polymers covalently linked to MoS_2 show enhancement in thermal and mechanical properties.[16] A more successful effort in forming covalent bonds between organic functional groups and the sulfur atoms of MoS_2 was reported by Chhowalla et al.[3] They carried out the covalent functionalization of MoS_2 starting with the metallic 1T phase of the material, obtained through lithium intercalation followed by exfoliation. The 1T phase is metallic with an octahedral coordination of the Mo atoms unlike the stable semiconducting 2H phase, which has a trigonal-prismatic coordination of the Mo atoms. The functionalization reaction is promoted by an electron transfer between the metallic 1T phase

and the organoiodine reactant to form covalent C−S bonds, leading to marked changes in the optoelectronic and other properties of the MoS_2. A similar reaction involving water-soluble electrophilic diazonium salts with 1T-MoS_2 has been reported, which showed that defects are not required to achieve covalent functionalization.[4] Pratap *et al.*[5b] recently reported the reaction of 1T- and 2H-MoS_2 nanosheets with *para*-substituted iodobenzenes and showed that the electron-withdrawing molecules favour covalent functionalization. First-principles calculations have shown that the benzene derivatives bind much more strongly to the 1T form than to the 2H form.[5b] The work function is considerably tunable with the functionalization of MoS_2 and increases the potential for applications in photocatalysis as well as electronic and optoelectronic devices.

Apart from functionalization, constructing 3D hierarchical architectures based on 2D MoS_2 nanosheets of is another effective approach to solve the problem of re-stacking of layers because of their high surface energy and interlayer van der Waals (vdW) attractions.[6] These architectures are highly desirable for practical applications (for example, high-energy anode materials, catalysis, and hydrogen generation by water splitting). Intercalation of guest molecules such as lithium, sodium and naphthalenide between the van der Waals gap of MoS_2 layers also enhance inter-layer spacing.[5a] Jeffery *et al.*[5b] synthesized assemblies of MoS_2 and RGO arranged in a layer-by-layer fashion (van der Waals heterostructures) by simple exfoliation-coastacking method which exhibit improved catalytic activity.[5c]

In this work, we report the synthesis of covalently cross-linked MoS_2 assemblies and of MoS_2-RGO assemblies obtained by Sonogashira coupling where individual 2D layers are pillared by rigid organic linkers. Pillaring of MoS_2 and RGO nanosheets with organic linkers generates slit shaped pores with the more exposed edge sites (catalytically more active), thereby results in enhanced photochemical HER activity compared to individual MoS_2 and RGO. Both the MoS_2 assemblies and MoS_2-RGO assemblies show enhanced CO_2 and H_2 uptake compared to individual MoS_2 and RGO nanosheets because of the pores generated due to cross-linking.

4.4.2: Scope of the present investigations

MoS_2 has the S–Mo–S sandwich structure in which the hexagonal molybdenum plane is sandwiched between layers of sulfur atoms with the van der Waals interactions between the layers. In most of the practical application such as catalysis, sensoring and lithium-ion battery, the main process in MoS_2 occur either on the surface or on the exposed edge sites which is closely related to the huge specific surface area of 2D layers. However, freshly prepared MoS_2 layers have a tendency to restack during practical applications even while drying process which causes reduction in the number of active sites as well as other unusual properties of ultrathin 2D layers. Constructing hierarchical 3D architectures based on 2D layers would be an efficient approach to solve this problem.[6] Graphene sheets pillared by rigid organic linkers have shown high surface area and good gas storage properties.[17] Covalent pillaring of MoS_2 sheets through rigid organic linkers could generate high surface areas and porous 3D assemblies. While Pd(0) catalyzed C–C coupling has been explored widely[18] to the best of our knowledge there are no reports of its application in chalcogenide chemistry. We have employed the Sonogashira coupling strategy to prepare assemblies of covalently cross-linked MoS_2 sheets by rigid organic linkers. We have also employed this reaction to prepare assemblies of covalently linked sheets of MoS_2 with reduced graphene oxide. Graphene composites of MoS_2 and other layered materials obtained through different synthetic strategies seem to show enhancement in their observed photochemical and electrochemical properties.[19-21] In this study, we have examined the surface area and gas adsorption properties of MoS_2 and MoS_2–RGO assemblies and studied their photochemical catalytic activity for hydrogen generation.

4.4.3: Experimental section

Iodobenzene functionalization of MoS_2 and RGO:

Exfoliated MoS_2 was prepared by the Li-intercalation of bulk MoS_2 with n-butyllithium followed by exfoliation using water as reported elsewhere in the literature.[3] Graphene oxide was prepared by modified Hummer's method[22] and reduction was carried out with hydrazine hydrate to obtain reduced graphene oxide (RGO). Iodobenzene functionalization of MoS_2 was carried out through an in-situ diazotization reaction. Initially, the diazonium salt was

prepared by dissolving 4-iodoaniline (9 mmol) in water through slow addition of conc. hydrochloric acid (HCl). The resultant solution cooled to ice cold temperature, $NaNO_2$ (15 mmol) and 8 ml 20% HCl (6.4 M) were added and allowed to stir until the colour changes to yellow confirming the diazonium salt formation. Exfoliated MoS_2 (100 ml, 1 mg ml^{-1}) in water was added drop-wise to the diazonium salt solution at ice-cold temperature for 2 h followed by stirring at room temperature for 4 h. The product was vacuum filtered and washed with copious amounts of water and acetone. Iodobenzene functionalized RGO (100 mg) prepared by dispersing RGO in 100 ml of 1 wt% dodecylbenzenesulfonate surfactant through probe sonication was added to the diazonium salt of 4-iodoaniline. The above procedure was repeated with RGO.

Synthesis of MoS_2 assemblies and MoS_2-RGO assemblies:

MoS_2 assemblies were prepared by dispersing MoS_2-IBz (20 mg) in N,N-dimethylformamide (DMF) (4 ml) and triethylamine (TEA) (4 ml) through bath sonication in a Schlenk flask. To the resultant dispersion, Pd $(PPh_3)_4$ (5 mg) and CuI (3 mg) were added under stirring and the temperature was increased to 80 °C. 4,4′-Diethynylbiphenyl (50 mg) dissolved in 1 ml DMF in a separate vial was added drop-wise to the reaction mixture in an inert atmosphere and the temperature was increased to 140 °C and was allowed to stir for 12 h. The final product obtained was collected by vacuum filtration and washed several times with hexane and DMF. Further purification was carried out in a Soxhlet extractor with methanol and dried at 60 °C in a vacuum oven. To prepare MoS_2–RGO (2 : 1) assemblies, MoS_2-IBz (14 mg) and RGO-IBz (7 mg) were mixed and dispersed in a solution of DMF (4 ml) and TEA (4 ml). The above mentioned procedure was repeated for the preparation of MoS_2–RGO assemblies.

The MoS_2/RGO (2:1) physical mixture was prepared in the absence of the 4,4′-diethynylbiphenyl linker by dispersing MoS_2-IBz (14 mg) and RGO-IBz (7 mg) in DMF through sonication. The resultant mixture was heated at 140 °C and the final product was collected through vacuum filtration.

Hydrogen evolution measurements:

MoS_2 and MoS_2-RGO assemblies were dispersed in a solution of water and triethanolamine (TEAO) (15% v/v) by sonication, to this 14 μmol of Eosin Y dye was added. The vessel was purged with N_2, and illuminated by 100 W halogen lamp under constant stirring. The evolved gases were manually collected from the headspace and analyzed in thermal conductivity detector (TCD) in a gas chromatograph (PerkinElmer Clarus ARNEL 580GC).

The turn over frequency (TOF) is calculated with respect to catalyst from formula,

$$TOF\ (/h) = \frac{moles\ of\ Hydrogen\ evovled\ per\ hour\ (activity\ of\ the\ catalyst)}{moles\ of\ the\ catalyst\ used}$$

4.4.4: Results and Discussion

The Sonogashira coupling strategy employed by us to pillar iodobenzene functionalized MoS_2 with a 4,4′-diethynylbiphenyl linker is shown in Scheme 1. The scheme shows the various steps involved in synthesizing covalently pillared MoS_2 and MoS_2–RGO assemblies. Initial exfoliation of bulk MoS_2 is achieved with n-butyllithium (n-BuLi) leading to the formation of mono- or bi-layers. Exfoliated MoS_2 is treated with the diazonium salt of 4-iodoaniline prepared in situ at 0 °C to obtain iodobenzene functionalized MoS_2 (MoS_2-IBz). Subsequent steps involve obtaining the MoS_2-IBz dispersion in dry N,N-dimethylformamide (DMF) and cross-linking it with the 4,4′-diethynylbiphenyl (DEBP) linker in the presence of Pd(0) and Cu(+1) salts. The synthetic steps involved in generating the MoS_2–RGO assemblies are similar to those of MoS_2 assemblies, except for the initial reduction of graphene oxide (GO) in hydrazine hydrate to obtain reduced graphene oxide (RGO). Prior to the coupling reaction, iodobenzene functionalized MoS_2 and RGO are mixed and dispersed in dry DMF through sonication (for details see the Experimental section). MoS_2 mentioned in this manuscript refers to exfoliated MoS_2, whereas the MoS_2–RGO assembly refers to the 2 : 1 (wt%) ratio of MoS_2 and RGO.

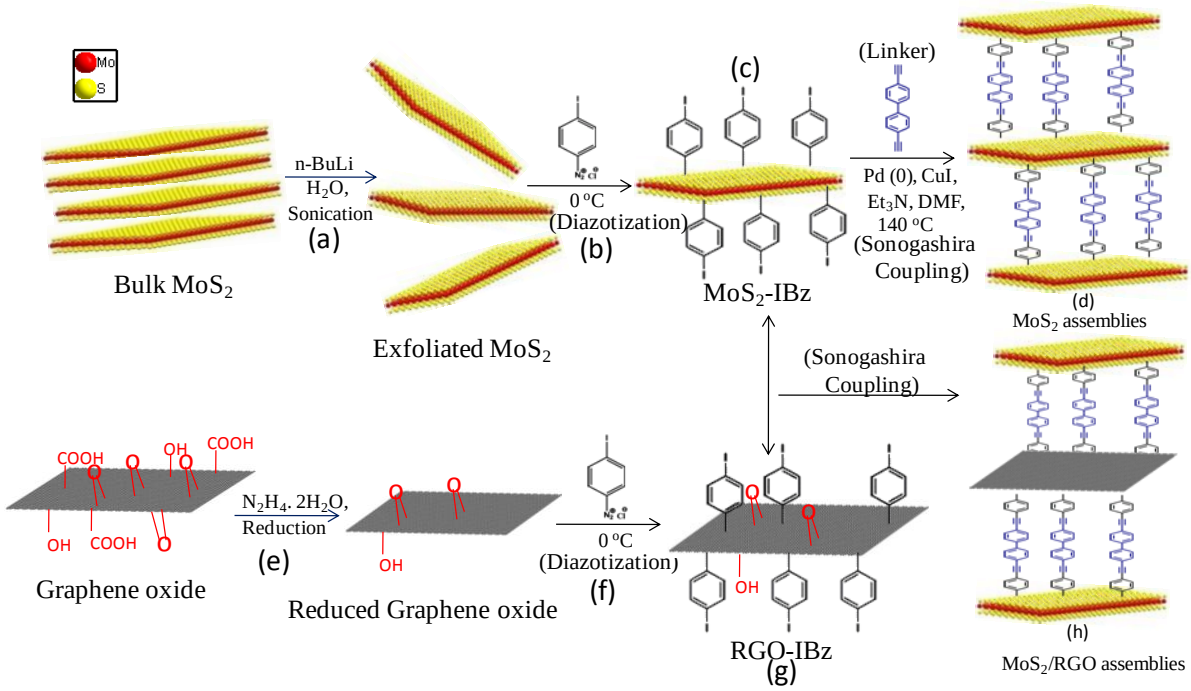

Scheme 1 Schematic representation of the synthesis of MoS_2 and MoS_2–RGO assemblies through Sonogashira coupling; (a) exfoliation of bulk MoS_2 with n-butyllithium, (e) reduction of graphene oxide with hydrazine hydrate, (b and f) diazotization of MoS_2 and reduced graphene oxide (RGO) with 4-iodobenzenediazonium chloride salt, (c and g) iodobenzene functionalized MoS_2 and RGO and (d and h) MoS_2 and MoS_2–RGO assemblies.

Figure 1a shows the Raman spectra of exfoliated MoS_2 and RGO. Exfoliated MoS_2 exhibits characteristic 1T-polytype J_1, J_2, J_3 Raman bands at 156, 236 and 330 cm^{-1} along with E^1_{2g} and A_{1g} modes from the 2H-phase at 384 and 405 cm^{-1}, respectively.[23] Iodobenzene functionalized MoS_2 (MoS_2-IBz, Figure 1b) shows an enhancement in the E^1_{2g} and A_{1g} band intensities with respect to exfoliated MoS_2 due to the partial 1T → 2H transition after functionalization. Raman spectra of RGO show the D and G bands at 1340 and 1590 cm^{-1}, respectively.[24] After functionalization, the relative intensity of the D band increases due to the formation of sp^3 centres (Figure 1b). The MoS_2 assemblies show only the E^1_{2g} and A_{1g} bands of 2H-MoS_2 and a band at 1590 cm^{-1} due to the C=C stretching bond of the linker.[25] In the MoS_2–RGO assemblies, we observed Raman modes of 2H-MoS_2 along with D and G bands of RGO. Enhancement in G-band intensity with respect to RGO is attributed to C=C stretching of the linker.

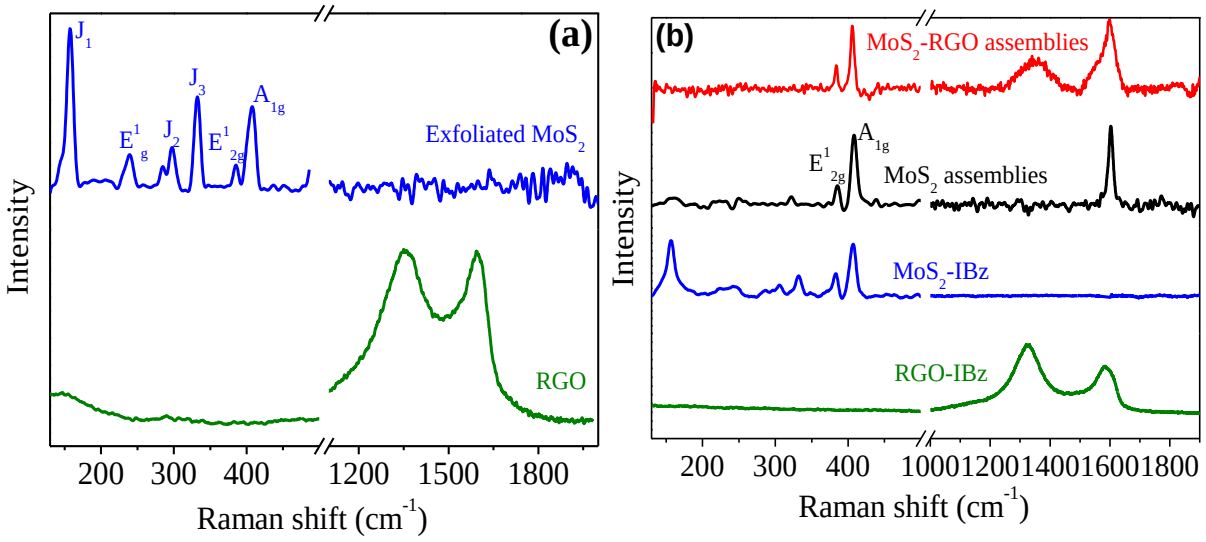

Figure 1. Raman spectra of (a) RGO (green), Exfoliated MoS_2 (black); (b) iodobenzene functionalized RGO (green), iodobenzene functionalized MoS_2 (black), (3) MoS_2 assemblies (blue) and MoS_2–RGO (red) assemblies.

Iodobenzene functionalization of MoS_2 and RGO results in anchoring of the functional groups on both sides of the 2D sheets. Figures 2a, b show the iodine (3d) core level spectrum of MoS_2-IBz and RGO-IBz, showing iodine signals at 620.5 and 632.0 eV due to I ($3d_{5/2}$) and I ($3d_{3/2}$), respectively.[26, 27] Sonogashira coupling involves the oxidative addition of Pd(0) to the C–I bond of iodobenzene to give a Pd(+2) intermediate, followed by the transmetallation of the Pd complex with copper acetylide by eliminating iodine and forming the C–C bond through reductive elimination by regenerating Pd(0).[28] The extent of cross-linking between MoS_2 sheets can be interpreted by comparing the intensity of the I (3d) signal in the initial MoS_2-IBz and the final assemblies. In Figure 2c we show the I (3d) core level spectra of MoS_2 assemblies to point out the absence of any significant signal from I, while MoS_2-IBz displays a strong I (3D) signal as shown in Figure 2a. The disappearance of the I (3d) signal confirms the efficient cross-linking of MoS_2-IBz sheets through C–C bonds leading to the elimination of iodine. The MoS_2–RGO assemblies also exhibit negligible I (3d) signals indicating the formation of C–C bonds between MoS_2 and RGO sheets.

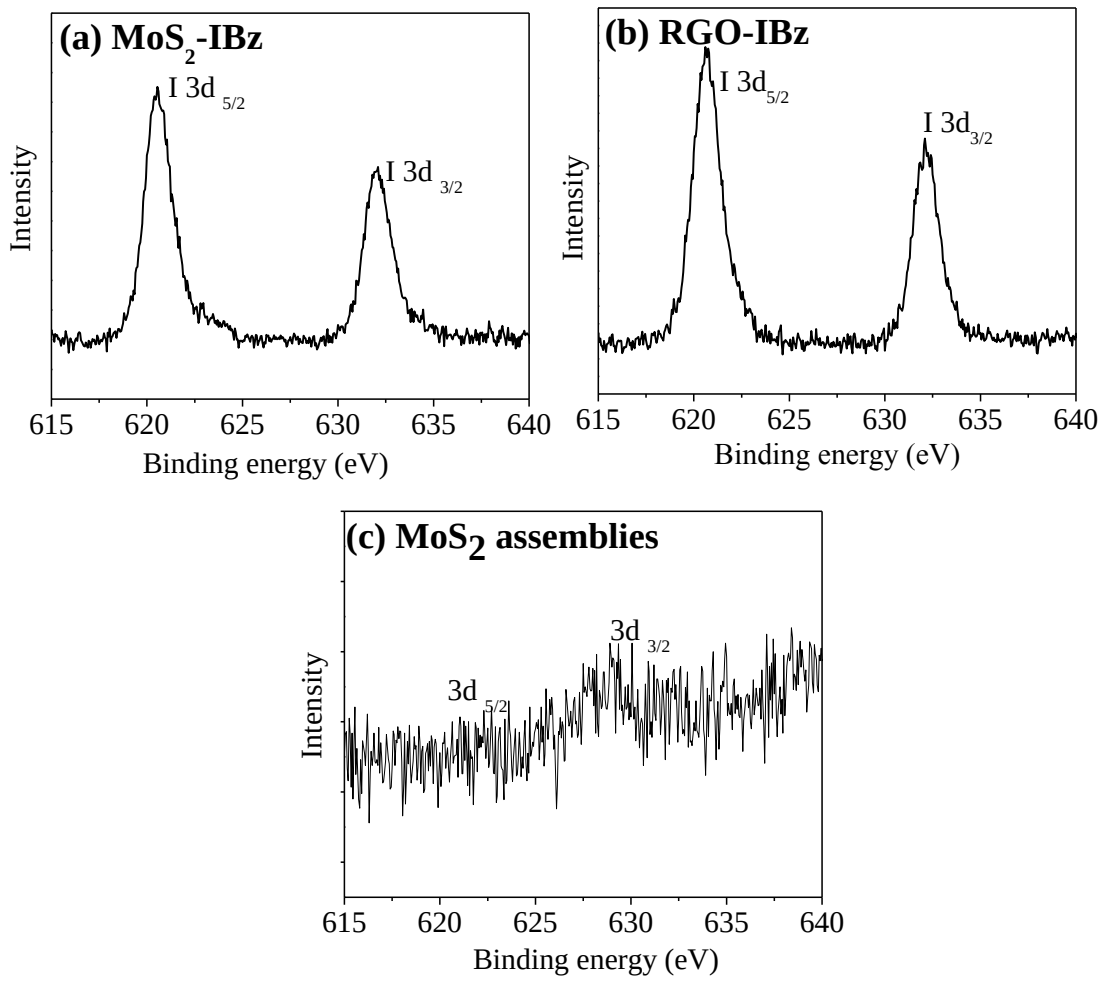

Figure 2. (a) Iodine (3d) X-ray photoelectron spectrum of iodobenzene functionalized MoS_2,iodobenzene functionalized RGO and MoS_2 assemblies.

Figure 3a shows the ATR-FTIR spectra of assemblies of MoS_2 and MoS_2–RGO. MoS_2 assemblies exhibit the C=C stretching bands of benzene at 1600, 1498 and 1390 cm^{-1} along with the Mo–S stretching band at 470 cm^{-1}. The bands at 2250 and 3060 cm^{-1} of the assemblies are attributed to C≡C and C–H stretching bands of the DEBP linker which confirm the presence of DEBP between MoS_2 sheets.[29, 30] In the MoS_2–RGO assemblies, in addition to the bands mentioned above, we see an additional band in the range of 1040–1320 cm^{-1} due to residual OH and epoxy groups of RGO. The C–S stretching band at 695 cm^{-1} in the IR spectra of assemblies as well as MoS_2-IBz confirms the covalent attachment of iodobenzene to MoS_2.[31]

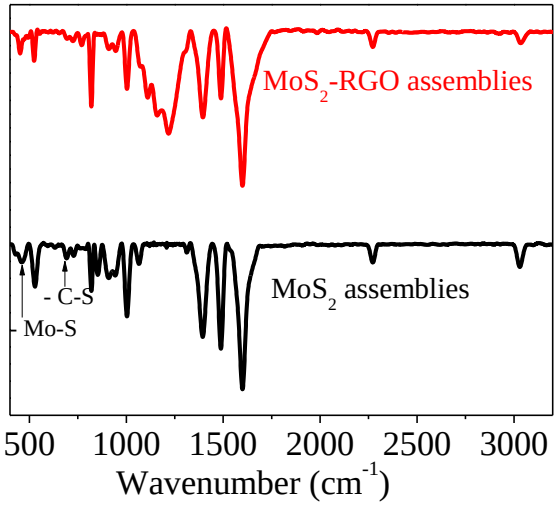

Figure 3. (a) ATR-FTIR spectra of MoS_2 assemblies (black) and MoS_2–RGO (red) assemblies.

In Figure 4a we have shown the PXRD patterns of MoS_2 and MoS_2–RGO assemblies. A broad reflection at 2θ of ~3.5° is observed corresponding to a separation of ~2 nm between the sheets in the assemblies. This value closely matches the length of the DEBP linker between the sheets. The PXRD pattern of MoS_2-IBz and RGO-IBz shows (002) peaks at 2θ of 14.3° and 26°, respectively, which are absent in the assemblies (Figure 4b).

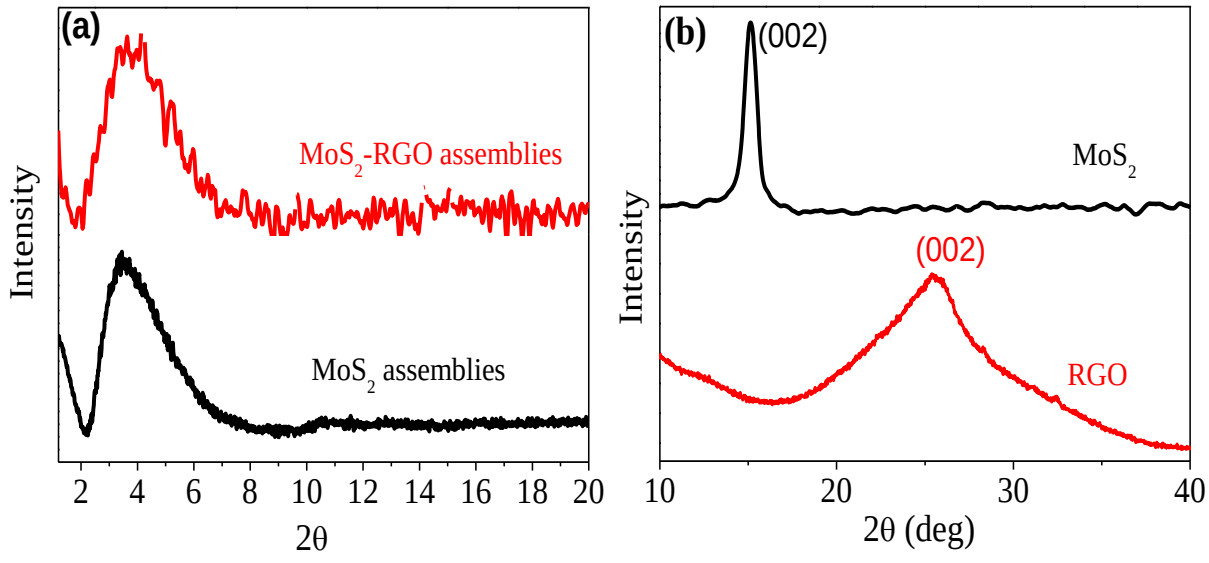

Figure 4. PXRD patterns of (a) MoS_2 assemblies (black) and MoS_2–RGO (red) assemblies; (b) MoS_2 (black) and RGO (red).

Thus the PXRD patterns along with the IR and XPS spectra of the assemblies confirm the covalent pillaring of MoS_2 and RGO sheets through the linker.

Figure 5a shows the transmission electron microscopy (TEM) images of exfoliated MoS_2 containing bi-layers with lateral dimensions of 200–300 nm.

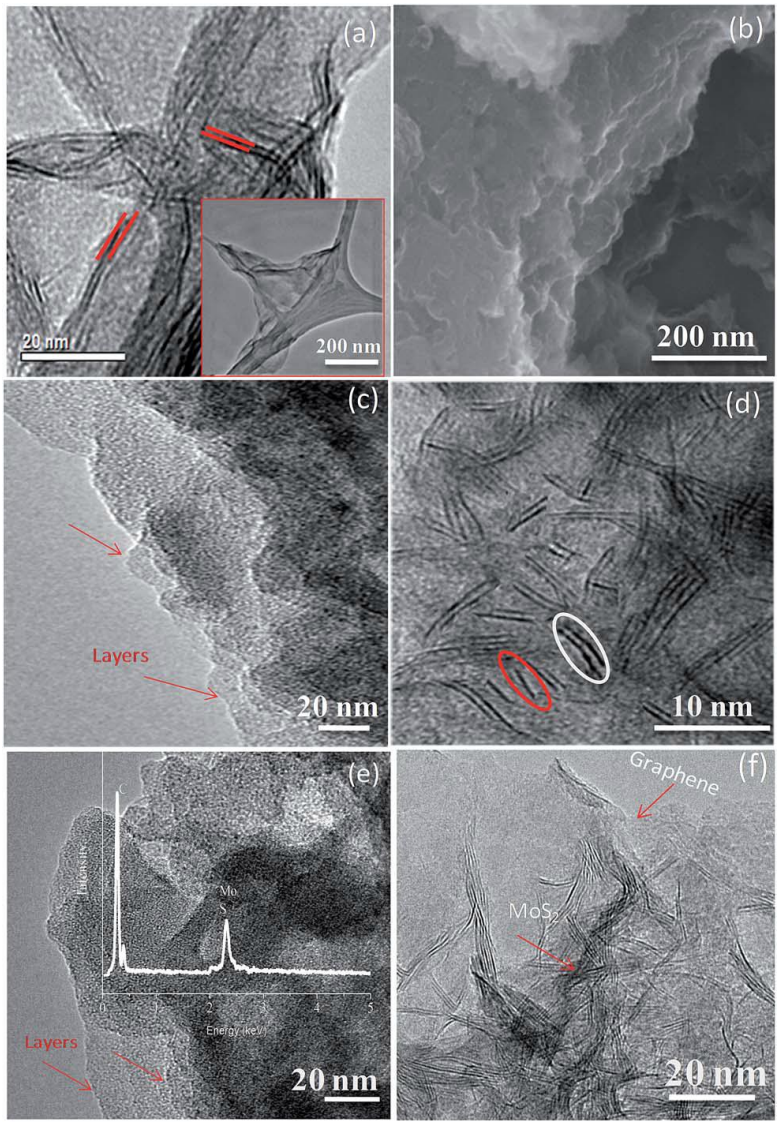

Figure 5. (a) HRTEM image of exfoliated MoS_2 (parallel lines indicate bi-layers) (inset: TEM), (b) FESEM image of MoS_2 assemblies, (c and d) TEM and HRTEM images of MoS_2 assemblies (red and white circles show mono- and bi-layers of MoS_2), (e) TEM image of MoS_2–RGO assemblies (inset: EDAX pattern), and (f) HRTEM image of the MoS_2/RGO physical mixture

Field emission scanning electron microscopy (FESEM) images of MoS_2 assemblies show that 2–5 μm sized monoliths are formed on pillaring unlike those of exfoliated MoS_2 (Figure 5b). Figure 5c presents a TEM image of MoS_2 assemblies, revealing stacking of several MoS_2 sheets due to pillaring. Figure 5d shows the HRTEM image of MoS_2 assemblies containing cross-linked MoS_2 bi-layers (white circle) with an interlayer spacing of ~0.7 nm. The TEM (Figure 5e) image of MoS_2–RGO assemblies shows the cross-linked MoS_2 and RGO sheets (confirmed by the EDAX pattern, inset in Figure 5e). FESEM and TEM images confirm the formation of 3D assemblies due to cross-linking. In contrast, the HRTEM image of the MoS_2/RGO physical mixture shows thick regions of non-uniformly distributed MoS_2 sheets over transparent graphene (Figure 5f).

We have studied surface area and gas adsorption characteristics of the MoS_2 and MoS_2–RGO assemblies. Figure 6a shows N_2 sorption profiles of MoS_2 assemblies, MoS_2–RGO assemblies, MoS_2 and RGO at 77 K. The N_2 isotherms of assemblies show type-I and type-II characteristics in low and high pressure regions, respectively, following the IUPAC classification.[32] The type-1 feature is attributed to the adsorption in micropores, whereas type-II is due to macropores on three dimensional assemblies. The steep increase in the low-pressure region up to $P/P_o \sim 0.1$ is attributed to adsorption in micropores. The Brunauer–Emmet–Teller (BET) surface areas of MoS_2 and MoS_2–RGO assemblies are 498 and 512 $m^2 g^{-1}$, respectively. RGO displays type-II characteristics and a BET surface area of 80 $m^2 g^{-1}$, whereas few-layer MoS_2 is non-porous with a low surface area of 30 $m^2 g^{-1}$. Figure 6b shows pore size distribution obtained from the nitrogen isotherms fitted using non-local density functional theory (NLDFT); we see pores majorly in the 1.2–2 nm range and some in the 2–3 nm range. The pore size distribution of assemblies depends on the length and density of the linker pillaring the sheets. The pore volumes of MoS_2 and MoS_2–RGO assemblies are 0.60 and 0.64 $cm^3 g^{-1}$, respectively, whereas RGO has a low pore volume of 0.15 $cm^3 g^{-1}$. The enhanced pore volume and surface area of the assemblies are attributed to the pillaring of the RGO and MoS_2 sheets, pores generated thereby. It is interesting that the MoS_2 assembly exhibits a high surface area comparable to that of the MoS_2–RGO assembly as evident from BET analysis. We have investigated cross-linked assemblies for the storage of CO_2 and H_2. MoS_2 and MoS_2–RGO assemblies show a CO_2 uptake of 11.4 and 12.8 wt%, respectively, at

298 K and 1 atm (Figure 6c), somewhat comparable with high surface area metal organic frameworks (MOFs).[33] The CO_2 adsorption is considered to be due to the interaction of CO_2 with the π-electron cloud of the aromatic molecules as well as with the sulphur defects in MoS_2.[34, 35] Even though the uptake efficiency of CO_2 is less than that of some of the highest reported MOFs and zeolite 13 X,[33, 36-38] these assemblies can be useful in harsh chemical and thermal atmospheres.

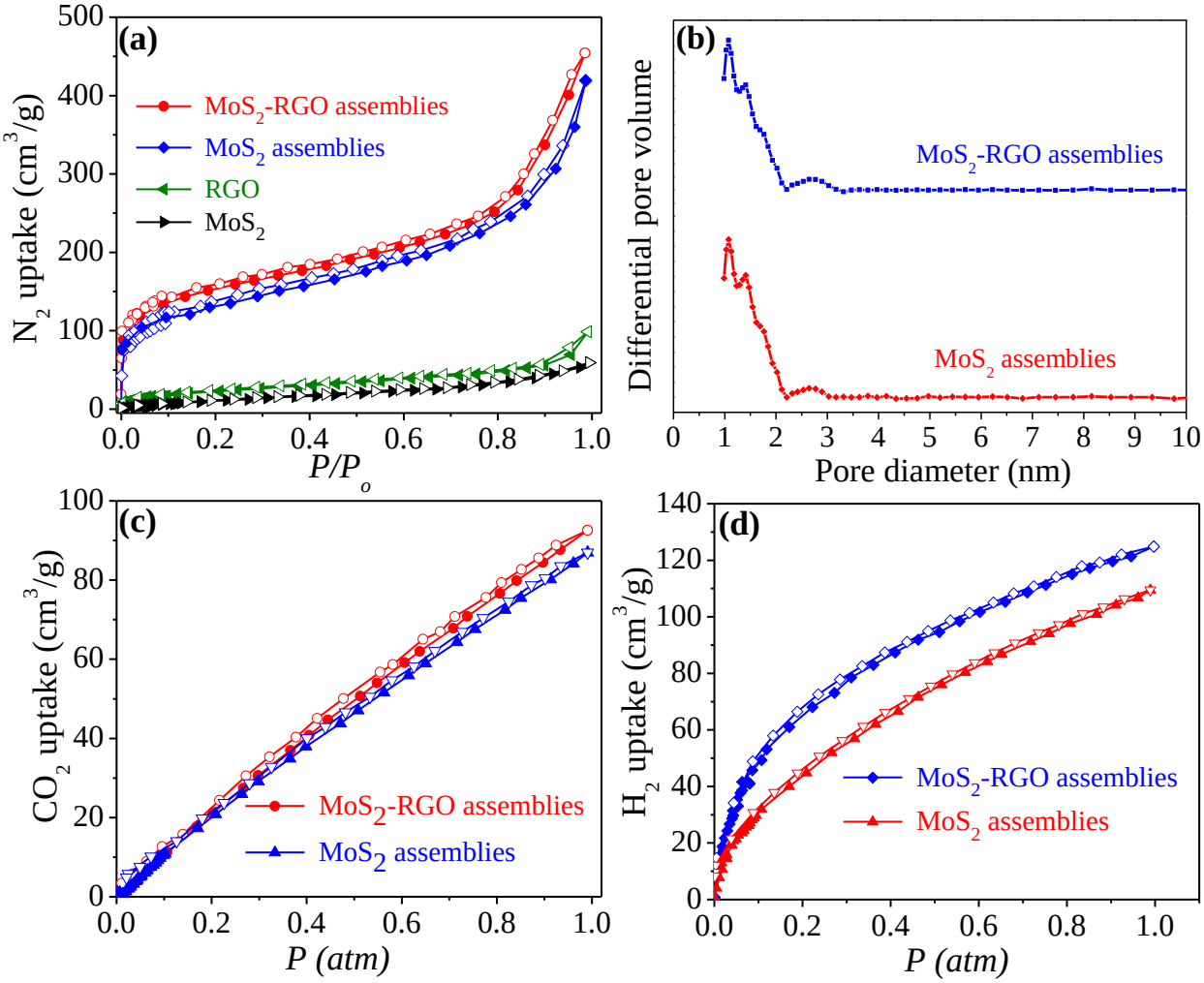

Figure 6. (a) Nitrogen sorption profile of MoS_2 (black), RGO (green), MoS_2 assemblies (blue) and MoS_2–RGO assemblies (red) at 77 K; (b) Pore size distribution curve; (c) CO_2 sorption profile of MoS_2 assemblies (blue) and MoS_2–RGO assemblies (red) at 298 K; (b) Hydrogen sorption profile at 77 K of MoS_2 assemblies (red) and MoS_2-RGO assemblies (blue).

The hydrogen uptake efficiency values of MoS_2 and MoS_2–RGO assemblies are 0.78 and 0.94 wt%, respectively, at 77 K and 1 atm (Figure 6d) which are comparable with some of the reported MOFs.[39, 40]

MoS_2 is a known promising catalyst for the hydrogen evolution reaction.[41, 42] The high surface area and uniform 3D porous (~1–2 nm) network of assemblies are motivational factors for us to examine the hydrogen evolution activity. The hydrogen evolution experiments are carried out in the presence of Eosin Y (EY) dye under visible light illumination (see experimental section for details of photocatalytic measurements). The mechanism of photochemical hydrogen evolution of MoS_2 in EY dye is described elsewhere in the literature.[23] In Figure 7a we show the yield of H_2 evolved by using assemblies of MoS_2 and MoS_2–RGO as well as by using few-layer MoS_2. The cross-linked MoS_2 assembly shows an activity of 1.75 mmol g^{-1} h^{-1} with a turnover frequency (TOF) of 0.84 h^{-1}, whereas few-layer 2H-MoS_2 exhibits an activity of 0.07 mmol g^{-1} h^{-1} with a TOF of 0.01 h^{-1}.

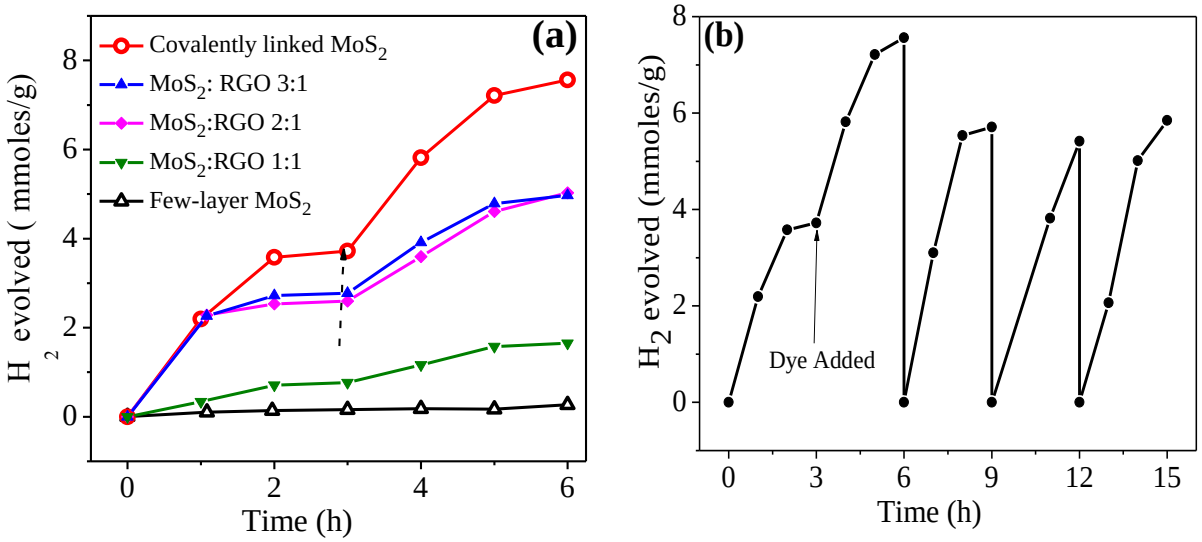

Figure 7. (a) H_2 evolved per gram of catalyst by using few-layer MoS_2 (black), MoS_2–RGO (1 : 1) (green), MoS_2–RGO (2 : 1) (magenta), MoS_2–RGO (3 : 1) (blue) and MoS_2 assemblies (red) (arrows indicate the addition point of eosin dye); (b) Cycling studies of MoS_2 assemblies.

The enhanced catalytic activity of MoS_2 assemblies is attributed to the increased surface area as well as more exposed edges on pillaring. The catalytic activities of MoS_2–RGO (3 : 1) and (2 : 1) assemblies are comparable with 3 : 1 assembly has an activity of 1.38 mmol g^{-1} h^{-1} (TOF = 0.98 h^{-1}) and the 2 : 1 assembly shows an activity of 1.30 mmol g^{-1} h^{-1} (TOF = 0.94 h^{-1}). The MoS_2–RGO (1 : 1) assembly shows a lower activity of 0.35 mmol g^{-1} h^{-1} (TOF = 0.40 h^{-1}) among the MoS_2–RGO assemblies. The above results suggest that MoS_2 is the active component for hydrogen evolution in these assemblies and the activity decreases with the increase in graphene content. Table 1 presents the hydrogen evolution activity of assemblies that are compared with the literature reports on MoS_2 based catalysis. Cycling studies on MoS_2 assemblies carried out over a period of 15 h (4 cycles) with a 14 μmol dye show that the activity increases in the second cycle and then becomes stable in subsequent cycles (Figure 7b).

Serial. No	**Composite**	**Activity (mmol h^{-1} g^{-1})**	**TOF (h^{-1})**	**References**
1	**FL-MoS_2**	**0.07**	**0.01**	**Present Work**
2	**MoS_2 assemblies**	**1.75**	**0.84**	**Present Work**
3	**MoS_2-RGO assemblies (3:1)**	**1.38**	**0.98**	**Present Work**
4	**MoS_2-RGO assemblies (2:1)**	**1.30**	**0.94**	**Present Work**
5	MoS_2-RGO Composite	3	0.68	Ref (8)
6	MoS-EG Composite	0.54	0.21	Ref (8)

Table 1: Comparison of activity of catalyst in terms of yield of H_2 evolved.

4.4.5: Conclusions

In conclusion, we have been able to generate robust MoS_2 and MoS_2-RGO frameworks with organic linkers using the Sonogashira coupling strategy. These frameworks display high surface area and marked storage capacity for CO_2 with an uptake of 11–13 wt% at 298 K and 1 atm due to uniform pores created by pillaring. The pillared frameworks generated by us are somewhat comparable to the 3D pillared layer MOFs reported by Kitagawa *et al.*[43] where 2D metal carboxylates are pillared by organic linkers. The entirely new metal chalcogenide-based porous solids based on pillared MoS_2 frameworks reported here imply the possibility of designing related materials with advantageous attributes. MoS_2 assemblies show superior hydrogen evolution activity as compared to few-layer MoS_2 possibly due to the more exposed catalytically active edge sites of MoS_2 on pillaring by organic linkers.

4.4.6: References

1. J. M. Englert, C. Dotzer, G. Yang, M. Schmid, C. Papp, J. M. Gottfried, H.-P. Steinrück, E. Spiecker, F. Hauke, A. Hirsch, *Nat. Chem.* 2011, **3**, 279–286.
2. T. Sainsbury, A. Satti, P. May, A. O'Neill, V. Nicolosi, Y. K. Gun′ko, J. N. Coleman, *Chem. Eur. J.* 2012, **18**, 10808.

3. D. Voiry, A. Goswami, R. Kappera, E. SilvaCecilia de Carvalho Castro, D. Kaplan, T. Fujita, M. Chen, T. Asefa, M. Chhowalla, *Nat. Chem.* 2014, ***7***, 45.

4. K. C. Knirsch, N. C. Berner, H. C. Nerl, C. S. Cucinotta, Z. Gholamvand, N. McEvoy, Z. Wang, I. Abramovic, P. Vecera, M. Halik, S. Sanvito, G. S. Duesberg, V. Nicolosi, F. Hauke, A. Hirsch, J. N. Coleman, C. Backes, *ACS Nano* 2015, *9*, 6018.

5. (a) J. Zheng, H. Zhang, S. Dong, Y. Liu, C. Nai, H. Shin, H. Jeong, B. Liu, K. Loh, Nat. Commun. **201**4, **DOI: 10.1038/ncomms3995**; (b) P.Vishnoi, A.Sampath, U. V. Waghmare,C. N. R. Rao, *Chem.Eur. J.* **2017**, *23*, 886; (c) A. Jeffery, S. R. Rao, M. Rajamathi, Carbon, **2017**, *112, 8.*
6. P. P. Wang, H. Y. Sun, Y. J. Ji, W. H. Li, X. Wang, *Adv. Mater.* 2014, *26*, 964.
7. X. Chia, A. Y. S. Eng, A. Ambrosi, S. M. Tan, M. Pumera, *Chem. Rev.* **2015**, *115*, 11941.
8. U. Maitra, U. Gupta, M. De, R. Datta, A. Govindaraj, C. N. R. Rao, *Angew. Chem. Int. Ed*. **2013**, *52*, 13057.
9. A. B. Laursen, S. Kegnaes, S. Dahl, I. Chorkendorff, *Energy Environ. Sci*. **2012**, *5*, 5577.
10. S. Presloski, M. Pumera, *Mater. Today.* **2015** doi:10.1016/j.mattod.2015.08.019
11. S. S. Chou, M. De, J. Kim, S. Byun, C. Dykstra, J. Yu, J. Huang, V. P. Dravid, *J. Am. Chem. Soc.* **2013**, *135*, 4584.
12. R. H. Gonçalves, R. Fiel, M. R. S. Soares, W. H. Schreiner, C. M. P. Silva, E. R. Leite, *Chem. Eur. J.* **2015**, *21*, 15583

13. E. P. Nguyen, B. J. Carey, J. Z. Ou, J. van Embden, E. D. Gaspera, A. F. Chrimes, M. J. S. Spencer, S. Zhuiykov, K. K. Zadeh, T. Daeneke, *Adv. Mater.* **2015**, *27*, 6225.

14. Y. Liu, Z. Tan, X. Xie, Z. Wang, X. Ye, *Chem. Asian J*, **2013**, *8*, 817.

15. C. Backes, N. C. Berner, X. Chen, P. Lafargue, P. LaPlace, M. Freeley, G. S. Duesberg, J. N. Coleman, A. R. McDonald, *Angew. Chem. Int. Ed.* **2015**, *54*, 2638.

16. X. Wang, E. N. Kalali, D-Y. Wang, *J. mater. Chem. A* **2015**, *3*, 24112.

17. R. Kumar, V. M. Suresh, T. K. Maji, C. N. R. Rao, *Chem. Commun.* 2014, *50*, 2015.

18. Y. Liu, Y. Zhao, L. Jiao, J. Chen, *J. Mater. Chem. A*, **2014**, *2*, 13109.

19. S. Min, G. Lu, *J. Phys. Chem. C*, **2012**, *116*, 25415.

20. Y. Liu, H. Kang, L. Jiao, C. Chen, K. Cao, Y. Wang, H. Yuan, *Nanoscale*, **2015**, *7*, 1325.

22. W. S. Hummers, R. E. Offeman, *J. Am. Chem. Soc.* 1958, *80*, 1339.

23. U. Gupta, B. S. Naidu, U. Maitra, A. Singh, S. N. Shirodkar, U. V. Waghmare and C. N. R. Rao, *APL Mater.* **2014**, *2*, 092802.

24. S. Stankovich, D. A. Dikin, R. D. Piner, K. A. Kohlhaas, A. Kleinhammes, Y. Jia, Y. Wu, S. T. Nguyen, R. S. Ruoff, *Carbon* **2007**, *45*, 1558.

25. K. Yoo, S.-W. Joo, *J. colloid interface sci.* **2007**, *311*, 491.

26. D. Sloan, Y. M. Sun, H. Ihm, J. M. White, *J. Phys. Chem. B*, **1998,** *102*, 6825.

27. H. Cabibil, H. Ihm, J. M. White, *Surf. Sci.* **2000,** *447*, 91.

28. R. Chinchilla, C. Najera, *Chem. Soc. Rev.* **2011**, *40*, 5084

29. T. Weber, J. C. Muijsers, J. H. M. C. van Wolput, C. P. J. Verhagen, J. W. Niemantsverdriet, *J. Phy. Chem.* **1996**, *100*, 14144.

30. D. W. Mayo, F. A. Miller, R. W. Hannah, *in course Notes on the Interpretation of Infrared and Raman Spectra*, *Wiley*, 2003 DOI:10.1002/0471690082 .

31. G. Socrates, *Infrared and Raman Characteristic Group Frequencies: Tables and Charts* , *Wiley*, 2001.

32. K. S. W. Sing, D. H. Everett, R. A. W. Haul, L. Moscou, R. A. Pierotti, J. Rouquerol, T. Siemieniewska, *Pure Appl. Chem.* **1984**, *57*, 603.

33. K. Sumida, D. L. Rogow, J. A. Mason, T. M. McDonald, E. D. Bloch, Z. R. Herm, T.-H. Bae, J. R. Long, *Chem. Rev.* **2012**, *112*, 724.

34. N. Yu, L. Wang, M. Li, X. Sun, T. Hou, Y. Li, *Phys. Chem. Chem. Phys.* **2015**, *17*, 11700.

35. A. M. Plonka, D. Banerjee, W. R. Woerner, Z. Zhang, N. Nijem, Y. J. Chabal, J. Li, J. B. Parise, *Angew. Chem. Int. Ed.* **2013**, *52*, 1692.

36. J.-S. Lee, J.-H. Kim, J.-T. Kim, J.-K. Suh, J.-M. Lee, C.-H. Lee, *J. Chem. Eng. Data.* **2002**, *47*, 1237.

37. A. Ö. Yazaydın, R. Q. Snurr, T.-H. Park, K. Koh, J. Liu, M. D. LeVan, A. I. Benin, P. Jakubczak, M. Lanuza, D. B. Galloway, J. J. Low, R. R. Willis, *J. Am. Chem. Soc.* **2009**, *131*, 18198.

38. Y. Wang, M. D. LeVan, *J. Chem. Eng. Data*, **2009**, *54*, 2839.

39. M. Dincă, A. Dailly, Y. Liu, C. M. Brown, D. A. Neumann, J. R. Long, *J. Am. Chem. Soc.* **2006**, *128*, 16876.

40. K. S. Park, Z. Ni, A. P. Côté, J. Y. Choi, R. Huang, F. J. Uribe-Romo, H. K. Chae, M. O'Keeffe, O. M. Yaghi, *Proc. Natl. Acad. Sci., U.S.A* **2006**, *103*, 10186.

41. J. Yang, H. S. Shin, *J. Mat. Chem. A*, **2014,** *2*, 5979.

42. X. Zong, Y. Na, F. Wen, G. Ma, J. Yang, D. Wang, Y. Ma, M. Wang, L. Sun, C. Li, *Chem. Commun*. **2009**, 4536.

43. R. Kitaura, K. Fujimoto, S. Noro, M. Kondo, S. Kitagawa, *Angew. Chem.* **2002**, *114*, 141.

4.5: Nanocomposites of C_3N_4 with Layers of MoS_2 and Nitrogenated RGO Obtained by Covalent Cross-linking: Synthesis, Characterization and HER Activity

Summary*

Composites of layered carbon nitride (C_3N_4) with MoS_2 and nitrogenated RGO are prepared using covalent cross-linking strategy by employing the carbodiimide reaction. The obtained C_3N_4-MoS_2 and C_3N_4-NRGO composites are characterized using a variety of spectroscopic techniques and electron microscopy. During cross-linking, residual amine functional groups on either side of the C_3N_4 layer form amide bonds with the carboxyl functionalized MoS_2 or NRGO giving rise to a layer-by-layer assembly. The photochemical HER activity of the C_3N_4-MoS_2 nanocomposite is found to be remarkable with an activity of 12778 μmoles $h^{-1}g^{-1}$ and a TOF of 2.35 h^{-1}. The physical mixture of C_3N_4 and MoS_2, on the other hand, does not exhibit notable catalytic activity. Encouraged by this result, we have studied electrochemical HER activity of these composites as well. C_3N_4-MoS_2 shows superior activity relative to a physical mixture of MoS_2 and C_3N_4. DFT calculations have been carried out to understand the HER activity of the nanocomposites. Charge-transfer between the components and greater planarity of cross-linked layers are important causes of the superior catalytic activity of the nanocomposites. Covalent linking of such 2D materials appears to be a worthwhile strategy for catalysis and other applications.

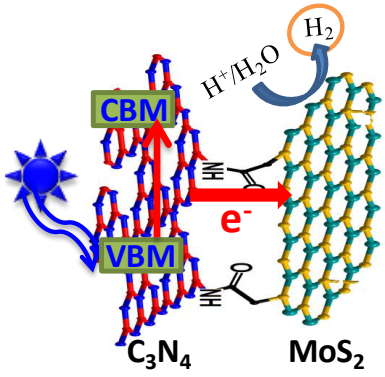

Paper based on this work has been published in *ACS Appl. Mater. Interfaces, (2017).*

4.5.1: Introduction

Energy and environmental issues constitute the biggest technological challenges today. The global energy demands are stipulated to rise from current level of 12 TW per day to 27 TW by 2050. The current sources of energy, primarily hydrocarbons, coal and petroleum are non-renewable and will not be able to sustain the increasing demands of energy. Hydrogen has emerged to be an important alternative fuel to solve problems related to energy and the environment. In this context, generation of H_2 has been investigated by means of several strategies, of which photochemical and electrochemical generation are significant ones.[1-6] Platinum which is the best known catalyst for electrochemical hydrogen evolution reaction (HER) suffers from issues related to stability and high cost.[7a] Photochemical generation of H_2 by using semiconductor structures has also been an active area of research. For a semiconductor to act as a water-splitting catalyst, it must satisfy the following energy level conditions. The bottom of the conduction band must be more negative than the reduction potential of $H+/H_2$ (0 V vs. SHE), and the top of the valence band must be more positive than the oxidation potential of O_2/H_2O (1.23 V), limiting the theoretical minimum band gap for water splitting to 1.23 eV. Based on the above criterion, several semiconductors have been identified for H_2 evolution or oxygen evolution or both (Figure 1). Semiconductors such as TiO_2, $SrTiO_3$, $BaTiO_3$, $FeTiO_3$, ZrO_2 and ZnO whose conduction band potential lie above the proton reduction potential can reduce water to produce H_2.

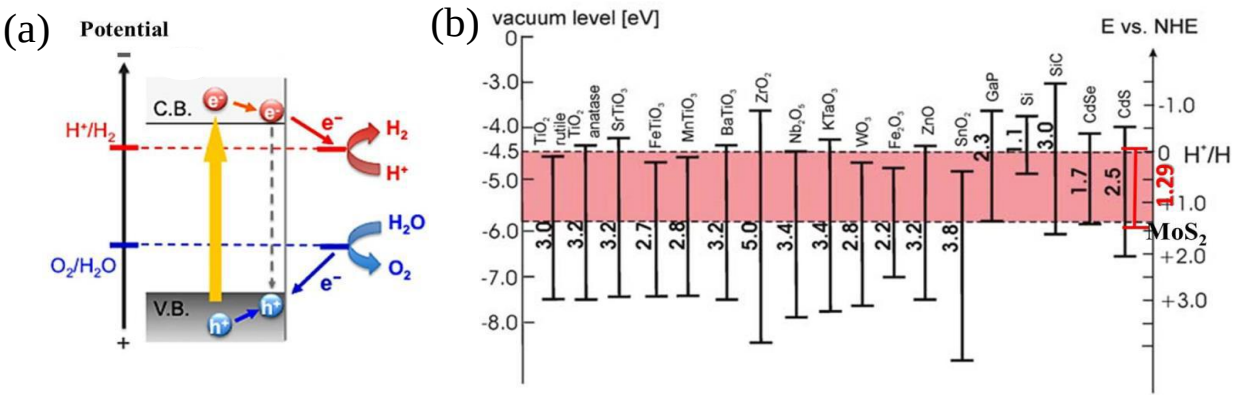

Figure 1. Schematic representations of (a) the energy level requirements in semiconductor photocatalysis and (b) semiconductor photocatalysts and their corresponding band positions with respect to the water redox potential. (From Ref. [7b]).

On the other hand, semiconductors such as Fe_2O_3, SnO_2, WO_3 *etc.* can only oxidize water to H_2. Semiconductors like CdS, CdSe and MoS_2 are ideal for visible light photocatalytic H_2 production by virtue negative conduction band potential and small band gap (Figure 1).

In the last few years, there is a major thrust in investigating cost-effective, stable catalysts for hydrogen evolution reaction (HER), preferably those which are metal-free.[6] Among metal-free catalysts, graphitic carbon nitride (C_3N_4) specially attractive because of the suitable band gap (E_g=2.7 eV) and stability in harsh chemical environments.[8, 9] However, pure g-C_3N_4 has low photochemical activity due to the rapid recombination of the photogenerated electron-hole pair. It has been suggested that coupling of C_3N_4 with a suitable co-catalyst like MoS_2 could improve the catalytic activity owing to effective charge separation.[10,11] Such composites would also be useful as catalysts for photoelectrochemical HER.[12, 13] Due to the poor electronic conductivity of MoS_2 and C_3N_4, their layers have been grown on reduced graphene oxide (RGO) to enhance the HER activity.[4, 14] The composite of MoS_2 with nitrogenated RGO (NRGO) is a reasonably good catalyst for dye-sensitized photochemical hydrogen evolution.[15] Synthesis of nanohybrids of C_3N_4 with MoS_2 or RGO has been achieved by solid state chemistry route or hydrothermal methods,[4,10] but such systems would consists of randomly distributed constituents with hetero domains. Assemblies of RGO with C_3N_4 or MoS_2 in a layer-by-layer fashion (van der Waals heterostructures) exhibit improved catalytic activity because of better interconnectivity.[16, 17] It has been recently reported that assemblies of covalently cross-linked nanosheets of MoS_2 with MoS_2 or RGO sheets display superior HER activity compared to the individual components.[18] In this scenario, we considered it most worthwhile to synthesize covalently bonded assemblies of C_3N_4 with MoS_2 and NRGO by using an appropriate coupling reaction, and to examine the effect of such bonding on the photochemical hydrogen generation. The present study presents the important results obtained by us on the catalytic activity of covalently cross-linked C_3N_4-NRGO and C_3N_4-MoS_2 composites in photochemical HER. Interestingly, we find significant improvement in photochemical HER catalytic activity of the covalently cross-linked composites, especially in the case of C_3N_4-MoS_2, compared to that of the physical mixture of the two. Encouraged by these results, we have extended the study to examine the use of these chemically bonded composites in electrochemical HER.

Furthermore, we have performed detailed density functional theoretical studies to get insights into the physical processes involved.

4.5.2: Scope of the present investigations

Generation of hydrogen by photochemical, electrochemical and other means is a vital area of research today and a variety of materials has been explored as catalysts for this purpose. C_3N_4, MoS_2 and nitrogenated RGO (NRGO) are some of the important catalytic materials investigated for the HER reaction but the observed catalytic activities are somewhat marginal. Composite of C_3N_4 with MoS_2 or NRGO showed enhanced H_2 evolution activity compared to individual components due to the effective charge separation. Most of the C_3N_4-MoS_2 and C_3N_4-NRGO composites reported in literature are prepared from either hydrothermal or solid state reactions. These routes often need high temperature and one cannot have precise control over composition of individual components in the final composites. Secondly, while preparing these composites at high temperatures there are chances of partial conversion of MoS_2 to MoO_3 due to oxygen impurity which decreases the catalytic activity. In this work for the first time we prepared covalently cross-linked composites of C_3N_4-MoS_2 and C_3N_4-NRGO by relatively simple carbodimide method at room temperature and composition of individual components in final composites can be controlled precisely since we start from known amount of functionalized C_3N_4 and MoS_2 or NRGO. Moreover, MoS_2 grown on C_3N_4 by hydrothermal method is few-layer. Cross-linking strategy allowed us to cross-link individual MoS_2 layer with C_3N_4 and vice versa where we can expect maximum interaction between heterolayers which reflected in their superior HER activity as compared to physical mixture of two. Additionally, covalent cross-linking of heterolayers generates pores, contributing to the enhanced HER activity which is absent in nanocomposites prepared from other reported methods. The catalytically active edge sites of MoS_2 are more exposed on covalent pillaring with C_3N_4 which can also contributes to the enhanced HER activity. In case of C_3N_4 or NRGO we have utilized the residual functional for cross-linking thereby preventing alterations in their electronic structure.

4.5.3: Experimental section

C_3N_4 was prepared by heating thiourea (2g) powder in an alumina crucible at 550 ^oC for 4 h.[19] To prepare 1T-MoS_2, bulk MoS_2 (300 mg) powder was stirred in a solution of n-

butyllithium (n-BuLi, 3ml, 1.6 M hexane), and refluxed at 70 ^oC under nitrogen atmosphere over a period of 48 h.[20] The black Li-intercalated (Li_xMoS_2) sample was collected by filtration under nitrogen, and washed extensively with hexane (3*100 ml). The obtained Li_xMoS_2 sample was ultrasonicated in water (1mg/ml) for 1 h, and the resultant solution centrifuged at high speed (8000 rpm) to remove LiOH, and any non-exfoliated material. From inductively coupled plasma (ICP) analysis we have obtained the final concentration of exfoliated MoS_2 in water, and it is ~ 0.7 mg/ml.

To synthesize carboxylate functionalized MoS_2, ten-fold excess of 2-Bromoacetic acid was added to the exfoliated 1T-MoS_2 (1mg/ml) solution and allowed to stir for 5 days at room temperature. The precipitated product was filtered and washed with 2-propanol, water and ethanol, and dried at 60 °C under vacuum.[20] NRGO sample was prepared by grinding graphene oxide (GO) with urea to obtain homogeneous mixture then pelletized, and heated in a microwave reactor (900 W) for 60 s.[21]

Synthesis of covalently cross-linked C_3N_4-NRGO and C_3N_4-MoS_2 composites:

C_3N_4 (50 mg) and NRGO (50 mg) were mixed in Schlenck flask, sealed using a septum and 5 ml dry DMF added under N_2 atmosphere to obtain a uniform dispersion of the mixture after bath sonication. To the above dispersion *N*-(3-dimethylaminopropyl)-*N*′-ethylcarbodiimidehydrochloride (EDC.HCl, 20 mg) and 1-hydroxybenzotriazole (HOBt, 20 mg) were added along with *N,N*-diisopropylethylamine (DIPEA, 300 μl) and stirred at room temperature for 48 h. An inert atmosphere was maintained during the reaction. The solid product obtained was collected by filtration (0.45 μm, PTFE membrane), washed with copious amounts of DMF and water to remove byproducts and dried at 60 °C under vacuum. For the synthesis of C_3N_4-MoS_2 composites, C_3N_4 (50 mg) and MoS_2-CH_2COOH (50 mg) were dispersed in dry DMF and the above mentioned procedure repeated. For the preparation of physical mixture of C_3N_4 and NRGO (MoS_2), C_3N_4 (50 mg) and NRGO (MoS_2) (50 mg) were dispersed in aqueous solution by bath sonication and then filtered to get a solid product. For comparison, C_3N_4-MoS_2 composite was prepared by the solid state route by heating few-layer MoS_2 with thiourea in a N_2 atmosphere at 550 ^oC for 4 hr.

Photochemical studies:

The catalyst (3 mg) was dispersed in water (40 mL) by sonication in a glass vessel. To this a solution of triethanolamine (20 % v/v; 10 mL) was added as the sacrificial agent and the

mixture thoroughly purged with N_2. The vessel was illuminated under Xenon lamp (400 W) with steady stirring of the mixture. 2 mL of evolved gas was collected from headspace of the glass vessel and analyzed using thermal conductivity detector equipped gas chromatograph (Perkin Elmer ARNL 580C). Turnover frequency (TOF) for individual catalyst was calculated per mole of C_3N_4, considering the fact that light absorption happens in C_3N_4 only. TOF values are estimated by using the following equation.

$$\text{TOF } (h^{-1}) = \frac{Activity\ of\ the\ catalyst}{\text{moles of the active catalyst}} \quad (1)$$

Electrochemical studies:

All the electrochemical studies were performed in standard 3-electrode system where Pt coil and Ag/AgCl (3M NaCl) were used as counter and reference electrodes, respectively. Working electrode was prepared by drop-casting the catalyst ink (obtained by dispersing catalyst in mixture of water, isopropanol and nafion (5 wt%); 4:1:0.5 v/v) on Glassy Carbon Electrode (GCE). The electrolyte used was 0.5 M H_2SO_4.

Computational Details:

The geometry of the composites was optimized using density functional theory (DFT) as implemented in the Gaussian 09 program package.[22] We have used the CAM-B3LYP functional which is the long range corrected version of B3LYP[23] and employs the Coulomb-attenuating method. This is important for the composite systems which show charge-transfer interactions.[24] We have used the 6-31g basis set for C, N, O, H and S atoms and LANL2DZ for Mo atoms. For the C_3N_4-MoS_2 composites, we kept the MoS_2 layer fixed and optimized the edge atom, linker bonds and C_3N_4 layers.

4.5.4: Results and discussion

In scheme 1, we present the synthetic strategy to obtain amide-bond cross-linked C_3N_4-NRGO and C_3N_4-MoS_2 composites. C_3N_4-NRGO composite was obtained by reacting nitrogen-doped reduced graphene oxide (NRGO), prepared from the microwave irradiation of mixture of graphene oxide (GO) and urea,[21] with amine-functionalized C_3N_4 in the presence of 1-ethyl-3-(3-dimethylaminopropyl)carbodiimide (EDC).

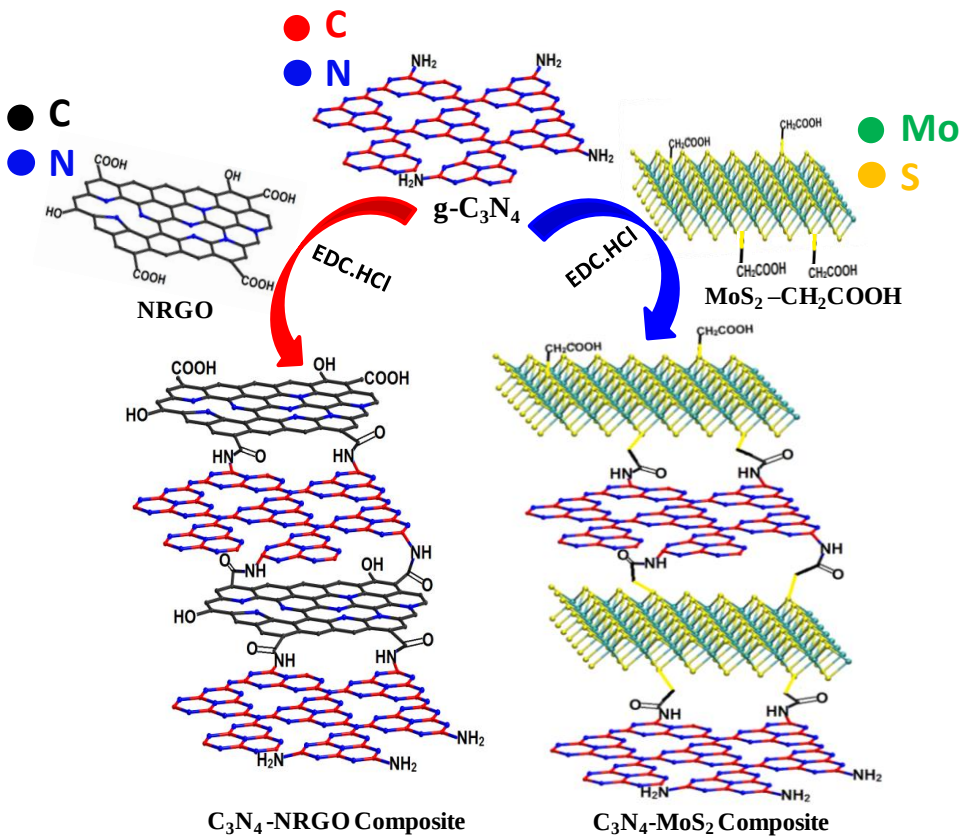

Scheme 1 Synthetic strategy for covalently bonded C_3N_4-NRGO and C_3N_4–MoS_2 composites

Carboxylate functionalized MoS_2 (MoS_2-CH_2COOH), obtained by the reaction of metallic 1T-MoS_2 with bromoacetic acid,[20] was reacted with amine-functionalized C_3N_4 in the presence of EDC to obtain the C_3N_4-MoS_2 assembly (1T-MoS_2 sheets were obtained by Li intercalation in bulk MoS_2 followed by exfoliation in water). These coupling reactions with EDC result in amide bonds between the C_3N_4 and NRGO or MoS_2. EDC coupling has an advantage over $SOCl_2$-based activation in that no HCl is liberated, and the urea byproduct is soluble in water. We have used the terms C_3N_4-NRGO and C_3N_4-MoS_2 in the manuscript to refer to the composites generated by the covalent cross-linking strategy.

We have established the identities of the composites by a variety of methods. Figures 2a, c and d present the transmission electron microscope (TEM) images of C_3N_4, NRGO and MoS_2 used as the starting materials, showing a wrinkled morphology due to the thin-layers.

Atomic force microscopy (AFM) images of MoS_2-CH_2COOH indicate it contains monolayers of MoS_2 (~ 80 %) with a layer thickness of ~ 0.8 nm (Figure 2f).

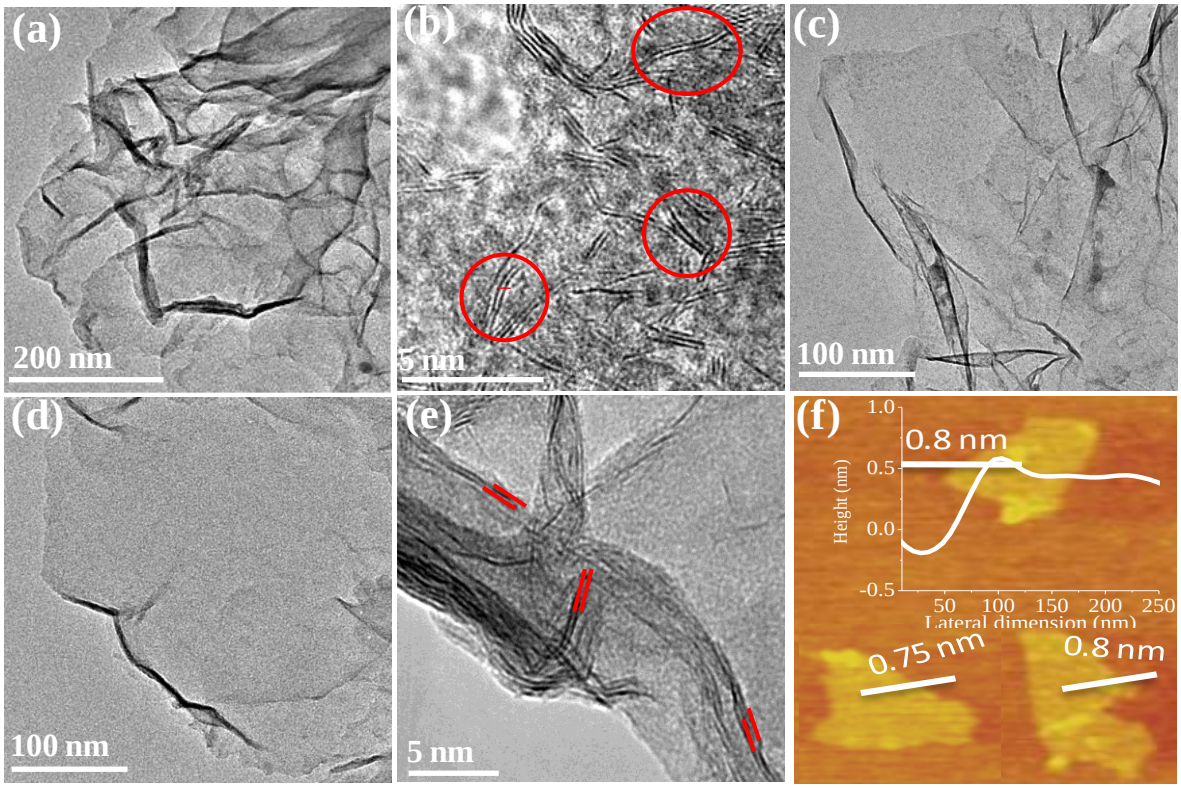

Figure 2. (a, b) TEM and HRTEM images (circles indicates layers with inter-layer spacing of ~0.4 nm) of C_3N_4, (c) TEM image of NRGO, (d, e) TEM and HRTEM images (parallel lines indicate layers with inter-layer spacing ~0.62 nm) of MoS_2 (f) AFM images of MoS_2-CH_2COOH.

Figure 3a shows the HRTEM image of the C_3N_4-MoS_2 composite with the edge region of the basal plane parallel to the direction of the electron beam. The inter-layer spacing (~0.75 nm, indicated by red lines) is higher compared to that in C_3N_4 (0.40 nm, Figure 2b) or in MoS_2 (0.62 nm, Figure 2e). We do not observe any region corresponding to either C_3N_4 or MoS_2 alone, clearly suggesting the occurrence of cross-linking between monolayers of MoS_2-CH_2COOH and C_3N_4 by forming the amide bond. The observed inter-layer spacing (~0.75, HRTEM) in the C_3N_4-MoS_2 composite is in agreement with the theoretically calculated bond distance (Mo-**S-CH_2-CO-NH-C_3N_4**) between cross-linked

C_3N_4 and MoS_2 layers. In Figures 3c we show the FESEM image of C_3N_4-MoS_2 composites, illustrating the formation of 3D assemblies due to layer-by-layer stacking.

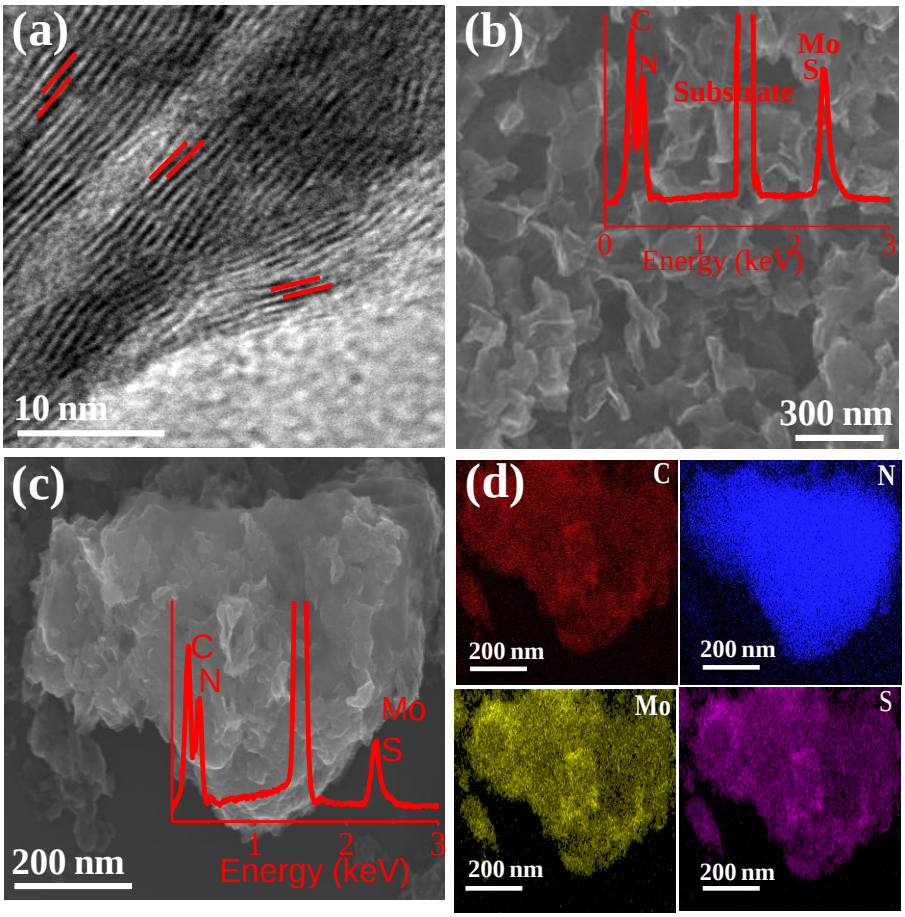

Figure 3. (a) HRTEM image of C_3N_4–MoS_2 composite, (b) FESEM image of physical mixture of C_3N_4 and MoS_2, (c) FESEM image (Inset; Energy dispersive spectrum) and d) elemental mapping (C (red), N (blue), Mo (yellow), S (magenta)) images of the C_3N_4-MoS_2 composite.

A physical mixture of C_3N_4 with MoS_2 or NRGO contains randomly oriented layers and does not display any stacking order due to lack of directing bonds (Figure 3b). During cross-linking, the amine functional groups on either side of the C_3N_4 layer form amide bonds with the carboxyl functionalized MoS_2 or NRGO giving rise to a layer-by-layer assembly takes place on both sides of the 2D sheets. Elemental mapping images of a typical cross-linked layers of MoS_2 with C_3N_4 using the energy dispersive X-ray spectroscopy (EDS) exhibits uniform distribution of C, N, Mo and S confirming the homogeneous nature of the

nanocomposite (Figure 3d). Sonication of a mixture of C_3N_4 and MoS_2-CH_2COOH or NRGO in DMF medium carried out prior to the coupling reaction, favors exfoliation as well as homogeneous mixing of layers (see Experimental section for more details).

Electron energy-loss spectrum (EELS) obtained at different locations of the C_3N_4-MoS_2 nanocomposite show characteristic peaks of C (K edge), N (K edge), Mo (M-edge) and S (L-edge), confirming the uniform nature of cross-linked assemblies (Figure 4a).[4]

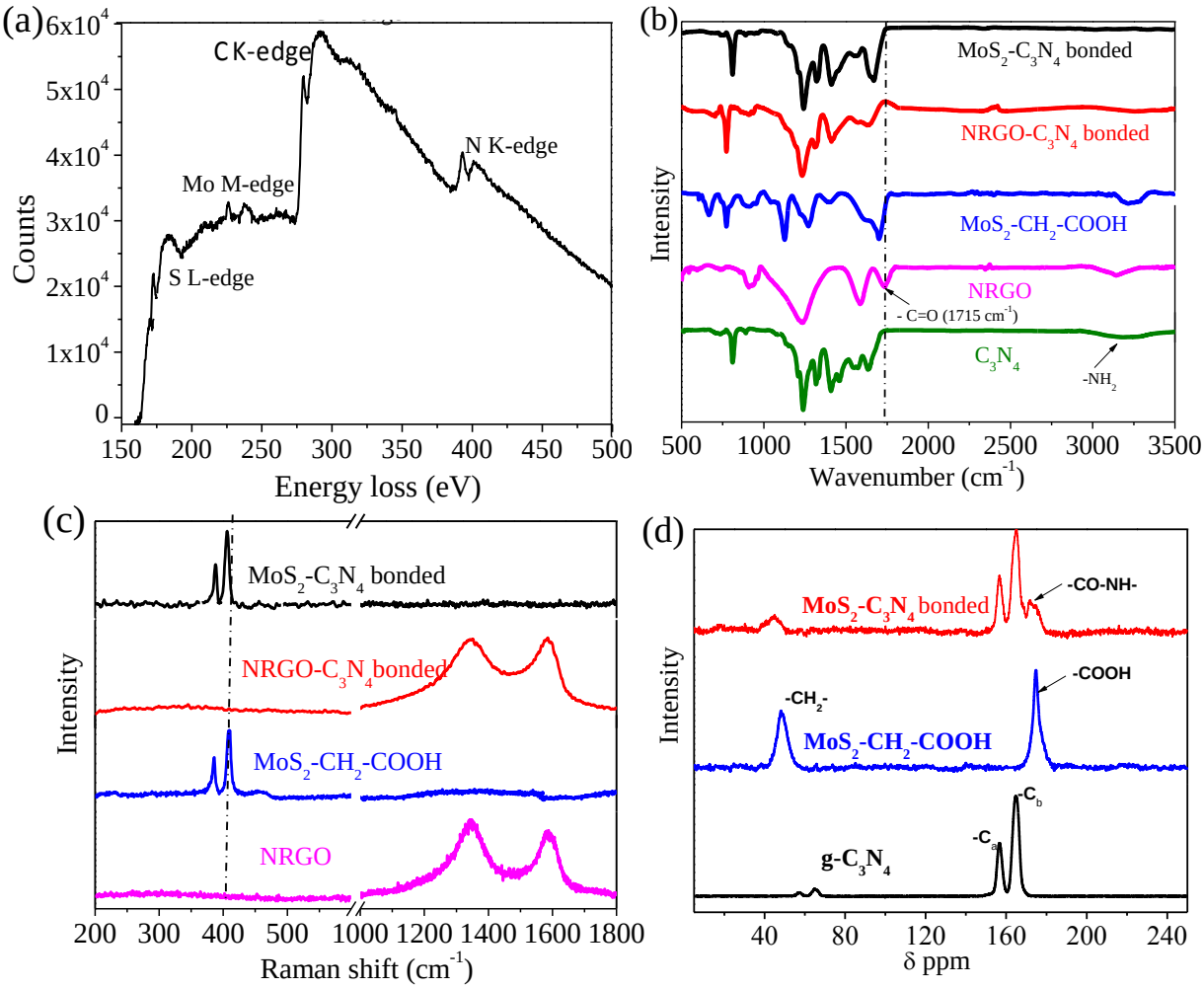

Figure 4. (a) EELS spectrum of C_3N_4-MoS_2 nanocomposites, showing S (L-edge), Mo (M-edge), C (K-edge) and N (K-edge); b) Infrared spectra of C_3N_4, NRGO, acid functionalized MoS_2, C_3N_4-NRGO and C_3N_4–MoS_2 composites; c) Raman spectra of NRGO, acid functionalized MoS_2, C_3N_4-NRGO and C_3N_4 -MoS_2 composites; (d) Solid-state ^{13}C CP-MAS NMR spectra of C_3N_4, acid functionalized MoS_2, C_3N_4-MoS_2 composite.

The infrared (IR) spectrum of C_3N_4 has bands at 1240, 1414, 1564 and 1634 cm^{-1} due to C=N and C–N stretching modes (Figure 4b) and a band at 812 cm^{-1} due to the breathing mode of the s-triazine ring. The broad band in the 3000-3400 cm^{-1} region is due to the presence of amine groups.[25] NRGO exhibits -C=O and –OH stretching modes at 1715 and 3110 cm^{-1}, assigned to the residual carboxyl groups in the basal plane, whereas MoS_2–CH_2COOH shows bands at 1702 and 3200 cm^{-1} corresponding to -C=O and –OH stretching modes along with a C-S stretching band at 700 cm^{-1} arising from covalent functionalization of MoS_2. The IR spectrum of the C_3N_4-NRGO composite (Figure 4b) exhibits a C=O stretching band at 1660 cm^{-1} due to the amide bond between the C_3N_4 and NRGO layers along with other characteristic vibration frequencies. C_3N_4-MoS_2 nanocomposites shows the carbonyl stretching band at 1660 cm^{-1}, confirming cross-linking of carboxylated MoS_2 nanosheets with amine functionalized C_3N_4 by amide bonds. Raman spectra of the C_3N_4-NRGO and C_3N_4-MoS_2 composites along with those of individual components are shown in Figure 4c. MoS_2-CH_2COOH shows only bands due to the 2H-polytype, similar to the behavior observed after reactions of 1T-MoS_2 with metal precursors and diazonium salts.[18, 26] Compared to MoS_2-CH_2COOH, the A_{1g} mode of the C_3N_4-MoS_2 composite is red-shifted, whereas the physical mixture does not exhibit any significant shift, this indicates that covalent cross-linking leads to better interconnectivity between the individual components which results in efficient charge-transfer from C_3N_4 to MoS_2 (Figure 4c).[27] Raman spectra of both NRGO and C_3N_4-MoS_2 composite show D and G-bands at 1346 and 1588 cm^{-1}, respectively with an enhancement in the FWHM of the bands in the latter case. Cross-linking causes intercalation of C_3N_4 between the NRGO layers and vice versa thereby increases the FWHM. Thus, IR and Raman spectra of the nanocomposites confirm cross-linking of C_3N_4 and NRGO or MoS_2 sheets by layer-by-layer assembly through amide bonds.

Nitrogen content in the NRGO sample is 8.2 wt% as obtained from elemental analysis as well as XPS measurements. To further confirm the formation of the amide bond in the composites we have performed solid-state ^{13}C CP-MAS NMR spectroscopy (Figure 4d). Two distinct signals dominate the spectrum of C_3N_4 at 165 and 154 ppm due to the sp^2 carbon atoms.[28] MoS_2-CH_2COOH shows characteristic ^{13}C signals at 46.5 and 171 ppm corresponding to aliphatic carbons (CH_2) and carbonyl groups, respectively. Compared to

MoS_2-CH_2COOH, the signals in the C_3N_4-MoS_2 composite are slightly downshifted to δ=169 ppm, indicating the cross-linking of C_3N_4 and MoS_2 nanosheets by forming amide bond.

Surface area and porosities of C_3N_4, NRGO, MoS_2, C_3N_4-NRGO and C_3N_4-MoS_2 composites were obtained by N_2 adsorption-desorption measurements at 77 K. The cross-linked composites show microporous type-1 adsorption behavior at low pressures along with a type H4 hysteresis loop associated with narrow slit-like pores (Figure 5). Brunauer-Emmet-Teller (BET) surface areas of cross-linked C_3N_4-NRGO and C_3N_4-MoS_2 composites are 186 and 151 m^2/g while physical mixture of C_3N_4 and NRGO or MoS_2 show low surface areas of 98 and 69 m^2/g, respectively.

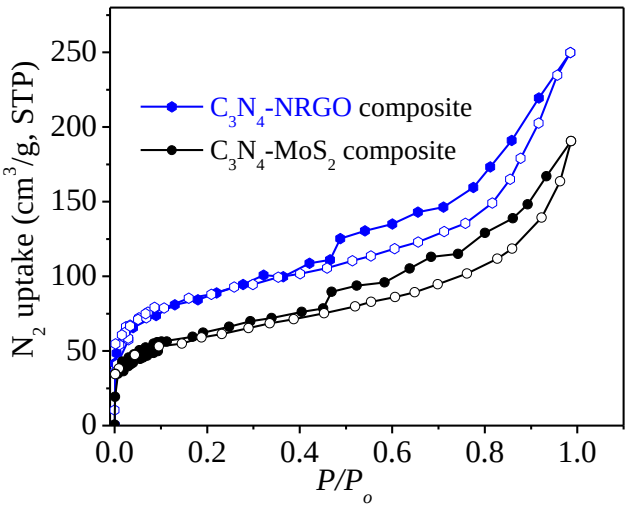

Figure 5. N_2 sorption profiles of C_3N_4-NRGO and C_3N_4–MoS_2 nanocomposites.

The enhanced surface area is attributed to the generated pores due to stacking and cross-linking between the C_3N_4 and NRGO (or) MoS_2 layers which is evident in the N_2 isotherms. It must be noted C_3N_4 and few-layer MoS_2 show much lower surface areas of 65 and 40 m^2/g respectively, NRGO has a surface area of 130 m^2/g with a type-IV mesoporous sorption profile.

Cross-linked C_3N_4-NRGO and C_3N_4-MoS_2 composites were examined for the photochemical hydrogen evolution in aqueous solution of triethanolamine (TEOA, 20% v/v) as sacrificial agent under UV-Vis light (Xenon lamp, 250-900 nm, see experimental section for more details) illumination. C_3N_4 alone has an activity of 52 μmoles $h^{-1}g^{-1}$ with a TOF 0.005 h^{-1}

while the chemically bonded C_3N_4-NRGO composite exhibits an enhanced activity of 308 µmoles $h^{-1}g^{-1}$ with a TOF of 0.06 h^{-1}.

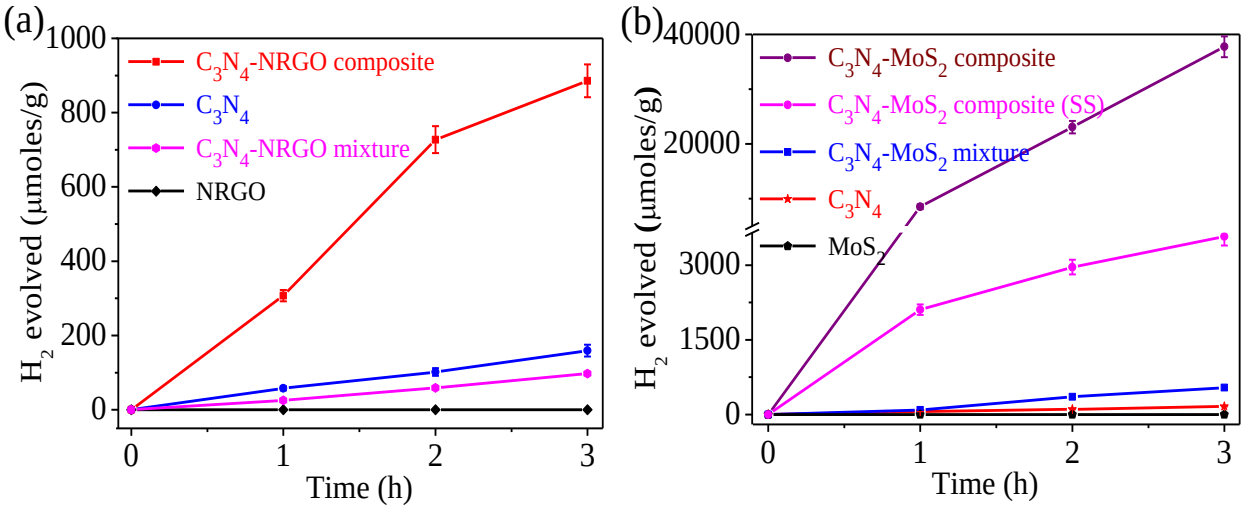

Figure 6. Comparison of the H_2 evolution activity of a) C_3N_4, NRGO, physical mixture of C_3N_4 and NRGO and the covalently bonded C_3N_4-NRGO nanocomposite; b) C_3N_4, MoS_2, physical mixture of C_3N_4 and MoS_2, C_3N_4-MoS_2 composite (SS, obtained by solid state route) and the covalently bonded C_3N_4-MoS_2 nanocomposite.

The physical mixture of C_3N_4 and NRGO shows activity of only 32 µmoles $h^{-1}g^{-1}$ with a TOF 0.006 h^{-1} (Figure 6a). The covalently linked C_3N_4-MoS_2 composite shows an extraordinarily high activity of 12778 µmoles $h^{-1}g^{-1}$ with a TOF of 2.35 h^{-1} (Table 1). The physical mixture of C_3N_4 and MoS_2, and their composite obtained by the solid state route exhibit low photochemical activity of 187 and 1157 µmoles $h^{-1}g^{-1}$ with a TOF 0.04 and 0.22 h^{-1}, respectively (Figure 6b).

We have carried out control experiments on individual C_3N_4, MoS_2 and NRGO in the presence of TEOA, C_3N_4 (52 µmoles $h^{-1}g^{-1}$) is photoactive for HER, while NRGO and MoS_2 are inactive (Figure 7a). We have also examined the H_2 evolution activity only in the presence of the photosensitizer (Eosin Y dye) to indicate active HER sites on NRGO or MoS_2, and found that NRGO is inactive whereas, MoS_2 shows H_2 evolution due to the appropriate band positions (Figure 7b).

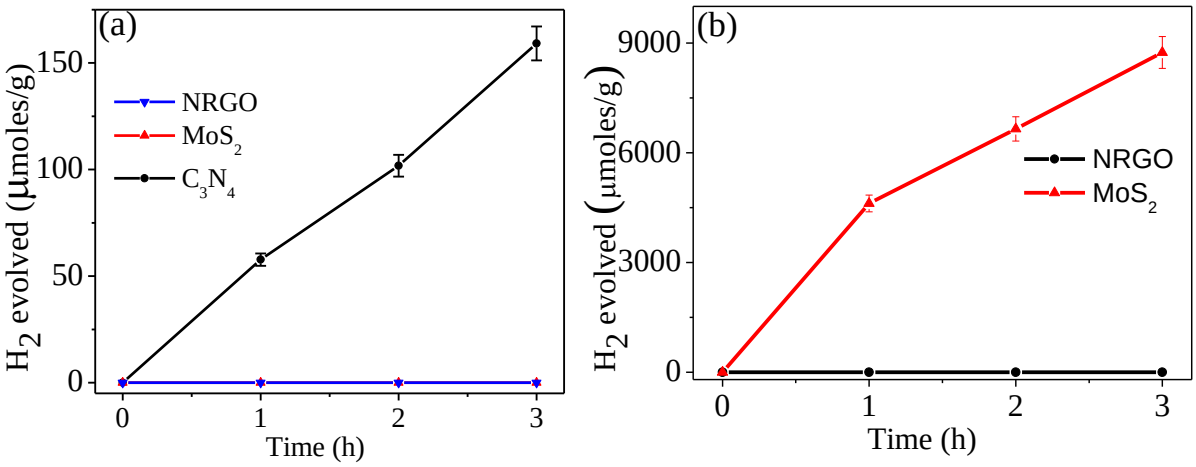

Figure 7. (a) Hydrogen evolution of C_3N_4, MoS_2 and NRGO in light and triethanolamine; (b) Eosin Y dye assisted hydrogen evolution in NRGO and MoS_2 under light in presence of triethanolamine.

Photoluminescence studies were carried on C_3N_4-NRGO and C_3N_4-MoS_2 composites to understand the photoexcited electron transfer mechanism between the cross-linked layers. These studies confirm that the PL signal of C_3N_4 at 440 nm is drastically quenched in the cross-linked composites due to charge-transfer (CT) from C_3N_4 to MoS_2 or NRGO (Figure 8).

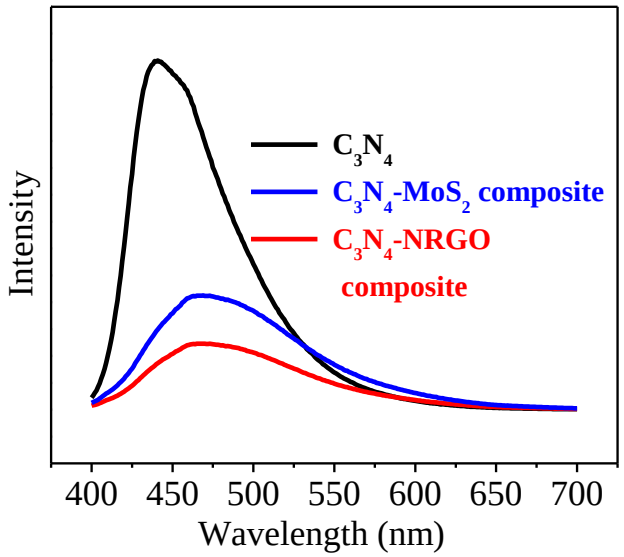

Figure 8. Photoluminescence spectra of C_3N_4, C_3N_4-NRGO composite and C_3N_4-MoS_2 composite.

Electron transfer from C_3N_4 to MoS_2 (NRGO) is thermodynamically favorable since the conduction band minimum (CBM) of C_3N_4 is higher in energy than that of MoS_2 (NRGO).[11, 13]

Using density functional theory (DFT), we have calculated the energy of the orbitals of cross-linked C_3N_4-NRGO and C_3N_4-MoS_2 composites and the corresponding wavefunction plots obtained by considering maximum contribution from the individual components to these orbitals (Figures 9a and b).

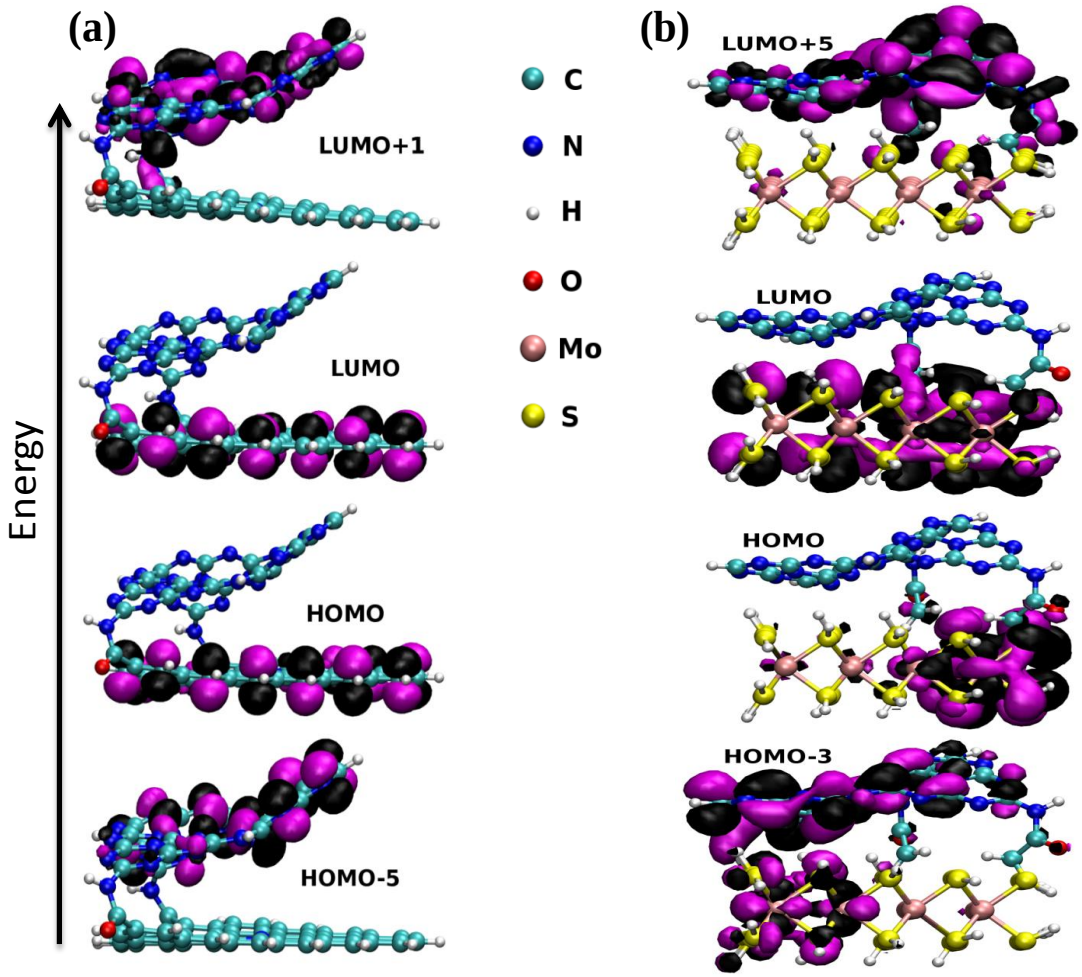

Figure 9. Wavefunction plots of (a) C_3N_4-NRGO nanocomposite and (b) C_3N_4-MoS_2 nanocomposites, where the upper layer is C_3N_4 for both the cases (Inter-layer spacing in C_3N_4-NRGO and C_3N_4-MoS_2 composites are 0.30 and 0.73 nm, respectively which are comparable with the experimentally observed values).

The wave function plots of the C_3N_4-NRGO composite shows that there is a possibility of CT from the highest occupied molecular orbital (HOMO), mainly contributed by NRGO to the lowest unoccupied molecular orbital (LUMO+1) with a major contribution from C_3N_4 (Figure 9a). On the other hand, the C_3N_4-MoS_2 composite shows that there is a possibility of CT from the HOMO-3 (on C_3N_4) to LUMO (on MoS_2) (Figure 9b). The magnitude of CT in C_3N_4-NRGO and C_3N_4-MoS_2 composites are 0.31 and 0.29 e^-. Without considering the cross-linked bonds, they show a decrease in CT to 0.23 and 0.18 e^-, respectively. This implies that CT in the composites occurs simultaneously through space and bonds between the cross-linked layers. Furthermore, the magnitude of CT in randomly slipped stack pattern of C_3N_4 and NRGO is similar to those observed experimentally in the case of physical mixtures, decreasing to 0.07 e^-. It is therefore suggested that cross-linked systems have better CT efficiency. DFT calculations also suggest that cross-linking induces planarity, which leads to efficient CT in composites due to better orbital overlapping. The wave function plots of composites also elucidate the photo-induced CT in cross-linked composites, since C_3N_4 LUMO is higher in energy and can transfer electron to LUMO of NRGO or MoS_2 on photo excitation. Schematic energy band diagrams for composites are derived on the basis of control experiments, PL studies as well as theoretical calculations which highlights electronic events during photoexcitation (Figures 10a and b).

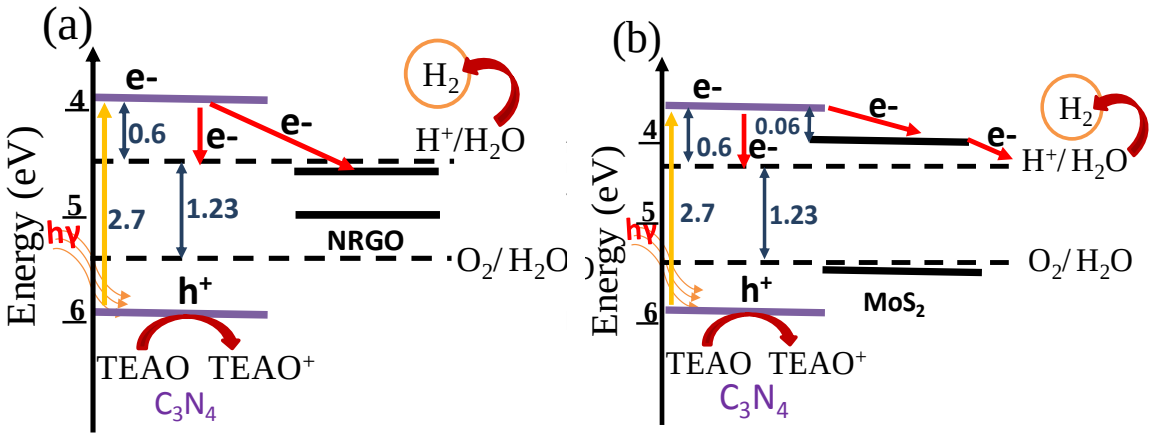

Figure 10. Schematic energy band diagram highlighting different electronic process during HER in (a) C_3N_4-NRGO and (b) C_3N_4–MoS_2 composites (orange arrow indicates photoexcitation of electron from VBM to CBM of C_3N_4 and red arrows indicates different electronic events in the composites during HER).

On photoexcitation, electron from valence band maxima (VBM, orange arrow) of C_3N_4 is excited to conduction band minima (CBM), and then transfers to CBM of NRGO or MoS_2 (red arrows). Since CBM of NRGO is below the water reduction potential, electrons transferred from C_3N_4 to NRGO will not participate in HER unlike in MoS_2. H_2 evolution occurs in the presence of TEOA which reduces the photogenerated holes by donating electrons to the VBM of C_3N_4, and favors the forward reaction.

The increase in photochemical catalytic activity with respect to C_3N_4 is more pronounced in the C_3N_4–MoS_2 composite compared to C_3N_4-NRGO. Cross-linked C_3N_4–MoS_2 exhibits an enhancement of ~246 times as compared to C_3N_4 whereas, C_3N_4-NRGO shows only ~6 times. The lower activity of C_3N_4-NRGO composite over C_3N_4–MoS_2 can be attributed to the different electronic processes occurring on catalytic surface during HER. In Figure 10a we show a schematic of the energy band diagram of C_3N_4-NRGO which indicates that photoexcited electrons (orange arrow) of C_3N_4 can either transferred to CBM of NRGO or undergo water reduction on C_3N_4 surface (red arrows). As the CBM energy gradient between C_3N_4 and NRGO is more compared to the water reduction potential, chances of electrons moving from the CBM of C_3N_4 to NRGO is less favored. DFT calculated relative binding energies of water molecule with the C_3N_4 and NRGO are 0.0 and 0.86 eV respectively suggesting that C_3N_4 is preferred for HER in the C_3N_4-NRGO composite. Furthermore, H_2 evolution occurs on the C_3N_4 surface alone since, the CBM of NRGO is below water reduction potential. This indicates that in the C_3N_4-NRGO composite enhanced activity arises mostly because of the increased planarity of the layers and the enhanced surface area due to cross-linking while some electrons can still shuttle across the network through NRGO. The physical mixture of C_3N_4 and NRGO does not show any increased activity as compared to C_3N_4 which supports this rationale. Figure 10b shows a schematic of the energy band diagram of the C_3N_4–MoS_2 composite, where the photoexcited electrons of C_3N_4 either reduce water or transfer to the CBM of MoS_2 (red arrows) for H_2 evolution. As the thermodynamic gradient between the CBM of C_3N_4 and of MoS_2 (0.06 eV) is less compared the HER potential (0.6 eV), there is a high probability of electron transfer from C_3N_4 to MoS_2 which also participate in water reduction (red arrows). The relative binding energy of water molecule (as calculated from DFT) for MoS_2 edge site, surface and on C_3N_4 is 0.0, 0.04 and 0.27 eV respectively, which shows that MoS_2 is preferred for HER,

particularly the edge sites. The physical mixture and solid state composite of C_3N_4 and MoS_2 also show increased activity compared to C_3N_4, supporting this reasoning. Apart from the achieved planarity and enhanced surface area, additional factors like favored CT due to cross-linking and active MoS_2 sites gives better H_2 evolution activity in C_3N_4–MoS_2 composite as compared to C_3N_4–NRGO.

In the case of physical mixture of C_3N_4 and MoS_2, enhancement in photochemical HER activity with respect to C_3N_4 is ~4 times, whereas the C_3N_4–MoS_2 composite obtained by the solid state route shows an increase by ~23 times (Figure 6b). This result clearly suggests that C_3N_4 grown on MoS_2 layers provides greater interaction between the two, thereby exhibiting higher HER activity compared to the physical mixture where layers are randomly oriented (Figure 3b). On the other hand, cross-linked C_3N_4-MoS_2 shows an enhancement of ~246 times with respect to C_3N_4 which is ~11 and 68 times higher than the sample obtained by solid state route and the physical mixture respectively. The superior performance of the cross-linked assemblies is attributed to the enhanced interfacial area as well as planarity between the layers due to directional layer-by-layer cross-linking which increases the magnitude of CT between C_3N_4 and MoS_2 as it occurs simultaneously through both space and bonds between the individual layers. Secondly, the 3D network formed due to cross-linking causes additional increment in the magnitude of CT due to effective electronic coupling between the heterolayers in the cross-linking direction, contributing to the improved HER performance. This reasoning is supported by both PL and theoretical studies. Lack of directional bonds in the physical mixture as well as in the composite obtained from the solid state route reduces the magnitude of CT between layers, homogeneity in the order of heterolayers, planarity as well as the formation of extended 3D network which limits their HER performance. We have compared the activity of covalently cross-linked C_3N_4-MoS_2 composite with other similar systems in the literature, and found it to be higher than any C_3N_4 or MoS_2 based system (Table 1). Furthermore, efficient electron channeling across 3D network through space as well as by bonds between cross-linked layers makes better charge separation and thereby enhancing the activity. We also note that in physical mixtures, the layers are stacked by weak van der Waals interaction which can get disrupted during sonication, as sample dispersion is a prerequisite for photochemical studies.

Table 1: Comparison of hydrogen evolution data of covalently bonded NRGO-C_3N_4 and MoS_2-C_3N_4 composites compared with few of the literature reports.

Catalyst	Activity (μmole h^{-1} g^{-1})	TOF [(a)] (h^{-1})	Reaction Conditions
C_3N_4	52±3	0.005±2x10^{-4}	TEOA:H_2O (1:4) (400 W Xe lamp; λ>250-900 nm)
C_3N_4-MoS_2 (Composite)	12778±638	2.35±0.1	
C_3N_4-MoS_2 (Composite SS)	1157±58	0.22±0.01	
C_3N_4-NRGO (Composite)	308±15	0.06±3x10^{-3}	
C_3N_4/Pt (1 wt%)[29]	122	0.011	Methanol: H_2O (1:3) (300 W Xe lamp; λ>400 nm)
C_3N_4/Pt-Co[30]	60	0.006	Pure H_2O (300 W Xe lamp; λ>300 nm)
C_3N_4-$Co^{III}(dmgH)_2pyCl$[31]	250	0.023	TEOA: H_2O (1:6) (300 W Xe lamp; λ>350-740 nm)
C_3N_4-Carbon Quantum Dots[8]	105	0.010	Pure H_2O (300 W Xe lamp; λ>420 nm)
C_3N_4-MoS_2 Quantum dots/Pt[32]	394	0.036	TEOA: H_2O (1:9) (300 W Xe lamp; λ>420 nm)
Layered C_3N_4-MoS_2 nanojunctions[10]	968	0.091	Lactic acid: H_2O (1:9) (300 W Xe lamp; λ>420 nm)
C_3N_4-MoS_2[11]	252	0.024	TEOA : H_2O (1:9) (300 W Xe lamp; λ>400 nm)

[(a)]TOF is calculated for photoactive component C_3N_4 since MoS_2, NRGO, Pt, Carbon Quantum Dots and Cobaltoxime are co-catalysts.

Encouraged by the results obtained with the photochemical HER by covalently bonded C_3N_4-MoS_2 and C_3N_4-NRGO composites, we have examined their performance in electrochemical HER. Linear Sweep Voltammetry (LSV) plots obtained for the cathodic reduction of H^+ ion to H_2 is given in Figures 11a and b. The onset potential which is the measure of extra energy needed to attain a faradic process of H_2 generation is improved in covalently cross-linked C_3N_4-NRGO and C_3N_4-MoS_2 catalysts in comparison to that of the

physically mixed counterparts (Table 2). The cross-linked C_3N_4-NRGO (-0.36 V) composite shows a shift of 60 mV in onset potential (η) as compared to that of physical mixture (-0.42 V). On the other hand, physical mixture of C_3N_4 and MoS_2 (-0. 29 V) shows 40 mV improvement in η in comparison to MoS_2 only (-0.33 V) whereas when the two are covalently linked, we obtained 100 mV shift in onset potential (-0.23 V) in positive direction. C_3N_4 alone showed negligible activity in HER whereas the physical mixture of C_3N_4 with NRGO or MoS_2 exhibits enhanced activity compared to the individual components.

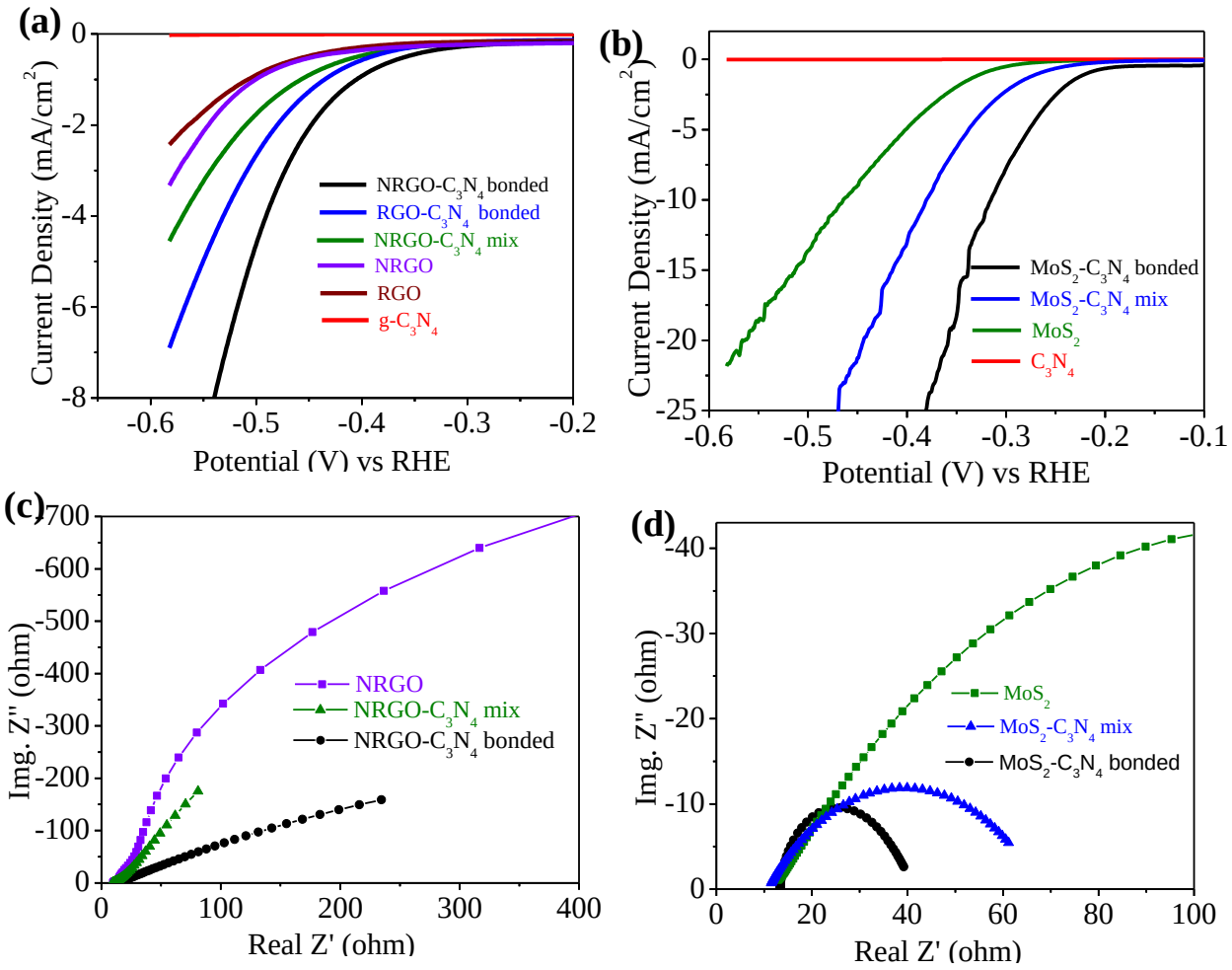

Figure 11. Linear Sweep Voltammogram (LSV) polarization curves of (a) C_3N_4, NRGO, physical mixture of C_3N_4 and NRGO and covalently bonded C_3N_4-NRGO nanocomposite; (b) C_3N_4, MoS_2, physical mixture of C_3N_4 and NRGO and covalently bonded C_3N_4-MoS_2 nanocomposite, and Nyquist plots of (c) NRGO, physical mixture of C_3N_4 and NRGO and covalently bonded C_3N_4-NRGO nanocomposite; (d) MoS_2, physical mixture of C_3N_4 and MoS_2 and covalently bonded C_3N_4-MoS_2 nanocomposite.

The enhancement is however, much more prominent in the cross-linked composites as compared to that of physical mixtures. A similar trend in HER activity was encountered in the photochemical studies as well. The minimum voltage required to increase the current density by ten-fold is given by the value of Tafel slope, smaller the slope better is the electrocatalytic activity. Cross-linked composites have smaller Tafel slope values compared to that of physical mixture. In Table 2, we compare the onset potential, Tafel slope values of covalently cross-linked C_3N_4-NRGO and C_3N_4-MoS_2 composites with those of physical mixture along with that of Pt/C (40 wt%, Sigma Aldrich). The observed trend was further probed by conducting Electrochemical Impedance Spectroscopy (EIS) studies on covalently bonded C_3N_4-NRGO and C_3N_4-MoS_2 composites as well as on their physical mixtures as shown in Figures 11c and d. Nyquist plots were measured within the frequency range of 10^5 Hz to 1 Hz at open circuit potential for all electrodes. The diameter of the semicircle in the high-frequency region gives the measure of resistance in charge-transfer (R_{ct}) process at the electrolyte/electrode interface.

Table 2: Comparison of electrocatalytic HER activity and Tafel slope values of covalently bonded C_3N_4-NRGO and C_3N_4-MoS_2 composites with other catalysts.

Sample	Overpotential (η) (V) vs RHE	η@5 mA/cm^2 (V) vs RHE	Tafel slope (mV/dec)
C_3N_4-NRGO (composite)	-0.368±0.02	-0.506±0.025	147
C_3N_4 -NRGO (mixture)	-0.429±0.02	-0.589±0.029	180
NRGO	-0.487±0.025	-	182
C_3N_4-MoS_2 (composite)	-0.234±0.011	-0.278±0.013	88
C_3N_4-MoS_2 (mixture)	-0.289±0.014	-0.33±0.016	95
MoS_2	-0.330±0.016	-0.401±0.02	99
Pt/C (40 wt%)	-0.002±0.0	-0.021±0.0	34

From Figures 11c and d, it is very clear that the cross-linked C_3N_4-NRGO and C_3N_4-MoS_2 catalysts have comparatively smaller R_{ct} than the physically mixed catalysts.

The broad, incomplete semicircle feature in the case of NRGO-based catalysts could arise from the non-uniform cathodic current due to the geometrically inhomogeneous electrode surface.[33] Comparison of R_{cat} values amongst the catalysts hints that the cross-linked C_3N_4-NRGO and C_3N_4-MoS_2 composites have minimum R_{cat} value, indicating relative ease in electron transport in the extended 3D network when polarized by the application of a negative potential. The well-defined interconnectivity between the cross-linked layers promotes appropriate coupling [34, 35] to minimize charge-transfer resistance,[36, 37] thereby improving the HER activity. Increased planarity due to cross-linking also leads to better orbital overlapping ensuing efficient CT between the cross-linked layers through both space and bonds can ease the mobilization of electrons, and results in reduction of the onset potential. Furthermore, increased surface area and the pores generated by cross-linking ensure the larger electrode/electrolyte interface area which also contributes to the enhanced activity.

4.5.5: Conclusions

We have been able to covalently cross-link nanosheets of C_3N_4 with sheets of MoS_2 as well as NRGO by the carbodimide method. The cross-linked composites show better catalytic activity relative to the physical mixtures or C_3N_4 alone. The present study clearly demonstrates the beneficial effects of covalent bonding in the case of C_3N_4-MoS_2 and C_3N_4-NRGO composites, particularly in the case of former. Photochemical HER activity of the C_3N_4-MoS_2 nanocomposite is noteworthy with ~246 times increased activity compared to C_3N_4. Furthermore, cross-linked C_3N_4-MoS_2 shows an enhancement of ~11 and 68 times higher photochemical HER activity than that obtained by the solid state method and the physical mixture respectively. We conclude from theoretical and experimental studies that enhanced HER activity in cross-linked composites arises from the increased planarity, enhanced charge-transfer and higher surface area. DFT calculations show that the magnitude of charge-transfer is maximum in the case of cross-linked composite since it occurs between the cross-linked layers simultaneously through space as well as bonds. Electrochemical HER activity of the nanocomposites is also superior, shows that covalent cross-linking to be useful

for HER and related catalytic reactions. This strategy may also be of value in a variety of other applications as well.

4.5.6: References

1. X. Wang, K. Maeda, A. Thomas, K. Takanabe, G. Xin, J. M. Carlsson, K. Domen, M. A. Antonietti, *Nat. Mater.* **2009,** *8*, 76.
2. Y. Shi, B. Zhang, *Chem. Soc. Rev.* **2016**, *45*, 1529.
3. C. N. R. Rao, S. R. Lingampalli, S. Dey, A. Roy, *Philos. Trans. R. Soc. A* **2016**, **DOI:** 10.1098/rsta.2015.0088.
4. Y. Zheng, Y. Jiao, Y. Zhu, L. H. Li, Y. Han, Y. Chen, A. Du, M. Jaroniec, S. Z. Qiao, *Nat. Commun.* **2014, DOI:10.1038/ncomms4783**.
5. Y. Li, H. Wang, L. Xie, Y. Liang, G. Hong, H. Dai, *J. Am. Chem. Soc.* **2011,** *133*, 7296.
6. M. Chhetri, S. Maitra, H. Chakraborty, U. V. Waghmare, C. N. R. Rao, *Energy Environ. Sci.* **2016,** *9*, 95.
7. H. Vrubel, X. Hu, *Angew. Chem., Int. Ed.* **2012,** *24*, 12703.
8. J. Liu, Y. Liu, N. Liu, Y. Han, X. Zhang, H. Huang, Y. Lifshitz, S.-T. Lee, J. Zhong, Z. Kang, *Science* **2015,** *47*, 970.
9. X. Zou, Y. Zhang, *Chem. Soc. Rev.* **2015**, *44*, 5148.
10. Y. Hou, A. B. Laursen, J. Zhang, G. Zhang, Y. Zhu, X. Wang, S. Dahl, I. Chorkendorff, *Angew. Chem. Int. Ed.* **2013**, *52*, 3621.
11. H. Zhao, Y. Dong, P. Jiang, H. Miao, G. Wang, J. Zhang, *J. Mater. Chem. A* **2015**, *3*, 7375.
12. L. Ye, D. Wang, S. Chen, *ACS Appl. Mater. Interfaces* **2016**, *8*, 5280.
13. Y. Hou, Z. Wen, S. Cui, X. Guo, J. Chen, *Adv. Mater.* **2013**, *25*, 6291.
14. D. Chen, W. Chen, L. Ma, G. Ji, K. Chang, J. Y. Lee, *Mater. Today* **2014**, *17*, 184.
15. U. Maitra, U. Gupta, M. De, R, Datta, A. Govindaraj, C. N. R. Rao, *Angew. Chem., Int. Ed.* **2013**, *52*, 13057.
16. J. Duan, S. Chen, M. Jaroniec, S. Z. Qiao, *ACS Nano* **2015**, *9*, 931.
17. D. Pierucci, H. Henck, J. Avila, A. Balan, C. H. Naylor, G. Patriarche, Y. J. Dappe, M. G. Silly, F. Sirotti, A. T. C. Johnson, M. C. Asensio, A. Ouerghi, *Nano Lett.* **2016**, *16*, 4054.
18. K. Pramoda, U. Gupta, I. Ahmad, R. Kumar, C. N. R. Rao, *J. Mater. Chem. A* **2016,** *4*, 8989.

19. Z. Zhao, Y. Sun, Q. Luo, F. Dong, H. Li, W.-K. Ho, *Sci. Rep.* **2015**, *5*, 14643.
20. D. Voiry, A. Goswami, R. Kappera, e. Castro, D. Kaplan, T. Fujita, M. Chen, T. Asefa, M. Chhowalla, *Nat. Chem.* **2015**, *7*, 45.
21. K. Gopalakrishnan, A. Govindaraj, C. N. R. Rao, *J. Mater. Chem. A* **2013**, *1*, 7563.
22. Gaussian 09, Revision D.01, M. J. Frisch, G. W. Trucks, H. B. Schlegel G. E. Scuseria, M. Robb, J. R. Cheeseman, G. Scalmani, V. Barone, B. Mennucci, G. A. Petersson, H. Nakatsuji, M. Caricato, X. Li, H. P. Hratchian, A. F. Izmaylov, J. Bloino, G. Zheng, J. L. Sonnenberg, M. Hada, M. Ehara, K. Toyota, R. Fukuda, J. Hasegawa, M. Ishida, T. Nakajima, Y. Honda, O. Kitao, H. Nakai, T. Vreven, J. A. Montgomery, Jr., J. E. Peralta, F. Ogliaro, M. Bearpark, J. J. Heyd, E. Brothers, K. N. Kudin, V. N. Staroverov, R. Kobayashi, J. Normand, K. Raghavachari, A. Rendell, J. C. Burant, S. S. Iyengar, J. Tomasi, M. Cossi, N. Rega, J. M. Millam, M. Klene, J. E. Knox, J. B. Cross, V. Bakken, C. Adamo, J. Jaramillo, R. Gomperts, R. E. Stratmann, O. Yazyev, A. J. Austin, R. Cammi, C. Pomelli, J. W. Ochterski, R. L. Martin, K. Morokuma, V. G. Zakrzewski, G. A. Voth, P. Salvador, J. J. Dannenberg, S. Dapprich, A. D. Daniels, Ö. Farkas, J. B. Foresman, J. V. Ortiz, J. Cioslowski, D. J. Fox, *Gaussian, Inc., Wallingford CT*, **2009**.
23. T. Yanai, D. P. Tew, N. C. Handy, Chem. Phys. Lett. 2004, 393, 51.
24. A. D. Becke, *J. Chem. Phys*. **1993**, *98*, 5648.
25. H. Xu, J. Yan, X. She, L. Xu, J. Xia, Y. Xu, Y. Song, L. Huang, H. Li, *Nanoscale* **2014**, *6*, 1406.
26. K. Pramoda, M. Kaur, U. Gupta, C. N. R. Rao, *Dalton Trans.* **2016**, *35*, 13810.
27. W. Fu, H. He, Z. Zhang, C. Wu, X. Wang, H. Wang, Q. Zeng, L. Sun, X. Wang, J. Zhou, Q. Fu, P. Yu, Z. Zhen, C. Jin, B. Yakobson, Z. Liu, *Nano Energy*, **2016**, *27*, 44.
28. Y. Chen, B. Lin, W. Yu, Y. Yang, S. M. Bashir, H. Wang, K. Takanabe, H. Idriss, J.-M. Basset. *Chem. Eur. J.* **2015**, *21*, 10290.
29. L. Ge, C. Han, X. Xiao, L. Guo, Y. Li, *Mater. Res. Bull.* **2013**, *48*, 3919.
30. G. Zhang, Z. Lan, L. Lin, S. Lin and X. Wang, *Chem. Sci.* **2016**, *7*, 3062.
31. S. W. Cao, X. F. Liu, Y. P. Yuan, Z. Y. Zhang, J. Fang, S. C. J. Loo, J. Barber, T. C. Sum, C. Xue, *Phys. Chem. Chem. Phys.* **2013**, *15*, 18363.
32. J. X. Jin, X. Fan, J. Tian, R. Cheng, M. Li, L. Zhang, *RSC Adv*. **2016**, *6*, 52611.

33. Q. Cheng, Z. Chen, *Int. J. Electrochem. Sci.* **2013,** *8***,** 8282.
34. Y. Zhao, L. Kuai, Y. Liu, P. Wang, H. Arandiyan, S. Cao, J. Zhang, F. Li, Q. Wang, B. Geng, H. Sun, *Sci. Rep.* **2015, doi:10.1038/srep08722.**
35. Q. Xiang, J. Yu, M. Jaroniec, *J. Am. Chem. Soc.* **2012**, *134*, 6575.
36. N. S. Alhajri, D. H. Anjum, K. Takanabe, *J. Mater. Chem. A* ***2*014**, *2*, 10548.
37. Y. Li, H. Wang, L. Xie, Y. Liang, G. Hong, H. Dai, *J. Am. Chem. Soc.* **2011,** *133*,7296.

Part 5

Borocarbonitride-based Nanocomposites

5.1: Borocarbonitride-Iron Pthalocyanine Composite as a Non-Precious Catalyst for the Oxygen Reduction Reaction

Summary*

Oxygen reduction reaction (ORR) is an important reaction occurring at the cathode of a fuel cell. In the present study, we demonstrate the use of a borocarbonitride (BC_5N) supported iron (II) phthalocyanine as a superior non-noble electrocatalyst for the ORR. To assess the ORR activity of BC_5N-FePc, cyclic voltammetry and rotating disk electrode measurements have been carried out. These measurements reveal that the BC_5N-FePc exhibits more positive onset potential and comparable current density relative to the commercially available Pt/C catalyst. Furthermore, BC_5N-FePc shows excellent selectivity towards ORR even in the presence of methanol.

Papers based on this worked have been published in *J. Mater. Chem. A (*2013**)**, *Nanomater. Energy, (2015).*

5.1.1: Introduction

The oxygen reduction reaction (ORR) at the cathode is of paramount importance in the performance of fuel cells.[1] The reduction process occurs via different mechanisms depending on the catalyst and pH of the electrolyte etc. The most effective reduction is a 4-electron process, in which O_2 is directly converted to H_2O. Platinum is an effective catalyst for this reduction reaction,[2, 3] but the high cost and the limited abundance restricts its use. Furthermore, when Pt is supported on conductive carbon, the catalyst leaches out due to the corrosion of carbon support in aggressive environments. This has given the motivation to search for alternative non-noble metal materials which fulfill the necessary criteria for good ORR catalysis. The non-Pt based materials reported for ORR include transition metal carbides,[4, 5] transition metal nitrides,[6-8] transition metal oxides[9-11] and transition metal chalcogenide.[12, 13] Several metal-free catalysts that have been studied include doped/undoped carbon materials such as graphene and carbon nanotubes (CNT).[14-22]

5.1.2: Scope of the present investigations

High onset potential and low current density are the major issues associated with non-Pt cathode catalysts used in ORR process. Catalyst with sufficient number of oxygen adsorption sites and good electronic conductivity cause reduction in onset potential and gives high current density during O_2 reduction at cathode. On this basis, researchers have made binary composites of graphene and CNTs with Iron Phthalocyanine (FePc). These studies revealed that FePc in combination with CNT (or) graphene showed better performance as O_2 reducing catalyst as compared to individual components. In this work, we report the use of BC_5N-FePc (designated as BCN-FePc for simplicity), both of which are intrinsically ORR active, as an efficient catalyst for the ORR process. Electrochemical experiments revealed that the ORR process occurred through a 4e- pathway and the onset potential was comparable to that of Pt/C. Moreover, the composite was very tolerant to the methanol cross over, showing good selectivity towards ORR.

5.1.3: Experimental section

BC_5N was synthesized by following the literature procedure reported elsewhere.[39] In a typical synthesis, 500mg of activated charcoal, boric acid and urea in 1:24 weight ratio were taken into 100ml beaker with water. This mixture was first sonicated for 30 min and then heated on an oil bath at 70 ^oC until the mixture became slurry. After this, the slurry was transferred into a quartz boat and kept in the tube furnace and heated at 900 ^oC in the presence of nitrogen for 10 hrs.

To prepare the BCN and Iron Pthalocyanine composite, equal proportions of BCN (5mg) and FePc (5mg) were sonicated in ethanol for 1hr. And the resulting dispersion was centrifuged to obtain the composite and dried under vacuum at 60 ^oC overnight. Thus dried product was collected and further used for characterization and the electrochemical experiments.

All the electrochemical measurements were carried out in electrochemical workstation coupled with Rotating disc electrode system. A conventional 3-electrode system was employed in which glassy carbon electrode (GCE) modified with BCN-FePc was used as the working electrode, Ag/ AgCl and Platinum coil are the reference and counter electrode, respectively. The modification of the GCE with BCN-FePc was done as follows. Prior to its use, the GCE was well polished sequentially using 1.0 micron, 0.3 micron and 0.05 micron alumina powder. Catalyst ink was prepared by dispersing the composite in ethanol (1mg/ml). A 6 µl of resultant dispersion was drop casted on the GCE using micropipette and allowed to dry at room temperature. Then 5 µl of nafion (0.5 wt %) is further drop casted as a binder. Cyclic Voltammetry and Linear Sweep Voltammetry measurements were performed in O_2 and N_2 saturated 0.1 M KOH at a scan rate of 100 mV/s and 5 mV/s respectively.

5.1.4: Results and discussion

TEM image of BCN/FePc composite (Figure 1a) indicates that FePC is well distributed on BCN matrix. Figure 1 b shows the Raman spectra of BCN, FePc, BCN-FePc.

The Raman spectrum of BCN-FePc show peaks originating from phthalocyanine as well as the G-band (E^1_{2g} mode) corresponds to sp^2 domains of BCN at 1600 cm^{-1} (Figure 2). From Raman and TEM we can conclude that FePc is well attached to the surface of BCN and the

electronic characteristics of FePc and BCN remain intact in the composite, indicating that the composite is homogenous.

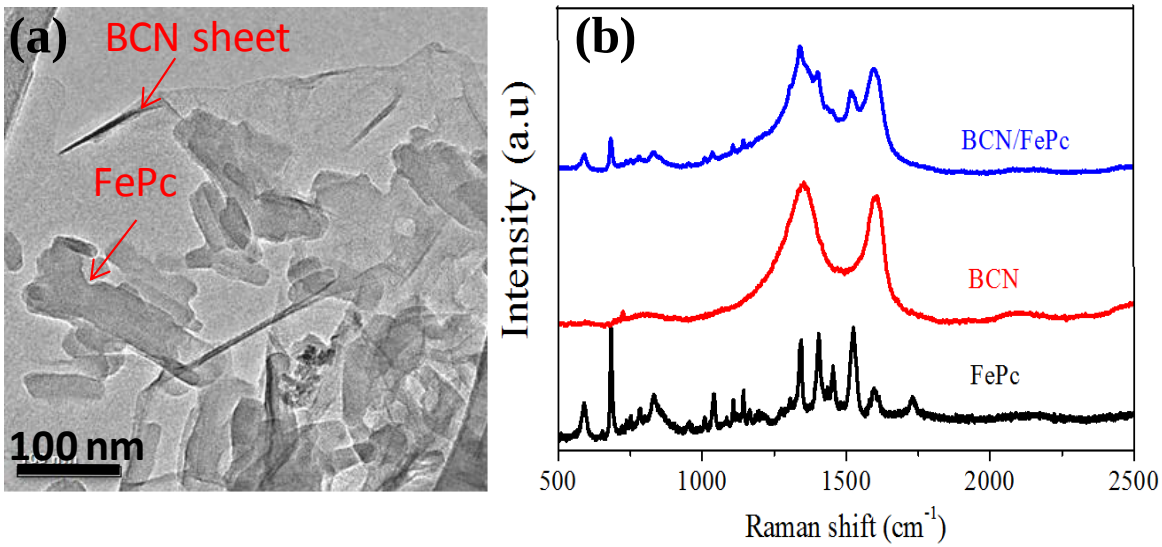

Figure 1. (a) TEM image of BCN/FePc, (b) Raman spectra of FePc, BCN and BCN/FePc.

To evaluate ORR activity, CV measurements are initially performed in 0.1 M KOH saturated with O_2. Figure 2a shows cyclic voltammograms of the BCN-FePc composite in the presence of O_2 and N_2-saturated electrolyte.

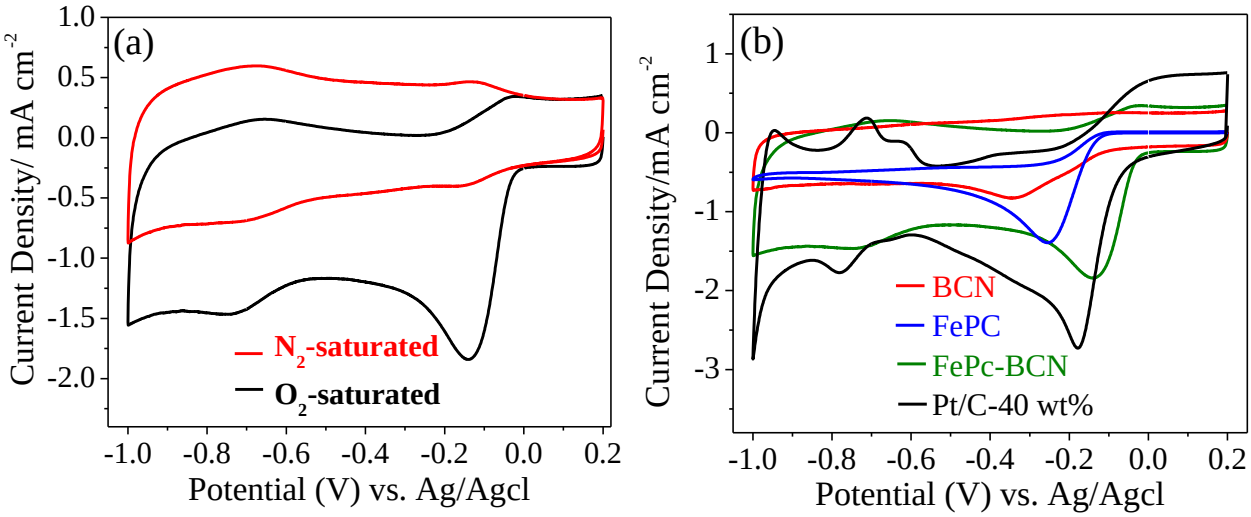

Figure 2. Cyclic voltommograms of (a) BCN/FePc on GCE in N_2 and O_2-saturated 0.1 M KOH solution at a scan rate of 100 mV/s, (b) BCN, FePc, BCN/FePc and Pt/C on GCE in O_2-saturated 0.1 M KOH solution at a scan rate of 100 mV/s.

The O_2-saturated KOH solution of BCN-FePc exhibits a pronounced ORR peak at -0.14 V indicating the reduction of oxygen, whereas no reduction peak is observed in the case of N_2-saturated solution. We compare the results with those of the individual components BCN, FePc and Pt/C under similar conditions. The ORR onset peak potential of BCN-FePc (-0.064 V) is more positive than that of pristine BCN, FePc and while the current density is larger than that of BCN or FePc as shown in Figure 2b. This is further corroborated by static linear sweep voltammetry (LSV).

In order to probe the mechanism of ORR and to understand reaction kinetics, rotating disc electrode (RDE) measurements were performed in the LSV mode in O_2 saturated KOH solution (0.1M) at 5 mV/s scan rate. Linear sweep voltammograms of BCN-FePc along with those of BCN, FePc, Pt/C 40 wt% are shown in Figure 3a.

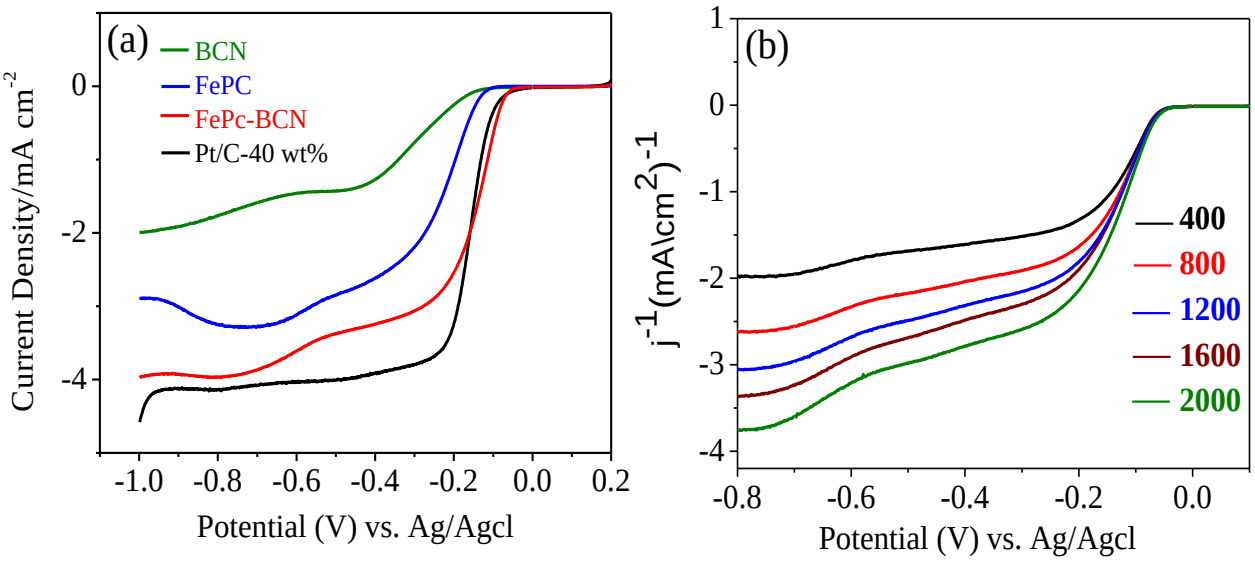

Figure 3. (a) LSV curves of the BCN, FePc, BCN/FePc and Pt/C electrodes in O_2-saturated 0.1 M KOH at a scan rate of 5 mV/s and at a rotation speed of 1600 rpm; (b) LSV curves of the BCN/FePc electrode in O_2-saturated 0.1 M KOH at a scan rate of 5 mV/s

It is interesting that BCN-FePc (-0.064V) shows a slightly more positive onset potential than Pt/C (-0.082V) (Figure 3a). The current density of BCN-FePc is close to that of Pt/C. The ORR current density of BCN-FePc increases with the increase in the rotation speed of the electrode due to the high availability of O_2 at the electrode interface as shown in Figure 3b. These results clearly establish the facile reduction of O_2 at BCN-FePc composite compared

with individual components. The half wave potential for BCN/FePc modified GCE is about -0.10 V which is slightly more positive than Pt/C (-0.15 V).

The number of electrons transferred per oxygen molecule from BCN/FePc modified electrode can be calculated by using Koutechy-Levich equation.[40]

$$1/I = 1/I_k + 1/I_d$$

$$1/I = -1/(nFkC_o) - 1/(0.2\ nFD_o^{2/3}\gamma^{-1/6}C_o\omega^{1/2})$$

In which **I** denotes measured current density at respective potentials. $\mathbf{I_k}$ and $\mathbf{I_d}$ represents kinetic and diffusion current density respectively. The variable **n** gives overall number of electrons transferred per O_2 molecule, F is the Faraday constant (96485 $Cmol^{-1}$), C_o is the bulk concentration of O_2 (1.2×10^{-6} $molmL^{-1}$), k is the electron transfer rate constant, D_o is the O_2 diffusion coefficient (1.73×10^{-5} cm^2s^{-1}) in 0.1 m KOH, **γ** is kinematic viscosity (0.0109 cm^2s^{-1}) and **ω** is the rotation speed of the electrode. Number of electrons transferred (n) was obtained by calculating the slope of I^{-1} versus ω^{-1}.

Figure 4 shows the K-L plots for BCN-FePc at various electrode potentials. Plot exhibits good linearity and the slope remain approximately constant over -0.4 to -0.6 V potential ranges, indicating similar electron transfer numbers at different potentials. The BCN-FePc shows an n value of 3.8 over a potential range from -0.4 to -0.6 V, suggesting that ORR proceeds by 4-electron pathway.

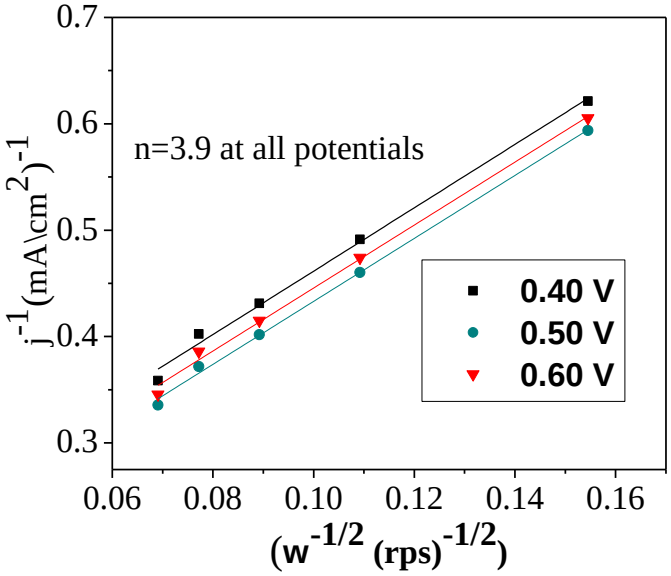

Figure 4. Koutecky–Levich plots for BCN/FePc at different electrode potentials.

The superior performance of BCN-FePc is attributed to the synergy between BCN and FePc molecules. We surmise that the synergy stems from the increase in number of adsorption sites for binding of the O_2 molecule along with the good electronic conductivity. FePc bind oxygen molecule through M-O_2 bond, whereas BCN provides active sites through heteroatoms (B and N), thereby increasing the number of binding sites. Furthermore, BCN also provides the necessary electronic conductivity (increased metallicity of BC_5N) to facilitate efficient electron transfer and also acts as support for the immobilization of FePC molecules.

In fuel cell applications methanol tolerance and CO poisoning are the critical issues associated with the ORR catalyst. An optimum ORR catalyst should have tolerance to methanol crossover and high selectivity for ORR. Therefore, we carried CV measurements for BCN-FePc and Pt/C modified GCE in O_2 saturated KOH in presence of 1M Methanol. As can be seen in Figure 5a oxygen reduction peak is completely vanished and pair of peaks at -0.21 and -0.11 V corresponds to methanol oxidation appeared in case of Pt/C. Whereas BCN/FePc showed no distinctive change in CV curves under similar conditions (Figure 5b). These results suggests that BCN/FePc shows excellent selectivity for ORR even when methanol coexists.

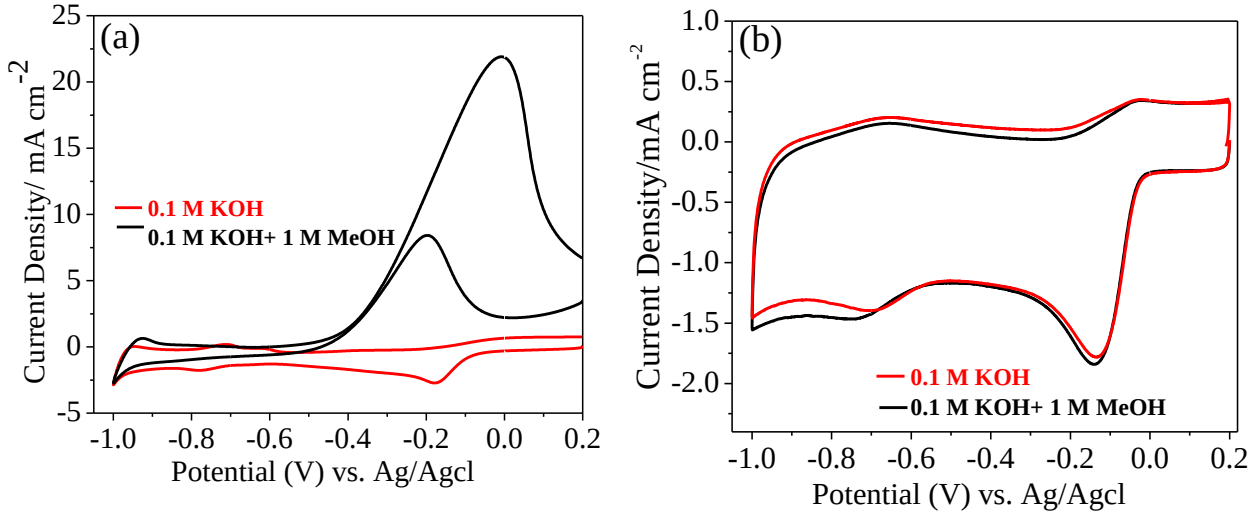

Figure 5. CVs of (a) Pt/C and (b) BCN/FePc electrodes in O_2-saturated 0.1 M KOH with and without 1 M methanol.

5.1.5: Conclusions

The BC_5N-FePc composite has been successfully prepared and used for the oxygen reduction reaction (ORR). The results proved that there is synergy between BCN and FePc and the composite shows better current density and a more positive onset potential which is comparable to commercially available Pt/C. Excellent methanol tolerance and good selectivity for ORR is exhibited by the BCN-FePc composite.

5.1.6: References

1. H. A. Gasteiger, N. M. MarkoviÄ‡, *Science*, **2009**, *324*, 48.
2. B. C. H. Steele, A. Heinzel, *Nature*, **2001**, *414*, 345.
3. K. Gong, F. Du, Z. Xia, M. Durstock, L. Dai, *Science*, **2009**, *323*, 760.
4. H. Meng, P. K. Shen, *Electrochem. Commun.* **2006**, *8*, 588.
5. V. Kiran, K. Srinivasu and S. Sampath, *PhysChemChemPhys* **2013**, *15*, 8744.
6. J. Giner, L. Swette, *Nature* **1966**, *211*, 1291.
7. S. Isogai, R. Ohnishi, M. Katayama, J. Kubota, D. Y. Kim, S. Noda, D. Cha, K. Takanabe, K. Domen, *Chem. Asian J.* **2012**, *7*, 286.
8. J. Chen, K. Takanabe, R. Ohnishi, D. Lu, S. Okada, H. Hatasawa, H. Morioka, M. Antonietti, J. Kubota, K. Domen, *Chem. Commun.* **2010**, *46*, 7492.
9. Y. Gorlin, C.-J. Chung, D. Nordlund, B. M. Clemens, T. F. Jaramillo, *ACS Catal.* **2012**, *2*, 2687.
10. F. Cheng, J. Shen, B. Peng, Y. Pan, Z. Tao, J. Chen, *Nat. Chem.* **2011**, *3*, 79.
11. J. Xu, P. Gao, T. S. Zhao, *Energy Environ. Sci.* **2012**, *5*, 5333.
12. Alonso-Vante, Nicolas, *Chem Phys Chem* **2010**, *11*, 2732.
13. H. Wang, Y. Liang, Y. Li, H. Dai, *Angew. Chem. Int. Ed.*, **2011**, *50*, 10969.
14. L. Yang, S. Jiang, Y. Zhao, L. Zhu, S. Chen, X. Wang, Q. Wu, J. Ma, Y. Ma, Z. Hu, *Angew. Chem. Int. Ed.* **2011**, *50*, 7132.
15. G. Ma, R. Jia, J. Zhao, Z. Wang, C. Song, S. Jia, Z. Zhu, *J. Phys. Chem. C* **2011**, *115*,25148.
16. S. Wang, D. Yu, L. Dai, D. W. Chang, J.-B. Baek, *ACS Nano*, **2011**, *5*, 6202.
17. Z. Yang, Z. Yao, G. Li, G. Fang, H. Nie, Z. Liu, X. Zhou, X. a. Chen, S.Huang, *ACS Nano* **2011**, *6*, 205.
18. H. R. Byon, J. Suntivich, Y. Shao-Horn, *Chem. Mater.* **2011**, *23*, 3421.
19. S. Yang, X. Feng, X. Wang and K. Müllen, *Angew. Chem. Int. Ed.* **2011**, *50*, 5339.
20. Z.-H. Sheng, H.-L. Gao, W.-J. Bao, F.-B. Wang, X.-H. Xia, *J. Mater. Chem.* **2012**, *22*, 390.
21. L. Qu, Y. Liu, J.-B. Baek, L. Dai, *ACS Nano* **2010**, *4*, 1321.
22. K. Gong, F. Du, Z. Xia, M. Durstock, L. Dai, *Science* **2009**, *323*, 760.
23. R. Li, Z. Wei, X. Gou, W. Xu, *RSC Adv.* **2013**, *3*, 9978.

24. S. Wang, L. Zhang, Z. Xia, A. Roy, D. W. Chang, J.-B. Baek, L. Dai, *Angew. Chem. Int. Ed.* **2012**, *51*, 4209.
25. Y. Xue, D. Yu, L. Dai, R. Wang, D. Li, A. Roy, F. Lu, H. Chen, Y. Liu, J. Qu, *Phys.Chem. Chem. Phys.* **2013**, *15*, 12220.
26. S. Wang , E. Iyyamperumal , A. Roy, Y. Xue, D. Yu, L. Dai, *Angew. Chem. Int. Ed.* **2011**, *50*, 11756.
27. L. Lai, J. R. Potts, D. Zhan, L. Wang, C. K. Poh, C. Tang, H. Gong, Z. Shen, J. Lin, R. S. Ruoff, *Energy Environ. Sci.* **2012**, *5*, 7936.
28. Y. Zheng, Y. Jiao, L. Ge, M. Jaroniec, S. Z. Qiao, *Angew. Chem. Int. Ed.* **2013**, *52*, 3110.
29. a) K. Moses, V. Kiran, S. Sampath, C. N. R. Rao, *Chem. Asian. J.* **2014**, *9*, 838. R. Li, Z.Wei, X. Gou, W. Xu, *RSC Adv.*, **2013**, *3*, 9978; b) Z. Chen, D. Higgins, A. Yu, L. Zhang, J. Zhang, *Energy Environ. Sci*. **2011**, *4*, 3167.
30. C. Zhang, R. Hao, H. Yin, F. Liu, Y. Hou, *Nanoscale* **2012**, *4*, 7326.
31. Y. Zhang, G. Mo, X. Li, J. Ye, *J. Power Sources* **2012**, *197*, 93.
32. R. Chen, H. Li, D. Chu, G. Wang, *J. Phys. Chem. C* **2009**, *113*, 20689.
33. Y. Jiang, Y. Lu, X. Lv, D. Han, Q. Zhang, L. Niu and W. Chen, *ACS Catalysis* **2013**, *3*, 1263.
34. T. Taniguchi, H. Tateishi, S. Miyamoto, K. Hatakeyama, C. Ogata, A. Funatsu, S. Hayami, Y. Makinose, N. Matsushita, M. Koinuma, Y. Matsumoto, *Part. Part. Sys. Charact*. **2013**, *30*, 1063.
35. A. Morozan, S. Campidelli, A. Filoramo, B. Jousselme, S. Palacin, *Carbon* **2011**, *49*, 4839.
36. G. Dong, M. Huang and L. Guan, *Phys. Chem. Chem. Phys*. **2012,** *14*, 2557.
37. N. kumar, K. Moses, K. Pramoda, S. N. Shirodkar, A. K. Mishra, U. V. Waghmare, A. Sundaresan, C. N. R. Rao, *J. Mater. Chem. A* **2013**, *1*, 5806.
38. K. Gopalakrishnan, K. Moses, A. Govindaraj, C. N. R. Rao, *Solid State Commun.* **2013**, *173*, 43.
39. S. Sen, K. Moses, A. J. Bhattacharyya, C. N. R. Rao, *Chem. Asian. J.* **2014**, *9*, 100.
40. Y. Li, W. Zhou, H. Wang, L. Xie, Y. Liang, F. Wei, J.-C. Idrobo, S. J. Pennycook, H. Dai, *Nat. Nano.* **2012,** *7*, 394.

5.2: BC_5N and MoS_2-RGO composite as electrode materials for selective electrochemical sensing of dopamine and uric acid in the presence of ascorbic acid

Summary*

A borocarbonitride (BC_5N) has been used as the electrode to selectively detect dopamine and uric acid in the presence of ascorbic acid. These electrodes show good electrocatalytic activity towards the detection of dopamine, with the detection limit of 2.1 μM and showing a linear range over 1-20 μM. BCN also exhibits satisfactory performance in the oxidation of uric acid with a detection limit of 3.8 μM and the linear range from 2 to 40 μM. Significantly, selective detection of dopamine and uric acid in the presence of ascorbic acid was observed by a way of complete peak elimination rather than potential peak separation.

MoS_2-RGO composites have also been used to selectively detect dopamine in the presence of ascorbic acid. The cyclic voltammogramms of DA in PBS at different MoS_2-RGO electrodes (1 : 2, 1 : 1 and 2 : 1) are measured. The oxidation currents for DA measured at MoS_2-RGO (1:2) electrode is higher than that of other composite, suggesting its better electrochemical performance. Hence MoS_2-RGO (1:2) composite is chosen for electrochemical detection of Dopamine. MoS_2-RGO (1:2) composite shows excellent eletrocatalytic activity towards the detection of dopamine with the minimum detection limits being 0.55 μM. This composite shows a linear range of current over the 1–110 μM concentrations of dopamine.

A Paper based on this work has been published *in Electroanalysis, (2015).*

5.2.1: Introduction

Graphene, is an attractive material because of its unusual properties such as high electron mobility, large surface area and mechanical strength.[1] It has potential applications in areas such as electronics,[2] sensors,[3] energy devices[4] and catalysis.[5] Thus, graphene has been extensively used as an electrode in electrochemical applications such as supercapacitors,[6] oxygen reduction reaction (ORR), biosensors[7] and electrochemical sensors.[8] Recently, inorganic graphene analogues like molybdenum sulfide (MoS_2) have also received great attention due to their unique properties.[9, 10] Graphene composites with metals, metal oxides and other materials have also been used for electrochemical applications, especially for electrochemical sensing of dopamine, uric acid and other bio-molecules.[11, 12]

Dopamine and uric acid are important molecules in human metabolism. Dopamine is a crucial neurotransmitter in the central nervous system and its main function is to maintain neuro physiological control of mental activities. Any deviation from optimal concentration of dopamine in the body causes Parkinson's disease [13] or schizophrenia.[14] Uric acid is the final product of purine metabolism and abnormal levels of UA results in gout and hyperuricemia disorders in humans.[15] It is therefore necessary to design sensing devices to determine the change in concentrations of these important biomolecules. Since dopamine and uric acid are electrochemically active, electrochemical oxidation offers a method for the successful detection of these compounds. Commercially available glassy carbon electrode detects but a very high concentrations of these molecules without any selectivity. Therefore there arises a need of materials that can be used as electrodes which can detect minimum amounts of concentration with high selectivity. The electrode materials used for this purpose include graphene,[16] reduced graphene-oxide[17] and graphene-composites.[18-21]

We have employed a borocarbonitride (BCN) to selectively detect dopamine (DA) and uric acid (UA) in the presence of ascorbic acid (AA) which commonly interferes in the detection of DA and UA. Accordingly, in the present study, the synergistic effect from both B and N can couple and results in higher sensitivity towards biomolecules. Borocarbonitrides[23] are structural analogues of graphene which has been previously used as an electrode material in supercapacitors,[24] ORR [25] and Li-ion batteries.[26] Encouraged by the results obtained with BCN modified glassy carbon electrode (GCE) as bio-molecular

sensors, we have also investigated MoS_2-RGO composites for selective detection of dopamine in the presence of ascorbic acid.

5.2.2: Scope of the present investigations

Development of sensitive electrodes for determining of trace amounts of biomolecules is very important. Especially is this true in the case of the selective determination of dopamine and uric acid in the presence of ascorbic acid. Various electrochemically and chemically modified electrodes have been fabricated to resolve the voltammetric peaks of UA, DA and AA. But determining the concentration of these molecules by complete elimination of interfering molecule is desirable. Present work demonstrates the use of borocarbonitrides as an electrode material for selective sensing dopamine and uric acid in the presence of ascorbic acid by completely eliminating the peak from ascorbic acid. Cyclic voltammetry (CV) and differential pulse voltammetry (DPV) were employed to study the electrochemical response of DA and UA molecules at the BCN modified electrode.

Layered MoS_2 in its stable form exist as a semiconductor and therefore as an electrocalyst has limited electronic conductivity. Stacking of MoS_2 layers on conductive graphene surface leads to decrease in resistance connection for the electrons transfer from the substrate to the active sites. This work also presents the use of MoS_2-RGO composite modified GCE for selective sensing of DA in the presence of AA by completely eliminating signal from latter.

5.2.3: Experimental section

Synthesis of $B_{0.15}C_{0.72}N_{0.12}$ (BC_5N): A borocarbonitride (BCN) with the composition $B_{0.15}C_{0.72}N_{0.12}$ was synthesized by following a procedure reported elsewhere.[26] In a typical synthesis, boric acid (60 mg), urea (2.4 g) and activated charcoal (500 mg) are taken in a beaker with water and sonicated for 30 min. The sonicated mixture was heated at 70 ^oC until it becomes slurry and finally transferred to quartz boat to be heated at 900 ^oC in nitrogen atmosphere for 10 hours. Thus obtained product is used for further characterization and analysis.

Preparation of MoS_2-RGO Composites: MoS_2-RGO composites of different compositions were prepared by varying the weight ratios of Mo and graphene. To prepare MoS_2-RGO (1 : 2), 6 mL of (20 mg/mL) GO solution was ultrasonicated with 100 mL distilled water for half an hour. To this, '0.63' mg of $(NH_4)_6Mo_7O_{24}\cdot 6H_2O$ and 0.2 g of NH_2CSNH_2 were added and stirred for an hour. The mixture was heated in an oven at 200 °C for 24 hours in a stainless steel autoclave. The product was washed and dried. Under the conditions of experiments, GO gets reduced to RGO. RGO had 3–5 layers on average. The specific surface area of graphene and the MoS_2-RGO composites calculated by the BET method are 120 and 147 m^2/g respectively.

All the electrochemical measurements were carried out using galvanostat from CH instruments in a three electrode system with GC (glassy carbon) as working electrode, Platinum wire as counter electrode and Ag/AgCl as reference electrode. For the preparation of catalyst ink, 5 mg of BCN was dispersed in 10ml of 1:1 water: ethanol mixture along with 2ul of Nafion and sonicated for 60 min. Glassy carbon electrode (pre-cleaned) was modified by drop casting the catalyst ink (3ul and 10ul) and air dried and used for different measurements. The electrolyte solution was stirred intermittently after each addition of the analyte to make sure homogenous mixing and then the specific measurements were carried out.

5.2.4: Results and Discussion

Figure 1a shows the typical TEM image of BCN sheets, which indicate that the sample is layered. Figure 1b displays the comparison between the **e**lectrochemical impedance spectra (EIS) of bare glassy carbon electrode (GCE) and BCN modified GCE (BCN/GCE) measured in 5mM $K_3Fe(CN)_6$ in 0.1M KCl at 5mV with frequency range of 0.01 to 10^5 Hz. EIS is an useful technique to study the electrochemical performance of the modified electrode surfaces. The diameter of the semicircle obtained in low frequency region gives a quantitative estimate of electron transfer resistance since it indicates electron transfer kinetics of the redox probe at the electrode surface. As shown in Figure 1, the Nyquist plot of bare GCE (denoted by red color) has large semicircular diameter extending beyond 25 MHz indicating a huge electron transfer resistance at the electrode surface, whereas the BCN modified GCE (BCN/GCE, Figure 1) has a very low frequency of 3 KHz.

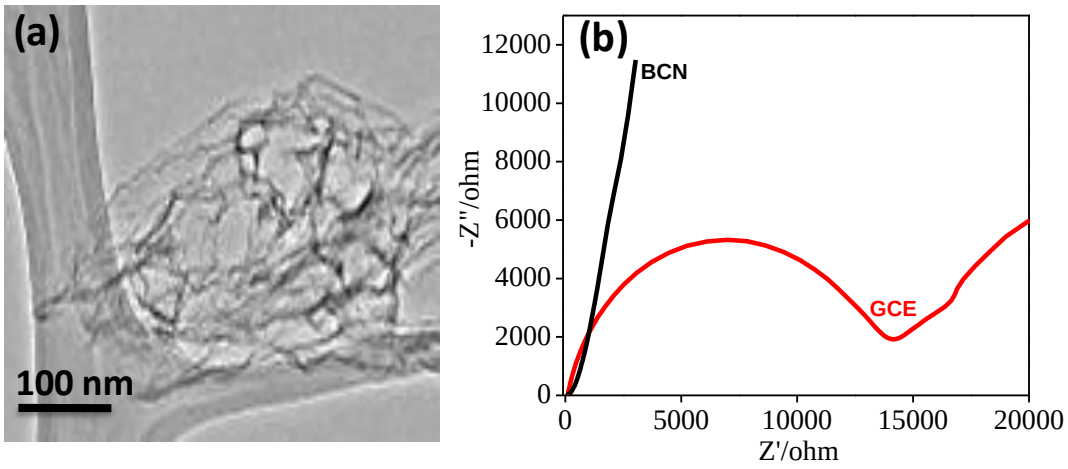

Figure 1. Electrochemical impedance (EI) measured in 5mM $K_3Fe(CN)_6$ in 0.1M KCl at 5mV amplitude with frequency range 0.01 to 105 KHz for BC_5N (black), GCE (red).

This difference in the frequency draws a conclusion that BCN modified GCE can facilitate electron transfer far better than the bare GCE. This evidence is further substantiated in cyclic voltammograms (CV) measured for solutions of Dopamine (DA) and Uric acid (UA). Figure 2a shows the CV of DA measured at BCN/GCE (black) and bare GCE (red) in 0.1 M PBS solution of 7.2 pH.

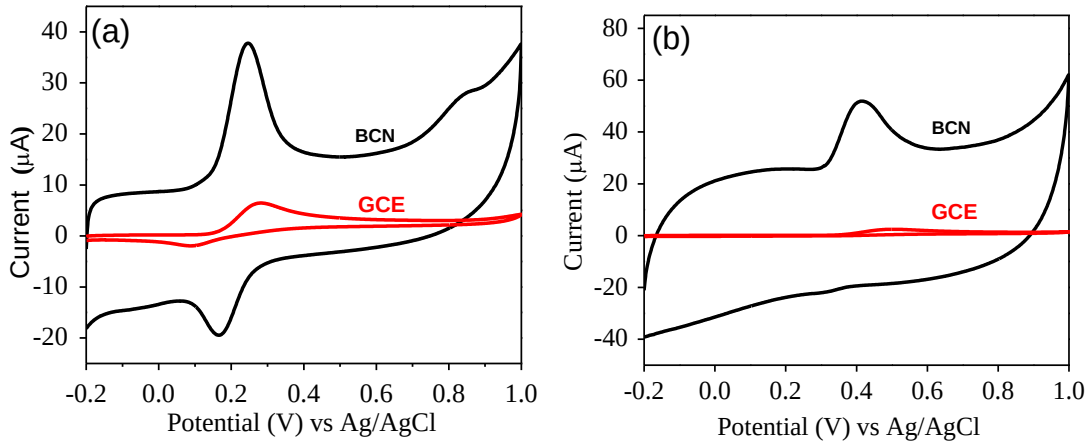

Figure 2. Cyclic voltammograms of 30 uM (a) Dopamine and (b) Uric acid in 0.1 M Phosphate buffer (pH = 7.2) at bare Glassy carbon electrode (red) and BC_5N modified electrode (black) with a scan rate of 40 mV/s.

CV measured at the BCN/GCE showed a well-defined oxidation peak at 0.246 V and reduction peak at 0.164 V with a peak separation of 82 mV, whereas the one measured at

bare GCE has very small redox peaks at 0.281 and 0.091, V respectively with a peak-to-peak separation of 191 mV. Moreover, the oxidation current of DA at BCN/GCE is six times greater than that of the bare GCE. This confirms the superior electrocatalytic performance and fast electron transfer of BCN compared to bare GCE. Figure 2b displays the CV of UA measured at BCN/GCE (black) and bare GCE (red). Similar trend has been observed as in the case of DA oxidation.

Electrochemical oxidation of UA at GCE is very weak with insignificant oxidation peak but a profound peak at 0.414 V for BCN/GCE. Anodic oxidation current in this case is 25 times higher than that was obtained at GCE. The performance of BCN is quite significant and comparable to many graphene modified electrodes. Another important point to be noticed pristine BCN is sufficient to detect dopamine and uric acid without having any modifying layer around it. Modifying layer at instances hampers the performance of the active material. In the present study, BCN has been used in the process without being modified by any external modifier.

The oxidation of dopamine in the experimental conditions is represented by the schematic below.[27]

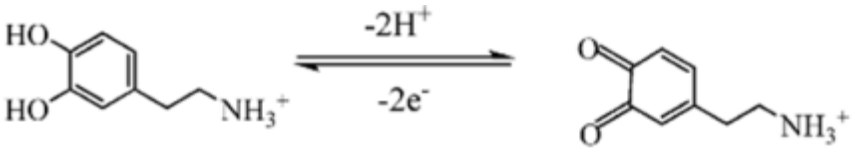

CVs at different scan rates from 40 to 300mV/s of dopamine (100 μM) at BCN modified GCE indicated that peak current was being affected by the scan rate and it increases linearly with increase in the scan rate. Linear dependence of peak current on scan rate reveals that the electrochemical process is controlled by diffusion and adsorption.[27]

Differential pulse voltammetry (DPV) was employed to determine the minimum concentration of DA and UA that can be detected electrochemically as DPV has much higher current sensitivity and resolution than CV. Electrochemical oxidation of DA is determined from 0.5×10^{-6} to 110×10^{-6} mol L^{-1} by DPV method. Figure 3a show the DPV at different concentrations of DA in 0.1 M PBS solution (pH 7.2) measured at BCN/GCE. The current shows a linear dependence with increase in concentration in the 2.3–20 μM range (Figure 3b). Although the anodic oxidation peak appears at 1.3 μM, the peak is not prominent and a

well-defined peak appears from 2.3 µM onwards. The regression equation, i_p (µA)=0.3021×[DA] µM+45.99 with R^2=0.990 is obtained from DPV plots.

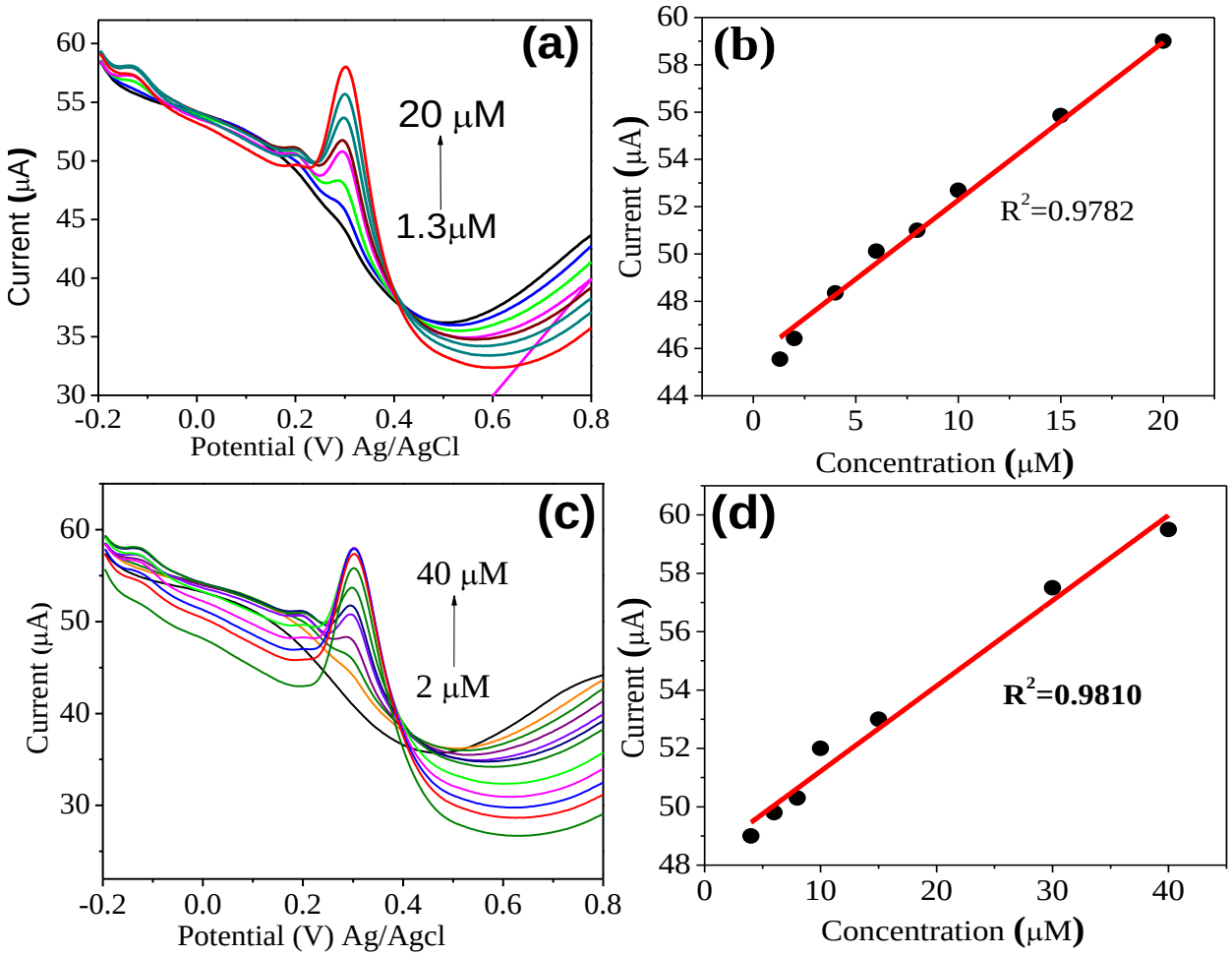

Figure 3. DPV in 0.1 M PBS at BCN modified electrode for different concentration of (a) dopamine and (c) uric acid. Plots of I_A as a function of (b) dopamine and (d) uric acid concentrations.

The minimum detection limit of DA at BCN/GCE is 2.1 µM, calculated from the formula 3σ/slope as reported in the literature.[28] This value is comparable to that of some graphene modified electrodes.[29, 30] In the case of uric acid also the current increases with the increase in concentration and is linear in the range of 4–40 µM and the minimum detection limit calculated according to formula 3σ/slope is 3.8 µM [i_p (µA) =0.2924×[UA] µM+48.29,

R^2=0.991] (Figure 3d). The results obtained here are quite comparable to that of graphene, graphene-composites and other layered analogues of graphene.[31, 32]

Selective and simultaneous detection of DA and UA has been observed with BCN/ GCE by way of complete elimination of AA rather than by separation of individual peaks.[16] Besides individual sensing of dopamine and uric acid, BCN/GCE shows impressive performance towards selective sensing of DA and UA in the presence of ascorbic acid (AA) without showing any oxidation peak of AA. Figure 4 gives the DPV measured at different concentrations of DA and UA from 30–200 μM in the presence of 10 mM AA. With increase in the concentration of DA and UA, the peak current increased linearly. The oxidation current observed for DA is higher than UA, since π–π interaction of DA with graphene-like conjugated surface facilitates easy electron transfer.

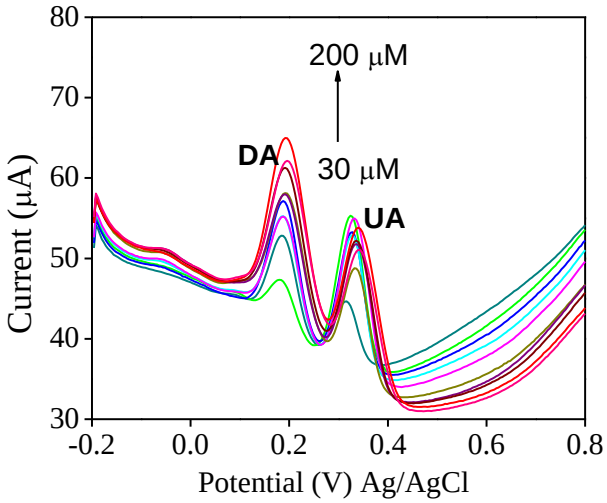

Figure 4: DPV of different concentrations of dopamine and uric acid in the presence of 10 mM ascorbic acid in 0.1M PBS at BCN modified electrode.

BCN showed significant stability for more than 300 cycles as an electrode material for sensing. Figure 5 shows the cyclic voltammograms recorded immediately after adding 100 μM of dopamine to 0.1 M PBS solution (black color) and after running 300 consecutive cycles (red color) at a scan rate of 100mV/s. Comparison between the cyclic voltammograms reveals that BCN showed appreciable reproducibility with minimum loss of current (only 20% after 300 cycles). These results prove that BCN modified can be stable for sensing of important molecules.

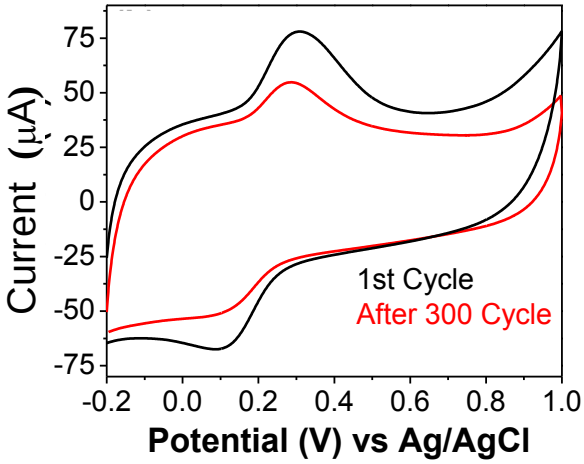

Figure 5. Cyclic voltammograms of 100 μM Dopamine in 0.1M Phosphate buffer (pH = 7.2) at BC_5N modified electrode with a scan rate of 100 mV/s, 1st cycle (black) and 300th cycle (red).

MoS_2-RGO composites for selective detection of dopamine in presence of ascorbic acid:

Figure 6a shows the Cyclic voltammograms (CV) of DA measured with GCE (1), RGO (2) And MoS_2-RGO (3) modified glassy carbon electrodes in 0.1 M PBS solution of 7.2 pH. For DA, the well-defined redox peak with a peak-to- peak separation (ΔE) of 110 mV is displayed by MoS_2-RGO/GCE, much better than by the RGO modified electrode with a ΔE of 140 mV. The oxidation currents for DA measured at MoS_2-RGO/GCE is twice as large as the RGO modified electrode, suggesting better electrochemical performance in the case of former as shown in Figure 6a. The improved electrocatalytic activity of MoS_2-RGO/GCE towards DA can be attributed to the increased surface area (147 m^2/g) and better electrical conductivity. The CV obtained at bare GCE has small redox peaks at 0.281 and 0.091 V, respectively with a peak-to-peak separation of 191 mV.

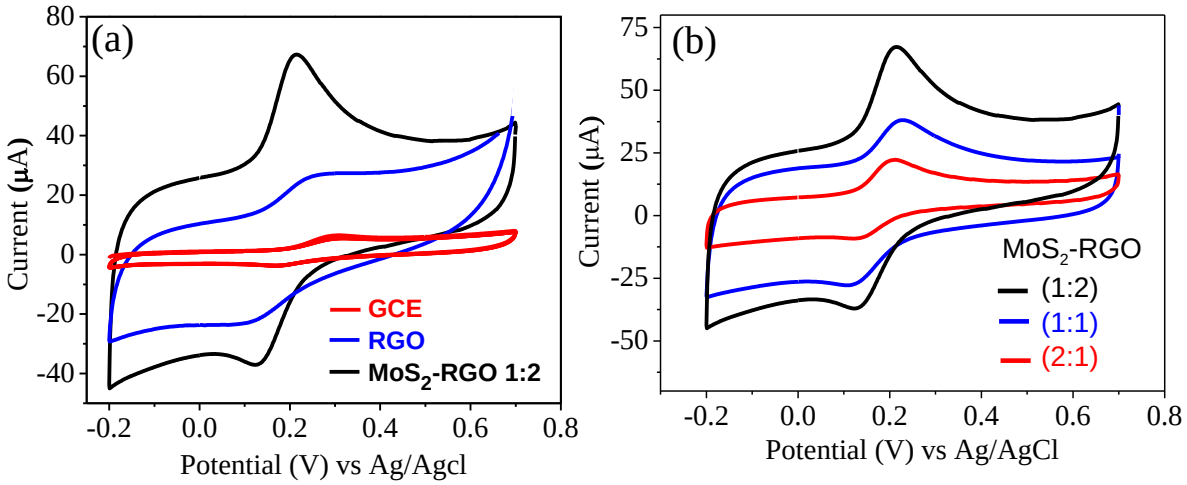

Figure 6. CV of 100 μM dopamine (a) at MoS_2- RGO (1:2, (black), RGO (blue) and GCE (red), (b) MoS_2-RGO (1:2, (black)), (1:1, (blue)) and (2:1, (red)) in 0.1M PBS with a scan rate of 100 mV/s.

The CVs of DA in PBS at different MoS_2-RGO electrodes (1 : 2, 1 : 1 and 2 : 1) are shown in Figure 6b. The oxidation currents for DA measured at MoS_2-RGO (1:2) electrode higher than that of other composite, suggesting its better electrochemical performance. Hence MoS_2-RGO (1:2) composite is chosen for electrochemical detection of Dopamine. The oxidation current for DA is found to be decreasing with increase in amount of MoS_2 in the composite.

Electrochemical oxidation of DA is determined from 0.5×10^{-6} to 110×10^{-6} mol L^{-1} by DPV as shown in Figure 7a. The anodic oxidation current (I_A) peak increases linearly with the concentration of DA in the concentration range 1–110 μM (Figure 7b). The calibration plot obeying the linear equation, i_p (μA)=0.2298×[DA] μM+73.9 with a correlation coefficient (R) of 0.991 (n=5) is obtained (Figure 7b). The minimum detection limit is 0.55 μM, calculated from the formula 3σ/slope as reported in the literature,[28] where σ is the standard deviation of the blank. It is known in the literature that the concentration of ascorbic acid (AA) is higher than that of DA in biological samples. It is therefore necessary to develop a sensitive and selective method for the determination of DA in the presence of AA for diagnostic application. In this regard, we have measured DPV of different concentration DA in the presence of 1 mM AA at MoS_2-Gr/GCE. The regression equation here is i_p (μA) =0.213×[DA] μM+90.57 (R^2=0.994) and the minimum detection limit is 0.94 μM as

calculated from the formula 3σ/slope (Figure 7d). This is comparable with some of the literature reports.[38, 39] The linear dependence of current is in the concentration range 1.5–100 μM is shown in Figure 7d.

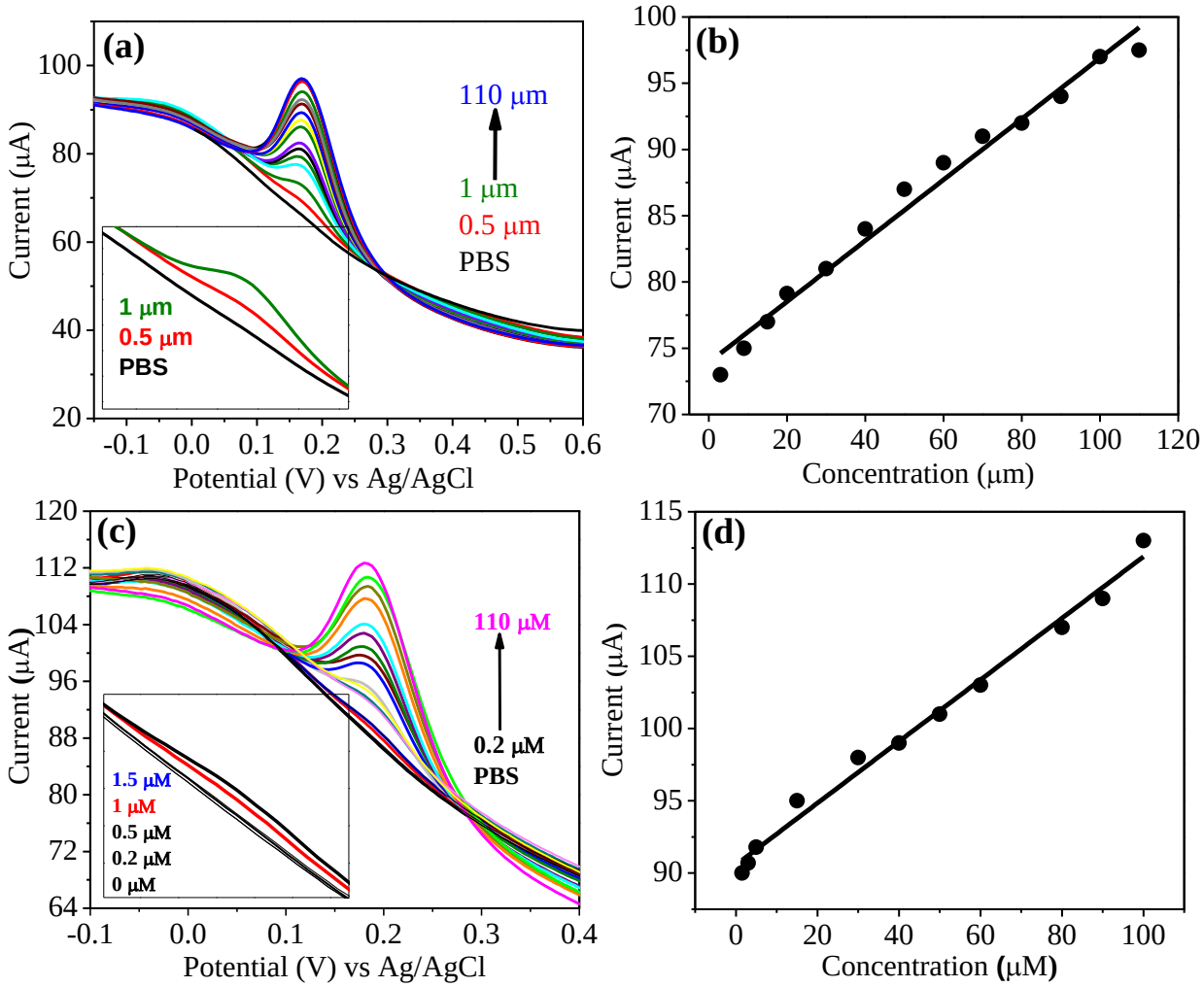

Figure 7. DPV at different concentrations of dopamine in 0.1 M PBS (a) at MoS_2-RGO modified electrode (c) at MoS_2-RGO modified electrode in presence of 1 mM ascorbic acid (Insets shows magnified portion of DPV at lower concentration of dopamine), (b) and (d) Plots of the anodic peak current (I_A) as a function of dopamine concentrations.

5.2.5: Conclusions

From the present study, it can be understood that BCN can be a potential material for being used as an electrode for electrochemical detection of biologically important molecules like dopamine and uric acid even in the presence of ascorbic acid. BCN modified GCE is also used for the simultaneous determination of dopamine and uric acid. This work also demonstrates the synergy in the properties of the MoS_2–RGO composite towards selective detection of dopamine in the presence of ascorbic acid with the 1:2 ratio exhibiting excellent electrocatalytic activities. The high electrocatalytic activity of BCN and MoS_2-RGO composites can be attributed to the enhanced electronic conductivity, large surface area and available edges which can facilitate electron transfer.

5.2.6: References

1. A. K. Geim, *Science*, **2009**, *324*, 1530.
2. A. H. C. Neto, F. Guinea, N. M. R. Peres, K. S. Novoselov, A. K. Geim, *Rev. Mod. Phy.* **2009**, *81*, 109.
3. M. Pumera, *Chem. Soc. Rev.* **2010**, *39*, 4146.
4. M. Pumera, *Energy Environ. Sci.* **2011**, *4*, 668.
5. C. N. R. Rao, A. K. Sood, K. S. Subrahmanyam, A. Govindaraj, *Angew. Chem. Int. Ed*. **2009**, *48*, 7752.
6. C. Liu, Z. Yu, D. Neff, A. Zhamu, B. Z. Jang, *Nano Lett.* **2010**, *10*, 4863.
7. X. Zhou, J. Qiao, L. Yang, J. Zhang, *Adv. Energy Mater.* **2014**, *4*, 1301523.
8. Y. Shao, J. Wang, H. Wu, J. Liu, I. A. Aksay, Y. Lin, *Electroanalysis* **2009**, *22*, 1027.
9. C. N. R. Rao, U. Maitra, U. V. Waghmare, *Chem. Phys. Lett.* **2014**, *609*, 172.
10. H. Li, J. Wu, Z. Yin, H. Zhang, *Acc. Chem. Res.* **2014**, *47*, 1067.
11. W. Hong, H. Bai, Y. Xu, Z. Yao, Z. Gu, G. Shi, *J. Phys. Chem. C* **2010**, *114*, 1822.
12. S.-J. Li, D.-H. Deng, Q. Shi, S.-R. Liu, *Microchim. Acta* **2010**, *177*, 325.
13. J. M. Savitt, V. L. Dawson,T. M. Dawson, *J Clin. Invest.* **2006**, *116*, 1744.
14. A. Zhang, J. L. Neumeyer, R. J. Baldessarini, *Chem. Rev.* **2006**, *107*, 274.
15. J. Ping, J. Wu, Y. Wang, Y. Ying, *Biosens. Bioelectron.* **2012**, *34*, 70.
16. Y. Wang, Y. Li, L. Tang, J. Lu, J. Li, *Electrochem. Commun.* **2009**, *11*, 889.
17. Z. Zhang, J. Yin, *Electrochim. Acta*, **2014**, *119*, 32.
18. K. Chang, W. Chen, *ACS Nano* **2011**, *5*, 4720.
19. Y. Fan, K.-J. Huang, D.-J. Niu, C.-P. Yang, Q.-S. Jing, *Electrochimica Acta*, **2011**, *56*, 4685.
20. K.-J. Huang, L. Wang, J. Li, Y.-M. Liu, *Sens. Actuators B* **2013**, *178*, 671.
21. E. G. da Silveira Firmiano, A. C. Rabelo, C. J. Dalmaschio, A. N. Pinheiro, E. C. Pereira, W. H. Schreiner, E. R. Leite, *Adv. Energy Mater.* **2014**, *4*, 1301523.
22. Z. Sheng, X. Zheng, J. Xu, W. Bao, F. Wang, X. Xia, *Biosens. Bioelectron.* **2012**, *34*, 125.
23. N. kumar, K. Moses, K. Pramoda, S. N. Shirodkar, A. K. Mishra, U. V. Waghmare, A. Sundaresan and C. N. R. Rao, *J. Mater. Chem. A* **2013**, *1*, 5806.

24. K. Gopalakrishnan, K. Moses, A. Govindaraj and C. N. R. Rao, *Solid State Commun.* **2013**, *175*, 43.
25. S. Sen, K. Moses, A. J. Bhattacharyya, C. N. R. Rao, *Chem. Asian J.* **2014**, *9*, 100.
26. K. Moses, V. Kiran, S. Sampath, C. N. R. Rao, *Chem. Asian J.* **2014**, *9*, 838.
27. Y. Zhou, W. Tang, J. Wang, G. Zhang, S. Chai, L. Zhang, T. Liu, *Analytical Methods*, **2014**, *6*, 3474.
28. B. Ntsendwana, B. B. Mamba, S. Sampath, O. A. Arotiba, *Int. J. Electrochem. Sci.* **2012**, *7*, 3501.
29. Y.-R. Kim, S. Bong, Y.-J. Kang, Y. Yang, R. K. Mahajan, J. S. Kim, H. Kim, Biosens. Bioelectron. **2010**, *25*, 2366.
30. M. C. Rodríguez, M. D. Rubianes, G. A. Rivas, *J. Nanosci. Nanotec.* **2008**, *8*, 6003.
31. D. Han, T. Han, C. Shan, A. Ivaska, L. Niu, *Electroanalysis* **2010**, *22*, 2001.
32. S. Su, H. Sun, F. Xu, L. Yuwen, L. Wang, *Electroanalysis* **2013**, *25*, 2523.